

A Dissertation for the Degree of Doctor of Philosophy

**Development of a rotary pump using the rotational clap
mechanism**

회전 클랩 기구를 이용한 로터리 펌프 개발에 관한 연구

February 2016

SungBo Shim

Major of Biosystems Engineering

Department of Biosystems & Biomaterials Science and Engineering

SEOUL NATIONAL UNIVERSITY

Development of a rotary pump using the rotational clap mechanism

지도교수 김 경 옥

이 논문을 공학박사 학위논문으로 제출함

2016년 2월

서울대학교 대학원

바이오시스템·소재학부 바이오시스템공학전공

심 성 보

심성보의 박사 학위논문을 인준함

2016년 2월

위 원 장 _____ (인)

부위원장 _____ (인)

위 원 _____ (인)

위 원 _____ (인)

위 원 _____ (인)

A Dissertation for the Degree of Doctor of Philosophy

**Development of a rotary pump using the rotational
clap mechanism**

February 2016

By

SungBo Shim

Major of Biosystems Engineering

Department of Biosystems & Biomaterials Science and Engineering

SEOUL NATIONAL UNIVERSITY

Development of a rotary pump using the rotational clap mechanism

SungBo Shim

Abstract

To avoid problems of the slider-crank mechanism, many attempts have been made to develop rotary-type machines. Nevertheless, none of them were practically successful except the Wankel engine, mainly due to poor sealing and manufacturing techniques. Furthermore, their theoretical analyses have not been advanced, and it still remains as just an idea or kinematic analysis stage. As technology has recently enough to solve the problems associated with the rotary-type machines, they have attracted attentions again.

In this study, the rotational clap mechanism that was first presented by Kim was improved, detailed mechanisms to realize the mechanism was developed, and the characteristics analysis and performance prediction of the rotational clap pump were conducted based on a prototype pump and its verification test.

A working principle of the mechanism and its design parameters were introduced with kinematic analysis of the pins and rotors. The vector equations developed in the analysis can be used to easily depict the motion characteristics of the mechanism for different design parameters. The inter-relationships between the design parameters were also examined to determine the proper crank radius and pin

distance within the allowable number of gear teeth and rotor size. The thickness angle of the jaw and inner radius of the rotor were found to be most significant constraints that affect the crank radius and pin distance of the mechanism.

The pressure, driving torque, and efficiency characteristics of the pump were evaluated to analyze the fundamental performance of the pump. The design constraints of the fixed internal gear and gear of shaft link using involute curves were examined, and the strength of the main components was designed.

The involute-type internal gear has design limits caused by three kinds of interferences. The kinematic constraints can aggravate this limits. As a result, designing a pump for high-pressure and low flow rate conditions with an involute-type internal gear can be difficult.

To verify the fundamental performances of this pump, a prototype pump was manufactured, and pump test equipment was installed. The simulated data of the flow rate, differential pressure, driving torque, and efficiencies were verified by comparison with experimental data.

The main parameters that affected the pump performance were the clearance between the rotor jaws and chambers, the number of jaws, the jaw width, and the jaw height. Therefore, the parameter studies that affect the pump performance were conducted, and the performance was then predicted under these conditions.

In these analysis results, the rotational clap mechanism can be realized as a pumping device on equal performance with conventional rotary pumps. In addition, It can have compact size, be good in a state of high viscosity and shear sensitive fluid, high flow rate, and works well with less vibration and power loss.

Keywords: Rotary pump, rotational clap mechanism, Pump performance, Pump efficiency, Pump slip, low shear pump.

Student Number: 2007-30311

TABLE OF CONTENTS

1. Introduction	1
2. Literature review	3
3. Rotational clap mechanism	5
3.1. Description of mechanism	5
3.2. Kinematic analysis	7
3.2.1. Displacement	7
3.2.2. Velocity	17
3.2.3. Accelerations	20
3.3. Mechanism parameters	23
3.3.1. Driving link	23
3.3.2. Rotor	24
3.4. Performance characteristics	26
3.4.1. Performance parameters	26
3.4.2. Interrelations of parameters	27
3.4.3. Performance characteristics	32
3.5. Conclusions	34
4. Pump performance analysis	35
4.1. Introduction	35
4.2. Pressure analysis	36
4.2.1. Assumptions	36
4.2.2. Pressure head	36

4.2.2.1. Pressure head due to friction	36
4.2.2.2. Pressure head due to mass acceleration	37
4.2.2.3. Pressure head due to piping components	37
4.2.2.4. Pressure head due to gravity	38
4.2.2.5. Total head	38
4.2.3. Pressure analysis in clap pump	39
4.3. Forces and driving torque analysis	42
4.3.1. Forces and driving torque calculation	42
4.3.2. Parametric study	49
4.4. Pump performance analysis	56
4.4.1. Theory of pump performance	56
4.4.1.1. Fundamental theory for the pump performance	56
4.4.1.2. Theory of pump slip and forces caused by fluid viscosity	57
4.4.1.3. Theory of efficiency for conventional positive-displacement pump	62
4.4.2. Performance analysis for rotational clap pumps	65
4.4.2.1. Analysis for slip and forces caused by fluid viscosity	65
4.4.2.2. Efficiency analysis for rotational clap pump	70
4.5. Conclusions	71
5. Design of a prototype rotational clap pump	73
5.1. Introduction	73
5.2. Gear of the shaft link and fixed internal gear	73
5.2.1. Geometric constraints	73
5.2.1.1. Involute interference	76
5.2.1.2. Trochoid interference	76

5.2.1.3. Trimming interference	77
5.2.1.4. Case studies to avoid interferences in this pump	78
5.2.2. Gear strength calculation for prototype pumps	82
5.3. Crank	89
5.3.1. Design for strength	89
5.3.2. Design for stiffness	98
5.4. Pins	102
5.4.1. Design for strength	102
5.5. Shaft link	107
5.5.1. Design for strength	107
5.5.2. Design for stiffness	116
5.6. Conclusions	118
6. Verification test	119
6.1. Prototype pump and test equipment	119
6.2. Pressure analysis of the pump and piping system	122
6.3. Verification	124
6.3.1. Clearances calculation and validation of performance parameters when the throttle valve is fully open	124
6.3.2. Pressure pulsation and cavitation	135
6.3.2.1. Using multi-pumps	135
6.3.2.2. Using a pulsation dampener	137
6.4. Conclusions	143
7. Performance prediction	144
7.1. Introduction	144

7.2. Parametric study	144
7.3. Performance prediction	147
7.4. Comparison among the conventional positive-displacement pumps and the clap pump	156
7.5. Conclusions	159
8. Overall conclusions and further studies	160
9. References	162
Appendix A: Specifications of piping system for the pump	166
Appendix B: Pump performance curves	172
Appendix C: Manufacturing specifications	179

LIST OF TABLES

Table 4.1 Parameters involved in the parametric study	50
Table 5.1 Calculation of a profile-shifted internal gear and external gear when the center distance is not given (Kohara Gear Industry Co., Ltd., 2015).	74
Table 5.2 Calculation of a profile-shifted internal gear and external gear when the center distance is given (Kohara Gear Industry Co., Ltd., 2015).	75
Table 5.3 Cases to prevent internal gear interference when gear module $m=1$, center distance $a=5\text{ mm}$ (=crank radius r_c), and reference pressure angle $\alpha=20^\circ$	79
Table 5.4 Cases to prevent internal gear interferences when gear module $m=1$, and reference pressure angle $\alpha=27^\circ$	80
Table 5.5 Example of the effect of diameter of internal and external gears on interference.	81
Table 5.6 Specifications of the clap pump used in performance test.	86
Table 5.7 Lewis form factor (Hong, 2013).	88
Table 6.1 Specifications of the test equipment for the pump.	121
Table 6.2 Loss coefficients for pipe components (Hydraulic Institute, 1990; E. S. Menon et al, 2010).	123
Table 6.3 Percentage errors of the simulated suction pressure, discharge pressure, and driving torque at the primary frequency 5.5 Hz.	131
Table 6.4 Effect of the number of pistons or rotor pairs on flow variation.	136
Table 7.1 Serviceability of positive-displacement pumps (Wilson, 1950)	158

Table 7.2 Characteristics of conventional positive-displacement pumps and clap pump	158
--	-----

LIST OF FIGURES

Fig.2.1. A patented rotational clap mechanism (Kim, 2011)	4
Fig.3.1. Components of the rotational clap mechanism	6
Fig.3.2. Motion of the pins relative to the center of rotor.	9
Fig.3.3. Rotating radius of the pin when $r_c = 5mm$, $L = 40mm$, $Z_r = 30$, and $Z_p = 20$	11
Fig.3.4 Relative angular displacement of the rotors, θ_{rel} , when $r_c = 5mm$, $L = 40mm$, $Z_r = 30$, and $Z_p = 20$	14
Fig.3.5. Clearances angle between two adjacent jaws when $r_c = 5mm$, $L = 40mm$, $Z_r = 30$, and $Z_p = 20$	14
Fig.3.6. Sequence of suction and discharge motions by the clearance angle between two adjacent jaws.	15
Fig.3.7. Suction and discharge motions occurring simultaneously when the rotors have 4 jaws	16
Fig.3.8. Pin velocity when $r_c = 5mm$, $L = 40mm$, $Z_r = 30$, $Z_p = 20$, and $\dot{\theta}_c = 740rpm$	19
Fig.3.9. Angular velocity of rotor when $r_c = 5mm$, $L = 40mm$, $Z_r = 30$, $Z_p = 20$, and $\dot{\theta}_c = 740rpm$	19
Fig.3.10. Pin accelerations when $r_c = 5mm$, $L = 40mm$, $Z_r = 30$, $Z_p = 20$, and $\dot{\theta}_c = 740rpm$	22
Fig.3.11. Angular acceleration of rotor when $r_c = 5mm$, $L = 40mm$, $Z_r = 30$, $Z_p = 20$, and $\dot{\theta}_c = 740rpm$	22

Fig.3.12. Rotor parameters.	25
Fig.3.13. Determination of the number of internal gear teeth and crank radius by the number of the gear teeth and rotor jaws.	28
Fig.3.14. Combinations of the crank radius, number of rotor jaws and pin distance to make the thickness angle positive.	30
Fig.3.15. Maximum rotating radius of the pin.	31
Fig.3.16. Minimum rotating radius of the pin.	31
Fig.3.17. Displacement of a clap mechanism having a jaw of 50 cm width and 40 cm height and a rotor of 65 cm outer radius.	33
Fig.4.1. Fluid flow through a pipe.	40
Fig.4.2. Fluid movement in the rotational clap mechanism.	41
Fig.4.3. A schematic diagram of the fluid movement	41
Fig.4.4 Direction changes in hydraulic forces acting on the rotors and the housing	43
Fig.4.5 Free-body diagram for forces acting on the rotors, gear of the shaft link, internal gear and the crank.	48
Fig.4.6 Rotor forces F_{R1} and F_{R2}	51
Fig.4.7 Pin forces R_{p1} and R_{p2}	51
Fig.4.8 Gear force R_p	52
Fig.4.9 Driving torque T_i	52
Fig.4.10 Driving torque vs. crank radius r_c	53
Fig.4.11 Pin forces vs. crank radius r_c	54
Fig.4.12 Gear forces vs. crank radius r_c	55
Fig.4.13 Drag due to the viscosity of the liquid(Wilson, 1950).	61
Fig.4.14 Viscous and pressure forces acting on fluid element(Wilson, 1950).	62

Fig.4.15 Wilson's efficiency curve for a pump(Wilson, 1950).	65
Fig.4.16 Jaw model simplified as a rectangle for the analysis of flow and torque losses.	69
Fig.4.17 Flow losses in suction and discharge chamber of the pump.	70
Fig.4.18 Force losses in suction and discharge chamber of the pump.	70
Fig.5.1. Meshing of the internal gear and external gear(Kohara Gear Industry Co., Ltd., 2015).	75
Fig.5.2. Forces acting on the gears	87
Fig.5.3. Cantilever model of a gear tooth (Shigley and Mischke, 2001).	87
Fig.5.4. Loads and dimensions for the main shaft of crank.	92
Fig.5.5. Shear force acting on the crank shaft	97
Fig.5.6. Bending Moment acting on the crank shaft	97
Fig.5.7. Maximum deflection of the main shaft of the crank.	101
Fig.5.8. Deflection of the main shaft of the crank.	101
Fig.5.9. Loads acting on the pin.	105
Fig.5.10. Shear force acting on the pin.	106
Fig.5.11. Bending moment acting on the pin.	106
Fig.5.12. Free-body diagram of forces acting on the shaft link	111
Fig.5.13. Force components with respect to the $x_c'-y_c'-z_c'$ plane.	112
Fig.5.14. Driving torque vs. the length of shaft link.	114
Fig.5.15. Shear force vs. the length of shaft link.	115
Fig.5.16. Bending moment vs. the length of shaft link.	115
Fig.5.17. Parameters for the deflection of the shaft link.	117
Fig.5.18. Deflection of the shaft link according to the length of the shaft.	117
Fig.6.1. A system used for pump testing.	120

Fig.6.2. Second-order polynomial model representing the differential pressure vs. flow rate of a flowmeter (Hydrotechnik, 2015).	124
Fig.6.3. Measured flow rate as a function of the crank speed with the throttle valve fully opened.	126
Fig.6.4. Comparison between the measured and simulated volumetric efficiency as a function of the crank speed when the clearances δ_1 and δ_2 were 0.2572 mm.	126
Fig.6.5. Comparison between the simulated and measured flow rates in the time domain.	127
Fig.6.6. Comparison between the simulated and measured suction pressures in the time domain.	127
Fig.6.7. Comparison between the simulated and measured discharge pressures in the time domain.	128
Fig.6.8. Comparison between simulated and measured driving torque in time domain.	128
Fig.6.9. Comparison between the simulated and measured flow rates in the frequency domain.	129
Fig.6.10. Comparison between the simulated and measured suction pressures in the frequency domain.	129
Fig.6.11. Comparison between the simulated and measured discharge pressures in the frequency domain.	130
Fig.6.12. Comparison between the simulated and measured driving torque in the frequency domain.	130
Fig.6.13. Comparison between the measured and simulated pump efficiency as a function of the crank speed.	132

Fig.6.14. Measurement of the clearances with a feeler gauge.	133
Fig.6.15. Measurement of the crank misalignment with a dial gauge.	134
Fig.6.16. Fluctuation of friction torque caused by the crank misalignment	134
Fig.6.17. Pulsation dampeners installed in the pump testing system.	139
Fig.6.18. Effect of the pulsation dampener on flow variations.	139
Fig.6.19. Effect of the pulsation dampener on discharge pressure variations.	140
Fig.6.20. Comparison between measured and simulated p-Q curves when the crank speed was 100 rpm.	140
Fig.6.21. Comparison between measured and simulated p-Q curves when the crank speed was 200 rpm.	141
Fig.6.22. Comparison between measured and simulated p-Q curves when the crank speed was 300 rpm.	141
Fig.6.23. Comparison between measured and simulated p-Q curves when the crank speed was 400 rpm.	142
Fig.6.24. Comparison between measured and simulated p-Q curves when the crank speed was 500 rpm.	142
Fig.7.1. Efficiency vs. clearance when $n = 100$ rpm, $h = 10$ mm, $N = 4$	145
Fig.7.2. Efficiency vs. jaw height when $n = 100$ rpm, $\delta_1 = \delta_2 = 0.06$ mm, and $N = 4$	146
Fig.7.3. Efficiency vs. number of jaws when $n = 100$ rpm, $\delta_1 = \delta_2 = 0.06$ mm, $h = 10$	146
Fig.7.4. Performance curves under the initial conditions (crank speed, $n = 100$ rpm).	148
Fig.7.5. Pump efficiency as a function of $\frac{\mu n}{\Delta p}$ under the initial conditions	

(crank speed, n = 100 rpm).	149
Fig.7.6. Performance curves under the second conditions (crank speed, n = 100 rpm).	150
Fig.7.7. Pump efficiency as a function of $\frac{\mu n}{\Delta p}$ under the second conditions (crank speed, n = 100 rpm).	151
Fig.7.8. Volumetric efficiency before and after the parameter optimization (crank speed, n = 100 rpm).	152
Fig.7.9. Torque efficiency before and after the parameter optimization (crank speed, n = 100 rpm).	153
Fig.7.10. Pump efficiency before and after the parameter optimization (crank speed, n = 100 rpm).	153
Fig.7.11. Performance curves under the final conditions (crank speed, n = 100 rpm).	154
Fig.7.12. Pump efficiency as a function of $\frac{\mu n}{\Delta p}$ under the final conditions (crank speed, n = 100 rpm).	155
Fig.7.13. Space between different types fo rotors and the housing	157
Fig.A.1. The flow in sudden contraction and expansion pipe.	167
Fig.A.2. Dimensions of $A_{2,s}$, $A_{2,d}$, $l_{2,s}$, $l_{2,d}$, $\theta_{2,s}$, and $\theta_{2,d}$	171
Fig.A.3. Dimensions of $l_{1-2,s}$, $l_{1-2,d}$, $\theta_{1-2,s}$, and $\theta_{1-2,d}$	171
Fig.A.4. Performance curve when $N=4$, $\omega_c=100$ rpm, $d_1=d_2=0.06$ m, $h=14$ mm, and $W=20.72$ mm.	172
Fig.A.5. Performance curve when $N=4$, $\omega_c=300$ rpm, $d_1=d_2=0.06$ m, $h=14$ mm, and $W=20.72$ mm.	173

Fig.A.6. Performance curve when $N=4$, $\omega_c=500$ rpm, $d_1=d_2=0.06$ m, $h=14$ mm, and $W=20.72$ mm.	174
Fig.A.7. Performance curve when $N=4$, $\omega_c=750$ rpm, $d_1=d_2=0.06$ m, $h=14$ mm, and $W=20.72$ mm.	175
Fig.A.8. Performance curve when $N=4$, $\omega_c=1000$ rpm, $d_1=d_2=0.06$ m, $h=14$ mm, and $W=20.72$ mm.	176
Fig.A.9. Comparison between flow rate vs pressure curves according to crank speed.	177
Fig.A.10. Comparison between volumetric efficiency vs pressure curves according to crank speed.	177
Fig.A.11. Comparison between torque efficiency vs pressure curves according to crank speed.	178
Fig.A.12. Comparison between overall efficiency vs pressure curves according to crank speed.	178

1. Introduction

Conventional rotary pumps intakes the fluid through the clearance between the rotating elements and pump housing and force it to move along the way to discharge out of the pump. Advantages of the rotary pump include self-priming, relatively smooth discharging and delivering fluid to high pressure. However, it has also have disadvantages such as small displacement, excessive wear due to erosion which are caused by the small clearance between the rotating elements and the pump housing, etc.

Slider-crank mechanism has been widely used in many types of plunger and piston pumps. They have also problems of high level of vibration and power losses due to excessive friction between the reciprocating piston and pump housing as the pump speed increases. To avoid such problems of the slider-crank mechanism, many attempts have been made to develop rotary-type machines (Deng et al. 2013; Fedorovich. 2006; Librovih. 2003; Librovich. 2004; Masmi Sakita. 2006; Morgado. 2004; Shih. 1993a; Shih. 1993b; Xu. 2014). Nevertheless, their theoretical analyses have not been advanced, and it still remains as just an idea or kinematic analysis stage. Furthermore, none of them were practically successful except the Wankel engine, mainly due to poor sealing and manufacturing techniques.

As technology has recently enough to solve the problems associated with the rotary-type machines, they have attracted attentions again.

This study also attempted to avoid problems of the reciprocating slider-crank mechanism, which has been used in many positive-displacement pumps, as a pumping device using a rotational clap mechanism that was first presented by Kim (Kim, 2011; Kim 2012), because the rotational clap mechanism is one of the most

simple rotary mechanism to realize a pumping device. It can increase the displacement and works well with less vibration and power loss although the pumping speed increases.

Research objectives

The detailed mechanisms to realize the rotational clap mechanism presented by Kim (Kim, 2011; Kim, 2012) have some problems for application to a pump. Therefore, the objectives of this study were to improve the rotational clap mechanism, develop a detailed mechanism, and conduct the characteristics analysis and performance prediction of a rotary pump using the advanced rotational clap mechanism. Details of the objectives are as follows:

1. To improve and develop for the detailed mechanism based on analysis of the basic mechanism,
2. To do kinematic analysis of the rotational clap mechanism so that the theoretical basis of its working principle, motions, and performance characteristics can be founded,
3. To develop a computer model to simulate the pressure, torque, flow rate, and efficiency of the pump when the rotational clap mechanism is used as a pumping device including prototype testings for the model verification,
4. To standardize the design process of the mechanism components based on the prototype pump design,
5. To investigate the effects of the design parameters and their constraints of the mechanism on its performance,
6. To predict the pump performance under the given condition, and compare among the conventional positive-displacement pumps and clap pump.

2. Literature review

In the late 19th century, Reuleaux(1876) already introduced various types of rotary machines in his book. However, the Wankel engine is only one that has been commercialized successfully. Main obstacle was lack of technology to solve the problems of poor sealing and manufacturing. Since he introduced the Wankel engine in 1954, much research has been conducted on the Wankel engine. Yamamoto (1981) has reviewed the history of rotary engine development from the late 16th to the late 19th centuries and classified the rotary engines into three different types: single rotating, oscillatory rotating, and planetary rotating engines. Hege (2006) also has summarized many endeavors for the commercialization of Wankel engines conducted in automobile companies from 1957 to 2000.

Advances in the sealing technology has made the commercialization of the Wankel engines possible. Performance improvement of other types of rotary machines may also be attributable to such advances.

Murphy (2012) introduced a number of rotary machines and their characteristics in his master's thesis. Shih (1993a; 1993b) analyzed the kinematics of the cycloidal internal combustion engine mechanism and compared the epicycloidal and hypocycloidal internal combustion engine mechanisms. Librovič (2003; 2004) presented the basic structure and work principles of the rotary vane engine (RVE) based on the Kauertz-Virmel-type rotary combustion engine along with the analysis, design, and modeling of a rotary vane engine. Hao Deng et al (2013), Masmi Sakita (2006), and Xu (2014) also conducted studies on the fundamental principles and its characteristics. Among these ideas, the closest to commercialization were those of Morgado (2004) and Fedorovich (2007). However, they have mainly

focused on the rotary engines. Few works have been made for the rotary pumps.

Kim (2011 and 2012) first presented the rotational clap mechanism in his patents. The mechanism is comprised of a cylindrical housing, a crank shaft, a crank pin, an internal gear, connecting rods and rotational pins, an external gear attached on the end of connecting shaft, and a pair of rotary pistons with several wings (see fig.2.1). A pair of rotary pistons that are driven at different angular velocities caused by the relative motions among the crankshaft, internal gear, and external gear make the clearance between the wings. This clearance results in suction and discharge motions. He insisted that the advantages of this mechanism are the high volumetric efficiency, small size, low weight, and low noise.

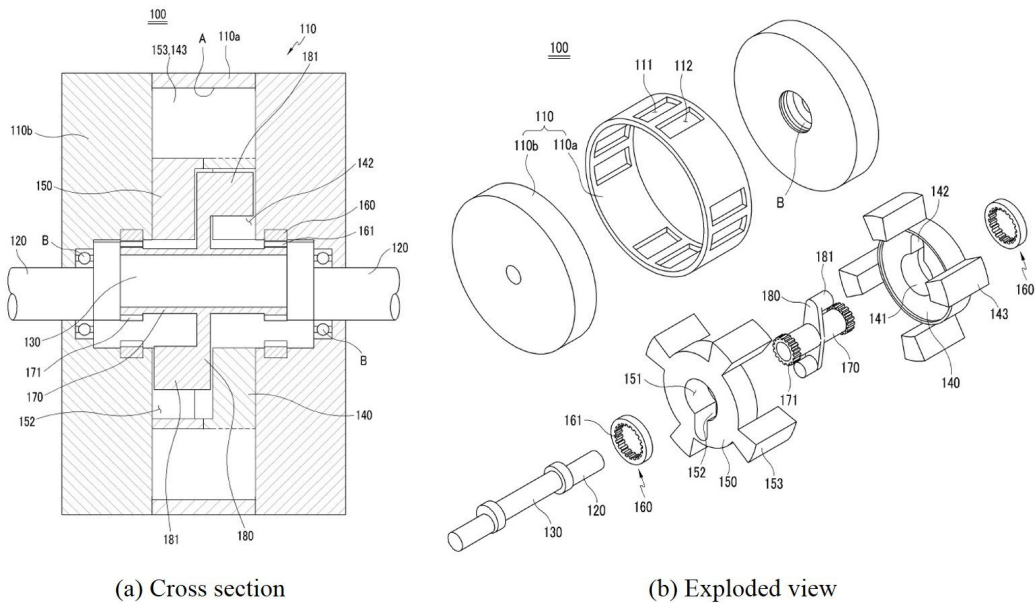


Fig.2.1. A patented rotational clap mechanism (Kim, 2011).

3. Rotational clap mechanism

3.1. Description of mechanism

The rotational clap mechanism is a five-link spatial mechanism which comprises of a crank as the driving link, a shaft link having two pins symmetrically located in opposite direction at a plate rigidly mounted on its middle and two gears rigidly attached to both ends, two rotors with jaws equally spaced along their circumferences and a fixed internal gear. The width of jaw is extended unilaterally twice of the rotor width so that the two rotors jaws can be engaged completely. Fig.3.1 illustrates the linkages of the mechanism. As the crank rotates, the gear pin-jointed to the crank rotates about the crank pin and at the same time about the center of the fixed internal gear, making the motions of a hypo-cyclic gear train. The shaft link also can rotate about the crank pin and about the center of the fixed internal gear at the same time. This motion of the shaft link makes the pins rotate about the center of the fixed internal gear with a periodically-varying radius. The rotors are driven by the pins on the shaft link through a pin-in-slot joint where the pins move along a radial slot on the contacting faces of two rotors. Since the rotational radius of the pin changes as the crank rotates at a constant velocity, angular velocities of the two rotors also change accordingly. The relative velocity between the two rotors makes one rotor lead and lag periodically with respect to the other. These lead and lag motions result in a continuous cycle of approach-contact-recess of two adjacent rotor jaws similar to a hand clapping from which the mechanism is named. The continuous lead and lag motions can be used for the suction and discharge motions required for pumping.

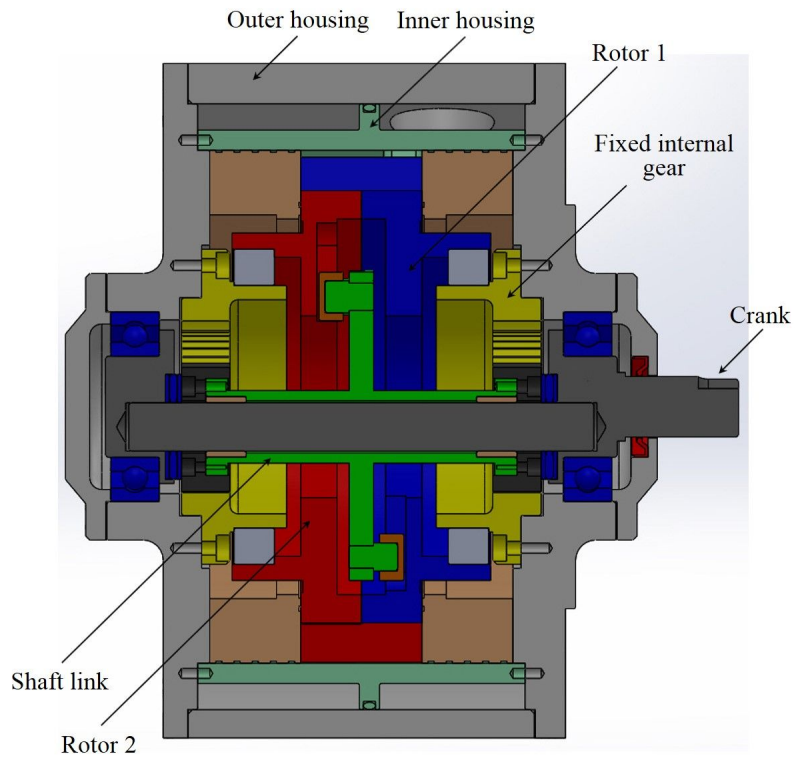
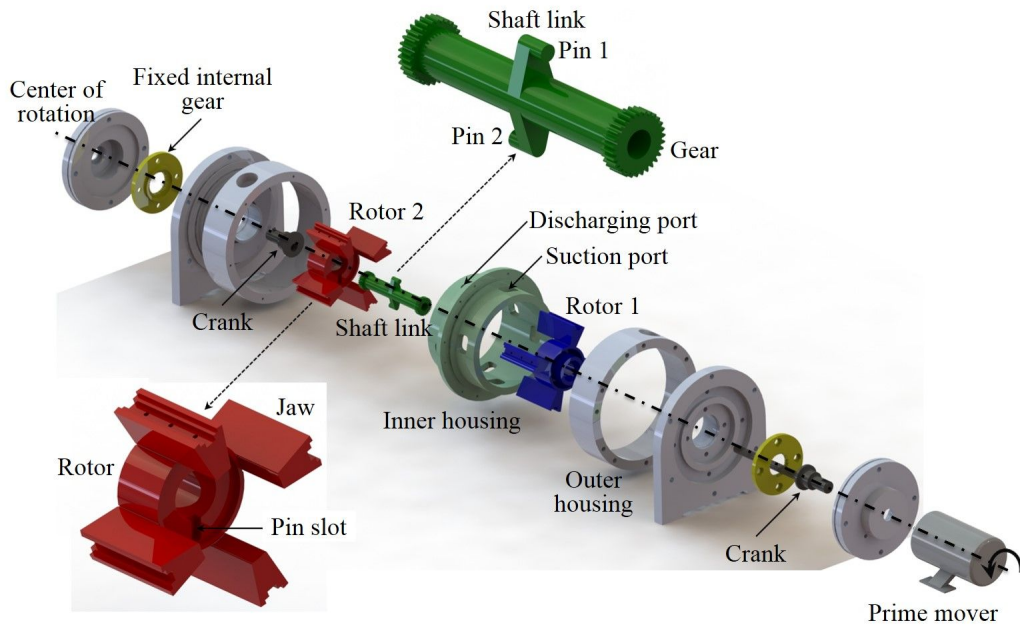


Fig.3.1. Components of the rotational clap mechanism.

3.2. Kinematic analysis

3.2.1. Displacement

Let O-X-Y be a rectangular coordinate with positive x axis to the right, y axis upwards, and its origin at the center of rotors, which also coincides with the center of the fixed internal gear. As the crank rotates counter-clockwise as shown in fig.3.2, the pin-jointed gear rotates clockwise with respect to the crank pin and at the same time rotates counter-clockwise about the center of the fixed internal gear. Then, absolute angular displacement of the gear can be expressed as equation (3.1). Let the pins on the shaft link be designated as and respectively. Then the position vector equations for the pins can be expressed as equations (3.2) and (3.3) respectively.

$$\phi = \left(1 - \frac{Z_r}{Z_p}\right)\theta_c \quad (3.1)$$

$$r_c e^{i\theta_c} + \frac{L}{2} e^{i\phi} - r_{p_1} e^{i\theta_{p_1}} = 0 \quad (3.2)$$

$$r_c e^{i\theta_c} - \frac{L}{2} e^{i\phi} + r_{p_2} e^{i\theta_{p_2}} = 0 \quad (3.3)$$

where, ϕ = absolute angular displacement of the gear

Z_r = number of teeth on the fixed internal gear

Z_p = number of teeth on the gear of the shaft link

θ_c = angular displacement of the crank

r_c = crank radius

L = distance between pins P_1 and P_2

r_{p_1} = radius of pin P_1 with respect to the center of rotor O

r_{p_2} = radius of pin P_2 with respect to the center of rotor O

θ_{p_1} = angular displacement of vector OP_1

θ_{p_2} = angular displacement of vector OP_2

It should be noted that the pins on the shaft link rotate negatively clockwise about the center of the rotors as the crank rotates positively counter-clockwise. In other words, θ_c is positive while ϕ , θ_{p_1} and θ_{p_2} are all negative in equations (3.2) and (3.3).

Substituting equation (3.1) into equation (3.2) and separating the real and imaginary parts of equation (3.2) yields,

$$r_c \cos \theta_c + \frac{L}{2} \cos \left[\left(1 - \frac{Z_r}{Z_p} \right) \theta_c \right] = r_{p_1} \cos \theta_{p_1} \quad (3.4)$$

$$r_c \sin \theta_c + \frac{L}{2} \sin \left[\left(1 - \frac{Z_r}{Z_p} \right) \theta_c \right] = r_{p_1} \sin \theta_{p_1} \quad (3.5)$$

solving for r_{p_1} yields,

$$r_{p_1} = \sqrt{r_c^2 + \frac{L^2}{4} + r_c L \cos \frac{Z_r}{Z_p} \theta_c} \quad (3.6)$$

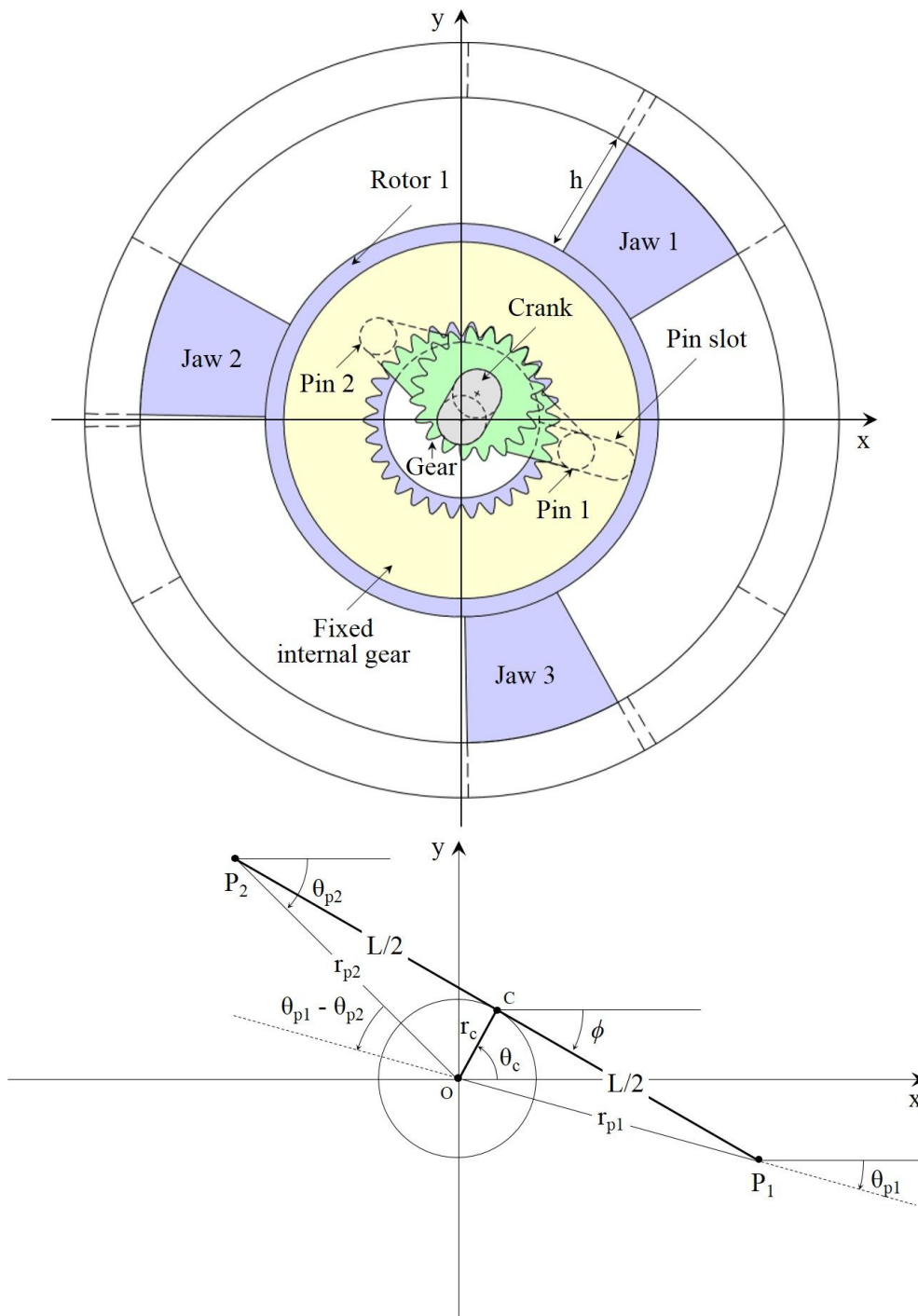


Fig.3.2. Motion of the pins relative to the center of the rotor.

For the clap mechanism to make one complete cycle, the gear on the shaft link must rotate through $\phi = 2\pi$ in clockwise and the crank accordingly in count-clockwise through an angle of $\theta_c = \frac{2\pi Z_p}{Z_r - Z_p}$ radians. Therefore, θ_{p_1} can be expressed as equation (3.7-a) for the first half of the cycle and as equation (3.7-b) for the second half. That is

$$\text{when } 0 \leq \theta_c \leq \frac{\pi Z_p}{Z_r - Z_p}$$

$$\theta_{p_1} = -\cos^{-1} \left[\frac{1}{r_{p_1}} \left\{ r_c \cos \theta_c + \frac{L}{2} \cos \left(1 - \frac{Z_r}{Z_p} \right) \theta_c \right\} \right] \quad (3.7-a)$$

$$\text{when } \frac{\pi Z_p}{Z_r - Z_p} < \theta_c \leq \frac{2\pi Z_p}{Z_r - Z_p}$$

$$\theta_{p_1} = -\pi - \cos^{-1} \left[\frac{1}{r_{p_1}} \left\{ -r_c \cos \theta_c - \frac{L}{2} \cos \left(1 - \frac{Z_r}{Z_p} \right) \theta_c \right\} \right] \quad (3.7-b)$$

Similarly, solving equation (3.3) for r_{p_1} and θ_{p_2} yields,

$$r_{p_2} = \sqrt{r_c^2 + \frac{L^2}{4} - r_c L \cos \frac{Z_r}{Z_p} \theta_c} \quad (3.8)$$

$$\text{when } 0 \leq \theta_c \leq \frac{\pi Z_p}{Z_r - Z_p}$$

$$\theta_{p_2} = -\cos^{-1} \left[\frac{1}{r_{p_2}} \left\{ -r_c \cos \theta_c + \frac{L}{2} \cos \left(1 - \frac{Z_r}{Z_p} \right) \theta_c \right\} \right] \quad (3.9-a)$$

$$\text{when } \frac{\pi Z_p}{Z_r - Z_p} < \theta_c \leq \frac{2\pi Z_p}{Z_r - Z_p}$$

$$\theta_{p_2} = -\pi - \cos^{-1} \left[\frac{1}{r_{p_1}} \left\{ r_c \cos \theta_c - \frac{L}{2} \cos \left(1 - \frac{Z_r}{Z_p} \right) \theta_c \right\} \right] \quad (3.9-b)$$

As the crank rotates with a constant angular velocity, the pins are constrained to move along the radial slots on the rotors and at the same time rotate about the center of the rotors with radii of r_{p_1} and r_{p_2} varying periodically with a period of $\tau = 2\pi \frac{Z_p}{Z_r}$ as shown in fig.3.3. It is also noted from fig.3.3 that r_{p_1} decreases as r_{p_2} increases and r_{p_1} is a minimum when r_{p_2} is a maximum, and vice versa.

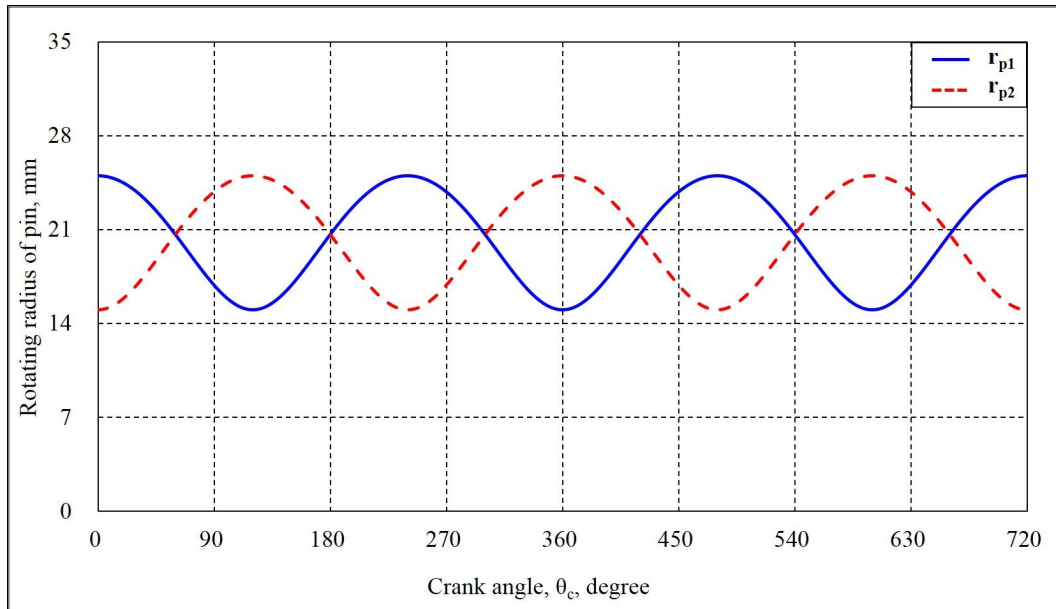


Fig.3.3. Rotating radius of the pin when $r_c = 5 \text{ mm}$, $L = 40 \text{ mm}$, $Z_r = 30$, and $Z_p = 20$.

When the two rotors having N jaws are assembled, a total of $2N$ clearances can

be formed by every two adjacent jaws and the rotor housing. The volume of the clearance varies with the relative angular displacement θ_{rel} of the two rotors, which also varies with a period of $\tau = 2\pi \frac{Z_p}{Z_r}$ as shown in fig.3.4 and determined as

$$\theta_{rel} = \theta_{p_1} - \theta_{p_2} \quad (3.10)$$

Then, as the crank rotates, the clearance angles in front and back of a jaw can be expressed respectively as follows:

$$\theta_{front} = (\theta_{rel})_{max} - \theta_{rel} \quad (3.11)$$

$$\theta_{back} = (\theta_{rel})_{max} + \theta_{rel} \quad (3.12)$$

Fig. 3.5 shows the front and back clearance angles as a function of crank angle. It is noted from fig.3.5 that the clearance angle varies with a period of $\tau = 2\pi \frac{Z_p}{Z_r}$ so that when two adjacent jaws are in contact, the clearances in the front and back of the two jaws in contact reach the maximum. Therefore, the maximum values of θ_{front} and θ_{back} are given as

$$(\theta_{front})_{max} = (\theta_{rel})_{max} - (-\theta_{rel})_{max} = 2(\theta_{rel})_{max} \quad (3.13)$$

$$(\theta_{back})_{max} = (\theta_{rel})_{max} + (\theta_{rel})_{max} = 2(\theta_{rel})_{max} \quad (3.14)$$

As the clearance angle increases from zero to a maximum, a suction motion occurs between the two adjacent jaws while it decreases from a maximum to zero, a

discharge motion occurs. These suction and discharge motions occur as many time as the number of clearances that can be formed by the rotors during a period of $\tau = 2\pi \frac{Z_p}{Z_r}$. Fig. 3.6 illustrates a sequence of the suction and discharge motions that

can be developed during one complete cycle of a rotational clap mechanism having 3-jaw rotors ($N=3$), 20-tooth gear ($Z_p=20$) and 30-tooth internal gear ($Z_r=30$).

Fig.3.4 shows that the two rotors come into contact at crank angles of

$\theta_c = \frac{\pi Z_p}{2Z_r}(2K-1)$, $K=1, 2, 3, \dots$. At these crank angles, r_{p_1} and r_{p_2} becomes equal,

that is,

$$r_{p_1} = \sqrt{r_c^2 + \frac{L^2}{4} + r_c \cos \frac{Z_r}{Z_p} \frac{\pi Z_p}{2Z_r}} = \sqrt{r_c^2 + \frac{L^2}{4}} \quad (3.15)$$

$$r_{p_2} = \sqrt{r_c^2 + \frac{L^2}{4} - r_c \cos \frac{Z_r}{Z_p} \frac{\pi Z_p}{2Z_r}} = \sqrt{r_c^2 + \frac{L^2}{4}} \quad (3.16)$$

and θ_{rev} between r_{p_1} and r_{p_2} becomes

$$\theta_{rev} = \cos^{-1} \frac{r_{p_1}^2 + r_{p_2}^2 - L^2}{2r_{p_1}^2 r_{p_2}^2} = \cos^{-1} \frac{4r_c^2 - L^2}{4r_c^2 + L^2} \quad (3.17)$$

Then, $(\theta_{rel})_{\max}$ can be obtained as follows as depicted in fig.3.2:

$$(\theta_{rel})_{\max} = \pi - \cos^{-1} \frac{4r_c^2 - L^2}{4r_c^2 + L^2} \quad (3.18)$$

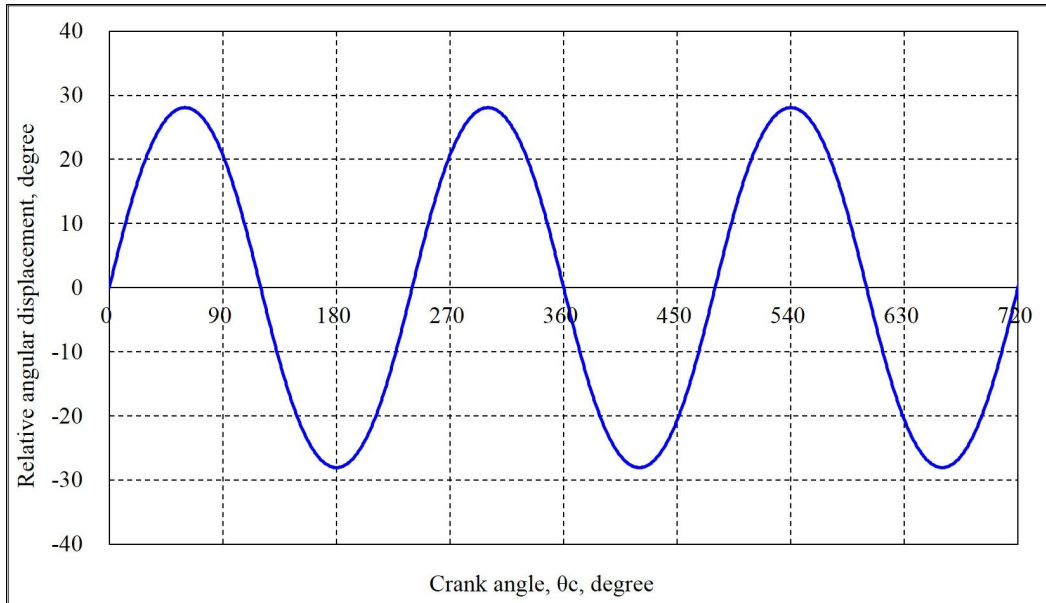


Fig.3.4 Relative angular displacement of the rotors θ_{rel} when $r_c = 5 \text{ mm}$, $L = 40 \text{ mm}$, $Z_r = 30$, and $Z_p = 20$.

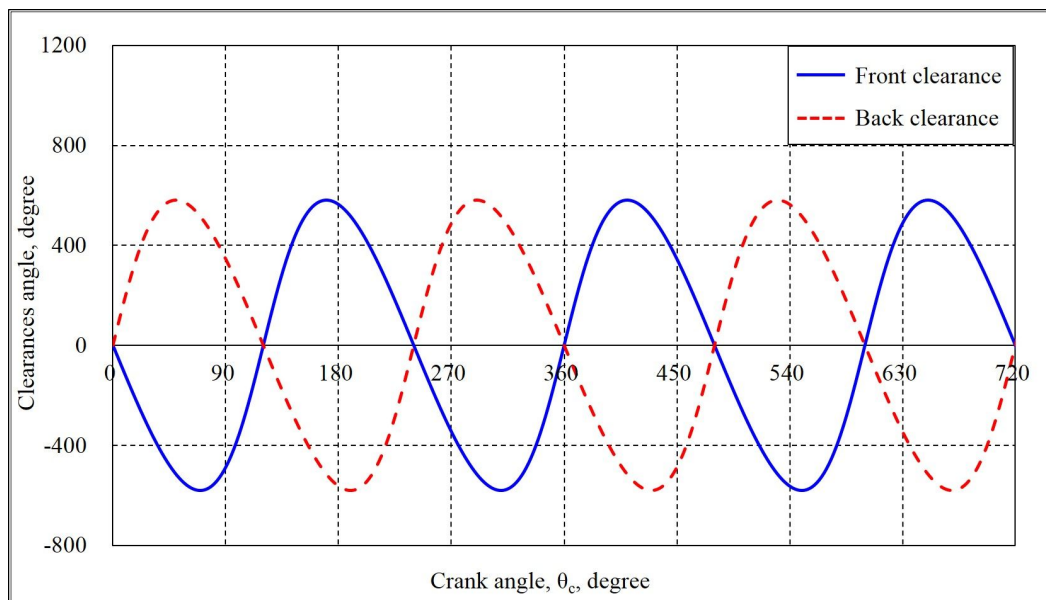


Fig.3.5. Clearances angle between two adjacent jaws when $r_c = 5 \text{ mm}$, $L = 40 \text{ mm}$, $Z_r = 30$, and $Z_p = 20$.

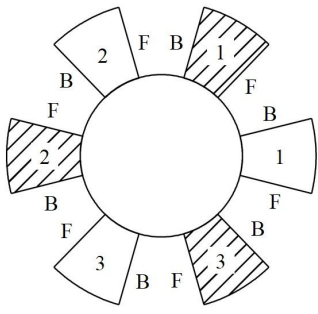
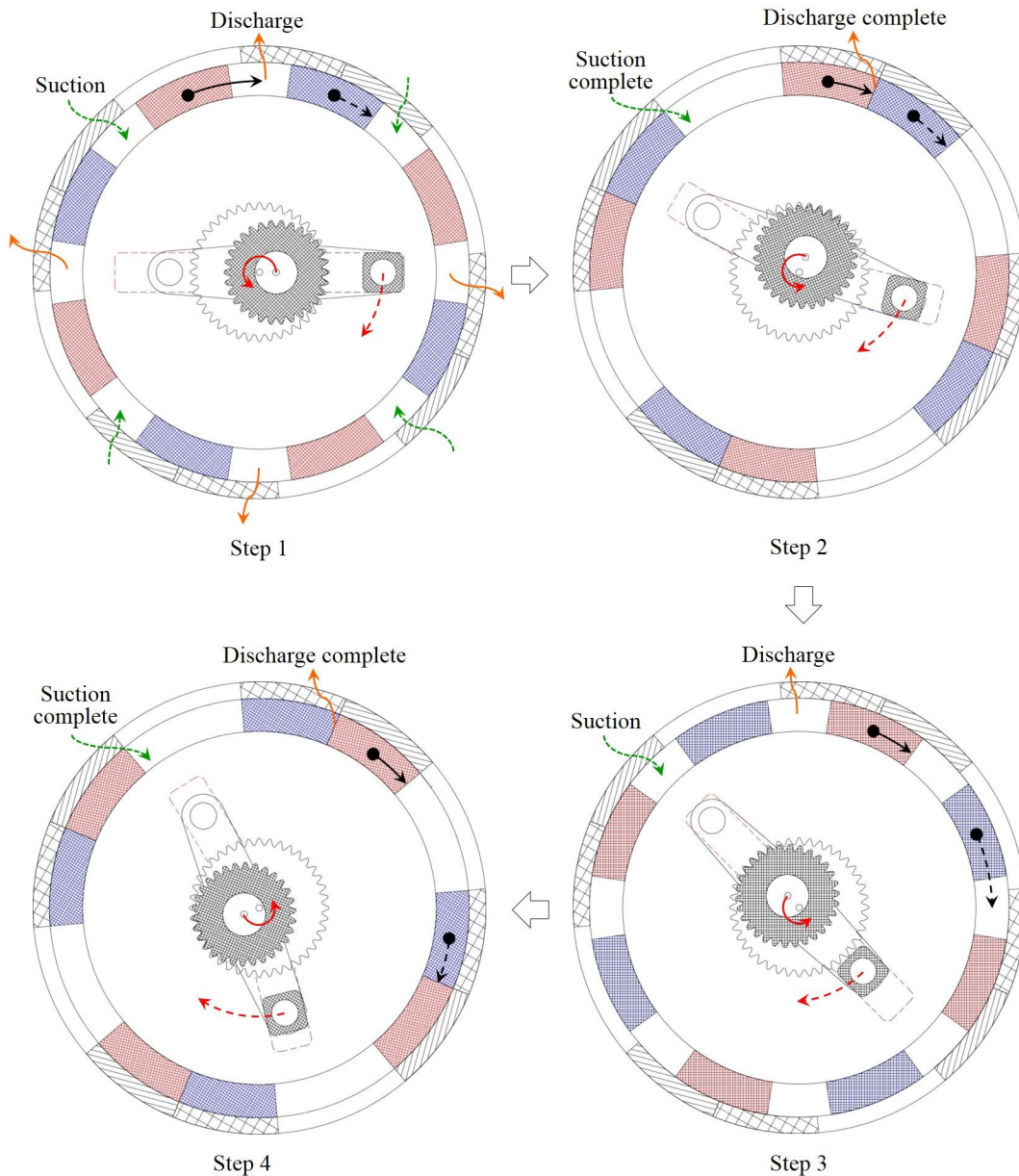
Crank angle, degree	Clearance between adjacent two jaws						Jaw arrangement  F : Front face of jaw B : Back face of jaw $\tau = 2\pi \times Z_p / Z_r = 240^\circ$ No. of jaws : 3 $Z_r = 30$ $Z_p = 40$
	1B-1F	1B-2F	2B-2F	2B-3F	3B-3F	3B-1F	
0	Discharge	Suction	Discharge	Suction	Discharge	Suction	
60	Suction	Discharge	Suction	Discharge	Suction	Discharge	
120	Discharge	Suction	Discharge	Suction	Discharge	Suction	
180	Suction	Discharge	Suction	Discharge	Suction	Discharge	
240	Discharge	Suction	Discharge	Suction	Discharge	Suction	
300	Suction	Discharge	Suction	Discharge	Suction	Discharge	
360	Discharge	Suction	Discharge	Suction	Discharge	Suction	
420	Suction	Discharge	Suction	Discharge	Suction	Discharge	
480	Discharge	Suction	Discharge	Suction	Discharge	Suction	
540	Suction	Discharge	Suction	Discharge	Suction	Discharge	
600	Discharge	Suction	Discharge	Suction	Discharge	Suction	
660	Suction	Discharge	Suction	Discharge	Suction	Discharge	
720	Discharge	Suction	Discharge	Suction	Discharge	Suction	

Fig.3.6. Sequence of suction and discharge motions by the clearance angle between two adjacent jaws.



1 cycle (1 revolution of rotors) \Rightarrow $4N$ steps, N : number of jaws

Fig.3.7. Suction and discharge motions occurring simultaneously when the rotors have 4 jaws.

3.2.2. Velocity

As the crank rotates with a constant angular velocity $\dot{\theta}_c$ the absolute angular velocity of the gear on the shaft link is obtained by taking time derivative of equation (3.1) as follows:

$$\dot{\phi} = \left(1 - \frac{Z_r}{Z_p}\right) \dot{\theta}_c \quad (3.19)$$

Differentiating the position vector equation (3.2) with respect to time yields

$$ir_c \dot{\theta}_c e^{i\theta_c} + i\dot{\phi} \frac{L}{2} e^{i\phi} - \dot{r}_{p_1} e^{i\theta_{p_1}} - ir_{p_1} \dot{\theta}_{p_1} e^{i\theta_{p_1}} = 0 \quad (3.20)$$

Equation (3.20) can be resolved into two equations (3.21) and (3.22) by equating the real and imaginary parts. That is

$$-r_c \dot{\theta}_c \sin\theta_c - \frac{L}{2} \dot{\phi} \sin\phi - \dot{r}_{p_1} \cos\theta_{p_1} + r_{p_1} \dot{\theta}_{p_1} \sin\theta_{p_1} = 0 \quad (3.21)$$

$$r_c \dot{\theta}_c \cos\theta_c + \frac{L}{2} \dot{\phi} \cos\phi - \dot{r}_{p_1} \sin\theta_{p_1} - r_{p_1} \dot{\theta}_{p_1} \cos\theta_{p_1} = 0 \quad (3.22)$$

Similarly, following equations can be obtained from equation (3.3).

$$-r_c \dot{\theta}_c \sin\theta_c + \frac{L}{2} \dot{\phi} \sin\phi + \dot{r}_{p_2} \cos\theta_{p_2} - r_{p_2} \dot{\theta}_{p_2} \sin\theta_{p_2} = 0 \quad (3.23)$$

$$r_c \dot{\theta}_c \cos\theta_c - \frac{L}{2} \dot{\phi} \cos\phi + \dot{r}_{p_2} \sin\theta_{p_2} + r_{p_2} \dot{\theta}_{p_2} \cos\theta_{p_2} = 0 \quad (3.24)$$

Solving equations (3.21) and (3.22) for \dot{r}_{p_1} and $\dot{\theta}_{p_1}$ gives velocities of pin P_1 and rotor 1 as

$$\dot{r}_{p_1} = -r_c \dot{\theta}_c \sin(\theta_c - \theta_{p_1}) - \frac{L}{2} \dot{\phi} \sin(\phi - \theta_{p_1}) \quad (3.25)$$

$$\dot{\theta}_{p_1} = \frac{r_c \dot{\theta}_c \cos(\theta_c - \theta_{p_1}) + \frac{L}{2} \dot{\phi} \sin(\phi - \theta_{p_1})}{r_{p_1}} \quad (3.26)$$

Similarly, velocities of pin P_2 and rotor 2, \dot{r}_{p_2} and $\dot{\theta}_{p_2}$, are obtained from equations (3.23) and (3.24) as follows:

$$\dot{r}_{p_2} = r_c \dot{\theta}_c \sin(\theta_c - \theta_{p_2}) - \frac{L}{2} \dot{\phi} \sin(\phi - \theta_{p_2}) \quad (3.27)$$

$$\dot{\theta}_{p_2} = \frac{-r_c \dot{\theta}_c \cos(\theta_c - \theta_{p_2}) + \frac{L}{2} \dot{\phi} \cos(\phi - \theta_{p_2})}{r_{p_2}} \quad (3.28)$$

Fig. 3.8 and 3.9 show \dot{r}_{p_1} , \dot{r}_{p_2} , $\dot{\theta}_{p_1}$ and $\dot{\theta}_{p_2}$ as a function of the crank angle during one complete cycle of the clap mechanism.

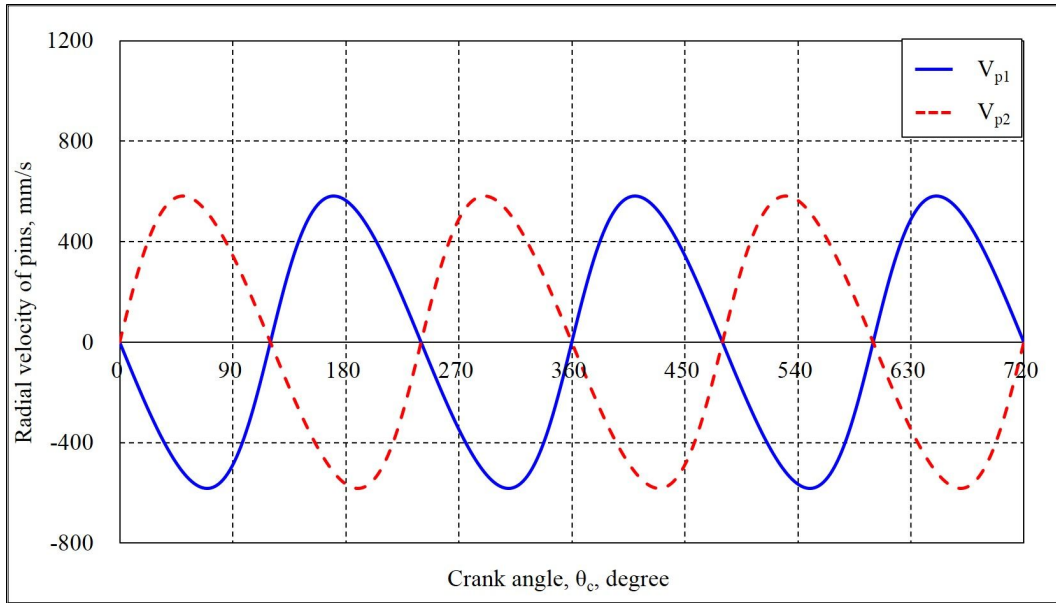


Fig.3.8. Pin velocity when $r_c = 5 \text{ mm}$, $L = 40 \text{ mm}$, $Z_r = 30$, $Z_p = 20$, and $\dot{\theta}_c = 740 \text{ rpm}$.

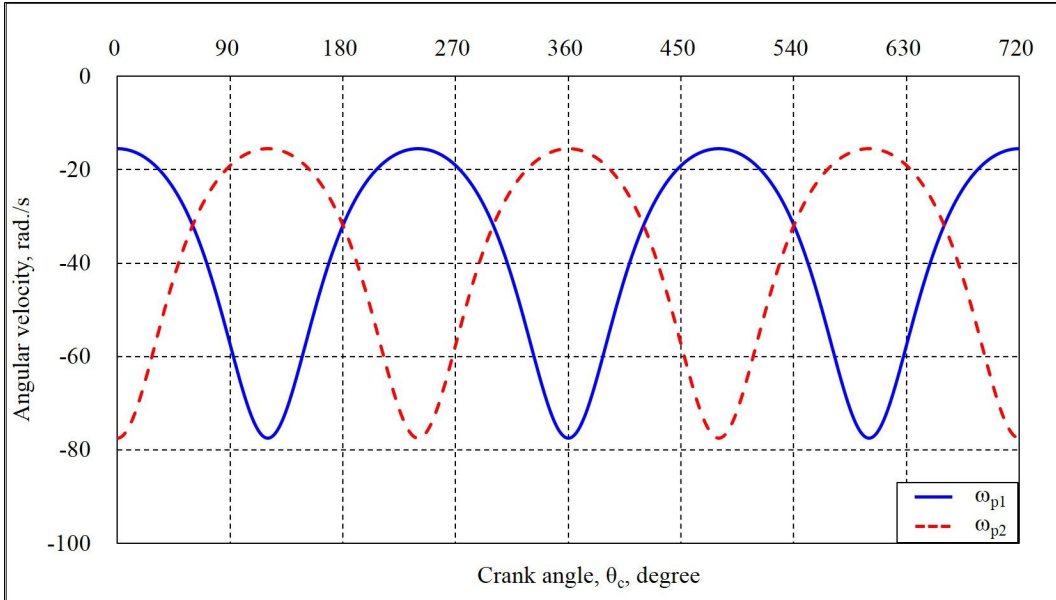


Fig.3.9. Angular velocity of rotor when $r_c = 5 \text{ mm}$, $L = 40 \text{ mm}$, $Z_r = 30$, $Z_p = 20$, and $\dot{\theta}_c = 740 \text{ rpm}$.

3.2.3. Accelerations

Accelerations of the pin and rotor are obtained by taking time derivative of the velocity vector equations. Differentiating equations (3.25) and (3.26) with respect to time and equating the real and imaginary parts yield a set of two simultaneous equations. Solving these equations for \ddot{r}_{p_1} and $\ddot{\theta}_{p_1}$ gives the accelerations of pin P_1 and rotor 1 as follows:

$$\begin{aligned} \ddot{r}_{p_1} = & -r_c \ddot{\theta}_c \sin(\theta_c - \theta_{p_1}) - \frac{L}{2} \ddot{\phi} \sin(\phi - \theta_{p_1}) - r_c \dot{\theta}_c^2 \cos(\theta_c - \theta_{p_1}) \\ & - \frac{L}{2} \dot{\phi}^2 \cos(\phi - \theta_{p_1}) + r_{p_1} \dot{\theta}_{p_1}^2 \end{aligned} \quad (3.29)$$

$$\begin{aligned} \ddot{\theta}_{p_1} = & \frac{1}{r_{p_1}} \left[r_c \ddot{\theta}_c \cos(\theta_c - \theta_{p_1}) + \frac{L}{2} \ddot{\phi} \cos(\phi - \theta_{p_1}) - r_c \dot{\theta}_c^2 \sin(\theta_c - \theta_{p_1}) \right. \\ & \left. - \frac{L}{2} \dot{\phi}^2 \sin(\phi - \theta_{p_1}) - 2\dot{r}_{p_1} \dot{\theta}_{p_1} \right] \end{aligned} \quad (3.30)$$

Similarly, the accelerations of the pin P_2 and rotor 2, \ddot{r}_{p_2} and $\ddot{\theta}_{p_2}$, can be obtained from equations (3.27) and (3.28). That is

$$\begin{aligned} \ddot{r}_{p_2} = & -r_c \ddot{\theta}_c \sin(\theta_c - \theta_{p_2}) - \frac{L}{2} \ddot{\phi} \sin(\phi - \theta_{p_2}) + r_c \dot{\theta}_c^2 \cos(\theta_c - \theta_{p_2}) \\ & - \frac{L}{2} \dot{\phi}^2 \cos(\phi - \theta_{p_2}) + r_{p_2} \dot{\theta}_{p_2}^2 \end{aligned} \quad (3.31)$$

$$\begin{aligned} \ddot{\theta}_{p_2} = & \frac{1}{r_{p_2}} \left[-r_c \ddot{\theta}_c \cos(\theta_c - \theta_{p_2}) + \frac{L}{2} \ddot{\phi} \cos(\phi - \theta_{p_2}) + r_c \dot{\theta}_c^2 \sin(\theta_c - \theta_{p_2}) \right. \\ & \left. - \frac{L}{2} \dot{\phi}^2 \sin(\phi - \theta_{p_2}) - 2\dot{r}_{p_2} \dot{\theta}_{p_2} \right] \end{aligned} \quad (3.32)$$

It should be noted that the accelerations $\ddot{\theta}_c$ and $\ddot{\phi}$ become zero if the angular velocity of the crank is constant. Fig. 3.10 and 3.11 shows accelerations, \ddot{r}_{p_1} , \ddot{r}_{p_2} , $\ddot{\theta}_{p_1}$ and $\ddot{\theta}_{p_2}$ as a function of the crank angle when the crank rotates with a constant angular velocity.

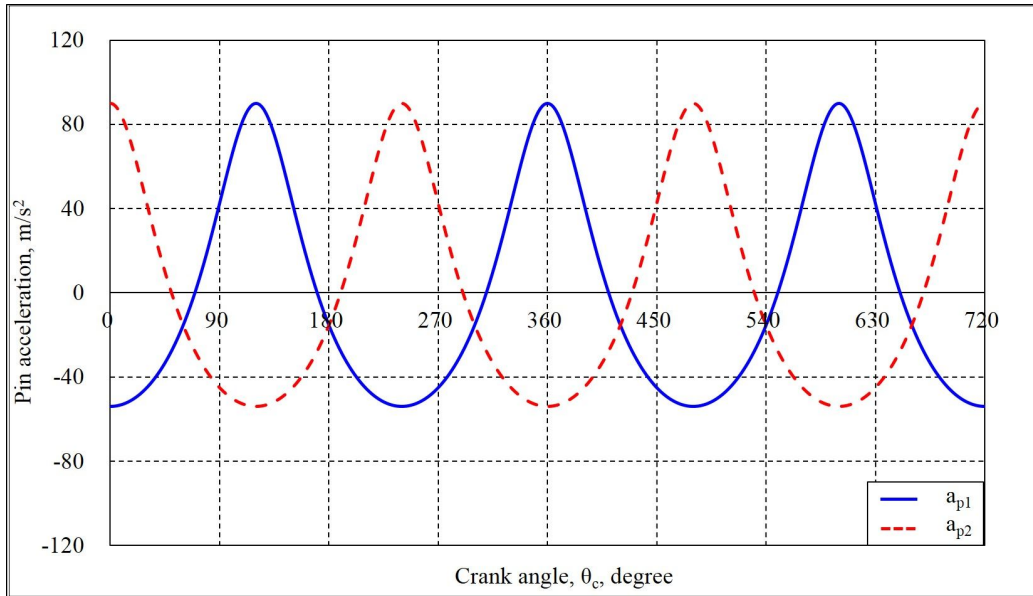


Fig.3.10. Pin accelerations when $r_c = 5 \text{ mm}$, $L = 40 \text{ mm}$, $Z_r = 30$, $Z_p = 20$ and $\dot{\theta}_c = 740 \text{ rpm}$.

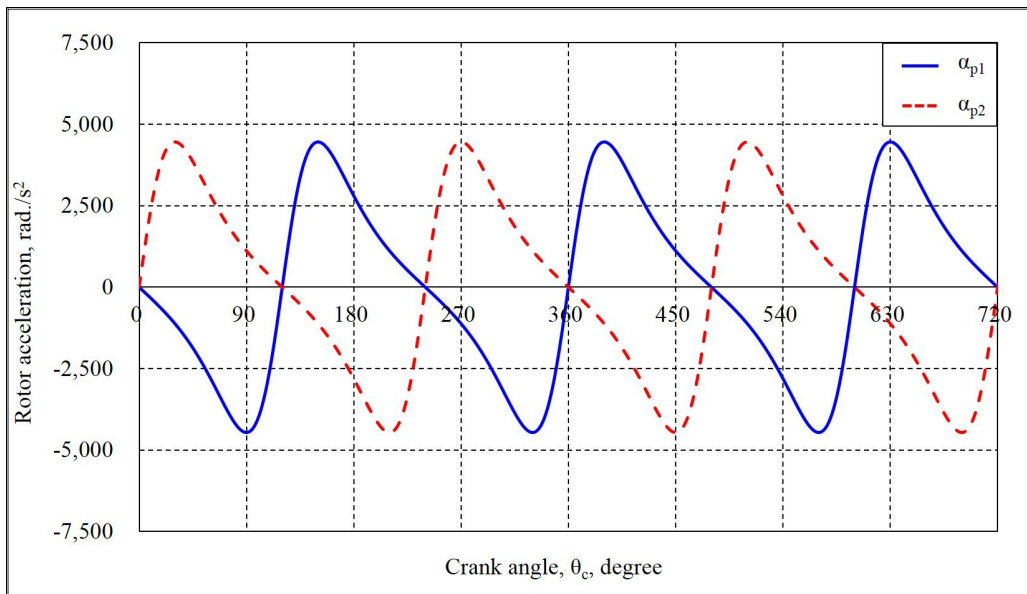


Fig.3.11. Angular acceleration of rotor when $r_c = 5 \text{ mm}$, $L = 40 \text{ mm}$, $Z_r = 30$, $Z_p = 20$, and $\dot{\theta}_c = 740 \text{ rpm}$.

3.3. Mechanism parameters

3.3.1. Driving link

Driving links of the rotational clap mechanism are those that drive the rotors. They includes the crank, the gears on the shaft link and the fixed internal gear. The parameters of those links are related to each other as follows:

$$\frac{2r_c}{m} + Z_p = Z_r \quad (3.33)$$

where, m = gear module

In addition to this relationship, the number of teeth on the gear in the shaft link and the fixed internal gear must satisfy the integer requirement that determines a relationship between the number of cycles for suction and discharge motions, and the working period of the mechanism. In other words, the frequency of the suction and discharge motions during a working cycle of the mechanism must be an integer to make the motions completed during the cycle. This relation can be expressed as follows:

$$N = \frac{\text{Period for one working cycle of mechanism}}{\text{Period for suction and discharge motions}} = \frac{\frac{2\pi Z_p}{Z_r - Z_p}}{\frac{2\pi Z_p}{Z_r}} = \frac{Z_r}{Z_r - Z_p}$$

or $\frac{NZ_p}{N-1} = Z_r \quad (3.34)$

where, N = an integer number

This also determines the number of jaws to be mounted on the rotors, and the suction and discharge ports. Equations (3.33) and (3.34) are the relationships that the parameters of the driving links must satisfy.

3.3.2. Rotor

Rotor parameters are those that describe the configuration of the rotors. They include the inner diameter, outer diameter and width of the rotor, number of jaws, pitch angle, thickness angle, height and width of the jaw, and length of the slot which are illustrated in fig.3.12.

From equation (3.34), the number of jaws is determined as N . Then, pitch angle of the jaw, ψ , defined as an angle between the jaws is given by

$$\psi = \frac{2\pi}{N} \quad (3.35)$$

To determine the thickness angle of the jaw, the maximum relative angular displacement between the rotors 1 and 2, that is, $(\theta_{rel})_{\max} = (\theta_{p_1} - \theta_{p_2})_{\max}$, must be known. Let θ_t be the thickness angle of the jaw, then the maximum relative angular displacement can be expressed as

$$2(\theta_{rel})_{\max} = \frac{2\pi - N(2\theta_t)}{N} \quad (3.36)$$

Substituting equation (3.18) into equation (3.36) and solving for the thickness angle

of the jaw yields

$$\theta_t = \frac{\pi}{N} - \left(\pi - \cos^{-1} \frac{4r_c^2 - L^2}{4r_c^2 + L^2} \right) \quad (3.37)$$

The inner radius of the rotor should be smaller than the minimum value of r_{p1} or r_{p2} and the outer radius larger than the maximum value of r_{p1} or r_{p2} , which all depend on the values of r_c and L . The length of the slot, s , on the rotor also depends on the values of r_c and L , and is given in equation form as follows

$$s = (r_{p1})_{\max} - (r_{p2})_{\min} = \sqrt{r_c^2 + \frac{L^2}{4} + r_c L} - \sqrt{r_c^2 + \frac{L^2}{4} - r_c L} \quad (3.38)$$

The width of jaw should be determined as twice of the rotor width.

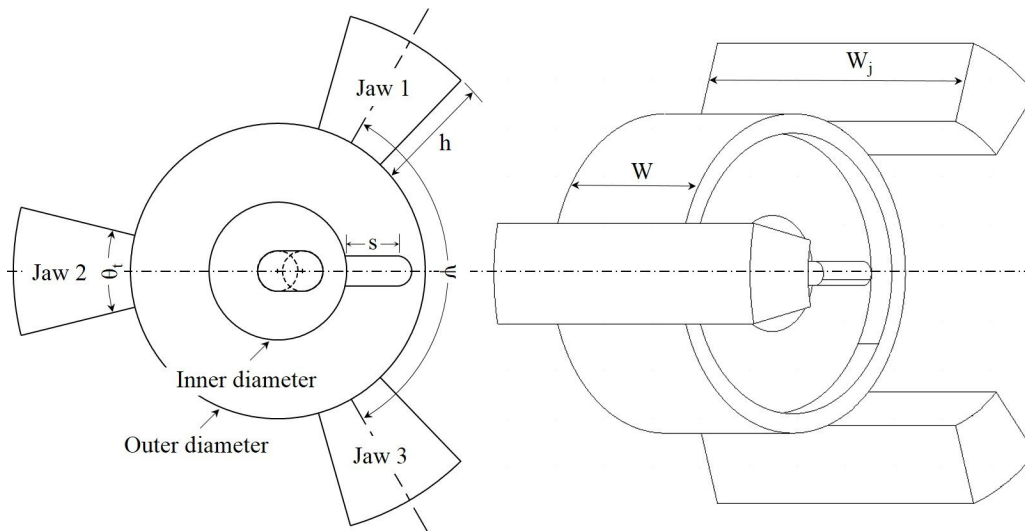


Fig.3.12. Rotor parameters.

3.4. Performance characteristics

3.4.1. Performance parameters

Displacement and flow may be the most important parameters to evaluate the performance of the rotational clap mechanism as a pumping device. During the suction motion, the volume V displaced by the two adjacent jaws can be expressed as

$$V = \pi [(r_o + h)^2 - r_o^2] W_j \frac{(\theta_{front})_{\max}}{2\pi} \quad (3.39)$$

where, r_o = outer radius of the rotor

h = jaw height

W_j = jaw width

When the crank makes one complete revolution, the number of cycles for the suction and discharge motions become $\frac{2\pi}{2\pi \frac{Z_p}{Z_r}} = \frac{Z_r}{Z_p}$. Therefore, the displacement of

the clap pump mechanism can be expressed by

$$D = \pi [(r_o + h)^2 - r_o^2] W_j \frac{(\theta_{front})_{\max}}{2\pi} \left(\frac{Z_r}{Z_p} \right) (2N) \quad (3.40)$$

If the crank rotates at a constant angular velocity of $\dot{\theta}_c$ rpm, the theoretical mean flow of the rotational clap pump can be calculated as follows:

$$Q_{avg} = \pi [(r_o + h)^2 - r_o^2] W_j \frac{(\theta_{front})_{max} \left(\frac{Z_r}{Z_p} \right)}{2\pi} (2N) \dot{\theta}_c \quad (3.41)$$

3.4.2. Interrelations of parameters

To investigate the performance characteristics of the rotational clap mechanism as a pumping device, the effects of some mechanism parameters on the displacement were investigated. As shown in equations (3.13), (3.18) and (3.40), displacement of the rotational clap mechanism is affected mainly by number of jaws, crank radius, pin distance, and number of teeth on the gears. However, since these parameters are inter-related each other, it is difficult to derive any unique effects of these parameters on the displacement.

From equations (3.33) and (3.34), the crank radius and number of the fixed internal gear teeth can be obtained from the number of the gear teeth on the shaft link and rotor jaws as shown in fig.3.13.

Another constraint to limit the crank radius is the thickness angle of the jaw. The thickness angle is affected by the crank radius, number of rotor jaws, and pin distance. Since the thickness angle should be positive and greater than a given value, the crank radius must be determined under such a constraint. fig.3.14 shows the positive thickness angles that can be obtained by the combinations of the crank radius, number of rotor jaws, and pin distance. It is noted from fig.3.14 that the crank radius must be reduced to have the positive thickness angle as the number of jaws increases. If necessary, the crank radius can be increased by increasing the pin distance. However, increasing the crank radius is limited because the thickness angle becomes negative as the crank radius increases no matter what value of the

pin distance is taken. Therefore, the crank radius must be determined to meet the lower limit value required to drive the mechanism taking the number of jaws and the pin distance into consideration.

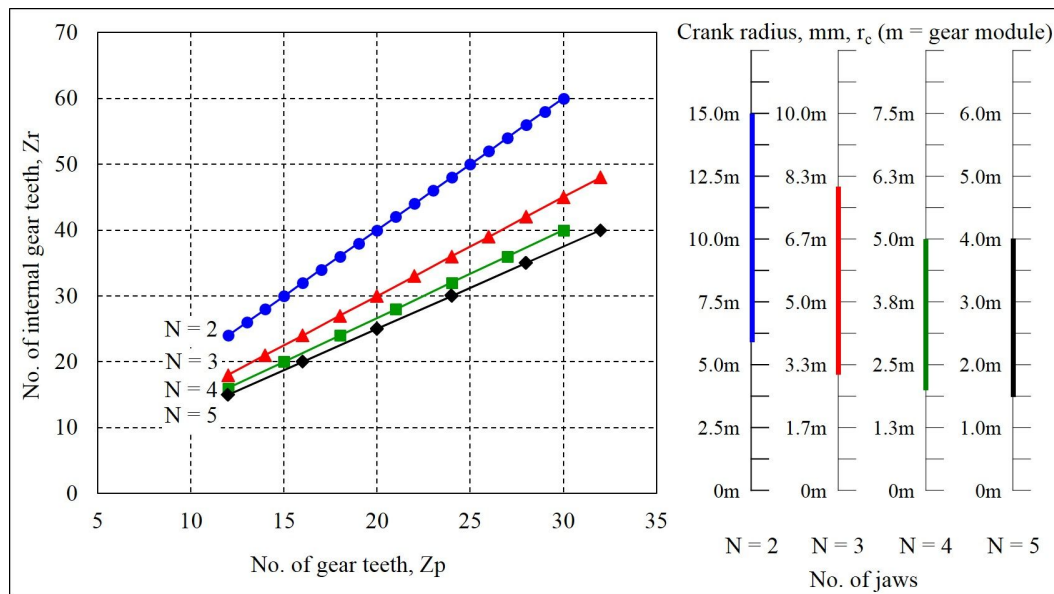


Fig.3.13. Determination of the number of internal gear teeth and crank radius by the number of gear teeth and rotor jaws.

The crank radius and pin distance are also affected by the minimum and maximum radii of the pin rotation with respect to the center of the rotor, from which the inner and outer radii of the rotor can be determined. The maximum rotating radius of the pin increases with the crank radius and pin distance while the minimum rotating radius increases only with the pin distance but decreases with the crank radius as shown in figs.3.15 and 3.16. The maximum and minimum rotating radii of the pin also determine the length of the slot on the rotor face as shown in equation (3.38).

It should be noted that the inner radius of the rotor must be less than the minimum rotating radius of the pin while the outer radius needs to be greater than the maximum rotating radius.

Since the crank radius and pin distance are limited by the thickness angle of the jaw and the inner radius of the rotor, they must be determined within the allowable range taking the overall size of the clap mechanism. Once the crank radius and pin distance are determined, the number of gear teeth and its module can be determined accordingly using fig.3.13.

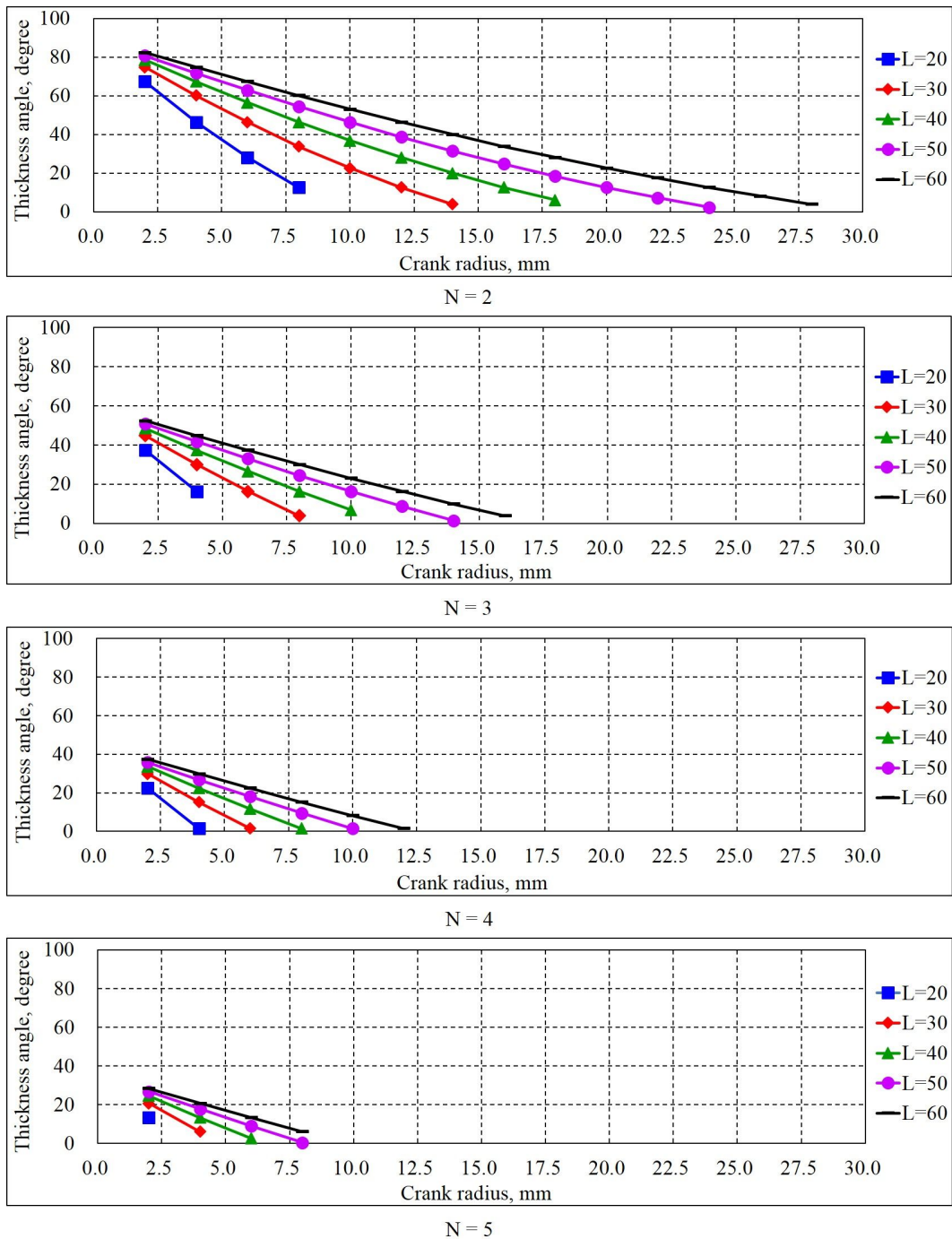


Fig.3.14. Combinations of the crank radius, number of rotor jaws and pin distance to make the thickness angle positive.

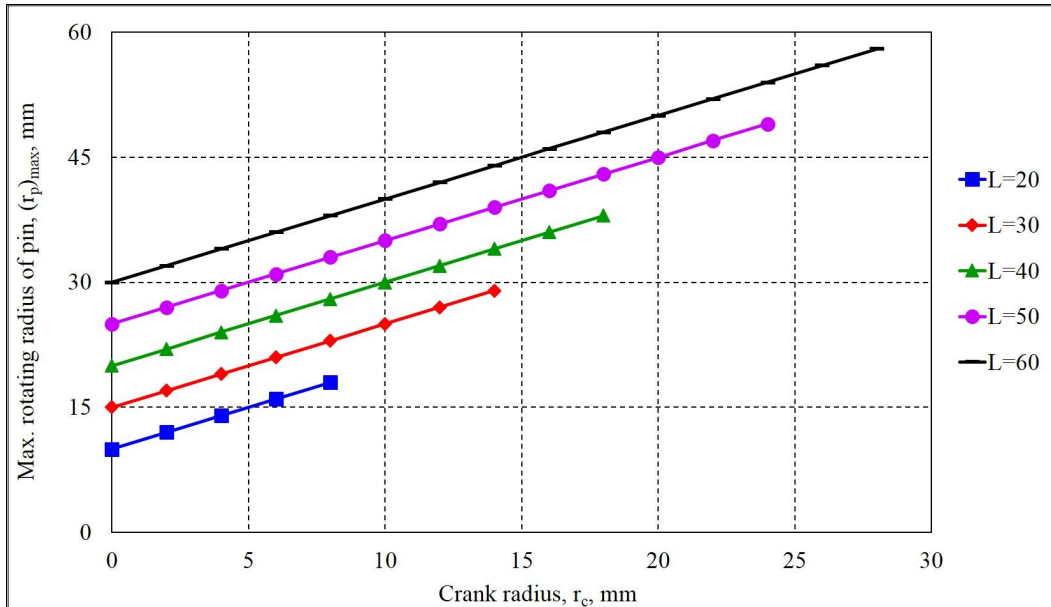


Fig.3.15. Maximum rotating radius of the pin.

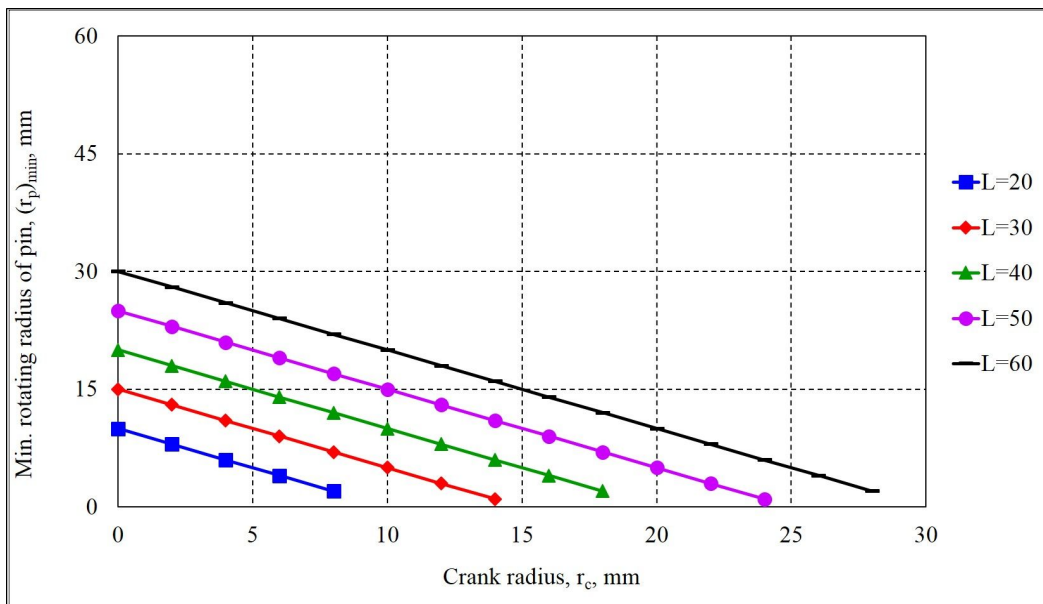
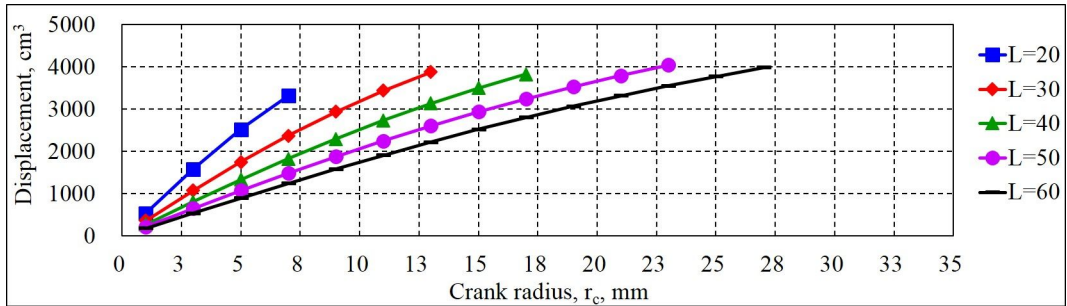


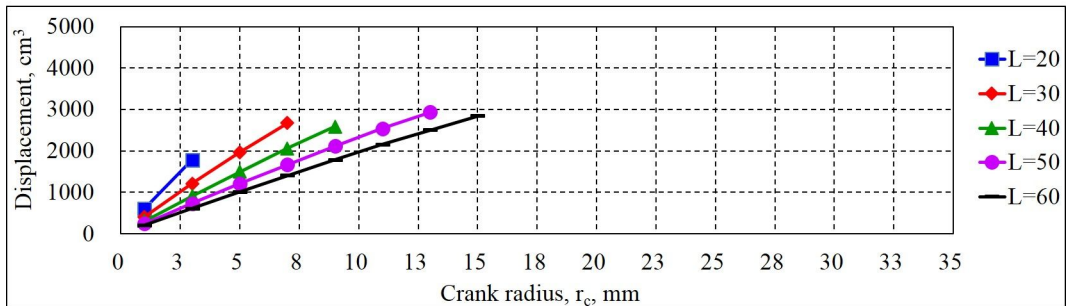
Fig.3.16. Minimum rotating radius of the pin.

3.4.3. Performance characteristics

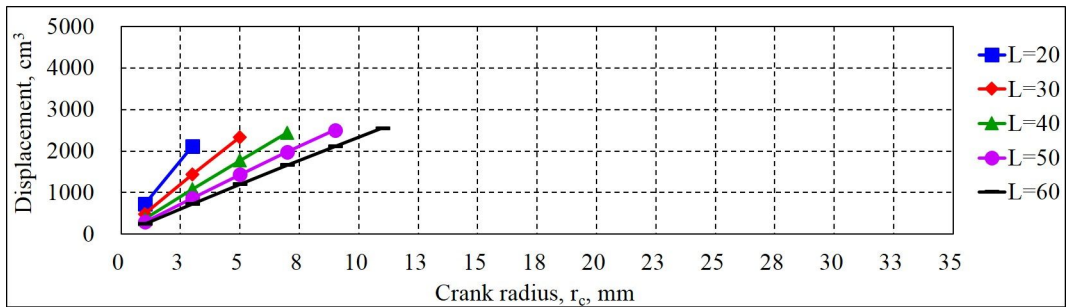
Displacement of the clap mechanism varies with crank radius, pin distance, number of jaws, and jaw width and height. fig.3.17 shows the displacement of the mechanism when the width and height of jaw are kept constant with a rotor of 65 cm outer radius. Displacement increases with the crank radius at a given number of jaws and pin distance. However, at a given crank radius it increases with the number of jaws and decreases with the pin distance. Since the crank radius is limited as the number of jaws increase, displacement performance of the clap mechanism is also limited accordingly with number of jaws. However, it can be increased as much as possible by increasing the jaw width and height once the crank radius, pin distance and the number of jaws are determined since they are not inter-related with other parameters of the mechanism.



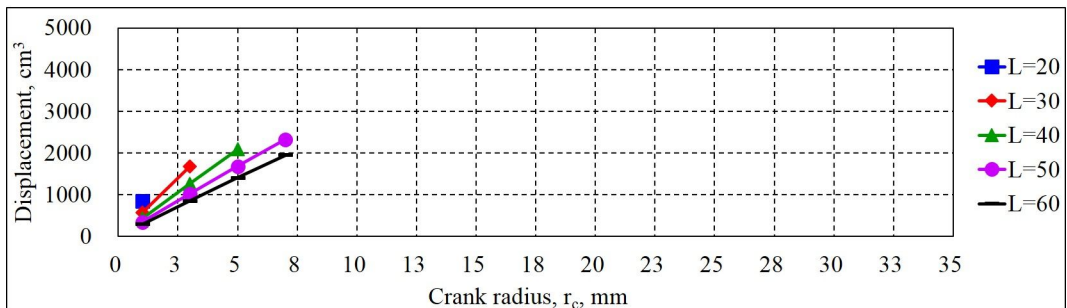
N = 2



N = 3



N = 4



N = 5

Fig.3.17. Displacement of a clap mechanism having a jaw of 50 cm width and 40 cm height and a rotor of 65 cm outer radius.

3.5. Conclusions

In this chapter, working principle of the rotational clap mechanism and its design parameters were introduced together with kinematic analysis for the pins and rotors. Vector equations developed for the analysis can be used to easily depict the motion characteristics of the mechanism by changing the design parameters. Inter-relationship between the design parameters was also presented to determine the proper crank radius and pin distance within the number of gear teeth and rotor size allowable for them. Thickness angle of the jaw and inner radius of the rotor were found to be most significant constraints affecting the crank radius and pin distance of the mechanism.

Displacement of the clap mechanism varies with crank radius, pin distance, number of jaws, jaw width and jaw height. It increases with the crank radius at a given number of jaws and pin distance while at a given crank radius it decreases with pin distance and increases with the number of jaws. However, the displacement can be increased as much as possible by increasing the jaw width and height once the crank radius, pin distance and the number of jaws are determined since they are not inter-related with other parameters of the mechanism.

Although there exist some limitations in its application due to constraints on the crank radius and pin distance, the rotational clap mechanism can be applied to a pumping device.

4. Pump performance analysis

4.1. Introduction

The fundamental factors to determine the pump performance are the pressure, flow rate, and efficiency. Therefore, in the case of a simple system, only the pressure and flow rate are represented on the performance curve. On the other hand, with a complex system, the performance curve must represent the efficiency, required power, and net positive suction head (NPSH) in addition to the flow rate and pressure. This is because other factors such as economic considerations and system safety may be more critical than the fundamental performance. A positive-displacement pump generates pressure pulsations, which can cause severe system safety and reliability problems and have a detrimental effect on the net positive suction head. Therefore, the pressure pulsation is an important factor that affects the performance of a positive-displacement pump.

A rotational clap pump was developed to convert the positive displacement reciprocating pump actions into a rotary mechanism. A previous chapter discussed the kinematic analysis and working principles of the rotational clap pump. The motion analysis, inter-relationships of design parameters, inherent constraints, and performance characteristics of the rotational clap mechanism as a pumping device were described.

This chapter presents the pressure, driving torque, and efficiency characteristics of a rotational clap pump for analysis of its fundamental performance.

4.2. Pressure analysis

4.2.1. Assumptions

Pressure and its pulsation in this pump were analyzed on the basis of the following assumptions:

- Incompressible flow.
- Ignoring the elasticity of the piping system.
- Pressure is the same in control volume.
- Each flow space in the pump is modified with the circular pipe.

4.2.2. Pressure head

Pressure is required to pump the liquid through the system for a given flow rate. A sufficiently high pressure is required to overcome the internal resistance of the system, which is also known as head. The total head is the sum of individual heads as follows:

4.2.2.1. Pressure head due to friction

Pressure head from flow friction in a pipe is given by the well-known Darcy equation. It can be expressed as follows using the parameters in fig.4.1.

$$\Delta p_{f_{1-2}} = \frac{1}{2} \rho \frac{f_{1-2} l_{1-2}}{D_{1-2}} \frac{Q_{1-2}^2}{A_{1-2}^2} \times \frac{10^{-4}}{9.81} \quad (4.1)$$

where, $\Delta p_{f_{1-2}}$ = pressure head due to friction, kgf/cm^2
 ρ = density of fluid, kgf/m^3
 f_{1-2} = friction factor
 l_{1-2} = distance between both sides of control volume, m
 D_{1-2} = diameter of pipe, m
 Q_{1-2} = flow rate, m^3/s
 A_{1-2} = cross section area of pipe, m^2

4.2.2.2. Pressure head due to mass acceleration

Pressure head due to mass acceleration in the control volume of the pipe can be calculated on the basis of Newton's law (Schlücker et al. 1997). It can also be expressed as follows with the parameters in fig.4.1.

$$\Delta p_{a_{1-2}} = \rho l_{1-2} \frac{\dot{Q}_{1-2}}{A_{1-2}} \times \frac{10^{-4}}{9.81} \quad (4.2)$$

where, $\Delta p_{a_{1-2}}$ = pressure head due to mass acceleration, kgf/cm^2
 \dot{Q}_{1-2} = derivative with respect to time of flow rate, m^3/s^2

4.2.2.3. Pressure head due to piping components

The flow in the piping system passes through a variety of components causing pressure losses like a nipple, tee, elbow, valve, orifice, etc. Such losses are generally termed minor losses and expressed as follows:

$$\Delta p_{K_{1-2}} = \frac{1}{2} K_{1-2} \rho \frac{Q_{1-2}^2}{A_{1-2}^2} \times \frac{10^{-4}}{9.81} \quad (4.3)$$

where, $\Delta p_{K_{1-2}}$ = pressure head due to minor losses, kgf/cm^2

K = loss coefficient for pipe component

4.2.2.4. Pressure head due to gravity

Pressure head due to gravity should also be considered. It can be positive or negative. The head can be expressed by

$$\Delta p_{h_{1-2}} = \rho h_{1-2} \times 10^{-4} \quad (4.4)$$

where, $\Delta p_{h_{1-2}}$ = pressure head due to gravity, kgf/cm^2

4.2.2.5. Total head

Therefore, based on the law of conservation of energy, the differential pressure shown in Fig. 4.1 can be expressed as follows:

$$\begin{aligned} p_2 - p_1 &= \Delta p_{f_{1-2}} + \Delta p_{a_{1-2}} + \Delta p_{K_{1-2}} + \Delta p_{h_{1-2}} \\ &= \left(\frac{1}{2} \rho \frac{f_{1-2} l_{1-2}}{D_{1-2}} \frac{Q_{1-2}^2}{A_{1-2}^2} + \rho l_{1-2} \frac{Q_{1-2}^2}{A_{1-2}^2} + \frac{1}{2} K_{1-2} \rho \frac{Q_{1-2}^2}{A_{1-2}^2} \right) \times \frac{10^{-4}}{9.81} \\ &\quad + 9.81 \times \rho h_{1-2} \end{aligned} \quad (4.5)$$

where, $p_2 - p_1$ = total pressure head(differential pressure) of the pipe, kgf/cm^2

4.2.3. Pressure analysis in clap pump

As discussed in a previous chapter, the volume variations between two adjacent rotor jaws caused by hypo-cycle mechanism produces the flow in the pump as shown in fig.4.2. In order to apply equation (4.5) to the flow in this pump, all of the suction and discharge spaces in the pump were simplified to circular pipes as shown in fig.4.3. As a result, each of the suction and discharge spaces is divided into five independent control volumes. In other words, in case of suction, the space between two adjacent rotor jaws, inner suction port, suction chamber, outer suction port and suction pipe are independent control volumes respectively. In addition, the start points of each control volume are named as k,s (k : number of control volume). The spaces of the discharge area are also divided in this manner, and those start points are named as k,d . The space between the two adjacent rotor jaws, and inner suction and discharge ports, are adjusted based on the number of jaws. However, each space is merged with one of the control volumes. Therefore, the pressure losses in this pump can be expressed as:

$$\Sigma(p_{k+1,s} - p_{k,s}) = \Sigma \left(\frac{1}{2} \rho \frac{f_{k-k+1,s} l_{k-k+1,s} Q_{k-k+1,s}^2}{D_{k-k+1,s} A_{k-k+1,s}^2} + \rho l_{k-k+1,s} \frac{Q_{k-k+1,s}^2}{A_{k-k+1,s}^2} + \frac{1}{2} \rho \Sigma K_{k-k+1,s} \frac{Q_{k-k+1,s}^2}{A_{k-k+1,s}^2} + 9.81 \times \rho h_{k-k+1,s} \right) \times \frac{10^{-4}}{9.81} \quad (4.6)$$

$$\Sigma(p_{k+1,d} - p_{k,d}) = \Sigma \left(\frac{1}{2} \rho \frac{f_{k-k+1,d} l_{k-k+1,d} Q_{k-k+1,d}^2}{D_{k-k+1,d} A_{k-k+1,d}^2} + \rho l_{k-k+1,d} \frac{\dot{Q}_{k-k+1,d}}{A_{k-k+1,d}} + \frac{1}{2} \rho \Sigma K_{k-k+1,d} \frac{Q_{k-k+1,d}^2}{A_{k-k+1,d}^2} + 9.81 \times \rho h_{k-k+1,d} \right) \times \frac{10^{-4}}{9.81} \quad (4.7)$$

where, k = number of control volume

s = suction

d = discharge

$\Sigma(p_{k+1,s} - p_{k,s})$ and $\Sigma(p_{k+1,d} - p_{k,d})$ = total pressure head in suction and discharge line of the pump respectively, kgf/cm^2

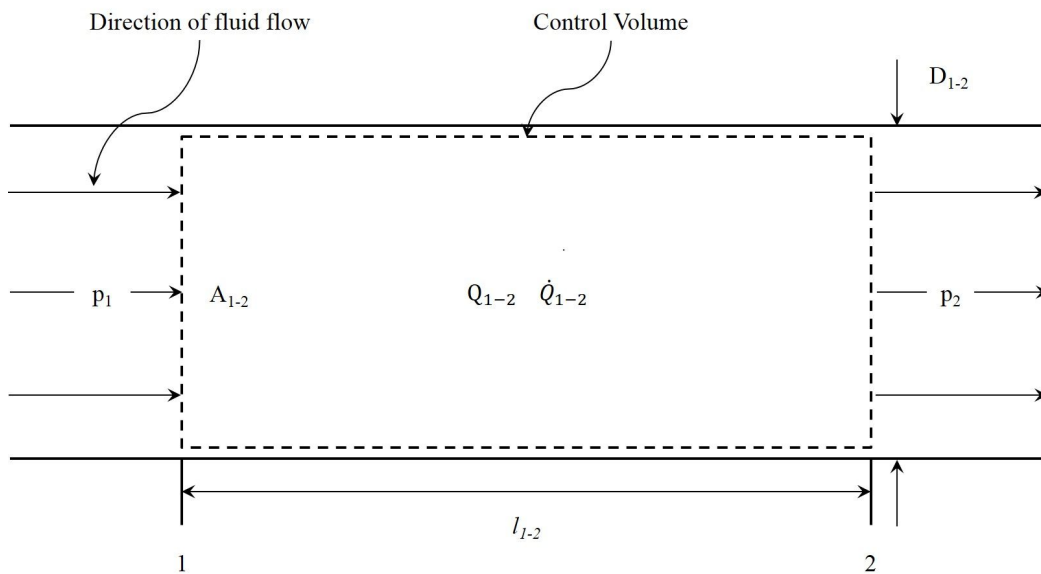


Fig.4.1. Fluid flow through a pipe.

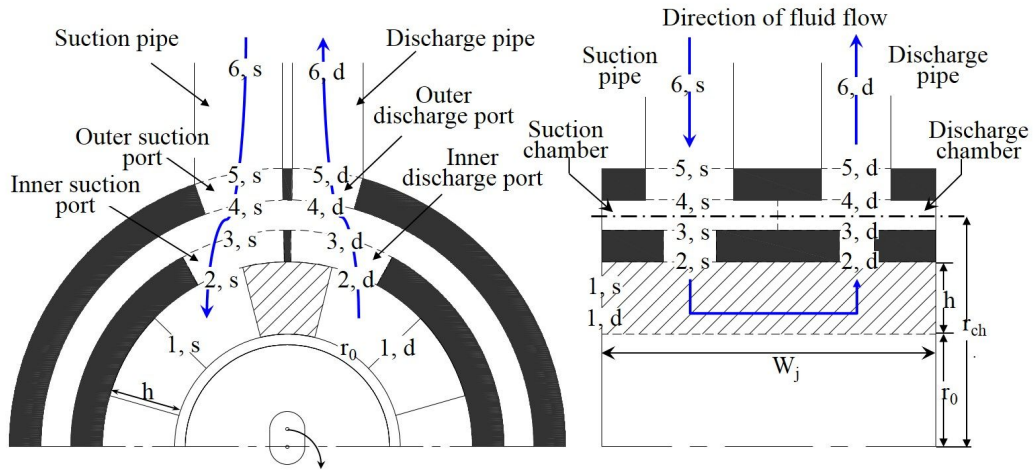


Fig.4.2. Fluid movement in the rotational clap mechanism.

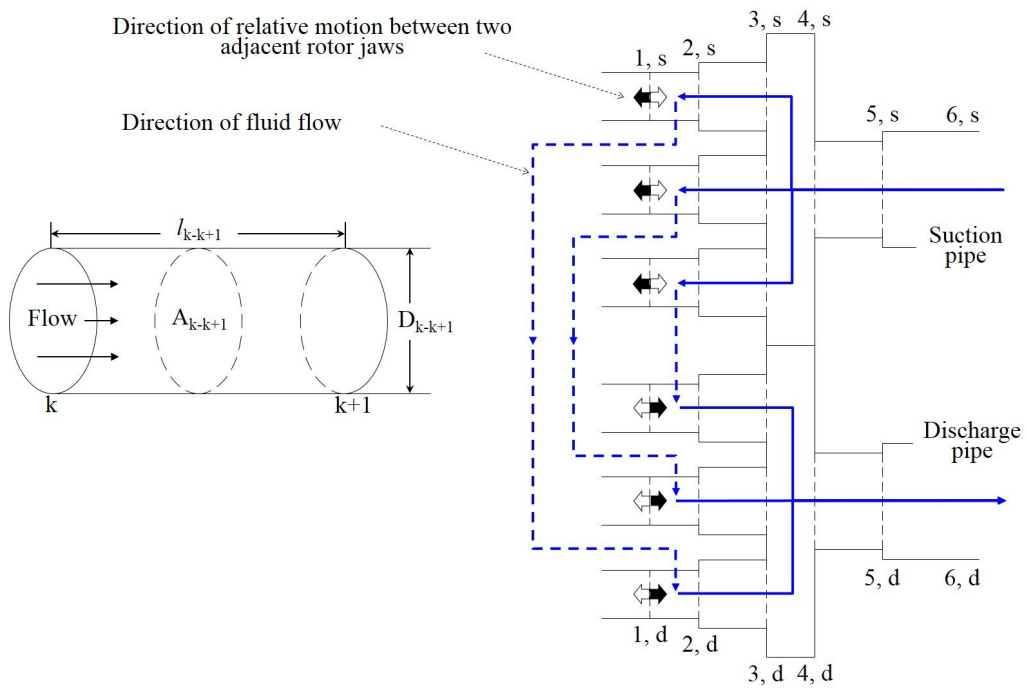


Fig.4.3. A schematic diagram of the fluid movement.

4.3. Forces and driving torque analysis

4.3.1. Forces and driving torque calculation

Parameters used for analysis of the forces and driving torque of the rotational clap mechanism have been defined the previous chapter. This chapter presented that the relative velocity between the two rotors makes one rotor lead and lag periodically with respect to the other. These lead and lag motions result in a continuous cycle of approach-contact-recess of two adjacent rotor jaws. The continuous lead and lag motions can be used for the suction and discharge motions required for pumping. Because of this motions, suction and discharge pressures are generated between two adjacent rotors and rotor housing. Fig.4.4 shows the hydraulic forces due to the suction and discharge pressures whose direction are changed vary periodically. These forces are transmitted sequentially to prime mover through each rotor, the gear, and the crank.

To simplify the forces and driving torque analysis of each component, any friction losses that result sliding conditions within the pump were neglected and the effect of the pressure difference, $p_d - p_s$, may now be considered as an uniformly distributed load in that plane. And definition of component parts and parameters of the pump have been presented by the previous chapter.

Fig.4.5 shows the free body diagram of main components. In fig.4.5(a) and (b), the discharge forces F_d act on one side of each jaw and at the same time the suction forces, F_s , act on the other side of them. Also two forces F_{p_1} and F_{p_2} act on pin slot joint of each rotor respectively. The forces F_{ct} and F_{cn} shown in fig.4.5(c), acting on the gear at point C, are tangential and normal components

respectively. And the reaction forces, R_p , R_{p_1} and R_{p_2} , act on the gear tooth and two pins respectively. T_i is the driving torque to maintain motion with the given condition, and R_{ct} and R_{cn} are the reaction forces acting on the crank as shown in fig.4.5(e). To analyze the forces of the components within the pump and driving torque, its position and force vectors are defined as equations (4.8) - (4.18).



Fig.4.4 Direction changes in hydraulic forces acting on the rotors and the housing.

$$\mathbf{r}_c = (r_c \cos \theta_c, r_c \sin \theta_c) \quad (4.8)$$

$$\mathbf{r}_{p_1} = (r_{p_1} \cos \theta_{p_1}, r_{p_1} \sin \theta_{p_1}) \quad (4.9)$$

$$\mathbf{r}_{p_2} = (-r_{p_2} \cos \theta_{p_2}, -r_{p_2} \sin \theta_{p_2}) \quad (4.10)$$

$$\mathbf{r}_p = (r_p \cos \theta_c, r_p \sin \theta_c) \quad (4.11)$$

$$\mathbf{L}_1 = (r_{p_1} \cos \theta_{p_1} - r_c \cos \theta_c, r_{p_1} \sin \theta_{p_1} - r_c \sin \theta_c) \quad (4.12)$$

$$\mathbf{L}_2 = (-r_{p_2} \cos \theta_{p_2} - r_c \cos \theta_c, -r_{p_2} \sin \theta_{p_2} - r_c \sin \theta_c) \quad (4.13)$$

$$-\mathbf{F}_{p_1} = \mathbf{R}_{p_1} = \left(R_{p_1} \cos \left(\theta_{p_1} - \frac{\pi}{2} \right), R_{p_1} \sin \left(\theta_{p_1} - \frac{\pi}{2} \right) \right) \quad (4.14)$$

$$-\mathbf{F}_{p_2} = \mathbf{R}_{p_2} = \left(R_{p_2} \cos \left(\theta_{p_2} - \frac{\pi}{2} \right), R_{p_2} \sin \left(\theta_{p_2} - \frac{\pi}{2} \right) \right) \quad (4.15)$$

$$\mathbf{R}_p = \left(R_p \cos \left(\theta_c + \frac{\pi}{2} + \theta_p \right), R_p \sin \left(\theta_c + \frac{\pi}{2} + \theta_p \right) \right) \quad (4.16)$$

$$\mathbf{F}_{cn} = -\mathbf{R}_{cn} = (F_{cn} \cos \theta_c, F_{cn} \sin \theta_c) \quad (4.17)$$

$$\mathbf{F}_{ct} = -\mathbf{R}_{ct} = \left(F_{ct} \cos\left(\theta_c + \frac{\pi}{2}\right), F_{ct} \sin\left(\theta_c + \frac{\pi}{2}\right) \right) \quad (4.18)$$

The direction of suction pressure p_s and discharging pressure p_d are changed periodically as shown in fig.4.1. Then the forces F_{R_1} and F_{R_2} of each rotor can be expressed as follows:

$$-F_{R_1} = F_{R_2} = Whn(p_d - p_s) = n(F_d - F_s) \quad (4.19)$$

and, the rotor torque about center of rotation O, T_{OR_1} and T_{OR_2} are

$$T_{OR_1} = -F_{R_1} \left(r_o + \frac{h}{2} \right) + F_{p_1} r_{p_1} = I_{R_1} \ddot{\theta}_{p_1} \quad (4.20)$$

$$T_{OR_2} = F_{R_2} \left(r_o + \frac{h}{2} \right) + F_{p_2} r_{p_2} = I_{R_2} \ddot{\theta}_{p_2} \quad (4.21)$$

The angular velocities of the shaft link and gear are $\left(1 - \frac{Z_r}{Z_p}\right)\omega_c$ when the angular velocity of crank is ω_c . In other words, the velocities of the shaft link and gear are kept constant. Then, summation of the fore vectors ΣF_{sum} and torque vectors ΣT_c acting on the gear and shaft link can be expressed as

$$\Sigma \mathbf{F}_{sum} = \mathbf{R}_{p_1} + \mathbf{R}_{p_2} + \mathbf{R}_p + \mathbf{F}_{cn} + \mathbf{F}_{ct} = 0 \quad (4.22)$$

$$\Sigma \mathbf{T}_c = \mathbf{L}_2 \times \mathbf{R}_{p_2} + \mathbf{L}_1 \times \mathbf{R}_{p_1} + \mathbf{r}_p \times \mathbf{R}_p = 0 \quad (4.23)$$

Converting the vectors of equation (4.23) into scalar and rearranging it gives,

$$\begin{aligned}
T_c = & (-r_{p_2} \cos\theta_{p_2} - r_c \cos\theta_c) R_{p_2} \sin\left(\theta_{p_2} - \frac{\pi}{2}\right) - (-r_{p_2} \sin\theta_{p_2} - r_c \sin\theta_c) R_{p_2} \cos\left(\theta_{p_2} - \frac{\pi}{2}\right) \\
& + (r_{p_1} \cos\theta_{p_1} - r_c \cos\theta_c) R_{p_1} \sin\left(\theta_{p_1} - \frac{\pi}{2}\right) - (r_{p_1} \sin\theta_{p_1} - r_c \sin\theta_c) R_{p_1} \cos\left(\theta_{p_1} - \frac{\pi}{2}\right) \\
& + r_p \cos\theta_c R_p \sin\left(\theta_c + \frac{\pi}{2} + \theta_p\right) - r_p \sin\theta_c R_p \cos\left(\theta_c + \frac{\pi}{2} + \theta_p\right) = 0
\end{aligned} \tag{4.24}$$

Rearranging about R_p gives,

$$R_p = \frac{\left\{ \begin{aligned} & (-r_{p_2} \cos\theta_{p_2} - r_c \cos\theta_c) R_{p_2} \sin\left(\theta_{p_2} - \frac{\pi}{2}\right) - (-r_{p_2} \sin\theta_{p_2} - r_c \sin\theta_c) R_{p_2} \cos\left(\theta_{p_2} - \frac{\pi}{2}\right) \\ & + (r_{p_1} \cos\theta_{p_1} - r_c \cos\theta_c) R_{p_1} \sin\left(\theta_{p_1} - \frac{\pi}{2}\right) - (r_{p_1} \sin\theta_{p_1} - r_c \sin\theta_c) R_{p_1} \cos\left(\theta_{p_1} - \frac{\pi}{2}\right) \end{aligned} \right\}}{-r_p \cos\theta_c \sin\left(\theta_c + \frac{\pi}{2} + \theta_p\right) + r_p \sin\theta_c \cos\left(\theta_c + \frac{\pi}{2} + \theta_p\right)} \tag{4.25}$$

Separating the x axis and y axis of equation (4.22) yields,

$$\begin{aligned}
\Sigma F_x = & R_{p_1} \cos\left(\theta_{p_1} - \frac{\pi}{2}\right) + R_{p_2} \cos\left(\theta_{p_2} - \frac{\pi}{2}\right) + R_p \cos\left(\theta_c + \frac{\pi}{2} + \theta_p\right) \\
& + F_{cn} \cos\theta_c + F_{ct} \cos\left(\theta_c + \frac{\pi}{2}\right) = 0
\end{aligned} \tag{4.26}$$

$$\begin{aligned}
\Sigma F_y = & R_{p_1} \sin\left(\theta_{p_1} - \frac{\pi}{2}\right) + R_{p_2} \sin\left(\theta_{p_2} - \frac{\pi}{2}\right) + R_p \sin\left(\theta_c + \frac{\pi}{2} + \theta_p\right) \\
& + F_{cn} \sin\theta_c + F_{ct} \sin\left(\theta_c + \frac{\pi}{2}\right) = 0
\end{aligned} \tag{4.27}$$

Solving for F_{cn} and F_{ct} yields,

$$F_{ct} = \frac{\left\{ \begin{array}{l} \sin\theta_c \left\{ R_{p_1} \cos\left(\theta_{p_1} - \frac{\pi}{2}\right) + R_{p_2} \cos\left(\theta_{p_2} - \frac{\pi}{2}\right) + R_p \cos\left(\theta_c + \frac{\pi}{2} + \theta_p\right) \right\} \\ - \cos\theta_c \left\{ R_{p_1} \sin\left(\theta_{p_1} - \frac{\pi}{2}\right) + R_{p_2} \sin\left(\theta_{p_2} - \frac{\pi}{2}\right) + R_p \sin\left(\theta_c + \frac{\pi}{2} + \theta_p\right) \right\} \end{array} \right\}}{\cos\theta_c \sin\left(\theta_c + \frac{\pi}{2}\right) - \sin\theta_c \cos\left(\theta_c + \frac{\pi}{2}\right)} \quad (4.28)$$

$$F_{cn} = \frac{\left\{ \begin{array}{l} \sin\left(\theta_c + \frac{\pi}{2}\right) \left\{ R_{p_1} \cos\left(\theta_{p_1} - \frac{\pi}{2}\right) + R_{p_2} \cos\left(\theta_{p_2} - \frac{\pi}{2}\right) + R_p \cos\left(\theta_c + \frac{\pi}{2} + \theta_p\right) \right\} \\ - \cos\left(\theta_c + \frac{\pi}{2}\right) \left\{ R_{p_1} \sin\left(\theta_{p_1} - \frac{\pi}{2}\right) + R_{p_2} \sin\left(\theta_{p_2} - \frac{\pi}{2}\right) + R_p \sin\left(\theta_c + \frac{\pi}{2} + \theta_p\right) \right\} \end{array} \right\}}{\cos\left(\theta_c + \frac{\pi}{2}\right) \sin\theta_c - \sin\left(\theta_c + \frac{\pi}{2}\right) \cos\theta_c} \quad (4.29)$$

The reaction force of the crank R_{ct} is opposite direction with the force F_{ct} .

Therefore, the driving torque about point O gives,

$$T_i = r_c \times R_{ct} \quad (4.30)$$

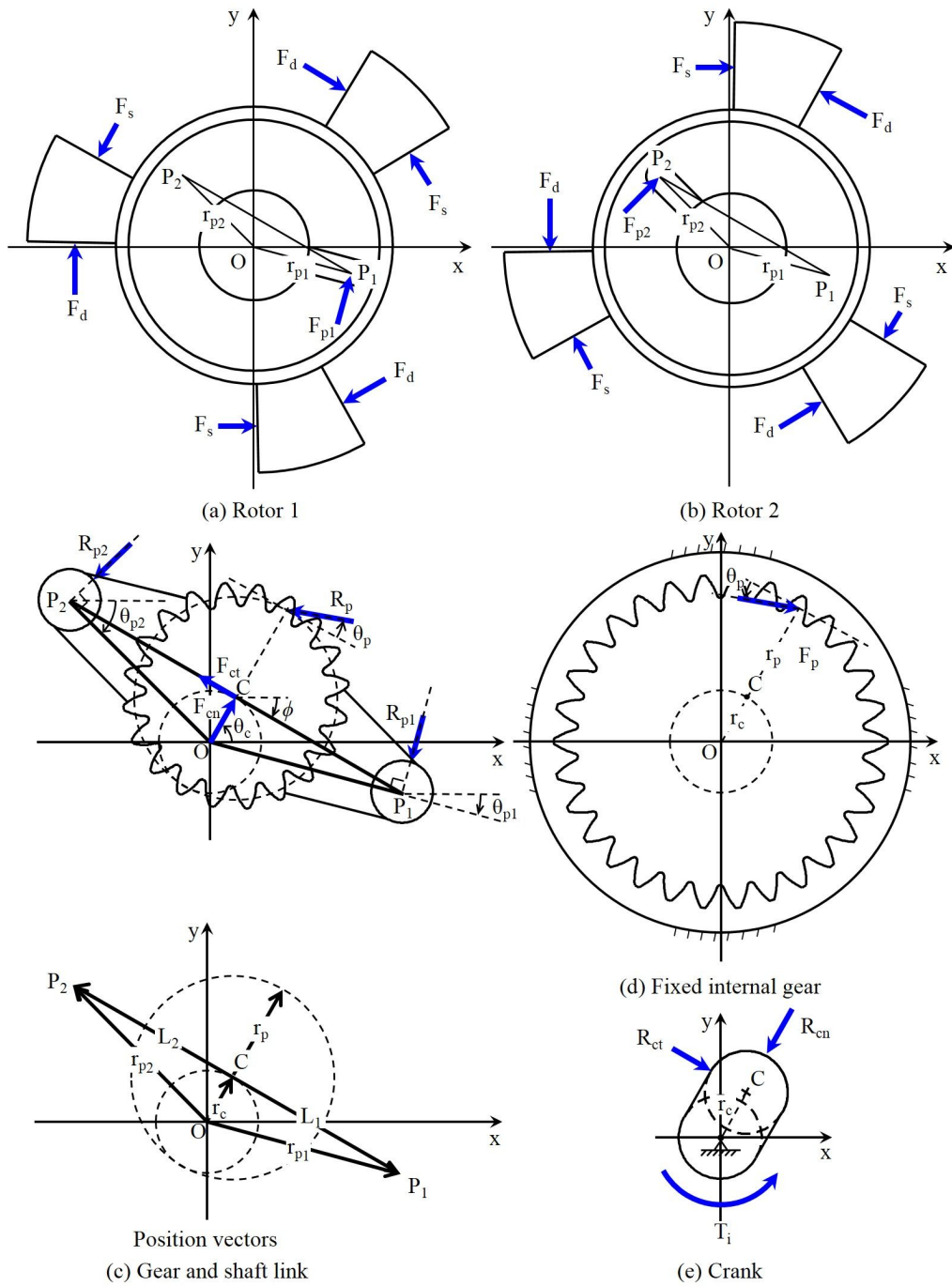


Fig.4.5 Free-body diagram for forces acting on the rotors, gear of the shaft link, internal gear and the crank.

4.3.2. Parametric study

Table 4.1 gives the parameters of the rotational clap mechanism being used as an example to demonstrate the characteristics of the forces and driving torque. Because the direction of the hydraulic forces changes periodically, the forces of the two rotors alternate between positive and negative values, as shown in fig.4.6. Thus, the forces of the two pins change periodically, and there are some differences between the magnitudes of the forces of the two pins $R_{p_1} - R_{p_2}$, as shown in fig.4.7. This difference makes the pump rotate. As shown in figs.4.8 and 4.9, the bending forces acting on the pair of the gear of the shaft link and the driving torque are maximum when θ_{rel} is zero and zero when θ_{rel} is maximum or minimum.

The driving torque characteristics of the rotational clap mechanism vary with the crank radius, pin distance, number of jaws, jaw width, and height. Fig.4.10 shows the driving torque when the width and height of the jaw are kept constant. The driving torque increases with the crank radius for a given number of jaws and pin distance. However, at a given crank radius, it increases with the number of jaws and decreases with the pin distance. Because the crank radius is limited as the number of jaws increase, the available maximum driving torque is also limited according to the number of jaws. The characteristics of the pin forces are the same for different driving torques, as shown in fig.4.11. However, the gear forces are the only opposite result for a given crank radius and pin distance. The gear force decreases with the number of jaws.

The driving torque, pin forces, and gear forces were analyzed to determine the component size and driving torque input that are required for operation of the rotational clap pump. Based on the results, the crank radius should be minimized

and the distance between two pins should be maximized to minimize the input power and forces acting on the components. In addition, the input power and pin forces could be minimized when the number of jaws was two. However, the gear force showed an opposite trend.

Table 4.1 Parameters involved in the parametric study.

Parameters	Values
$\Delta p = p_d - p_s$	5 kgf/cm ²
r_c	5 mm
L	40 mm
W_j	50 mm
h	40 mm
r_o	65 mm
Z_r	30
Z_p	20
I_{R_1}	0 kg·m ²
I_{R_2}	0 kg·m ²

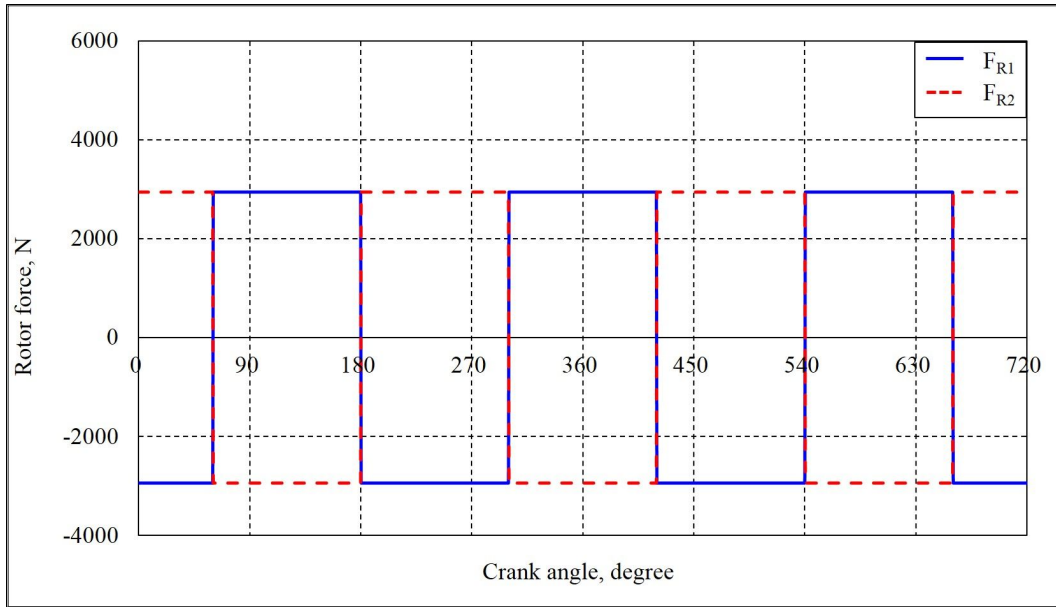


Fig.4.6 Rotor forces F_{R_1} and F_{R_2} .

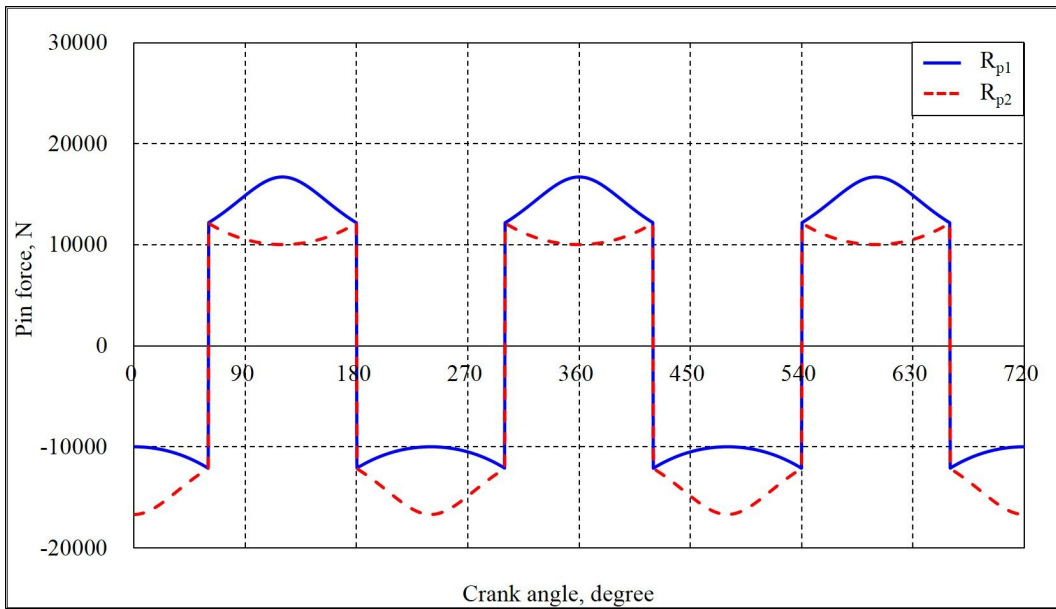


Fig.4.7 Pin forces R_{p_1} and R_{p_2} .

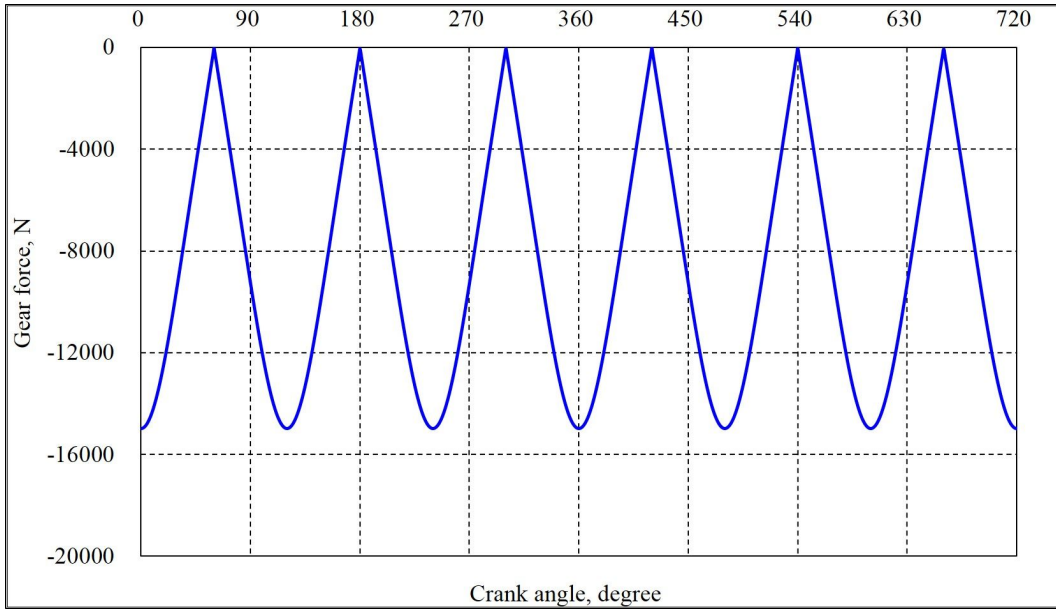


Fig.4.8 Gear force R_p .

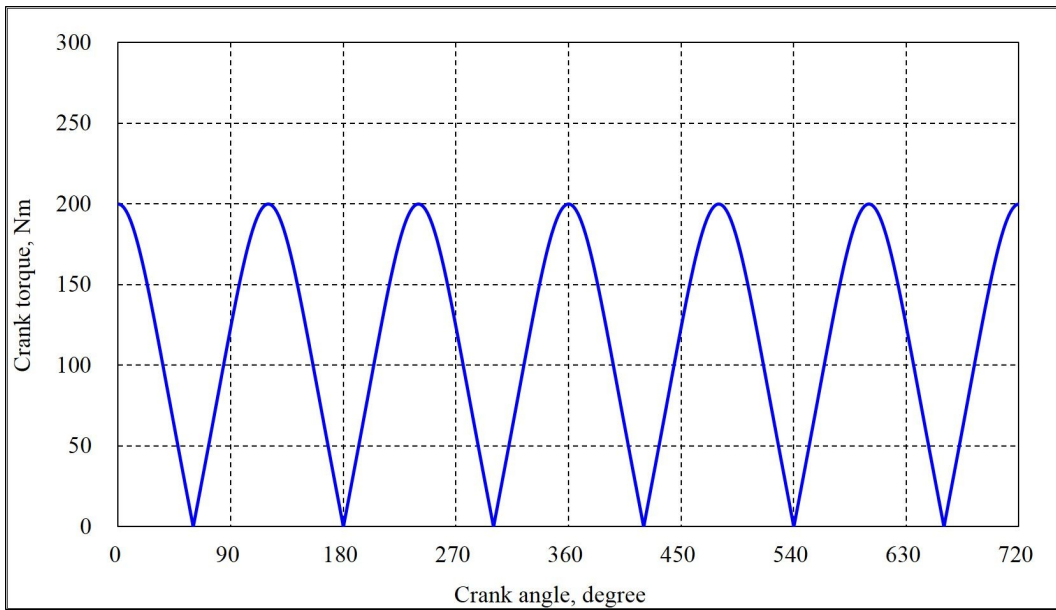
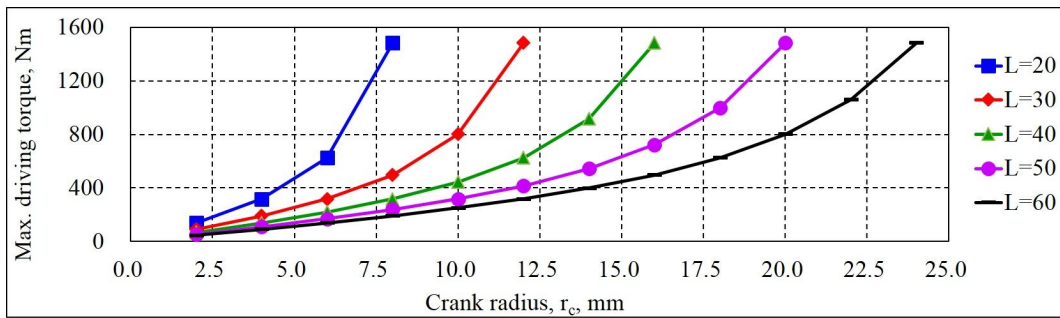
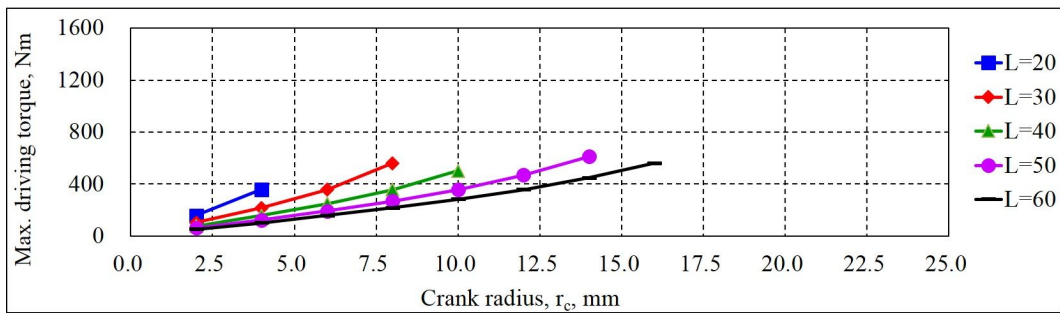


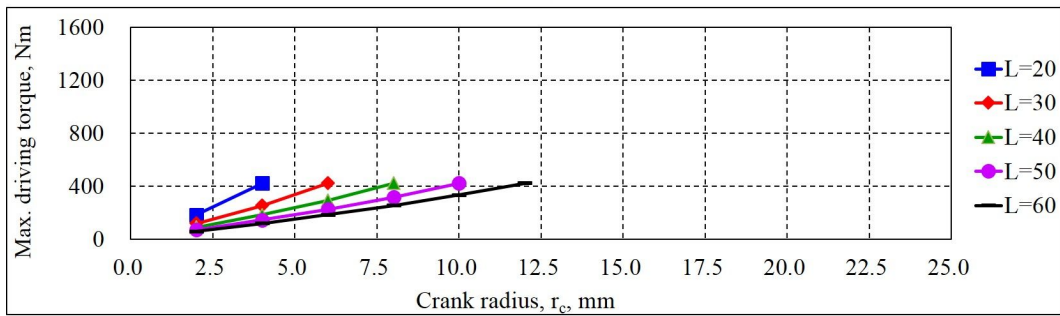
Fig.4.9 Driving torque T_i .



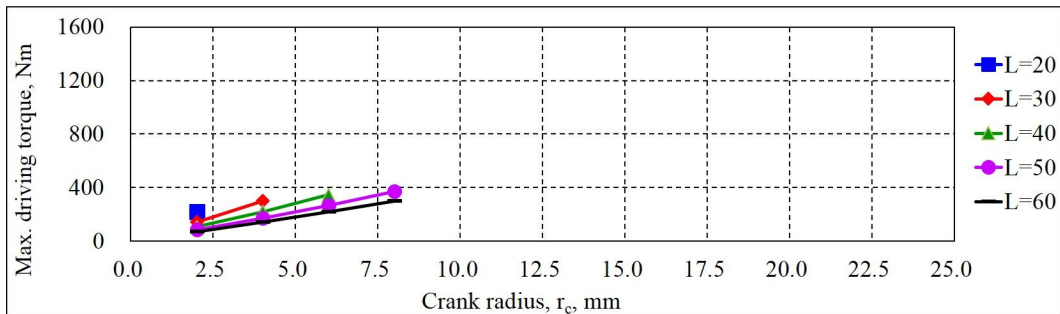
N = 2



N = 3

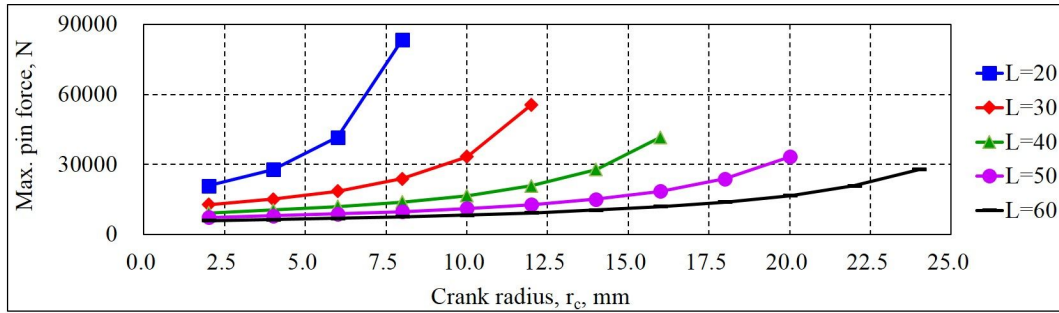


N = 4

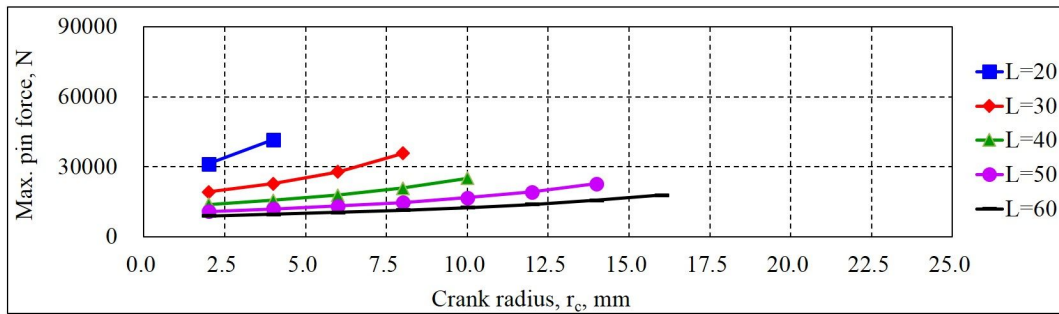


N = 5

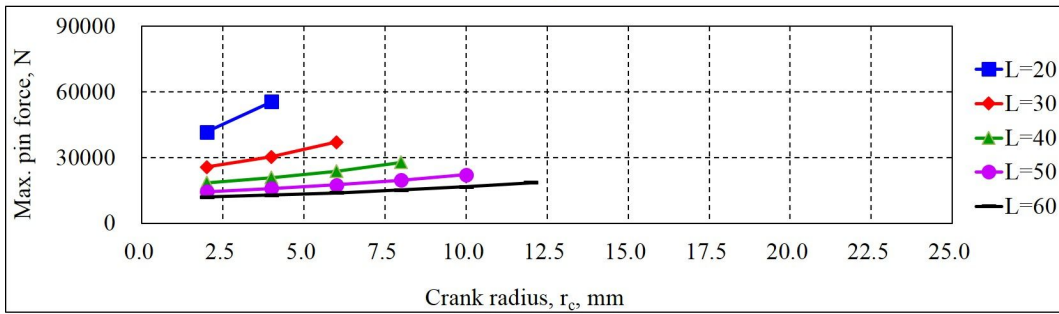
Fig.4.10 Driving torque vs. crank radius r_c .



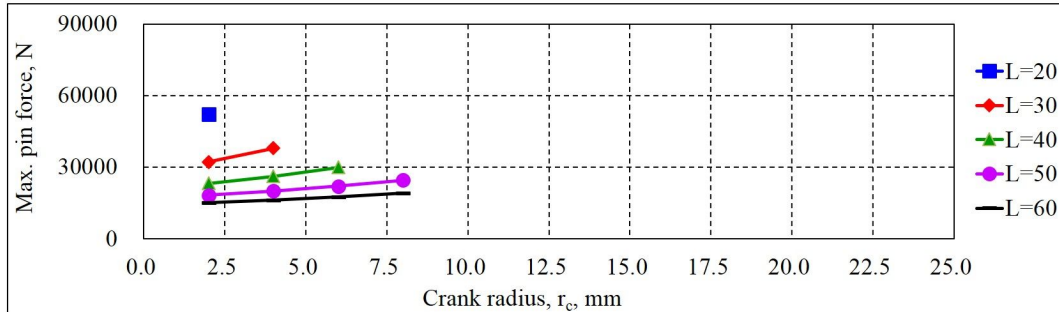
N = 2



N = 3

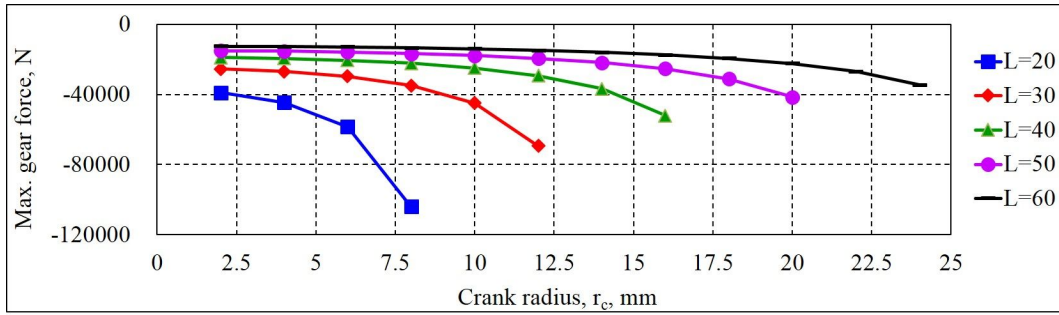


N = 4

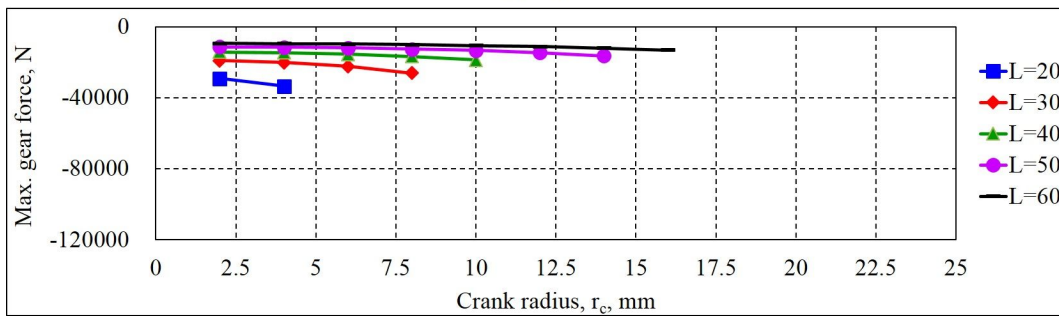


N = 5

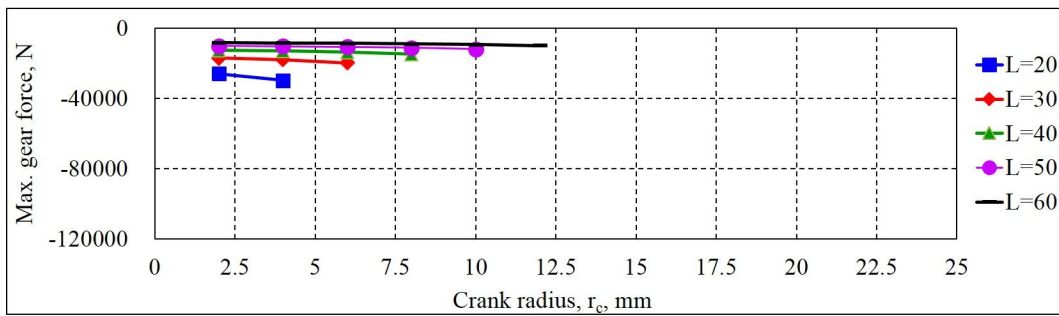
Fig.4.11 Pin forces vs. crank radius r_c .



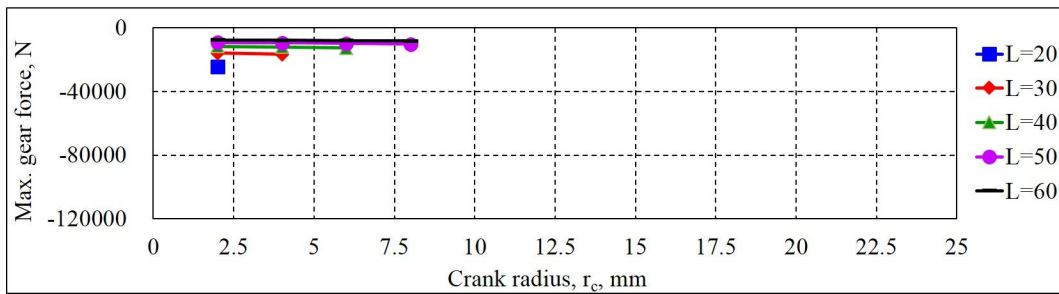
N = 2



N = 3



N = 4



N = 5

Fig.4.12 Gear forces vs. crank radius r_c .

4.4. Pump performance analysis

4.4.1. Theory of pump performance

4.4.1.1. Fundamental theory for the pump performance

The displacement D is the volumetric flow rate per revolution of the shaft. Therefore, the volumetric flow rate Q_{vol} when the pump shaft speed is $n \text{ rad/s}$ is given by

$$Q_{vol} = \frac{D}{2\pi} n = D_p n \quad (4.31)$$

where, $D_p = D/2\pi$ is the displacement per degree

The ideal input power, where the losses are neglected, is given by

$$T_{th} n = p Q_{vol} = p D_p n \quad (4.32)$$

where, T_{th} = theoretical torque

p = discharge pressure

From equation (4.32),

$$T_{th} = p D_p \quad (4.33)$$

However, in reality the torque losses and flow leakage take place when the pump

is driving. The torque losses are represented by T_{loss} , and the flow leakage is represented by Q_s . Then, the actual driving torque of the shaft and flow are given by

$$T = T_{th} + T_{loss} \quad (4.34)$$

$$Q = Q_{vol} - Q_s \quad (4.35)$$

Therefore, the volumetric efficiency, torque efficiency, and overall efficiency are defined as follows:

$$\eta_v = \frac{Q}{Q_{vol}} \quad (4.36)$$

$$\eta_t = \frac{T_{th}}{T} = \frac{D_p p}{T} \quad (4.37)$$

$$\eta = \frac{p Q}{T n} = \frac{Q}{Q_{vol}} \frac{Q_{th} p}{T n} = \frac{Q}{Q_{vol}} \frac{D_p p}{T} = \eta_v \eta_t \quad (4.38)$$

4.4.1.2. Theory of pump slip and forces caused by fluid viscosity

A positive-displacement pump needs a clearance between the rotating elements and chamber to move the fluid. This makes it inevitable for some leakage to occur through the clearance. This is known as slip. Because slip affects the pump performance, it is very important to quantify of the total slip to design and develop the pump.

The conventional method to analyze the pump slip is to use the Newton's law of viscosity. It is assumed that all of the flow in the pump is laminar and passes

between moving and fixed flat plates. Then, the shear stress caused by the fluid viscosity can be expressed as follows:

$$\tau = \mu \frac{dv}{dy} \quad (4.39)$$

where, v = the velocity in the direction of the x axis

τ = the shear stress on a plane parallel to the xz plane

μ = the coefficient of viscosity of the fluid

It is assumed that the pressure is constant throughout the fluid. Then, the total shear force acting on each plate surface parallel to these plates is given by

$$F = \tau A \quad (4.40)$$

where, A = the area of the flat plate

To obtain the velocity of fluid v , equation (4.39) is integrated:

$$\int \tau dy = \int \mu dv$$

$$\tau y = \mu v + C \quad (4.41)$$

Substituting the boundary conditions $v = V$, $y = \delta$ into equation (4.41) gives

$$v = V - \frac{\tau}{\mu}(\delta - y) \quad (4.42)$$

Fig.4.14 shows the fluid of viscosity μ in a laminar and steady-state flow between parallel flat plates with the width W . Then, the equation of equilibrium for a fluid element can be written as

$$p Wdy - \left(p + \frac{dp}{dx} dx\right) Wdy + \left(\tau + \frac{d\tau}{dy} dy\right) Wdx - \tau Wdx = 0 \quad (4.43)$$

Integrating this and substituting it into equation (4.39) produces

$$\mu \frac{dv}{dy} = \frac{dp}{dx} y + C_1 \quad (4.44)$$

Substituting the boundary conditions $y=0$ at $v=0$ and $y=\delta$ at $v=V$ into this equation after integrate on produces

$$v = \frac{Vy}{\delta} + \frac{1}{2\mu} \frac{dp}{dx} (y^2 - y\delta) \quad (4.45)$$

Then, the total flow between two plates can be expressed as

$$Q = \int v dA = \int_0^\delta v W dy = W \int_0^\delta \left[\frac{Vy}{\delta} + \frac{1}{2\mu} \frac{dp}{dx} (y^2 - y\delta) \right] dy \quad (4.46)$$

Integration between the indicated limits gives,

$$Q = \frac{VW\delta}{2} - \frac{W\delta^3}{12\mu} \frac{dp}{dx} \quad (4.47)$$

The total forces F_m acting on the moving plate and F_f acting on the fixed plate are given by

$$F_m = \tau_m l W \quad (4.48-a)$$

$$F_f = \tau_f l W \quad (4.48-b)$$

where, τ_m = the shear stress at the moving plate located at $y = \delta$

τ_f = the shear stress at the fixed plate located at $y = 0$

l = the length of the plate

Then, the total forces can be expressed by

$$F_m = \left(\mu \frac{V}{\delta} + \frac{\delta}{2} \frac{dp}{dx} \right) l W \quad (4.49-a)$$

$$F_f = \left(\mu \frac{V}{\delta} - \frac{\delta}{2} \frac{dp}{dx} \right) l W \quad (4.49-b)$$

With this equation, if the distance to the axis of rotation is given by r , then the torque due to the forces acting on this element is given by

$$T = F_m r = \left(\mu \frac{V}{\delta} + \frac{\delta}{2} \frac{dp}{dx} \right) l W r \quad (4.50)$$

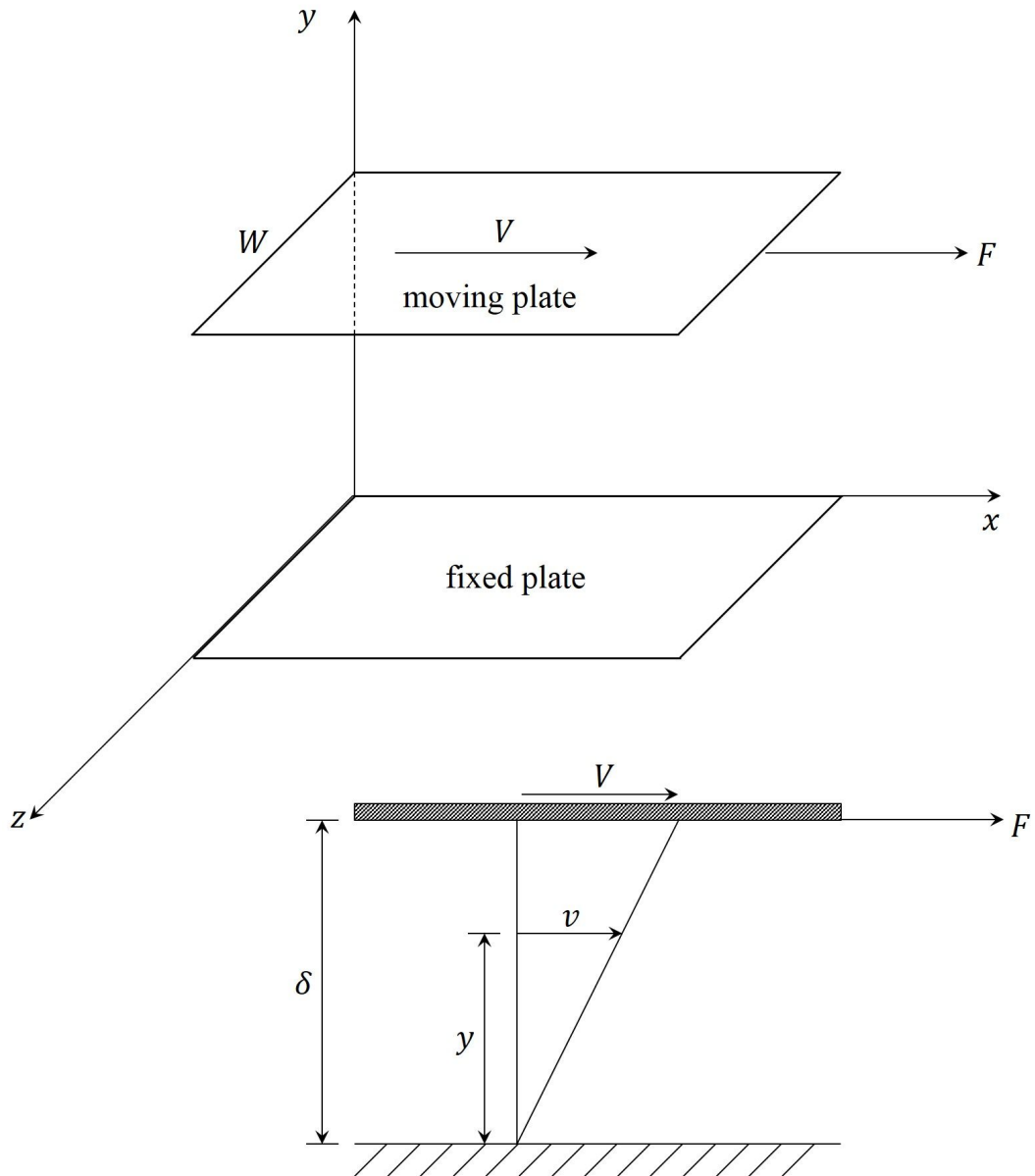


Fig.4.13 Drag due to the viscosity of the liquid (Wilson, 1950).

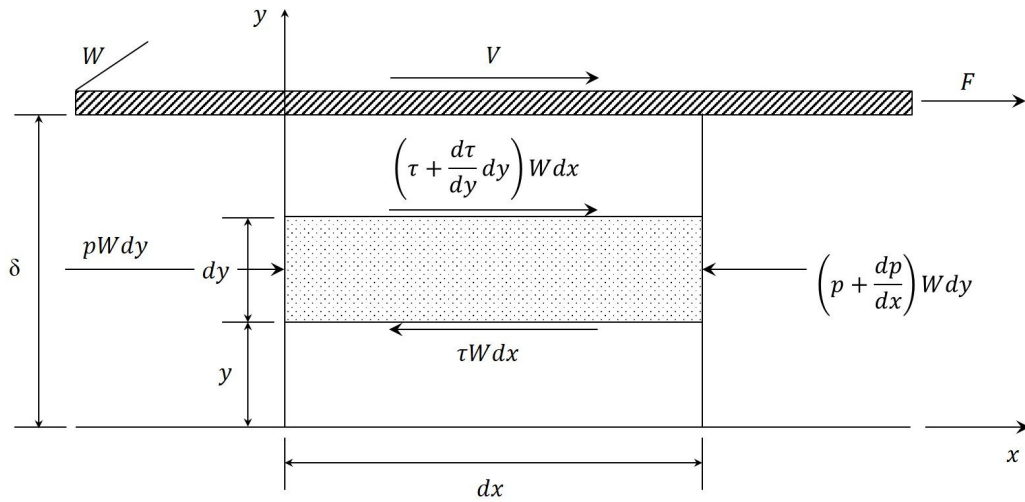


Fig.4.14 Viscous and pressure forces acting on a fluid element (Wilson, 1950).

4.4.1.3. Theory of efficiency for conventional positive-displacement pump

The basic and representative method for evaluating the efficiency of a conventional positive-displacement pump is to use Wilson's equation (Wilson, 1950). The slip flow is assumed to take place in the laminar range between parallel plates, and the viscosity is assumed to remain constant along the path of the flow. Under this assumption, and using equation (4.47), the effect of speed can be neglected. Thus, the slip flow of a conventional positive-displacement pump can be expressed as follows:

$$\Delta Q_s = \frac{W\delta^3}{12\mu} \frac{\Delta p}{\Delta l} \quad (4.51)$$

where, ΔQ_s = the rate of flow

Δp = the pressure drop through the passage

From equations (4.31) and (4.51), the total slip flow Q_s can be simplified as

$$Q_s = C_s D_p \frac{\Delta p}{\mu} \quad (4.52)$$

where, C_s = a dimensionless coefficient

Therefore, the actual flow for the pump is given by

$$Q = Q_{vol} - C_s D_p \frac{\Delta p}{\mu} \quad (4.53)$$

From equation (4.36), the volumetric efficiency of the pump can be expressed as

$$\eta_v = \frac{Q}{Q_{vol}} = \frac{D_p n - C_s D_p \frac{\Delta p}{\mu}}{D_p n} = 1 - C_s \frac{\Delta p}{\mu n} \quad (4.54)$$

With the same method, the first term of equation (4.50) can be expressed as

$$T_v = C_d D_p \mu n \quad (4.55)$$

where, T_v = the viscous torque

C_d = coefficient of the viscous drag dependent upon the pump geometry

The second term of equation (4.50) is given by

$$T_f = C_f D_p \Delta p \quad (4.56)$$

where, T_f = the pressure-dependent frictional torque

C_f = coefficient of friction dependent upon the pump geometry

Therefore, the total torque T can be represented as

$$T = T_{th} + T_v + T_f = \Delta p D_p + C_d D_p \mu n + C_f D_p \Delta p \quad (4.57)$$

From equation (4.37), the torque efficiency of the pump can be expressed as

$$\eta_t = \frac{T_{th}}{T} = \frac{1}{1 + \left(C_d \frac{\mu n}{\Delta p} + C_f \right)} \quad (4.58)$$

The overall efficiency is given by

$$\eta = \frac{1 - C_s \frac{\Delta p}{\mu n}}{1 + C_d \frac{\mu n}{\Delta p} + C_f} \quad (4.59)$$

All of the efficiencies can be represented as a function of $\frac{\mu n}{\Delta p}$ as shown in fig.4.15.

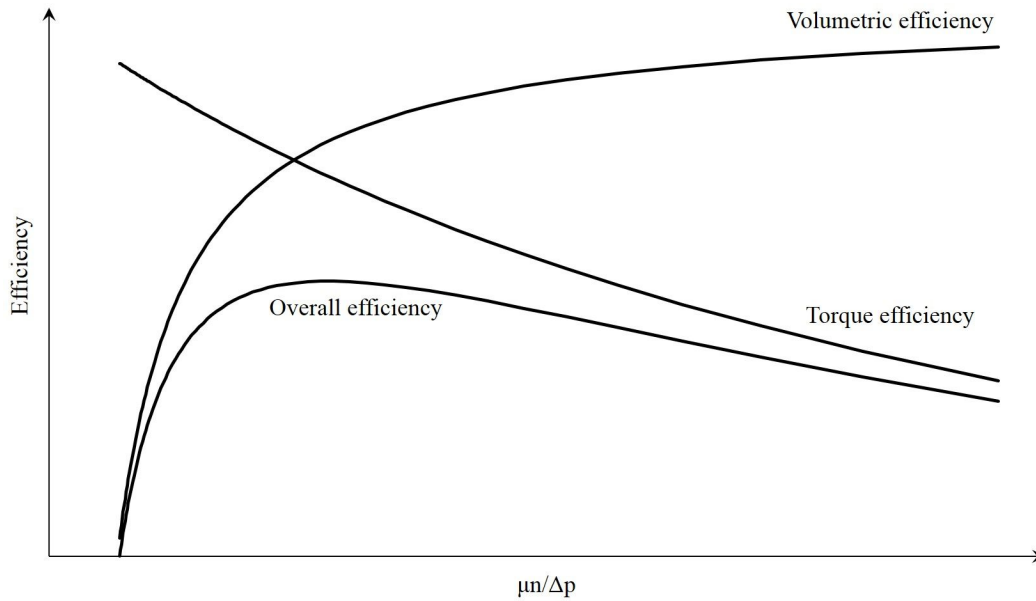


Fig.4.15 Wilson's efficiency curve for a pump (Wilson, 1950).

4.4.2. Performance analysis for rotational clap pumps

4.4.2.1. Analysis for slip and forces caused by a fluid viscosity

To apply the performance theory discussed previously to this pump, the rotor jaws can be simplified into parallel flat plates, as shown in fig.4.16. The slip flow and forces caused by the fluid viscosity in the suction and discharge chamber can be expressed as shown in figs.4.17 and 4.18, respectively.

As presented in chapter 3 and fig.4.4, the direction of the suction and discharge pressures p_s and p_d are changed periodically by the lead-lag motion of the rotors.

Therefore, when $V_1 \geq V_2$, $\frac{dp}{dx}$ of equations (4.47), (4.49), and (4.50) is a positive value. When $V_1 < V_2$, $\frac{dp}{dx}$ is a negative value. The velocities of V_1 and V_2 are

given by

$$V_1 = \dot{\theta}_{p1} \times \left(r_o + \frac{h}{2} \right) \quad (4.60-a)$$

$$V_2 = \dot{\theta}_{p2} \times \left(r_o + \frac{h}{2} \right) \quad (4.60-b)$$

where, $\dot{\theta}_{p1}$, $\dot{\theta}_{p2}$, r_o and h have been defined previously

Because the velocities V_1 and V_2 vary periodically as given in equations (3.26), (3.28), and (4.60) and the pump has several ports for suction and discharge, the first term of equation (4.47) can not be neglected for this pump. Therefore, the total slip flow and forces caused by fluid viscosity in the suction and discharge chambers are given as follows:

$$1) V_1 \geq V_2$$

$$(Q_{scl})_{tot} = 2N \left\{ \frac{V_1 W_j \delta_1}{2} - \frac{W_j \delta_1^3}{12\mu} \frac{p_s - p_d}{l} \right\} \quad (4.61-a)$$

$$(Q_{ss1})_{tot} = Q_{ss1f} + Q_{ss1b} = 2N \left\{ \frac{V_1 h \delta_2}{2} - \frac{h \delta_2^3}{12\mu} \frac{p_s - p_d}{l} \right\} \quad (4.61-b)$$

$$(Q_{sc2})_{tot} = -2N \left\{ \frac{V_2 W_j \delta_1}{2} - \frac{W_j \delta_1^3}{12\mu} \frac{p_d - p_s}{l} \right\} \quad (4.61-c)$$

$$(Q_{ss2})_{tot} = -(Q_{ss2f} + Q_{ss2b}) = -2N \left\{ \frac{V_2 h \delta_2}{2} - \frac{h \delta_2^3}{12\mu} \frac{p_d - p_s}{l} \right\} \quad (4.61-d)$$

2) $V_1 < V_2$

$$(Q_{sc1})_{tot} = -2N \left\{ \frac{V_1 W_j \delta_1}{2} - \frac{W_j \delta_1^3}{12\mu} \frac{p_d - p_s}{l} \right\} \quad (4.61-e)$$

$$(Q_{ss1})_{tot} = -2N \left\{ \frac{V_1 h \delta_2}{2} - \frac{h \delta_2^3}{12\mu} \frac{p_d - p_s}{l} \right\} \quad (4.61-f)$$

$$(Q_{sc2})_{tot} = 2N \left\{ \frac{V_2 W_j \delta_1}{2} - \frac{W_j \delta_1^3}{12\mu} \frac{p_s - p_d}{l} \right\} \quad (4.61-g)$$

$$(Q_{ss2})_{tot} = 2N \left\{ \frac{V_2 h \delta_2}{2} - \frac{h \delta_2^3}{12\mu} \frac{p_s - p_d}{l} \right\} \quad (4.61-h)$$

$$(Q_s)_{tot} = (Q_{sc1})_{tot} + (Q_{ss1})_{tot} + (Q_{sc2})_{tot} + (Q_{ss2})_{tot} \quad (4.61-i)$$

where, $(Q_{sc1})_{tot}$ = the total slip flow between the upper and bottom surfaces of jaw 1 and the chamber

$(Q_{ss1})_{tot}$ = the total slip flow between the side surfaces of jaw 1 and the chamber

Q_{ss1f} = the slip flow between the front side surface of jaw 1 and the chamber

Q_{ss1b} = the slip flow between the back side surface of jaw 1 and the chamber

$(Q_{sc2})_{tot}$ = the total slip flow between the upper and bottom surfaces of jaw 2 and the chamber

$(Q_{ss2})_{tot}$ = the total slip flow between the side surfaces of the jaw 2 and chamber

$V_1, V_2, W_j, h, \delta_1, \delta_2, \mu, p_s, p_d, l, N$ are defined in Figs. 4.15 - 4.17 or were previously given.

$$1) V_1 \geq V_2$$

$$(F_{sc1}')_{tot} = 2N \left\{ \mu \frac{V_1}{\delta_1} - \frac{\delta_1}{2} \frac{p_s - p_d}{l} \right\} l W_j \quad (4.62-a)$$

$$(F_{ss1}')_{tot} = F_{ss1f}' + F_{ss1b}' = 2N \left\{ \mu \frac{V_1}{\delta_2} - \frac{\delta_2}{2} \frac{p_s - p_d}{l} \right\} lh \quad (4.62-b)$$

$$(F_{sc2}')_{tot} = 2N \left\{ \mu \frac{V_2}{\delta_1} - \frac{\delta_1}{2} \frac{p_d - p_s}{l} \right\} l W_j \quad (4.62-c)$$

$$(F_{ss2}')_{tot} = 2N \left\{ \mu \frac{V_2}{\delta_2} - \frac{\delta_2}{2} \frac{p_d - p_s}{l} \right\} lh \quad (4.62-d)$$

$$2) V_1 < V_2$$

$$(F_{sc1}')_{tot} = 2N \left\{ \mu \frac{V_1}{\delta_1} - \frac{\delta_1}{2} \frac{p_d - p_s}{l} \right\} l W_j \quad (4.62-e)$$

$$(F_{ss1}')_{tot} = 2N \left\{ \mu \frac{V_1}{\delta_2} - \frac{\delta_2}{2} \frac{p_d - p_s}{l} \right\} lh \quad (4.62-f)$$

$$(F_{sc2}')_{tot} = 2N \left\{ \mu \frac{V_2}{\delta_1} - \frac{\delta_1}{2} \frac{p_s - p_d}{l} \right\} l W_j \quad (4.62-g)$$

$$(F_{ss2}')_{tot} = 2N \left\{ \mu \frac{V_2}{\delta_2} - \frac{\delta_2}{2} \frac{p_s - p_d}{l} \right\} lh \quad (4.62-h)$$

$$(F_{slip}')_{tot} = (F_{sc1}')_{tot} + (F_{ss1}')_{tot} + (F_{sc2}')_{tot} + (F_{ss2}')_{tot} \quad (4.62-i)$$

where, $(F_{sc1}')_{tot}$ = the total forces at jaw 1 caused by the fluid viscosity between the upper and bottom surfaces of jaw 1 and the chamber

$(F_{ss1}')_{tot}$ = the total forces at jaw 1 caused by fluid viscosity between the side surfaces of jaw 1 and the chamber

F_{ss1f}' = the forces at jaw 1 caused by the fluid viscosity between the front side surface of jaw 1 and the chamber

F_{ss1b}' = the forces at jaw 1 caused by the fluid viscosity between the back side surface of jaw 1 and the chamber

$(F_{sc2}')_{tot}$ = the total forces at jaw 2 caused by the fluid viscosity between the upper and bottom surfaces of jaw 2 and the chamber

$(F_{ss2}')_{tot}$ = the total forces at jaw 2 caused by the fluid viscosity between the side surfaces of jaw 2 and the chamber

$V_1, V_2, W_j, h, \delta_1, \delta_2, \mu, p_s, p_d, l, N$ are defined in Figs. 4.16 - 4.18 or were previously given

$(F_{sc1})_{tot}, (F_{ss1})_{tot}, (F_{sc2})_{tot}, (F_{ss2})_{tot}$ = the forces at the chamber

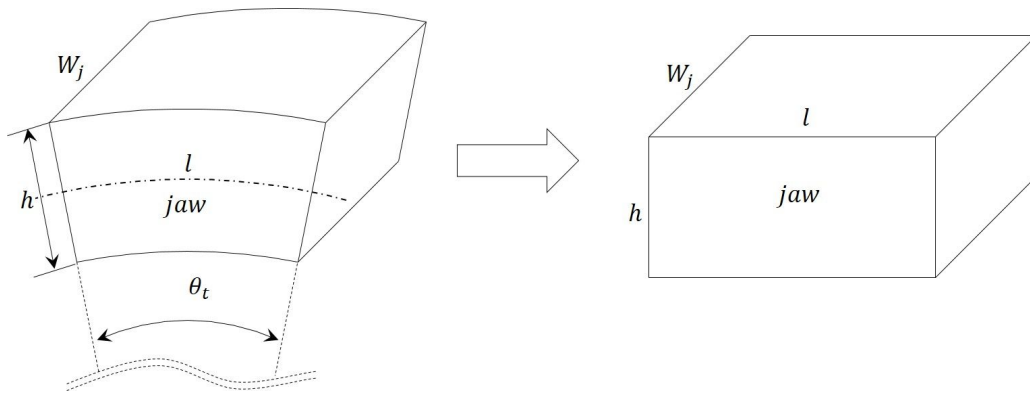


Fig.4.16 Jaw model simplified as a rectangle for the analysis of flow and torque losses.

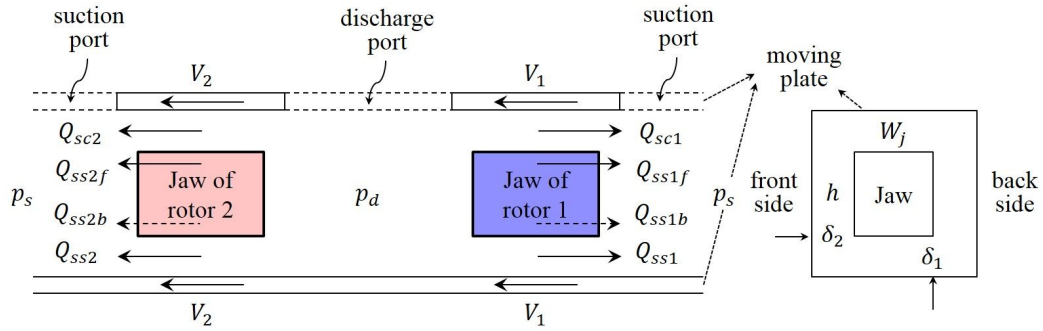


Fig.4.17 Flow losses in suction and discharge chambers of the pump.

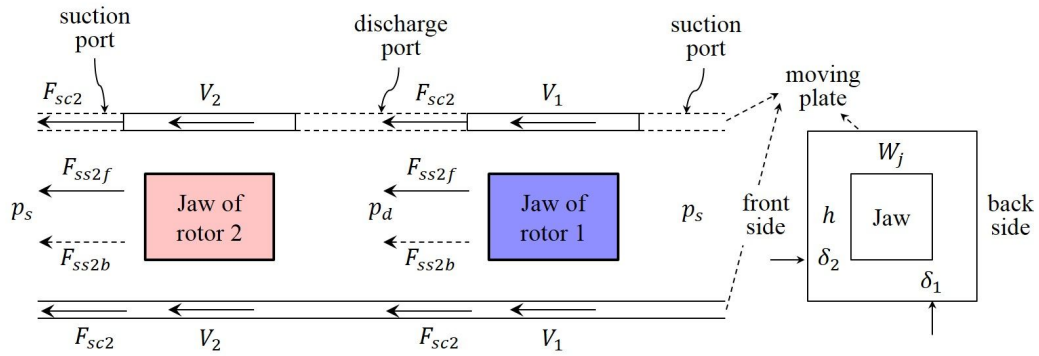


Fig.4.18 Force losses in suction and discharge chambers of the pump.

4.4.2.2. Efficiency analysis for rotational clap pump

The efficiencies of the rotational clap pump can be obtained with equations (4.54), (4.58), and (4.59). From equations (3.41), (4.54), and (4.61), the volumetric efficiency is given by

$$\eta_v = \frac{Q_{vol} - (Q_s)_{tot}}{Q_{vol}} \quad (4.63)$$

Because of the forces $(F_{slip}')_{tot}$ caused by the fluid viscosity, the forces acting on each rotor are increased. Therefore, the total torque T can be obtained by substituting $-F_{R1} + (F_{sc1}')_{tot} + (F_{ss1}')_{tot}$ and $F_{R2} + (F_{sc2}')_{tot} + (F_{ss2}')_{tot}$ into equation (4.19). From equations (4.8) - (4.30) and (4.62), the torque efficiency is then given by

$$\eta_t = \frac{T_i}{T} \quad (4.64)$$

The overall efficiency is given by

$$\eta = \eta_v \times \eta_t = \frac{Q_{vol} - (Q_{slip})_{tot}}{Q_{vol}} \times \frac{T_i}{T} \quad (4.65)$$

4.5. Conclusions

This chapter presents the pressure, driving torque, and efficiency characteristics of the pump for an analysis of its the fundamental performance. The pressures due to the friction, mass acceleration, piping components, and gravity were analyzed based on Newton's law of viscosity. The forces acting on the pump components were calculated by using vector equations based on the kinematic analysis presented in chapter 3. The volumetric, torque, and overall efficiencies were analyzed by calculating the slip flow and frictional forces caused by fluid viscosity.

To analyze the pressure of the pump, the suction and discharge spaces in the pump were divided into five independent control volumes and the spaces were

simplified to circular pipes.

Because the axial forces were negligible, the driving torque and forces of the main components were calculated on two-dimensional Cartesian coordinates.

To minimize the input power and forces acting on the components, the crank radius should be minimized and the distance between two pins should be maximized. In addition, the input power and pin forces can be minimized when the number of jaws is two. However, the gear force showed the opposite trend.

The slip flow and viscous forces of the pump were analyzed by using the conventional method based on Newton's law of viscosity. Because the suction and discharge pressure change periodically with the lead-lag motion of the rotors and the pump has several ports for suction and discharge, the velocity term of the equations for the slip flow and viscous forces could not be neglected in the case of this pump. The efficiencies were evaluated by using Wilson's equation.

5. Design of a prototype rotational clap pump

5.1. Introduction

Chapter 3 presented the relationships among the design parameters. For the fixed internal gear and gear of the shaft link, the relationships among the number of teeth of two gears and crank radius, the number of jaws, and the performance parameters were examined. However, more detailed analysis of the geometric relationships between the two gears should be conducted for the pump design.

This chapter, discusses the geometric constraints of the main components not presented in chapter 3 in more detail. The strengths of the main components of a prototype pump were calculated to manufacture the pump for validation of the basic performance.

5.2. Gear of the shaft link and fixed internal gear

5.2.1. Geometric constraints

As discussed in chapter 3, the rotational clap mechanism is a five-link spatial mechanism that comprises a crank as the driving link, a shaft link having two pins symmetrically located in opposite directions with a plate rigidly mounted at the middle and two gears rigidly attached to both ends, two rotors with jaws equally spaced along their circumferences, and a fixed internal gear. To realize this mechanism, the geometric relationships of these design parameters need to be determined. In the case of gears of the shaft link and fixed internal gears, the relationships between the external and internal gears should also be considered in more detail.

The fixed internal gear is composed of a cylindrical gear having teeth inside a circular ring. To design the internal and external gears, the calculation process in tables 5.1 and 5.2 should be followed, and three kind of interferences should be considered. Fig.5.1 presents the mesh of an internal gear and external gear (Kohara Gear Industry Co., Ltd. 2015).

Table 5.1 Calculation of a profile-shifted internal gear and external gear when the center distance is not given (Kohara Gear Industry Co., Ltd. 2015).

No.	Item	Symbol	Formula
1	Module	m	Set value
2	Reference pressure angle	α	
3	Number of teeth	z	
4	Profile shift coefficient	x	
5	Involute function α_w	$inv \alpha_w$	$2 \tan \alpha \left(\frac{x_2 - x_1}{z_2 - z_1} \right) + inv \alpha$
6	Working pressure angle	α_w	Find from involute function table
7	Center distance modification coefficient	y	$\frac{z_2 - z_1}{2} \left(\frac{\cos \alpha}{\cos \alpha_w} - 1 \right)$
8	Center distance	a	$\left(\frac{z_2 - z_1}{2} + y \right) m$
9	Reference diameter	d	$z m$
10	Base diameter	d_b	$d \cos \alpha$
11	Working pitch diameter	d_w	$\frac{d_b}{\cos \alpha_w}$
12	Addendum	h_{a1} h_{a2}	$(1 + x_1) m$ $(1 - x_2) m$
13	Tooth depth	h	$2.25 m$
14	Tip diameter	d_{a1} d_{a2}	$d_1 + 2 h_{a1}$ $d_2 - 2 h_{a2}$
15	Root diameter	d_{f1} d_{f2}	$d_{a1} - 2 h$ $d_{a2} + 2 h$

Table 5.2 Calculation of a profile-shifted internal gear and external gear when the center distance is given (Kohara Gear Industry Co., Ltd. 2015).

No.	Item	Symbol	Formula
1	Center distance	a	Set value
2	Center distance modification coefficient	y	$\frac{a}{m} - \frac{z_2 - z_1}{2}$
3	Working pressure angle	α_w	$\cos^{-1} \left(\frac{\cos \alpha}{\frac{2y}{z_2 - z_1} + 1} \right)$
4	Difference of profile shift coefficients	$x_2 - x_1$	$\frac{(z_2 - z_1)(\text{inv } \alpha_w - \text{inv } \alpha)}{2 \tan \alpha}$
5	Profile shift coefficient	x	-

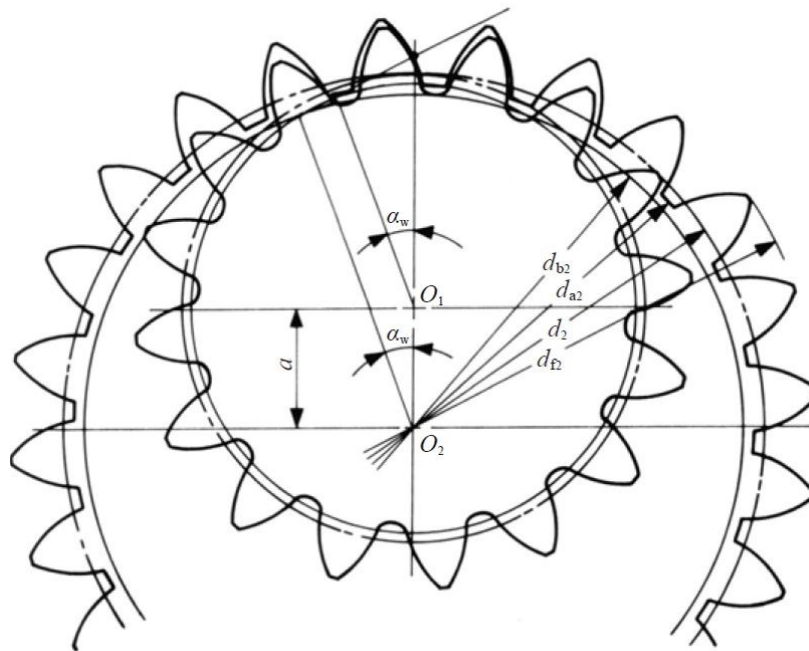


Fig.5.1. Meshing of the internal gear and external gears (Kohara Gear Industry Co., Ltd. 2015).

5.2.1.1. Involute interference

Involute interference can occur between the dedendum of the external gear and the addendum of the internal gear when the number of teeth of the external gear is small. To avoid this interference, the following equation should be satisfied (Kohara Gear Industry Co., Ltd. 2015):

$$\frac{z_1}{z_2} \geq 1 - \frac{\tan \alpha_{a2}}{\tan \alpha_w} \quad (5.1)$$

where, α_{a2} = pressure angle at a tip of the internal gear tooth.

$$= \cos^{-1} \left(\frac{d_{b2}}{d_{a2}} \right)$$

α_w = working pressure angle

$$= \cos^{-1} \left(\frac{(z_2 - z_1)m \cos \alpha}{2a} \right)$$

5.2.1.2. Trochoid interference

This interference occurs when the difference between the numbers of teeth of the two gears is small. It can be avoided as long as the following equation is satisfied (Kohara Gear Industry Co., Ltd. 2015):

$$\theta_1 \frac{z_1}{z_2} \operatorname{inv} \alpha_w - \operatorname{inv} \alpha_{a2} \geq \theta_2 \quad (5.2)$$

$$\text{where, } \theta_1 = \cos^{-1} \left(\frac{r_{a2}^2 - r_{a1}^2 - a^2}{2ar_{a1}} \right) + inv \alpha_{a1} + inv \alpha_w$$

$$\theta_2 = \cos^{-1} \left(\frac{a^2 + r_{a2}^2 - r_{a1}^2}{2ar_{a2}} \right)$$

α_{a1} = the pressure angle of the spur gear tooth tip

$$= \cos^{-1} \left(\frac{d_{b1}}{d_{a1}} \right)$$

5.2.1.3. Trimming interference

Trimming interference occurs in the radial direction and prevents the gears from apart. The mesh must be assembled by sliding the gears together with an axial motion. This interference tends to occur when the numbers of teeth of the two gears are very similar. Equation (5.3) indicates how to prevent this type of interference (Kohara Gear Industry Co., Ltd. 2015):

$$\theta_1 + inv \alpha_{a1} - inv \alpha_w \geq \frac{z_2}{z_1} (\theta_2 + inv \alpha_{a2} - inv \alpha_w) \quad (5.3)$$

$$\text{where, } \theta_1 = \sin^{-1} \sqrt{\frac{1 - (\cos \alpha_{a1} / \cos \alpha_{a2})^2}{1 - (z_1 / z_2)^2}}$$

$$\theta_2 = \sin^{-1} \sqrt{\frac{(\cos \alpha_{a2} / \cos \alpha_{a1})^2 - 1}{(z_2 / z_1)^2 - 1}}$$

5.2.1.4. Case studies to avoid interferences in this pump

In chapter 3, equations (3.33) and (3.34), represent the relationships among the crank radius, number of jaws, gear module, number of teeth on the fixed internal gear and number of teeth on the gear of shaft link.

In order to design the fixed internal gear and gear of the shaft link, all of these kinematic constraints and gear interferences should be avoided. Tables 5.3 and 5.4 present cases to prevent fixed internal gear interference when the gear module $m=1$, center distance (=crank radius) $a = r_c = 5mm$, and reference pressure angle $\alpha = 20^\circ$ and 27° . The number of cases where the number of teeth of internal and external gears can be selected increases with the pressure angle and number of jaws for a given gear module and center distance. Even if these are impossible conditions, as given in tables 5.3 and 5.4, the conditions can be made possible by using smaller d_{a1} or larger d_{a2} than the calculated values given in tables 5.1 and 5.2. For example, interference occurs when the number of jaws N is 4, the gear module m is 1, the pressure angle α is 27° , the number of external gears Z_p is 27, and the number of internal gears, Z_r is 36, as given in table 5.5. However, it can be resolved adjusting d_{a1} or d_{a2} .

Table 5.3 Cases to prevent internal gear interference when the gear module $m=1$, center distance $a=5mm$ (=crank radius r_c), and reference pressure angle $\alpha=20^\circ$.

N=2			N=3			N=4		
Z_p	Z_r	Design possibility	Z_p	Z_r	Design possibility	Z_p	Z_r	Design possibility
9	18	impossible	18	27	impossible	27	36	impossible
10	20		20	30		30	40	
11	22		22	33		33	44	
12	24		24	36		36	48	
13	26		26	39		39	52	
14	28		28	42		42	56	
15	30		30	45		45	60	
16	32		32	48		48	64	possible
17	34		34	51		51	68	
18	36		36	54		54	72	
19	38		38	57		57	76	
20	40		40	60		60	80	
21	42		42	63		63	84	
22	44		44	66		66	88	
23	46		possible	46		69	possible	
24	48	48		72	72	96		
25	50	50		75	75	100		
26	52	52		78	78	104		
27	54	54		81	81	108		
28	56	56		84	84	112		
29	58	58		87	87	116		
30	60	60		90	90	120		

Table 5.4 Cases to prevent internal gear interference when the gear module $m = 1$ and reference pressure angle $\alpha = 27^\circ$.

N=2			N=3			N=4		
Z_p	Z_r	Design possibility	Z_p	Z_r	Design possibility	Z_p	Z_r	Design possibility
9	18	impossible	18	27	impossible	27	36	impossible
10	20		20	30	possible	30	40	possible
11	22		22	33		33	44	
12	24		24	36		36	48	
13	26	possible	26	39		39	52	
14	28		28	42		42	56	
15	30		30	45		45	60	
16	32		32	48		48	64	
17	34		34	51		51	68	
18	36		36	54		54	72	
19	38		38	57		57	76	
20	40		40	60		60	80	
21	42		42	63		63	84	
22	44		44	66		66	88	
23	46		46	69		69	92	
24	48		48	72		72	96	
25	50		50	75		75	100	
26	52		52	78	78	104		
27	54		54	81	81	108		
28	56		56	84	84	112		
29	58	58	87	87	116			
30	60	60	90	90	120			

Table 5.5 Example of the effect of the diameter of internal and external gears on the interference.

Symbol		Ex. Gear	In. Gear
m		1	
α		27	
z		27	36
x		0	0
$inv \alpha_w$		0.038	
α_w		36.688	
y		0.500	
a		5.000	
d		27	36
d_b		24.057	32.076
d_w		30.000	40.000
h_{a1}	h_{a2}	1.000	1.000
h		2.250	
d_{a1}	d_{a2}	d_{a1}	d_{a2}
d_{f1}	d_{f2}	24.500	38.500
$x_2 - x_1$		0.000	

$d_{a1} = 29.0, d_{a2} = 34.0$: impossible

$d_{a1} = 28.5, d_{a2} = 34.0$: possible

$d_{a1} = 29.0, d_{a2} = 34.5$: possible

5.2.2. Gear strength calculation for prototype pumps

The forces for the gear of the shaft link and fixed internal gear are represented by F_p and R_p , respectively, and can be calculated by using table 5.6, equations (4.16) and (4.25), and fig.4.5. The maximum and minimum forces $(F_p)_{\max}$, $(F_p)_{\min}$, $(R_p)_{\max}$, and $(R_p)_{\min}$ are 401.71 N, 0 N, 0 N, and -401.71 N respectively as shown in fig.5.2.

As shown in fig.4.5, the bending forces between two gears are given by

$$(F_p)_t = -(R_p)_t = F_p \cos \alpha = -R_p \cos \alpha \quad (5.4)$$

where, α = reference pressure angle, 25°

Therefore, the maximum bending forces of the gear and fixed internal gear $((F_p)_{\max})_t$ and $((R_p)_{\max})_t$ are given by

$$((F_p)_{\max})_t = -((R_p)_{\max})_t = 401.71 \times \cos 25^\circ = 339.54 \text{ N} \quad (5.5)$$

The gear strength is calculated from only the bending stress in the gear teeth by using the Lewis equation, which still remains the basis for most gear designs today (Shigley and Mischke, 2001). The forces acting on the gear can be derived by simplifying the tooth as a simple cantilever, as shown in fig.5.3. This gives

$$\sigma_{Flim} = \frac{W^t}{b Y m} \quad (5.6)$$

where, b = gear width

Y = Lewis form factor (see table 5.7)

m = gear module

In this thesis, the modified Lewis equation that adds the dynamic factor, stress concentration factor, and impact factor is used. This gives

$$\sigma_{Flim} = \frac{W^t}{b_{\min} Y m} \times \frac{K_f}{f_v f_w} \quad (5.7)$$

Rearranging the above equation about the gear width b gives

$$b_{\min} = \frac{W^t}{\sigma_{Flim} Y m} \times \frac{K_f}{f_v f_w} \quad (5.8)$$

where, K_f = fatigue stress-concentration factor

f_v = dynamic factor

f_w = impact factor(overload factor)

(1) Fatigue stress-concentration factor K_f (Shigley and Mischke. 2001).

$$K_f = H + \left(\frac{t}{r}\right)^L \left(\frac{t}{l}\right)^M \quad (5.9)$$

where, $H = 0.34 - 0.4583662 \phi$
 $L = 0.316 - 0.4583662 \phi$
 $M = 0.290 - 0.4583662 \phi$

$$r = \frac{(b_d - r_f)^2}{(d/2) + b_d - r_f}$$
 $r_f = \text{fillet radius}$
 $b_d = \text{dedendum}$
 $d = \text{pitch diameter}$

(2) Dynamic factor, f_v (Hong. 2013).

$$f_v = \frac{3.05}{3.05 + v}$$

(cast iron, low speed : $v = 0.5 \sim 10 \text{ m/s}$)

$$f_v = \frac{6.1}{6.1 + v}$$

(cut or milled profile, middle speed : $v = 5 \sim 20 \text{ m/s}$)

$$f_v = \frac{3.56}{3.56 + \sqrt{v}}$$

(5.10)

(hobbed or shaped profile, high speed : $v = 20 \sim 50 \text{ m/s}$)

$$f_v = \sqrt{\left(\frac{5.56}{5.56 + \sqrt{v}} \right)}$$

(shaved or ground profile, high speed)

$$f_v = 1$$

(very low speed : $v = 0 \sim 0.5 \text{ m/s}$)

(3) Impact (or overload) factor, f_w (Hong. 2013).

Buckingham's impact factor

$$f_w = 0.80$$

(constant, normal load)

$$f_w = 0.74 \tag{5.11}$$

(variable load)

$$f_w = 0.67$$

(impact load)

Therefore, the minimum gear width $b_{\min.}$ can be calculated by using figs.5.2 and 5.3, tables 5.6 and 5.7, and equations (5.4) - (5.11). Then, the result is

$$\begin{aligned} b_{\min.} &= \frac{W^t}{\sigma_{Flim} \times Y \times m} \times \frac{K_f}{f_v \times f_w} \\ &= \frac{370.33 \text{ N}}{299.21 \text{ MPa} \times 0.425 \times (1 \times 10^{-3})} \times \frac{1.751}{1 \times 0.740} \times 10^3 = 6.89 \text{ mm} \end{aligned} \tag{5.12}$$

where, $\sigma_{Flim} = 299.21 \text{ MPa}$: allowable gear bending stress (Kohara Gear Industry Co., Ltd. 2015).

Table 5.6 Specifications of the rotary clap pump used in the performance test.

Parameters		Values
Performance	Flow rate	11.5 l/min.@100 rpm
	Max. differential pressure	5 kgf/cm ²
	Kinematic viscosity of fluid	32 mm ² /sec
Kinematic	No. of rotor jaws	4
	Crank radius r_c	5 mm
	Distance between pins P_1 and P_2 L	64.6 mm
	Maximum relative angular displacement between rotors 1 and 2 $(\theta_{rel})_{max}$	26°
	Jaw width W_j	30 mm
	Jaw height h	10 mm
	Outer radius of rotor r_o	53.5 mm
	Gear module m	1
	No. of teeth on the gear of the shaft link Z_p	30
	No. of teeth on the fixed internal gear Z_r	40
	Reference pressure angle α	25°
Moment of inertia of the rotors, I_R	9.99×10^{-4} kg·m ²	

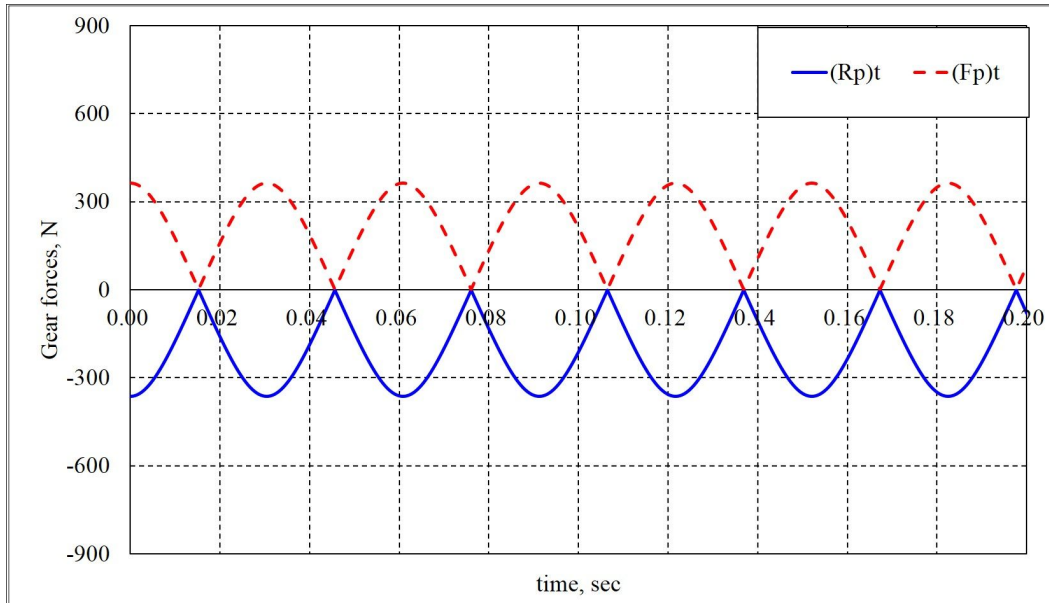


Fig.5.2. Forces acting on the gears.

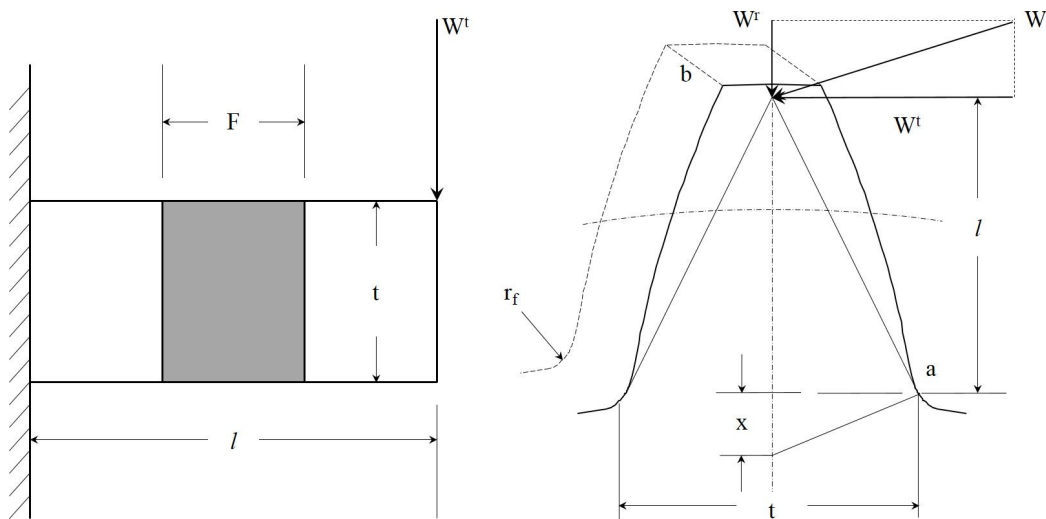


Fig.5.3. Cantilever model of a gear tooth (Shigley and Mischke. 2001).

Table 5.7 Lewis form factor (Hong. 2013).

Number of teeth	Lewis form factor, Y	Number of teeth	Lewis form factor, Y
10	0.238	33	0.436
11	0.259	34	0.440
12	0.277	35	0.443
13	0.293	36	0.446
14	0.307	37	0.449
15	0.320	38	0.452
16	0.332	39	0.454
17	0.342	40	0.457
18	0.352	43	0.464
19	0.361	45	0.468
20	0.369	50	0.477
21	0.377	55	0.484
22	0.384	60	0.491
23	0.390	65	0.496
24	0.396	70	0.501
25	0.402	75	0.506
26	0.407	80	0.509
27	0.412	90	0.516
28	0.417	100	0.521
29	0.421	150	0.537
30	0.425	200	0.545
31	0.429	300	0.554
32	0.433		

5.3. Crank

The crank is an eccentric shaft, as shown in figs.3.1 and 4.5-(e). However, this crank consists of three parts, and the main shaft is a solid circular shaft. The bearings at points A and B take the pure radial loads R_a and R_b , and the two bushes act as the dynamic loads on the shaft, as shown in fig.5.4-(a). The weight of the crank can be neglected; the shaft is assumed to be simply supported, and the loads and bearing reactions are assumed to be concentrated. Then the loads for the main shaft of the crank can be expressed as shown in fig.5.4-(b).

5.3.1. Design for strength

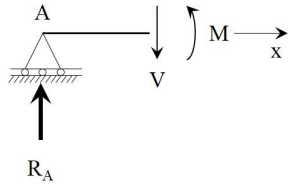
As shown in fig.5.4-(b), the relationships among the bearing reaction loads R_a and R_b and the dynamic load $2q$ are given by

$$R_A + R_B = 2ql \quad (5.13)$$

$$R_A = R_B = \frac{ql \left(a + \frac{l}{2} \right) + ql \left(L - a - \frac{l}{2} \right)}{L} = ql \quad (5.14)$$

Therefore,

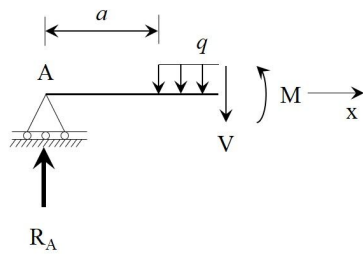
① $0 \leq x < a$



$$V = R_A = ql \quad (5.15-a)$$

$$M = R_A x = qlx \quad (5.16-a)$$

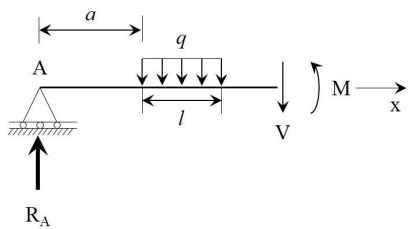
② $a \leq x < a+l$



$$V = R_A - q(x-a) \quad (5.15-b)$$

$$M = R_A x - \frac{q}{2}(x-a)^2 \quad (5.16-b)$$

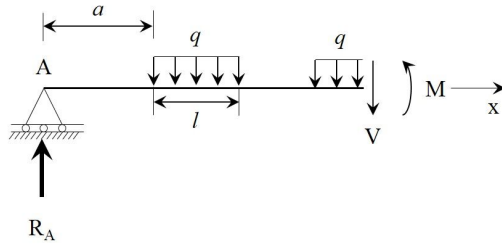
③ $a+l \leq x < L-a-l$



$$V = R_A - ql \quad (5.15-c)$$

$$M = R_A x - ql \left(x - a - \frac{l}{2} \right) \quad (5.16-c)$$

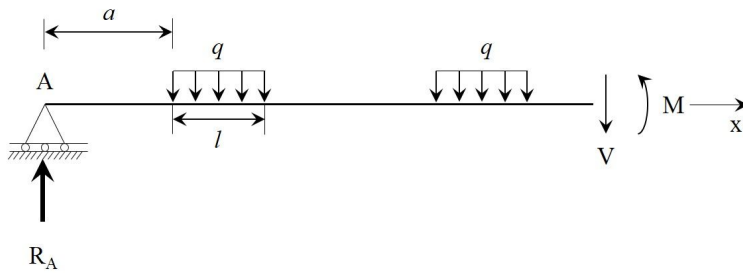
④ $L - a - l \leq x < L - a$



$$V = R_A - q(x - L + 2l - a) \quad (5.15-d)$$

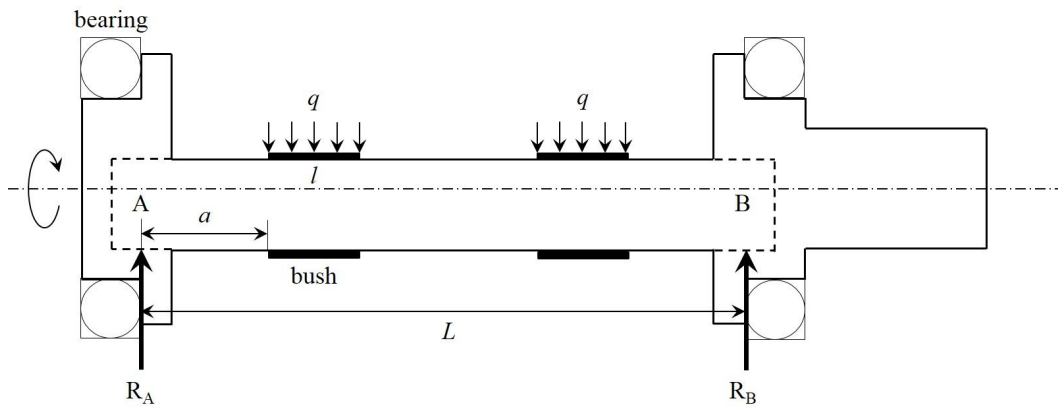
$$M = R_A x - ql \left(x - a - \frac{l}{2} \right) - \frac{q}{2} (x - L + a + l)^2 \quad (5.16-d)$$

⑤ $L - a \leq x < L$

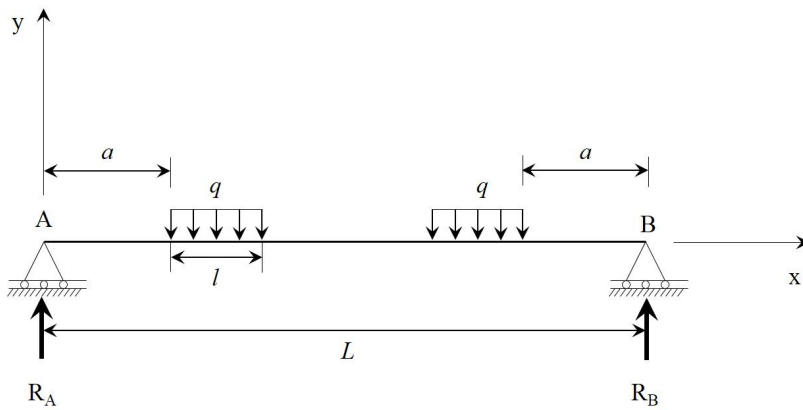


$$V = R_A - 2ql \quad (5.15-e)$$

$$M = R_A x - ql(2x - L) \quad (5.16-e)$$



(a) Crank loads and dimensions



(b) Simplified loading diagram for crank

Fig.5.4. Loads and dimensions for the main shaft of the crank.

The bearing reaction forces R_A and R_B can be calculated by using table 5.6, equation (4.17), (4.18), (4.28), and (4.29) and fig.4.5 when $a = 14.5 \text{ mm}$, $l = 10 \text{ mm}$, and $L = 106 \text{ mm}$. These forces can be expressed as follows:

$$R_A = R_B = \frac{1}{2} \sqrt{(R_{cn}^2 + R_{ct}^2)} \quad (5.17)$$

Because the loads R_{cn} and R_{ct} are variable, the maximum bearing reaction forces $(R_A)_{\max}$ and $(R_B)_{\max}$ can be obtained as follows:

$$(R_A)_{\max} = (R_B)_{\max} = \frac{1}{2} \sqrt{(R_{cn}^2 + R_{ct}^2)_{\max}} = 1,476 \text{ N} \quad (5.18)$$

The minimum bearing reaction forces are given by

$$(R_A)_{\min} = (R_B)_{\min} = \frac{1}{2} \sqrt{(R_{cn}^2 + R_{ct}^2)_{\min}} = 1,027 \text{ N} \quad (5.19)$$

With these equations, the shear force V and bending moment M can be obtained as shown in figs.(5.5) and (5.6). As a result, the shear force V has a maximum value when $0 \leq x < a$, and the bending moment has a maximum value when $a+l \leq x < L-l-a$. Therefore, the amplitude of the moment M_a is given by

$$M_a = \frac{M_{\max} - M_{\min}}{2} = \frac{28.78 \text{ N} - 20.04 \text{ N}}{2} = 4.4 \text{ N} \quad (5.20)$$

$$M_m = \frac{M_{\max} + M_{\min}}{2} = \frac{28.78 N + 20.04 N}{2} = 24.4 N \quad (5.21)$$

The torsion of the main shaft of the crank is small enough to neglect. Therefore, the torque of this shaft is given by

$$T_a = T_m = 0 N \quad (5.22)$$

with these calculation results, the minimum diameter of this shaft can be obtained by using three well-known equations (Westing house code, Distribution energy-Gerber, and DE-ASME elliptic). The diameter of this shaft can then be used to obtain the maximum values of the results.

① Westing house code

$$d_{\min} = \sqrt[3]{\frac{32n}{\pi} \sqrt{\left(\frac{M_a}{S_e} + \frac{M_m}{S_y}\right)^2 + \left(\frac{T_a}{S_e} + \frac{T_m}{S_y}\right)^2}} \quad (5.23-a)$$

where, n = safety factor

② Distortion energy-Gerber

$$d_{\min} = \sqrt[3]{\frac{8nB}{\pi S_e} \left(1 + \sqrt{1 + \left(\frac{2AS_e}{BS_u}\right)^2}\right)} \quad (5.23-b)$$

$$\text{where, } A = \sqrt{4M_m^2 + 3T_m^2}$$

$$B = \sqrt{4M_a^2 + 3T_a^2}$$

③ DE-ASME elliptic

$$d_{\min} = \sqrt[3]{\frac{16n}{\pi} \sqrt{\frac{B^2}{S_e^2} + \frac{A^2}{S_y^2}}} \quad (5.23-c)$$

$$\text{where, } A = \sqrt{4M_m^2 + 3T_m^2}$$

$$B = \sqrt{4M_a^2 + 3T_a^2}$$

When the material of the shaft is S45C,

$$S_u = 569 \text{ MPa} \quad (5.24)$$

$$S_y = 343 \text{ MPa (normalized) (MatWeb, 2015)}$$

$$S'_e = \frac{1}{2} S_u = 284.5 \text{ MPa} \quad (5.25)$$

Then,

$$S_e = k_a k_b k_c k_d k_e S'_e \quad (\text{Joseph Marin, 1962}) \quad (5.26)$$

where, k_a = surface condition modification factor

k_b = size modification factor

k_c = load modification factor

k_d = temperature modification factor

k_e = miscellaneous-effects modification factor

S'_e = rotary-beam endurance limit

by solving for S_e under a given condition,

$$S_e = 0.83 \times 1 \times 1 \times 1 \times 0.81 \times 284.5 \text{ MPa} = 191.9 \text{ MPa} \quad (5.27)$$

The shaft diameter reaches its maximum value when the Westing house code equation is used:

$$d_{\min} = \sqrt[3]{\frac{32 \times 1.2}{\pi} \sqrt{\left(\frac{4.4 \text{ Nm}}{191.9 \text{ MPa}} + \frac{24.4 \text{ Nm}}{343 \text{ MPa}}\right)^2 + 0^2}} = 10.47 \text{ mm} \quad (5.28)$$

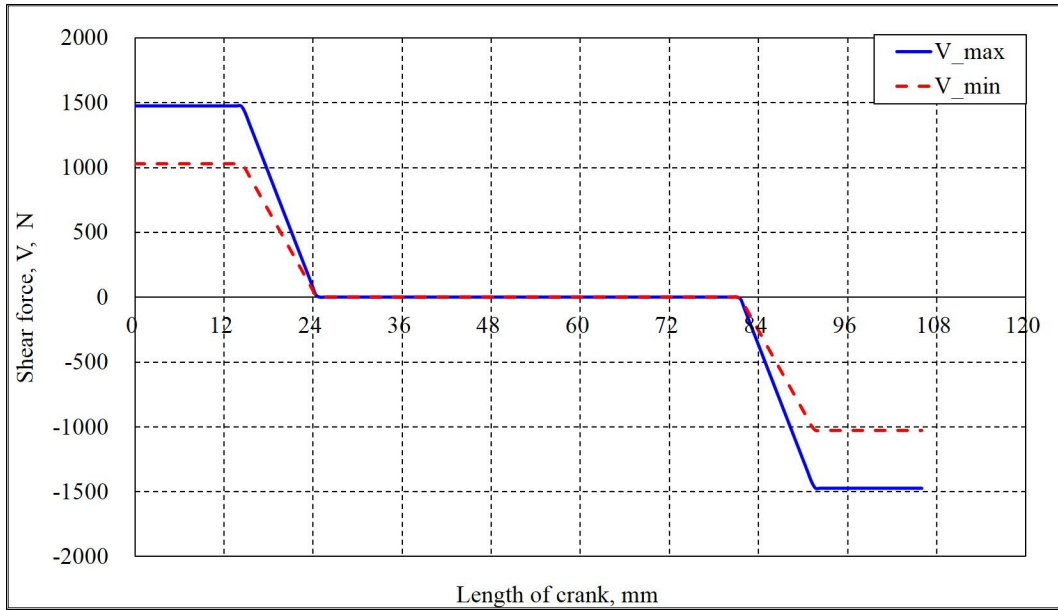


Fig.5.5. Shear force acting on the crank shaft

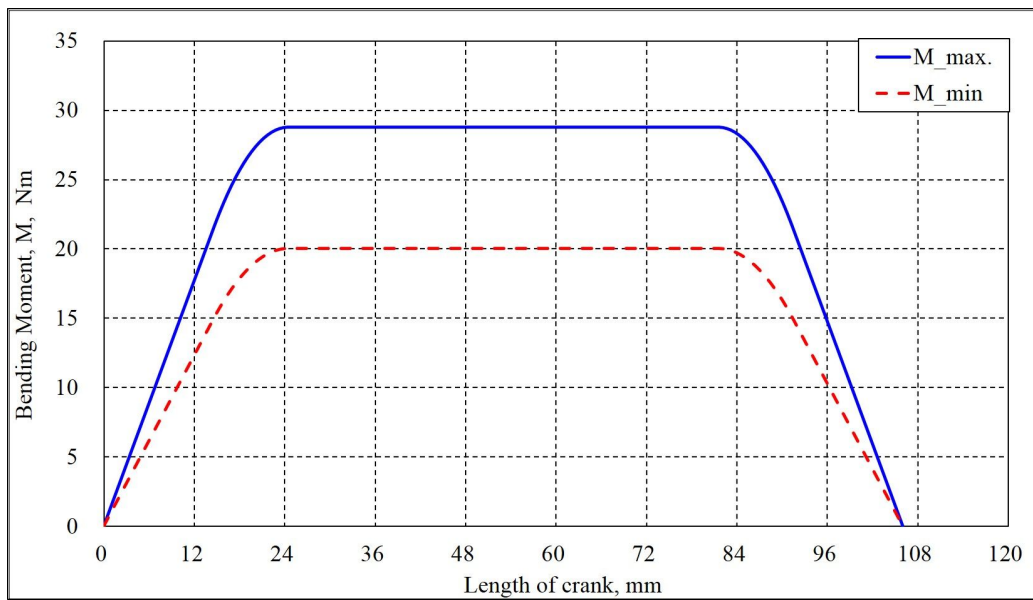


Fig.5.6. Bending moment acting on the crank shaft

5.3.2. Design for stiffness

The life of bearings that support the shaft can decrease rapidly when the shaft deflection is excessive. Therefore, the deflection due to bending should be considered in the shaft design.

As discussed above, the loads acting on the shaft have bilateral symmetry at the center of the shaft. Therefore, the maximum deflection due to bending occurs at the center of the shaft, as shown in fig.5.7.

The relationship between the shaft deflection δ and bending moment M is given by

$$\frac{d^2 \delta}{dx^2} = \frac{M}{EI} \quad (5.29)$$

where, E = modulus of elasticity

I = moment of inertia

Therefore, the shaft deflection δ can be calculated by using equations (5.16) and (5.29):

$$\textcircled{1} \quad 0 \leq x < a$$

$$\delta = \frac{1}{EI} \left(\frac{1}{6} R_A x^3 + C_1 x + C_2 \right) \quad (5.30-a)$$

$$\textcircled{2} \quad a \leq x < a+l$$

$$\delta = \frac{1}{EI} \left(\frac{q}{24} x^4 + \frac{R_A + aq}{6} x^3 - \frac{qa^2}{4} x^2 + C_3 x + C_4 \right) \quad (5.30-b)$$

$$\textcircled{3} \quad a+l \leq x < L-a-l$$

$$\delta = \frac{1}{EI} \left(\frac{R_A - ql}{6} x^3 + \frac{1}{2} ql \left(a + \frac{l}{2} \right) x^2 + C_5 x + C_6 \right) \quad (5.30-c)$$

$$\textcircled{4} \quad L-a-l \leq x < L-a$$

$$\delta = \frac{1}{EI} \left(\frac{q}{24} (L-x)^4 + \frac{R_A + aq}{6} (L-x)^3 - \frac{qa^2}{4} (L-x)^2 + C_3 (L-x) + C_4 \right) \quad (5.30-d)$$

$$\textcircled{5} \quad L-a \leq x < L$$

$$\delta = \frac{1}{EI} \left(\frac{1}{6} R_A (L-x)^3 + C_1 (L-x) + C_2 \right) \quad (5.30-e)$$

$$\text{where, } C_1 = -\frac{q}{6} a^3 + \frac{R_A + aq}{2} a^2 - \frac{qa^3}{2} + C_3 - \frac{1}{2} R_A a^2$$

$$C_2 = 0$$

$$C_3 = \frac{R_A - ql}{2} (a+l)^2 + ql \left(a + \frac{l}{2} \right) (a+l) + C_5 + \frac{q}{6} (a+l)^3 - \frac{R_A + aq}{2} (a+l)^2 + \frac{qa^2}{2} (a+l)$$

$$C_4 = \frac{1}{6} R_A a^3 + C_1 a + \frac{q}{24} a^4 - \frac{R_A + aq}{6} a^3 + \frac{qa^4}{4} - C_3 a$$

$$C_5 = \frac{ql - R_A}{8} L^2 - ql \frac{L}{2} \left(a + \frac{l}{2} \right)$$

$$C_6 = -\frac{q}{24} (a+l)^4 + \frac{R_A + aq}{6} (a+l)^3 - \frac{qa^2}{4} (a+l)^2 + C_3 (a+l) + C_4 - \frac{R_A - ql}{6} (a+l)^3 - \frac{1}{2} ql \left(a + \frac{l}{2} \right) (a+l)^2 - C_5 (a+l)$$

Therefore, the maximum deflection of the shaft δ_{\max} is given by

$$\delta_{\max} = 0.184 \text{ mm} \left(x = \frac{L}{2} = 53 \text{ mm} \right) \quad (5.31)$$

The maximum deflection angle θ_{\max} is given by

$$\theta_{\max} = 0.34^\circ \quad (x = 0 \text{ and } x = L = 106 \text{ mm}) \quad (5.32)$$

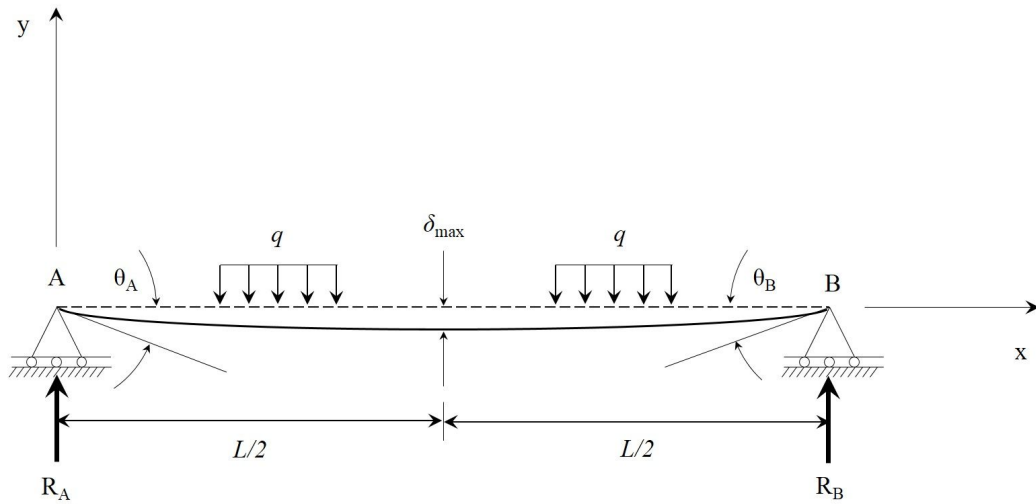


Fig.5.7. Maximum deflection of the main shaft of the crank.

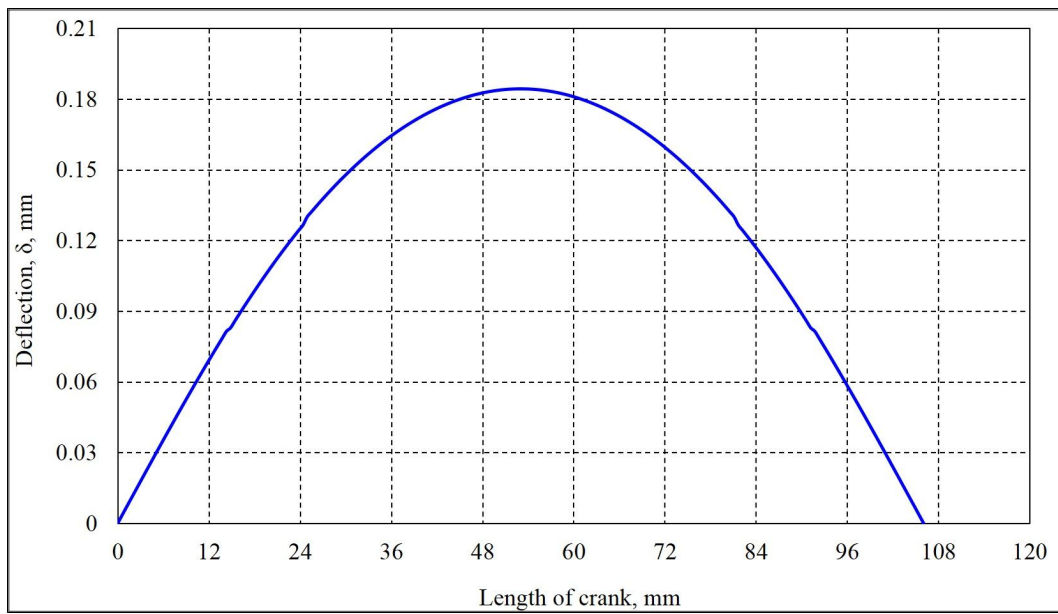


Fig.5.8. Deflection of the main shaft of the crank.

5.4. Pins

As discussed above, the pins drive the rotors on the shaft link through a pin-in-slot joint. The loads acting on the pins that are caused by this motion can be simplified, as shown in fig.5.9.

5.4.1. Design for strength

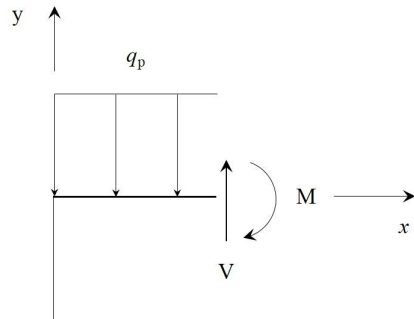
In fig.5.9, the relationship between the reaction loads R and dynamic loads q_p is given by

$$R = q_p l_1 \quad (5.33)$$

$$M = -q_p l_1 \left(L_p - \frac{1}{2} l_1 \right) \quad (5.34)$$

Therefore,

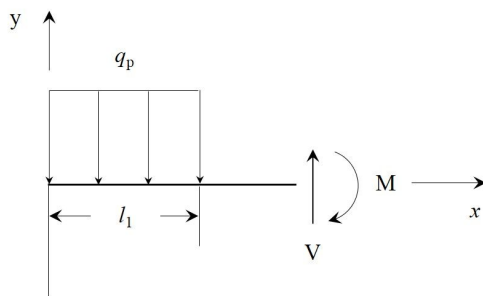
$$\textcircled{1} \quad 0 \leq x < l_1$$



$$V = q_p x \tag{5.35-a}$$

$$M = -\frac{1}{2} q_p x^2 \tag{5.36-a}$$

$$\textcircled{2} \quad l_1 \leq x < L$$



$$V = q_p l_1 \tag{5.35-b}$$

$$M = -q_p l_1 x + \frac{1}{2} q_p l_1^2 \tag{5.36-b}$$

The reaction force R (R_{p1} or R_{p2}) can be calculated by using table 5.6, equation (4.14), (4.15), (4.20), and (4.21), and fig.(4.5) when $l_1 = 4.5 \text{ mm}$, $l_2 = 1.5 \text{ mm}$, and $L_p = 6 \text{ mm}$.

Because the loads R_{p1} and R_{p2} are variable, the maximum and minimum reaction forces can be calculated as follows:

$$R_{\max} = 1,261.3 \text{ N} \quad (5.37)$$

$$R_{\min} = -1,053.5 \text{ N} \quad (5.38)$$

Using these equations, the shear force V and bending moment M can be obtained as shown in fig.5.10 and 5.11. As a result, the shear force V has a maximum value when $l_1 \leq x \leq L_p$, and the bending moment has a maximum value when $x = L_p$. Therefore, the amplitude and mean moment of the pins M_a and M_m are given by

$$M_a = \frac{M_{\max} - M_{\min}}{2} = \frac{2.96 \text{ N} - (-3.55 \text{ N})}{2} = 3.26 \text{ N} \quad (5.39)$$

$$M_m = \frac{M_{\max} + M_{\min}}{2} = \frac{2.96 \text{ N} + (-3.55 \text{ N})}{2} = -0.29 \text{ N} \quad (5.40)$$

The torsion of the pins is small enough to neglect. Therefore, the torque of these pins is given by

$$T_a = T_m = 0 \text{ N} \quad (5.41)$$

These calculation results can be used to obtain the minimum diameter of the pins. The calculation equations and material are the same as those for the main shaft of the crank. Consequently, the minimum diameter $(d_p)_{\min}$ can be obtained

when the distortion energy-Gerber equation is used:

$$\begin{aligned}
 d_{p_{\min}} &= \sqrt[3]{\frac{8nB}{\pi S_e} \left(1 + \sqrt{1 + \left(\frac{2AS_e}{BS_u} \right)^2} \right)} \\
 &= \sqrt[3]{\frac{8 \times 1.2 \times 6,510.2}{\pi \times 191.9 \text{ MPa}} \left(1 + \sqrt{1 + \left(\frac{2 \times 584.55 \times 191.9 \text{ MPa}}{6,510.2 \times 569 \text{ MPa}} \right)^2} \right)} \\
 &= 5.92 \text{ mm}
 \end{aligned}
 \tag{5.42}$$

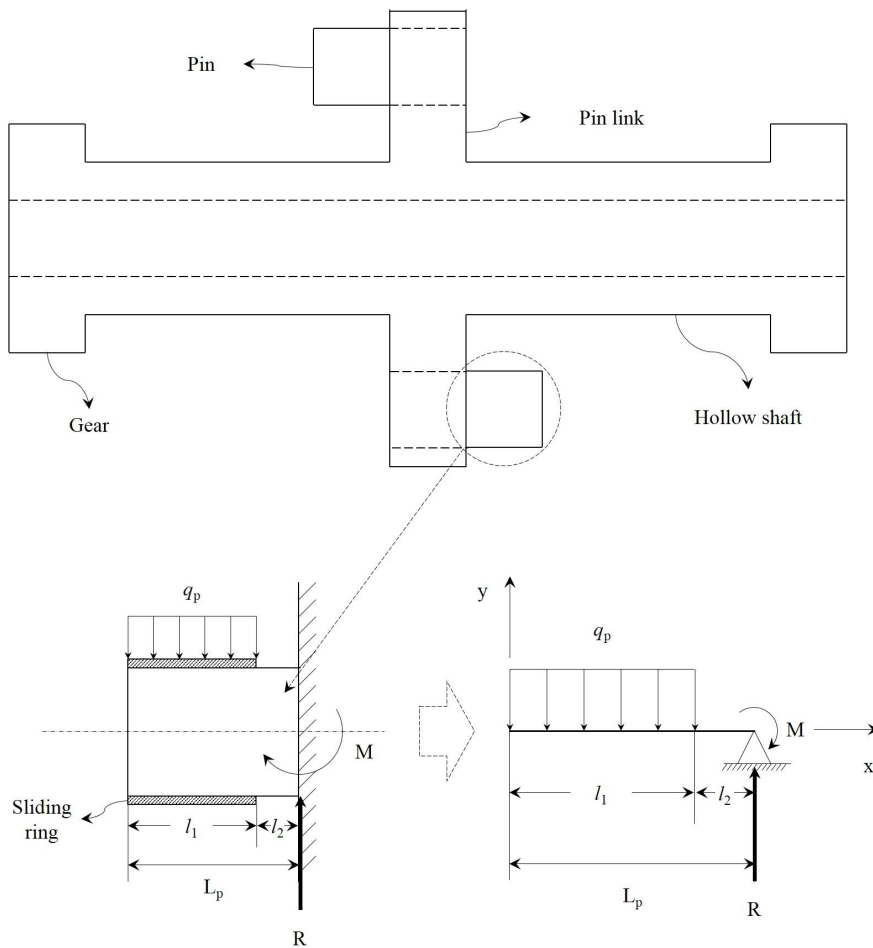


Fig.5.9. Loads acting on the pin.

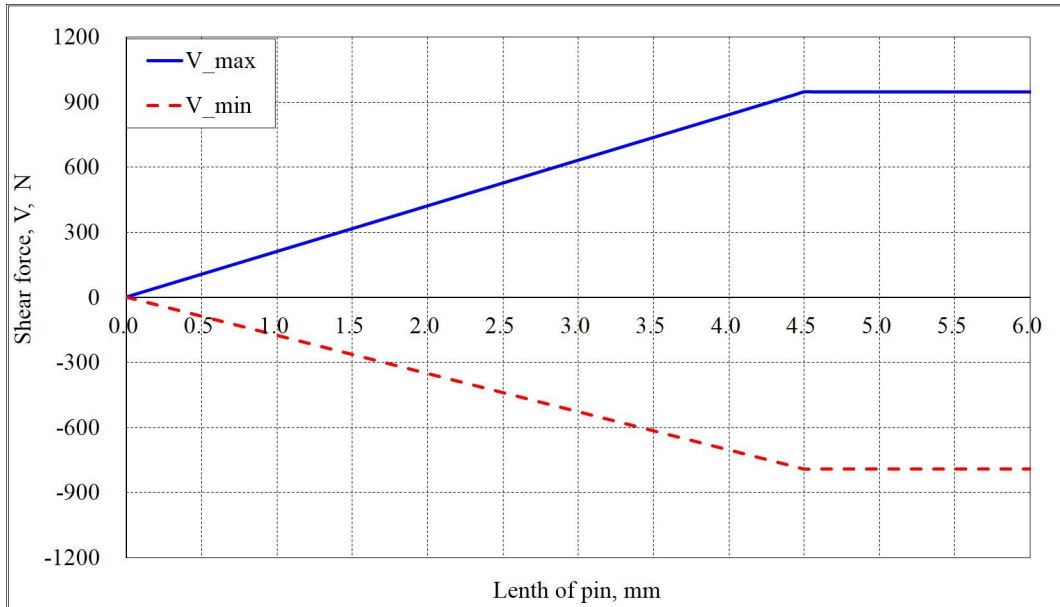


Fig.5.10. Shear force acting on the pin.

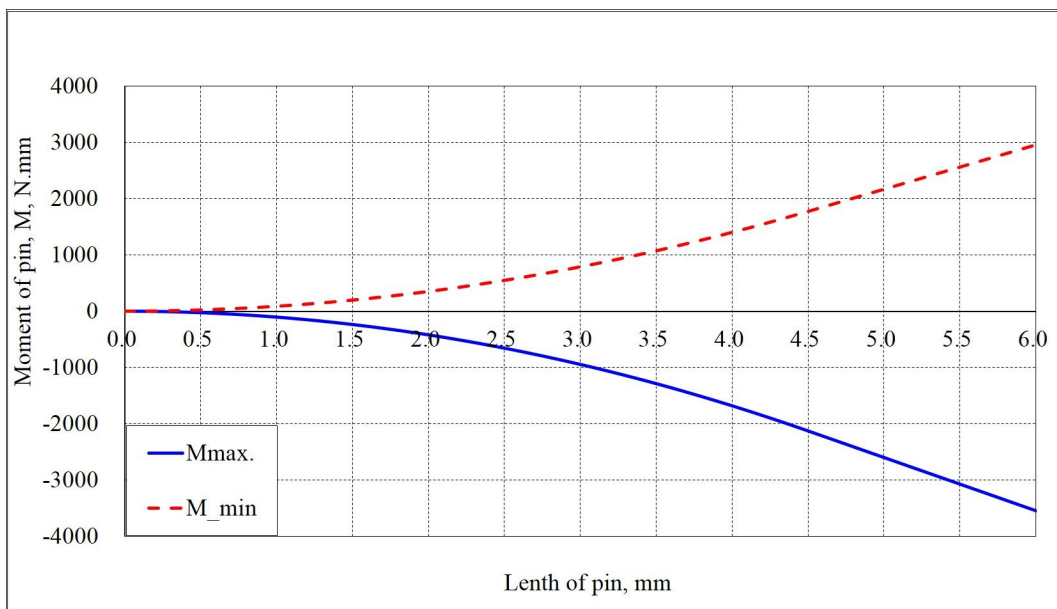


Fig.5.11. Bending moment acting on the pin.

5.5. Shaft link

The relationships among the forces R_p , R_{p1} , R_{p2} , F_{cn} , and F_{ct} acting on the shaft link were previously presented in fig.4.5. For analysis of the free-body diagram of the shaft link, however, it should be represented on a 3D space. The rotation center of the crank is the z_o axis, and the rotation center of the shaft link is the z_c axis. Therefore, the force vectors and free-body diagram of the shaft link can be expressed as shown in fig.5.12 and 5.13 when the crank rotates by θ_c .

5.5.1. Design for strength

As shown in figs.5.12 and 5.13, the relationships among the forces acting on the shaft link R_p , R_{p1} , R_{p2} , F_{cn} , and F_{ct} are given by

$$\sum F_{x'_c} = (R_p)_{x'_c} + (R_{p1})_{x'_c} + (R_{p2})_{x'_c} + (q)_{x'_c} = 0 \quad (5.43)$$

$$\sum F_{y'_c} = (R_p)_{y'_c} + (R_{p1})_{y'_c} + (R_{p2})_{y'_c} + (q)_{y'_c} = 0 \quad (5.44)$$

where, $(R_p)_{x'_c} = R_p \cos\left(\frac{\pi}{2} + \theta_p\right)$

$$(R_{p1})_{x'_c} = R_{p1} \cos\left(-\frac{\pi}{2} + \theta_{p1} - \phi\right)$$

$$(R_{p2})_{x'_c} = R_{p2} \cos\left(-\frac{\pi}{2} + \theta_{p2} - \phi\right)$$

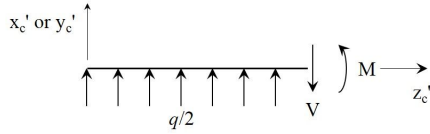
$$(q)_{x'_c} = F_{cn} \cos(\theta_c - \phi) + F_{ct} \cos\left(\frac{\pi}{2} + \theta_c - \phi\right)$$

$$(R_p)_{y'_c} = R_p \sin\left(\frac{\pi}{2} + \theta_p\right)$$

$$\begin{aligned}
(R_{p1})_{y_c'} &= R_{p1} \sin\left(-\frac{\pi}{2} + \theta_{p1} - \phi\right) \\
(R_{p2})_{y_c'} &= R_{p2} \sin\left(-\frac{\pi}{2} + \theta_{p2} - \phi\right) \\
(q)_{y_c'} &= F_{cn} \sin(\theta_c - \phi) + F_{ct} \sin\left(\frac{\pi}{2} + \theta_c - \phi\right)
\end{aligned}$$

Therefore,

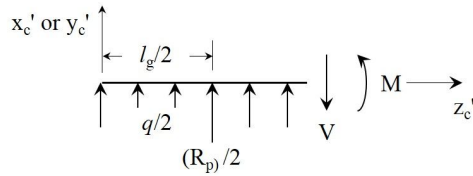
$$1) \text{ ① - ②, } 0 \leq z < \frac{l_g}{2}$$



$$V_{x_c'} = \frac{q_{x_c'}}{2} z, \quad V_{y_c'} = \frac{q_{y_c'}}{2} z, \quad V = \sqrt{V_{x_c'}^2 + V_{y_c'}^2} \quad (5.45-a)$$

$$M_{x_c'} = \frac{q_{x_c'}}{4} z^2, \quad M_{y_c'} = \frac{q_{y_c'}}{4} z^2, \quad M = \sqrt{M_{x_c'}^2 + M_{y_c'}^2} \quad (5.46-a)$$

$$2) \text{ ② - ④ } \frac{l_g}{2} \leq z < l_b$$

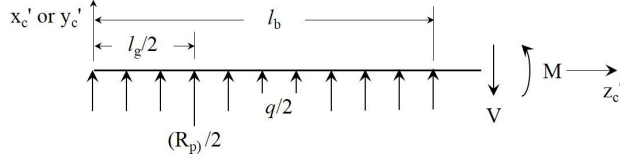


$$V_{x_c'} = \frac{q_{x_c'}}{2} z + \frac{(R_p)_{x_c'}}{2}, \quad V_{y_c'} = \frac{q_{y_c'}}{2} z + \frac{(R_p)_{y_c'}}{2} \quad (5.45-b)$$

$$M_{x_c'} = \frac{q_{x_c'}}{4} z^2 + \frac{(R_p)_{x_c'}}{2} \left(z - \frac{l_g}{2}\right), \quad (5.46-b)$$

$$M_{y_c'} = \frac{q_{y_c'}}{4} z^2 + \frac{(R_p)_{y_c'}}{2} \left(z - \frac{l_g}{2}\right)$$

3) ④ - ⑥, $l_b \leq z < l$

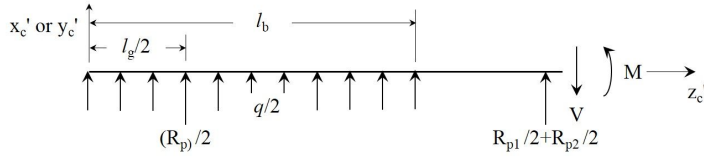


$$V_{x_c'} = \frac{q_{x_c'}}{2} l_b + \frac{(R_p)_{x_c'}}{2}, \quad V_{y_c'} = \frac{q_{y_c'}}{2} l_b + \frac{(R_p)_{y_c'}}{2} \quad (5.45-c)$$

$$M_{x_c'} = \frac{q_{x_c'}}{2} l_b \left(z - \frac{l_b}{2} \right) + \frac{(R_p)_{x_c'}}{2} \left(z - \frac{l_b}{2} \right), \quad (5.46-c)$$

$$M_{y_c'} = \frac{q_{y_c'}}{2} l_b \left(z - \frac{l_b}{2} \right) + \frac{(R_p)_{y_c'}}{2} \left(z - \frac{l_b}{2} \right)$$

4) ⑥ - ⑧ $l \leq z < 2l - l_b$



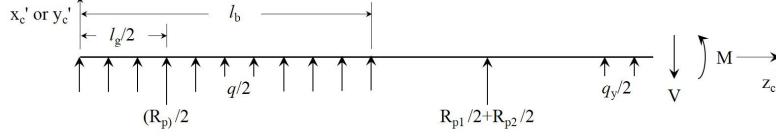
$$V_{x_c'} = \frac{q_{x_c'}}{2} l_b + \frac{(R_p)_{x_c'}}{2} + (R_{p1})_{x_c'} + (R_{p2})_{x_c'}, \quad (5.45-d)$$

$$V_{y_c'} = \frac{q_{y_c'}}{2} l_b + \frac{(R_p)_{y_c'}}{2} + (R_{p1})_{y_c'} + (R_{p2})_{y_c'}$$

$$M_{x_c'} = \frac{q_{x_c'}}{2} l_b \left(z - \frac{l_b}{2} \right) + \frac{(R_p)_{x_c'}}{2} \left(z - \frac{l_b}{2} \right) + \{ (R_{p1})_{x_c'} + (R_{p2})_{x_c'} \} (z - l), \quad (5.46-d)$$

$$M_{y_c'} = \frac{q_{y_c'}}{2} l_b \left(z - \frac{l_b}{2} \right) + \frac{(R_p)_{y_c'}}{2} \left(z - \frac{l_b}{2} \right) + \{ (R_{p1})_{y_c'} + (R_{p2})_{y_c'} \} (z - l)$$

$$5) \textcircled{8} - \textcircled{10}, \quad 2l - l_b \leq z < 2l - \frac{l_g}{2}$$



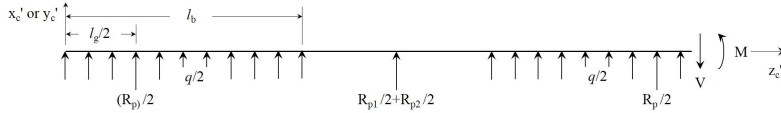
$$V_{x_c'} = \frac{q_{x_c'}}{2} l_b + \frac{(R_p)_{x_c'}}{2} + (R_{p1})_{x_c'} + (R_{p2})_{x_c'} + \frac{q_{x_c'}}{4} (z - 2l + l_b)^2, \quad (5.45-e)$$

$$V_{y_c'} = \frac{q_{y_c'}}{2} l_b + \frac{(R_p)_{y_c'}}{2} + (R_{p1})_{y_c'} + (R_{p2})_{y_c'} + \frac{q_{y_c'}}{4} (z - 2l + l_b)^2$$

$$M_{x_c'} = \frac{q_{x_c'}}{2} l_b \left(z - \frac{l_b}{2} \right) + \frac{(R_p)_{x_c'}}{2} \left(z - \frac{l_g}{2} \right) + \{ (R_{p1})_{x_c'} + (R_{p2})_{x_c'} \} (z - l) + \frac{q_{x_c'}}{4} (z - 2l + l_b)^2$$

$$M_{y_c'} = \frac{q_{y_c'}}{2} l_b \left(z - \frac{l_b}{2} \right) + \frac{(R_p)_{y_c'}}{2} \left(z - \frac{l_g}{2} \right) + \{ (R_{p1})_{y_c'} + (R_{p2})_{y_c'} \} (z - l) + \frac{q_{y_c'}}{4} (z - 2l + l_b)^2 \quad (5.46-e)$$

$$6) \textcircled{6} - \textcircled{8} \quad l \leq z < 2l - l_b$$



$$V_{x_c'} = \frac{q_{x_c'}}{2} l_b + \frac{(R_p)_{x_c'}}{2} + (R_{p1})_{x_c'} + (R_{p2})_{x_c'} + \frac{q_{x_c'}}{4} (z - 2l + l_b)^2 + \frac{(R_p)_{x_c'}}{2}, \quad (5.45-f)$$

$$V_{y_c'} = \frac{q_{y_c'}}{2} l_b + \frac{(R_p)_{y_c'}}{2} + (R_{p1})_{y_c'} + (R_{p2})_{y_c'} + \frac{q_{y_c'}}{4} (z - 2l + l_b)^2 + \frac{(R_p)_{y_c'}}{2}$$

$$\begin{aligned}
M_{x_c'} &= \frac{q_{x_c'}}{2} l_b \left(z - \frac{l_b}{2} \right) + \frac{(R_p)_{x_c'}}{2} \left(z - \frac{l_g}{2} \right) + \left\{ (R_{p1})_{x_c'} + (R_{p1})_{x_c'} \right\} (z - l) \\
&\quad + \frac{q_{x_c'}}{4} (z - 2l + l_b)^2 + \frac{(R_p)_{x_c'}}{2} \left\{ z - \left(2l - \frac{l_g}{2} \right) \right\} \\
M_{y_c'} &= \frac{q_{y_c'}}{2} l_b \left(z - \frac{l_b}{2} \right) + \frac{(R_p)_{y_c'}}{2} \left(z - \frac{l_g}{2} \right) + \left\{ (R_{p1})_{y_c'} + (R_{p1})_{y_c'} \right\} (z - l) \\
&\quad + \frac{q_{y_c'}}{4} (z - 2l + l_b)^2 + \frac{(R_p)_{y_c'}}{2} \left\{ z - \left(2l - \frac{l_g}{2} \right) \right\}
\end{aligned}
\tag{5.46-f}$$

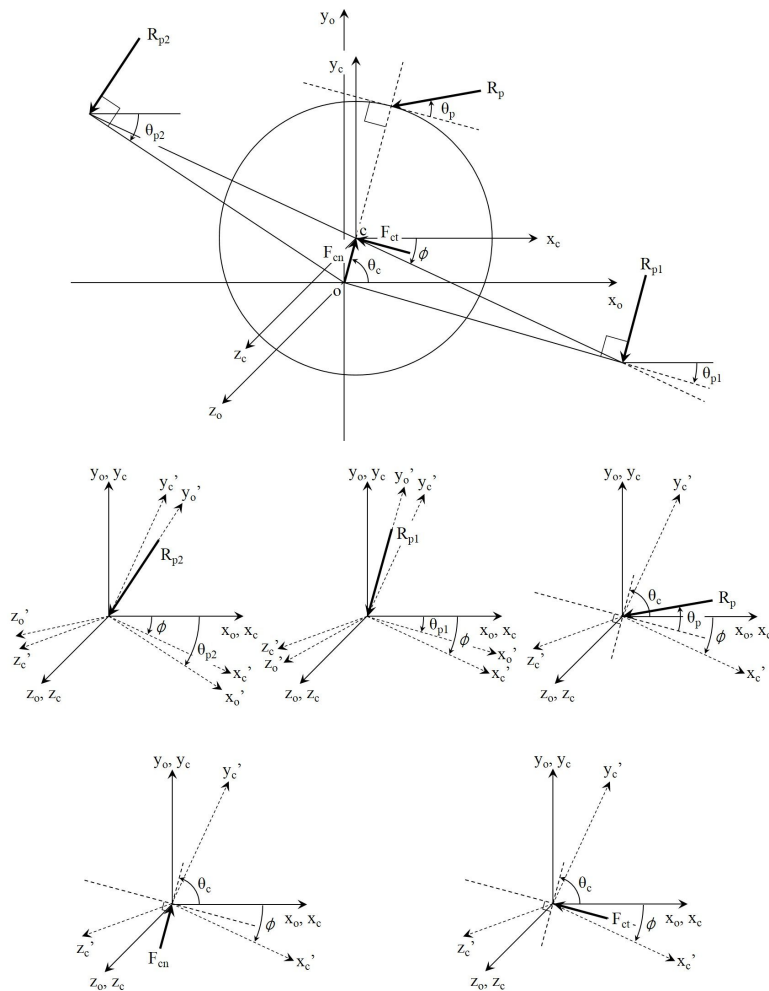


Fig.5.12. Free-body diagram of forces acting on the shaft link.

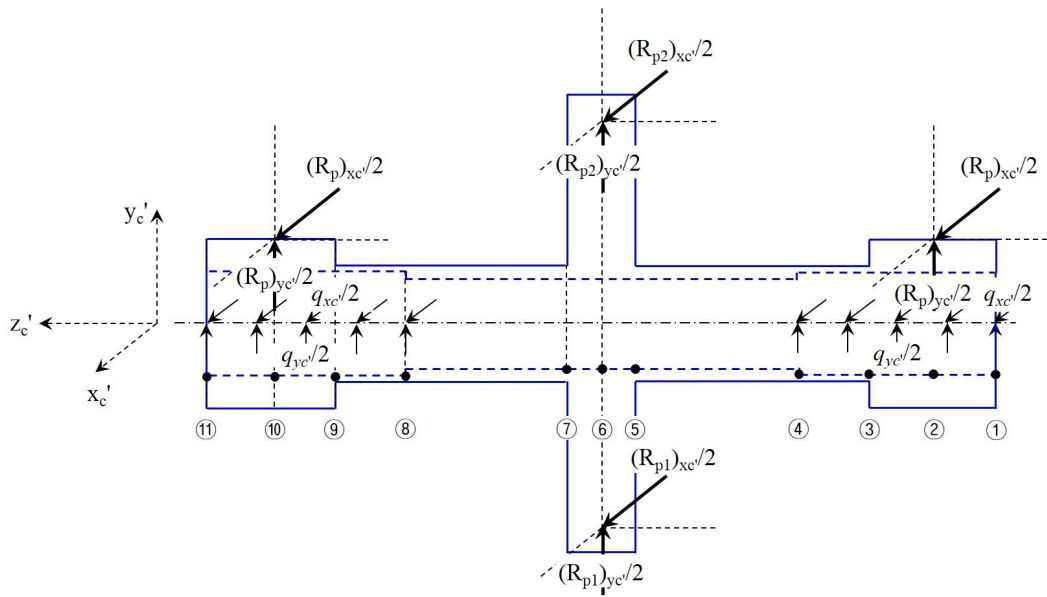


Fig.5.13. Force components with respect to the x_c '- y_c '- z_c ' coordinates.

The forces R_p , R_{p1} , R_{p2} , F_{cn} and F_{ct} , can be calculated by using table 5.6, equation (4.8) - (4.29). As discussed previously, the forces acting on the shaft link change periodically. However, the shear force V and bending moment acting on the shaft link M have constant values. In contrast, the torque acting on the shaft link according to the length of the shaft link changes periodically. Fig.5.14 - 5.16 show the torque, shear force, and bending moment of the shaft link under given conditions.

Based on these calculation results, the minimum diameter of the shaft link can be obtained by using the same equations in equation (5.23). However, because the shaft link is a hollow shaft, equation (5.23) should be replaced by equation (5.48), and d_o can be calculated by using iterative procedures.

① Westing house code

$$d_o(1-K^4)^{1/3} = \sqrt[3]{\frac{32n}{\pi} \sqrt{\left(\frac{M_a}{S_e} + \frac{M_m}{S_y}\right)^2 + \left(\frac{T_a}{S_e} + \frac{T_m}{S_y}\right)^2}} \quad (5.47-a)$$

where, $K = \frac{d_i}{d_o}$

d_i is the inner diameter of the shaft link

d_o is the outer diameter of the shaft link

② Distortion energy Gerber

$$d_o(1-K^4)^{1/3} = \sqrt[3]{\frac{8nB}{\pi S_e} \left(1 + \sqrt{1 + \left(\frac{2AS_e}{BS_u}\right)^2}\right)} \quad (5.47-b)$$

where, $A = \sqrt{4M_m^2 + 3T_m^2}$

$B = \sqrt{4M_a^2 + 3T_a^2}$

③ DE-ASME elliptic

$$d_o(1-K^4)^{1/3} = \sqrt[3]{\frac{16n}{\pi} \sqrt{\frac{B^2}{S_e^2} + \frac{A^2}{S_y^2}}} \quad (5.47-c)$$

where, $A = \sqrt{4M_m^2 + 3T_m^2}$

$B = \sqrt{4M_a^2 + 3T_a^2}$

By using the same method as for the crank, the maximum value for the shaft link is obtained with the distortion energy Gerber or DE-ASME elliptic equation:

$$d_o = 15.73 \text{ mm} \quad (5.48)$$

where, $K = \frac{d_i}{d_o} = 0.826$

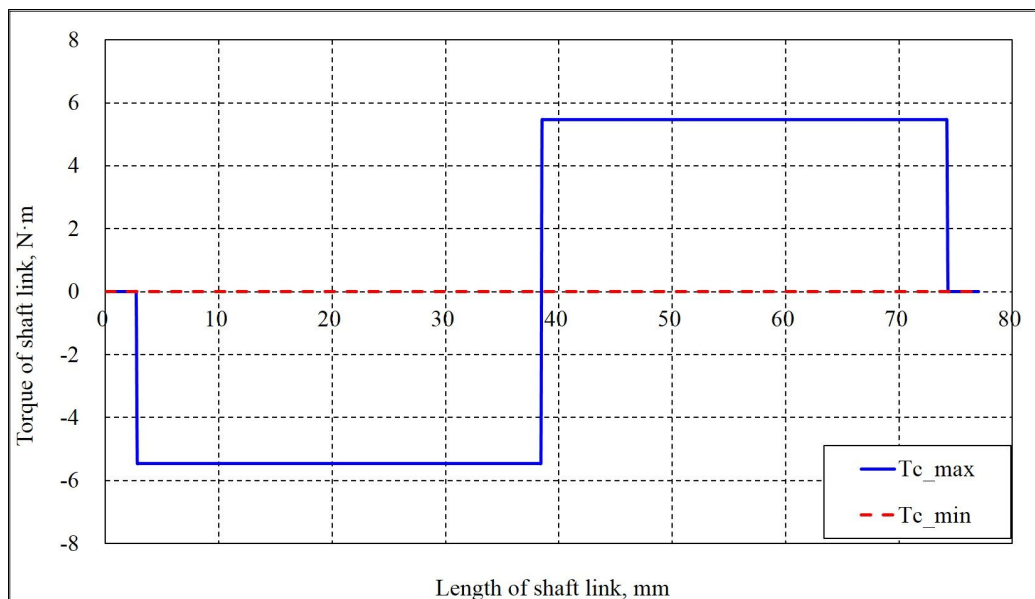


Fig.5.14. Driving torque vs. the length of shaft link.

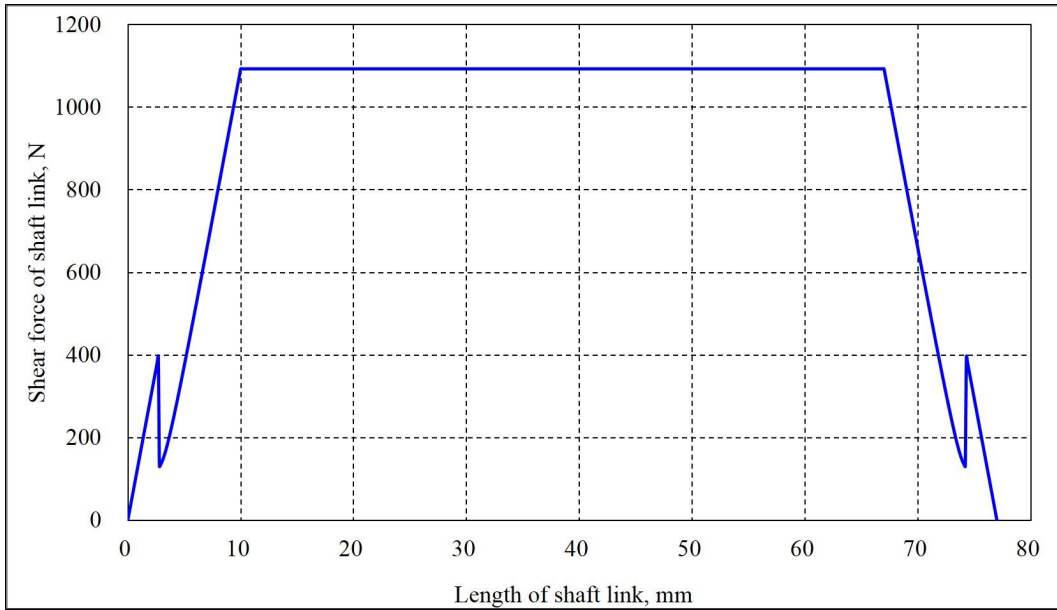


Fig.5.15. Shear force vs. the length of shaft link.

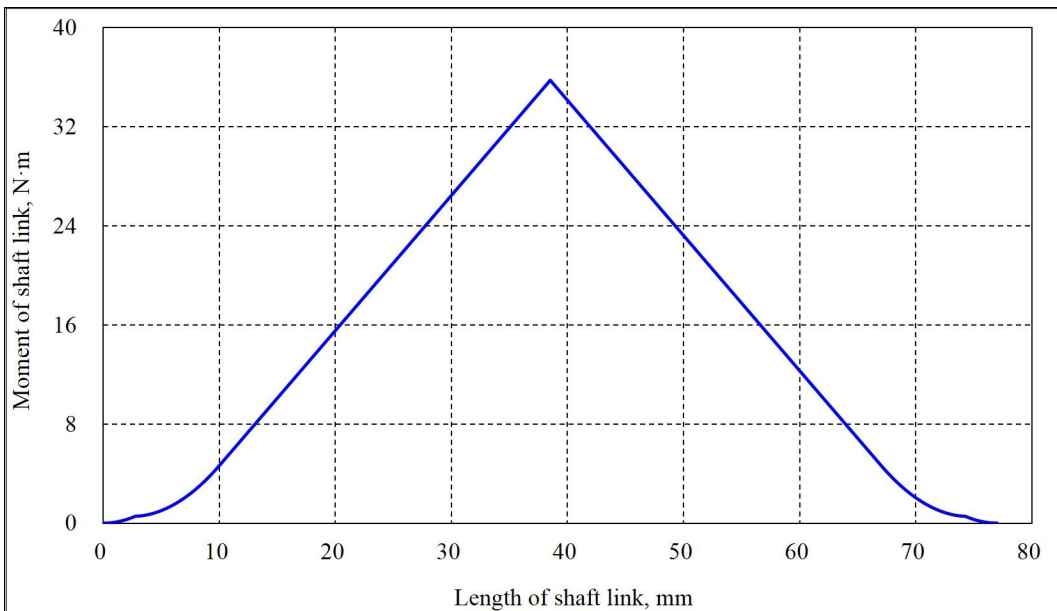


Fig.5.16. Bending moment vs. the length of shaft link.

5.5.2. Design for stiffness

The moment of inertia of the hollow shaft is given by $\frac{\pi}{64}(d_o^4 - d_i^4)$. The deflection of the shaft link can be calculated by using equations (5.29) and (5.46).

$$1) \textcircled{1} - \textcircled{2}, 0 \leq z < \frac{l_g}{2}$$

$$\delta_{y_c'} = \frac{1}{EI} \left(\frac{q_{y_c'}}{48} z^4 + C_1 z + C_2 \right) \quad (5.49-a)$$

$$2) \textcircled{2} - \textcircled{4}, \frac{l_g}{2} \leq z < l_b$$

$$\delta_{y_c'} = \frac{1}{EI} \left(\frac{q_{y_c'}}{48} z^4 + \frac{(R_p)_{y_c'}}{12} z^3 - \frac{(R_p)_{y_c'} l_g}{8} z^2 + C_3 z + C_4 \right) \quad (5.49-b)$$

$$3) \textcircled{4} - \textcircled{6}, l_b \leq z < l$$

$$\delta_{y_c'} = \frac{1}{EI} \left(\frac{q_{y_c'} l_b}{12} z^3 - \frac{q_{y_c'} l_b^2}{8} z^2 + \frac{(R_p)_{y_c'}}{2} z^3 - \frac{(R_p)_{y_c'} l_g}{8} z^2 + C_5 z + C_6 \right) \quad (5.49-c)$$

$$\text{where, } C_1 = -\frac{q_y}{12EI} l^3$$

$$C_2 = 0$$

$$C_3 = \frac{(R_p)_y l_g^2}{16} + C_1$$

$$C_4 = C_1 \frac{l_g}{2} + \frac{(R_p)_y l_g^3}{48} - C_3 \frac{l_g}{2}$$

$$C_5 = \frac{q_y l_b^3}{12} + C_3$$

$$C_6 = \frac{q_y l_b^4}{16} + C_3 l_b + C_4 - C_5 l_b$$

Therefore, the deflection of the shaft link is as shown in fig. 5.18.

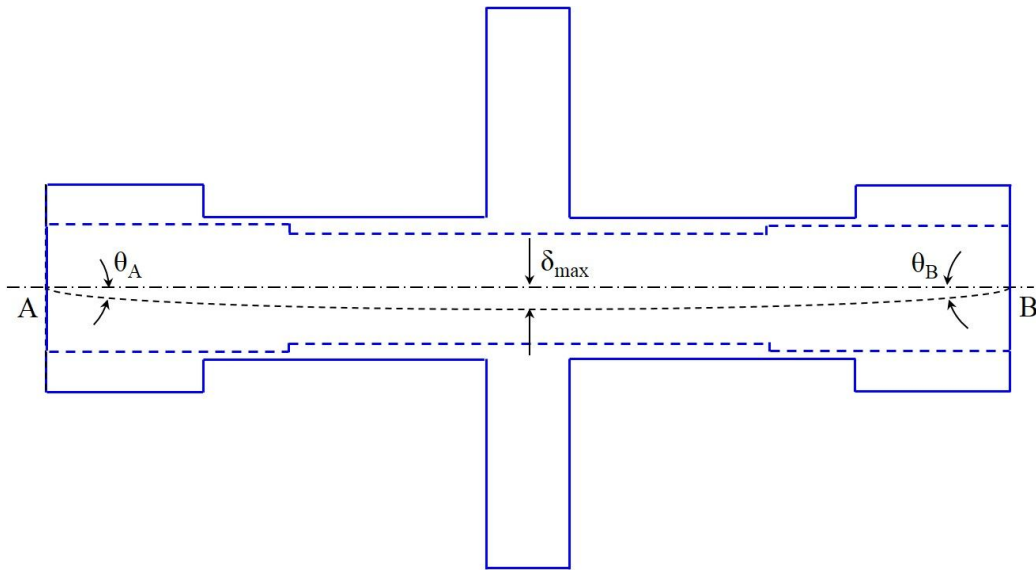


Fig.5.17. Parameters for the deflection of the shaft link.

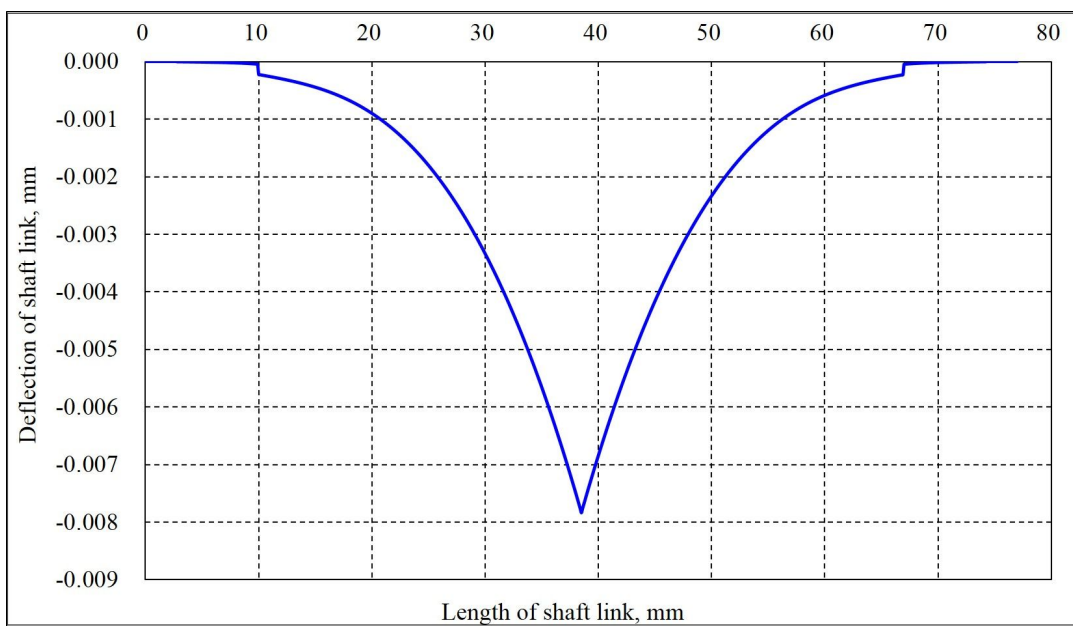


Fig.5.18. Deflection of the shaft link according to the length of the shaft.

5.6. Conclusions

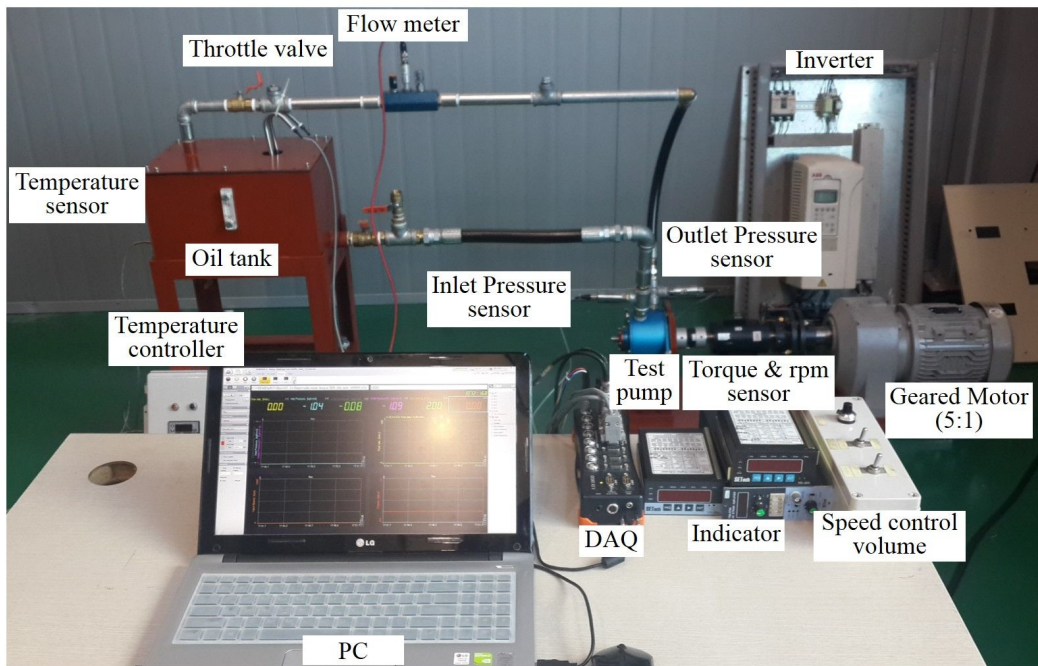
This chapter presented the design constraints of the fixed internal gear and gear of the shaft link using involute curves along with the strength design of the main components. The involute-type internal gear has design limits caused by three kind of interference. The kinematic constraints discussed in chapter 3 can aggravate this limits. As a result, designing a pump for high-pressure and low-flow rate conditions with an involute-type internal gear can be difficult.

The gear strength calculated by using the Lewis equation, and the strength and deflection of the crank, shaft link, and pins are calculated on the 3D space with the origin at the center of rotation of the shaft link.

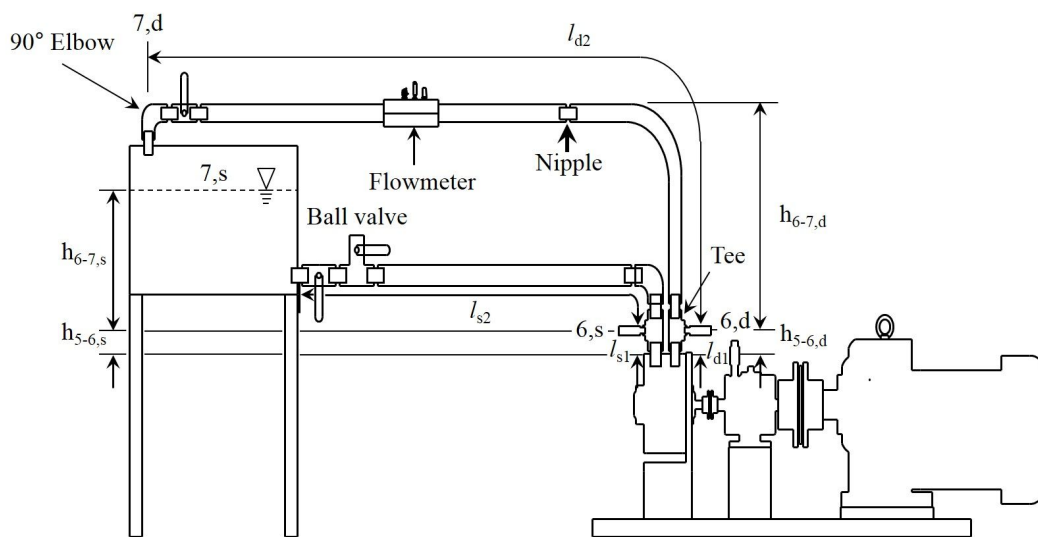
6. Verification test

6.1. Prototype pump and test equipment

A prototype pump was manufactured to verify its fundamental performances (see table 5.6 and appendix C), and pump test equipment was installed as shown in fig.6.1. A flowmeter, suction and discharge pressure sensor, torque meter, and speed sensor were installed to measure the flow, suction and discharge pressure, input torque, and speed, respectively. A throttle valve was installed at the end of the discharge port to increase the pressure at the pump. A geared motor and inverter were used to precisely control the input at low speed. The rated power and torque of the motor were 3.7 kW and 9.6 kgf · m respectively, and the gear ratio was 1/5. The rated power of the inverter was 3.7 kW, and the efficiency was 98 %. All of sensor signals were stored in a computer through a DAQ that had eight analog and digital channels with a 32-bit resolution. The accuracy of the torque and speed sensor was 0.09%, and the signals were amplified through indicators. The measurement range of the flowmeter was 7.5-75 l/min. The oil temperature was maintained at 40 °C with a controller. Table 6.1 presents the component specifications.



(a) Test equipment



(b) Piping system

Fig.6.1. A system used for pump testing.

Table 6.1 Specifications of pump testing equipment.

Items	Specifications
Geared motor	Model : Samyang Max II, 3-phase Power : 3.7 kW Ratio : 1/5 RPM : 350 Torque : 9.6 kgf · m
Torque and rpm sensor	Model : SETech YDR-1K(Torque) & MP-981(rpm) Type : Brush Rated capacity : 1 kgf · m Accuracy : 0.09%
Pressure transducer (suction and discharge)	Model : Sensys PSHB C010K Range : -1 ~ 10 kgf/cm ² Accuracy : 0.15%F.S
Flowmeter	Model : Hydrotechnik Hysense QT 110 Type : Volumetric, turbine Measuring range : 7.5 ~ 75 l/min. Error limit : ±2.5% Allowed working pressure : 420 bar Viscosity range : 1 ~ 100 mm ² /s
Inverter	Model : ABB ACS 800 Power : 3.7 kW Efficiency : 98%
Test oil	Model : Kixx RD HD 32 ISO viscosity grade : ISO 32 Kinematic viscosity : 31.3 mm ² /s @ 40 °C
DAQ	Model : DEWE-43 Power supply : 6-36 VDC Analog No. of channels : 8 Sampling rate : simultaneous 200 kS/sec. Counter No. of channels : 8 Modes : counting, waveform, timing, encoder, tacho, geartooth sensor Resolution : 32-bit

6.2. Pressure analysis of the pump and piping system

Four different kinds of piping components were used in the design of the piping system in the test equipment. The numbers of each component used, and their coefficients are in listed table 6.2. The flowmeter on the discharge pipe also caused pressure head. Most manufacturers present the pressure losses according to the increase in flow rates. Fig. 6.2 shows a second-order polynomial regression model between flow rate and pressure differences, which are developed using data provided by the manufacturer (Hydrotechnik, 2015). Accordingly, the pressure loss caused by the flowmeter can be expressed as follows.

$$\Delta p_{FM} = \frac{0.007Q^2 + 0.0453Q + 0.1614}{2} \quad (6.1)$$

where, Δp_{FM} = pressure head due to flowmeter, kgf/cm^2

As a result, the total pressure losses in discharge pipe from 6,d to 7,d can be expressed as

$$p_{7,d} - p_{6,d} = \left(\begin{aligned} & \frac{1}{2} \rho \frac{f_{6-7,d} l_{6-7,d}}{D_{6-7,d}} \frac{Q_{6-7,d}^2}{A_{6-7,d}^2} + \rho l_{6-7,d} \frac{\dot{Q}_{6-7,d}}{A_{6-7,d}} \times \frac{10^{-4}}{9.81} \\ & + \frac{1}{2} \Sigma K \rho \frac{Q_{6-7,d}^2}{A_{6-7,d}^2} \\ & + \frac{0.007Q_{6-7,d}^2 + 0.0453Q_{6-7,d} + 0.1614}{2} \\ & + 9.81 \times \rho h_d \end{aligned} \right) \quad (6.2)$$

where, $p_{7,d} - p_{6,d}$ = differential pressure in the discharge pipe, kgf/cm^2

In the same way, the total pressure losses in suction pipe from 6,s to 7,s can be expressed as

$$p_{7,s} - p_{6,s} = \left(\frac{1}{2} \rho \frac{f_{6-7,s} l_{6-7,s}}{D_{6-7,s}} \frac{Q_{6-7,s}^2}{A_{6-7,s}^2} + \rho l_{6-7,s} \frac{\dot{Q}_{6-7,s}}{A_{6-7,s}} \right) \times \frac{10^{-4}}{9.81} + \frac{1}{2} \Sigma K \rho \frac{Q_{6-7,s}^2}{A_{6-7,s}^2} + 9.81 \times \rho h_s \quad (6.3)$$

where, $p_{7,s} - p_{6,s}$ = differential pressure in the suction pipe, kgf/cm^2

Using equations (4.6), (4.7), (6.2), and (6.3) the pressure in the pump and piping system can be simulated.

Table 6.2 Loss coefficients for pipe connections (Hydraulic Institute, 1990; Menon E. S., and Menon P. S. 2010).

Components	suction line		Discharge line	
	No.	Coefficients	No.	Coefficients
Nipple	6 EA	0.85	6 EA	0.90
Ball valve	2 EA	0.07	1 EA	0.08
90° Elbow	1 EA	0.69	1 EA	0.75
Tee	1 EA	0.46	1 EA	0.50

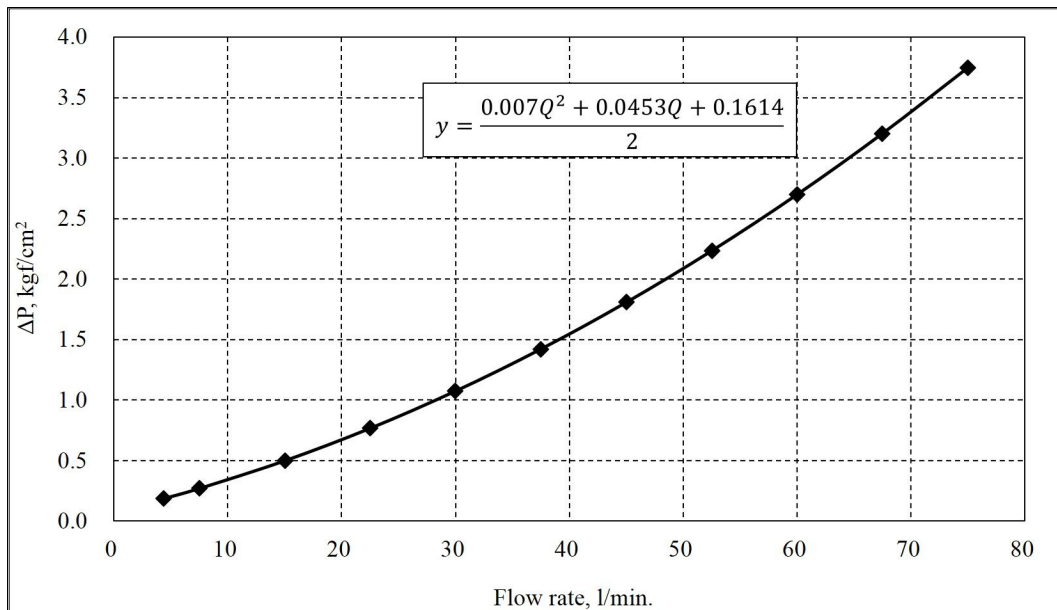


Fig.6.2. Second-order polynomial model representing the differential pressure vs. flow rate of a flowmeter (Hydrotechnik. 2015).

6.3. Verification

6.3.1. Clearances calculation and validation of performance parameters when the throttle valve is fully open

To verify the pump performance, the clearances between the rotor jaws and pump chamber δ_1 and δ_2 in equation (4.61) should be known. However, it is very difficult to measure this values. Therefore, they were calculated from the test results. Fig.6.3 shows the measured flow rate as a function of the crank speed when the throttle valve was fully open. The volumetric efficiency reached its maximum value when the crank speed was 125 rpm. Therefore, the clearances δ_1 and δ_2 were calculated based on this speed. The clearances δ_1 and δ_2 were

assumed to have the same values. As a result, the volumetric efficiencies of the measured and simulated data had the same values when the clearances δ_1 and δ_2 were 0.2572 mm. Fig. 6.4 compares the test and simulated data for the volumetric efficiency as a function of the crank speed. Although there were some differences between the the measured and simulated data when the crank speed was low, in the general the data showed good agreement.

The simulated data of the flow rate, differential pressure, and driving torque were verified by comparison with experimental data under the same conditions. The flow rate was measured by using a flowmeter that was installed between points 6,d and 7,d, as shown in fig.6.1. The suction and discharge pressure sensors were installed at points 6,s and 6,d, respectively. Therefore, the measured and simulated pressures were compared at this points. Fig.6.5 shows the measured and simulated flow rates when speed of the driving shaft was 125 rpm. The measured and simulated values agreed well in terms of their magnitudes and periods.

Figs 6.6-6.8 compare the measured and simulated pressure and driving torque. These values were also correlated in terms of their magnitudes and periods. For a more precise comparison, the flow rate, suction and discharge pressures, and torque were analyzed to identify their primary components in the frequency domain, as given in figs.6.9-6.12 and table 6.3. The flow rate component at the frequency of 5.5 Hz was measured as 2.993 and was 3.745 in the simulation for a simulation error of 20.09%. Under the same applied conditions, the simulation errors of the suction pressure, discharge pressure, and driving torque were 22.88%, 4.87%, and -23.89% respectively.

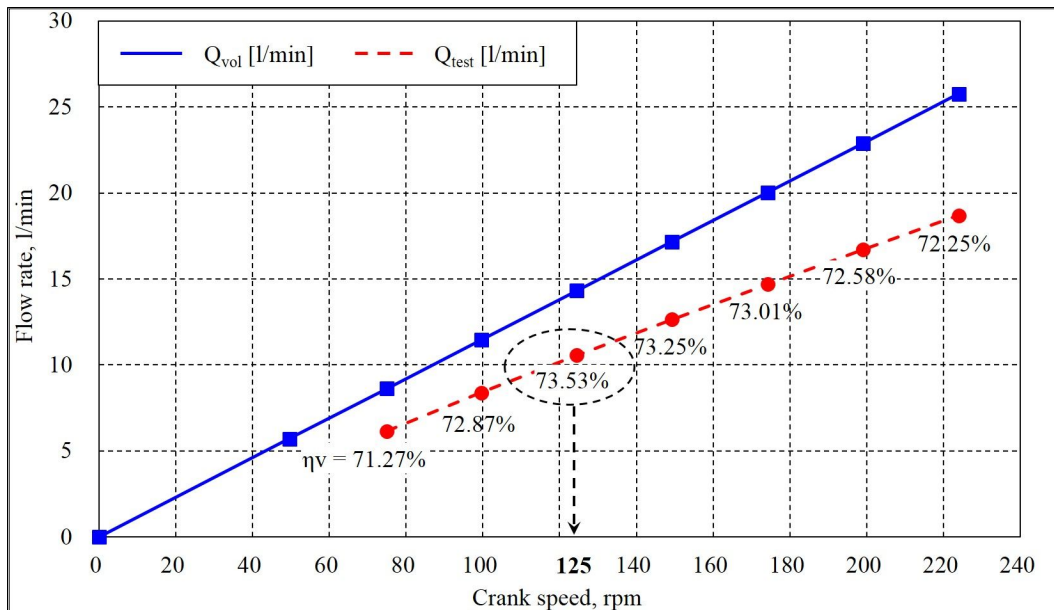


Fig.6.3. Measured flow rate as a function of the crank speed with the throttle valve fully opened.

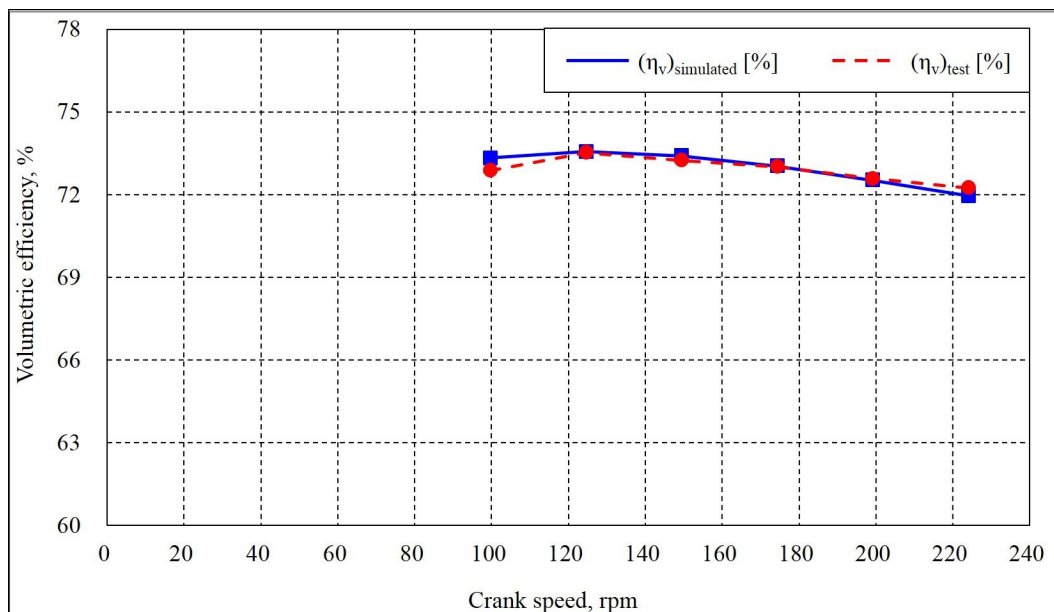


Fig.6.4. Comparison between the measured and simulated volumetric efficiency as a function of the crank speed when the clearances δ_1 and δ_2 were 0.2572 mm.

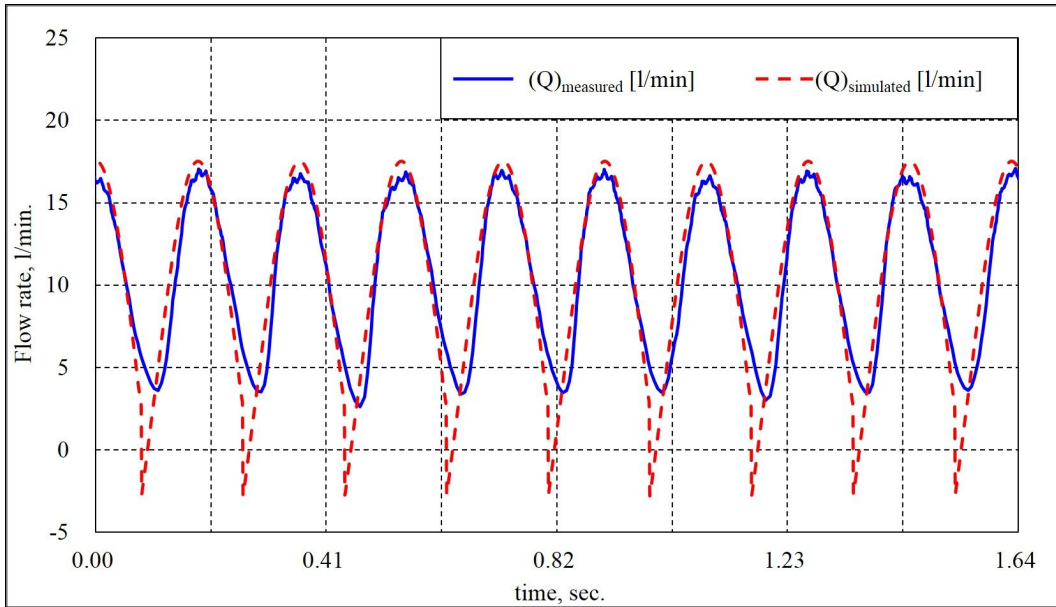


Fig.6.5. Comparison between the simulated and measured flow rates in the time domain.

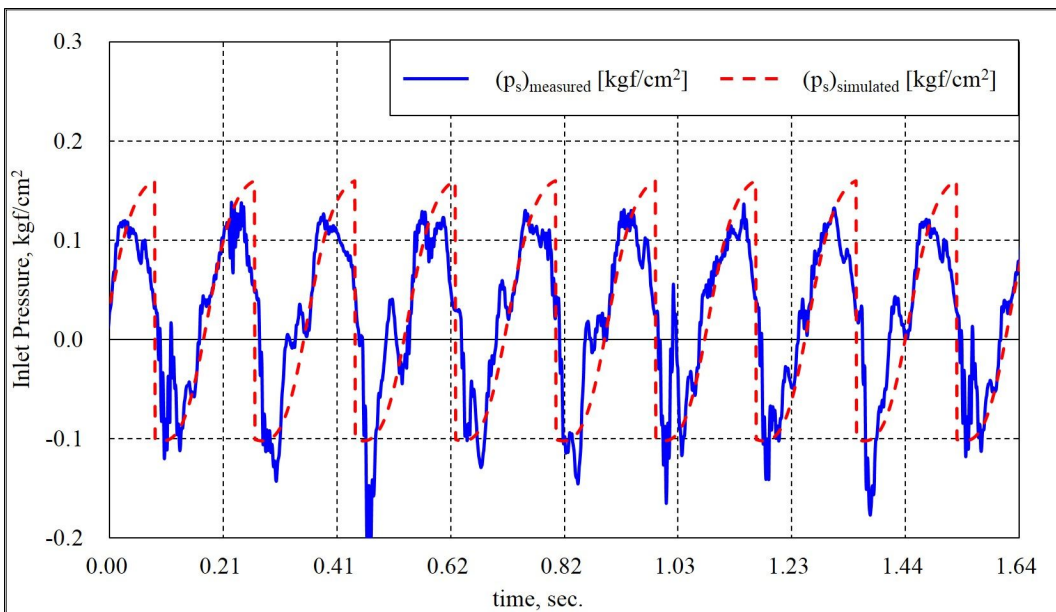


Fig.6.6. Comparison between the simulated and measured suction pressures in the time domain.

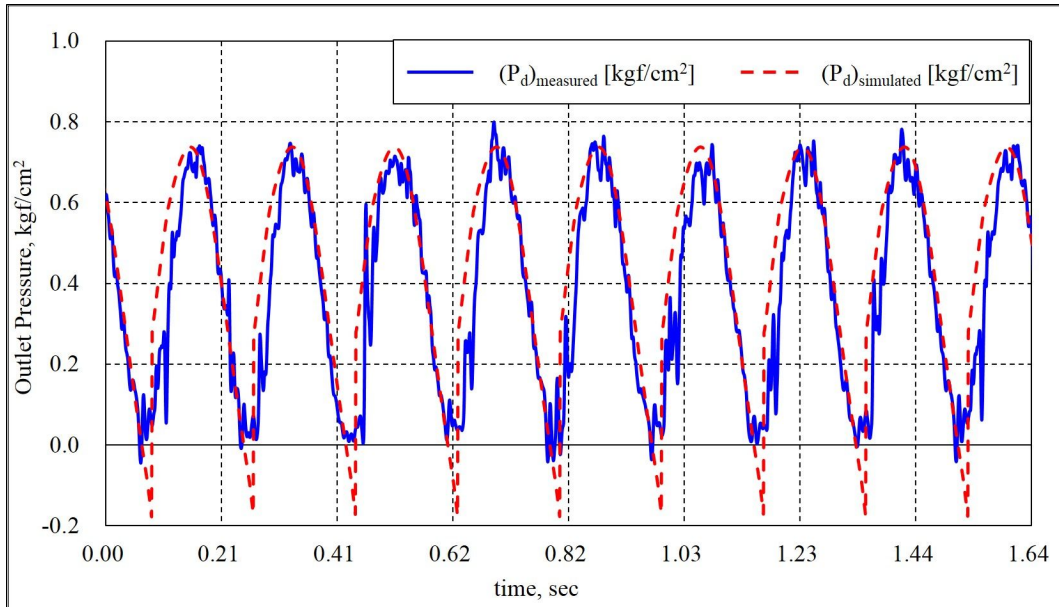


Fig.6.7. Comparison between the simulated and measured discharge pressures in the time domain.

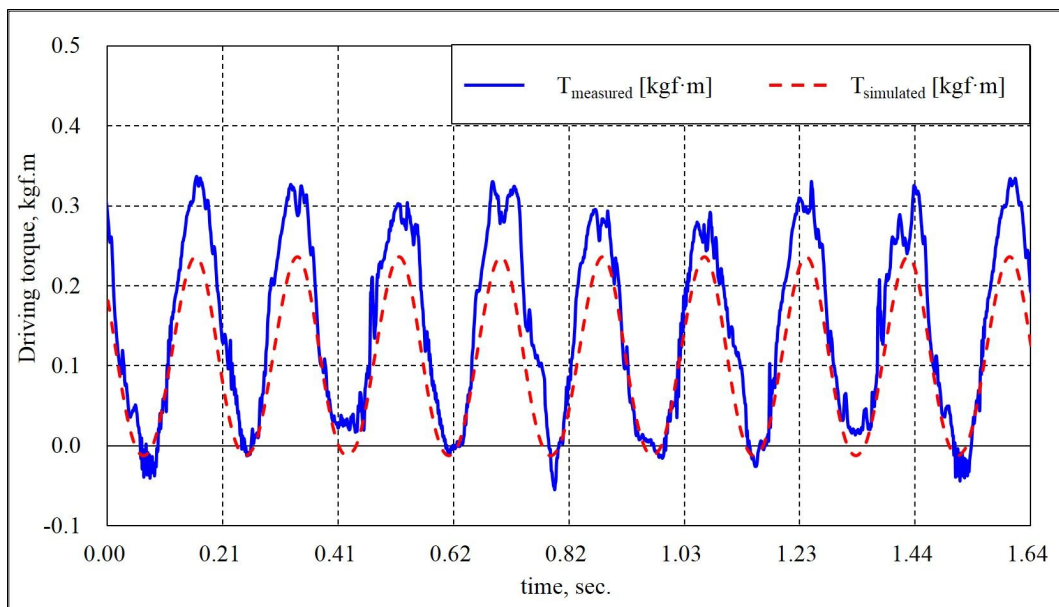


Fig.6.8. Comparison between the simulated and measured driving torques in the time domain.

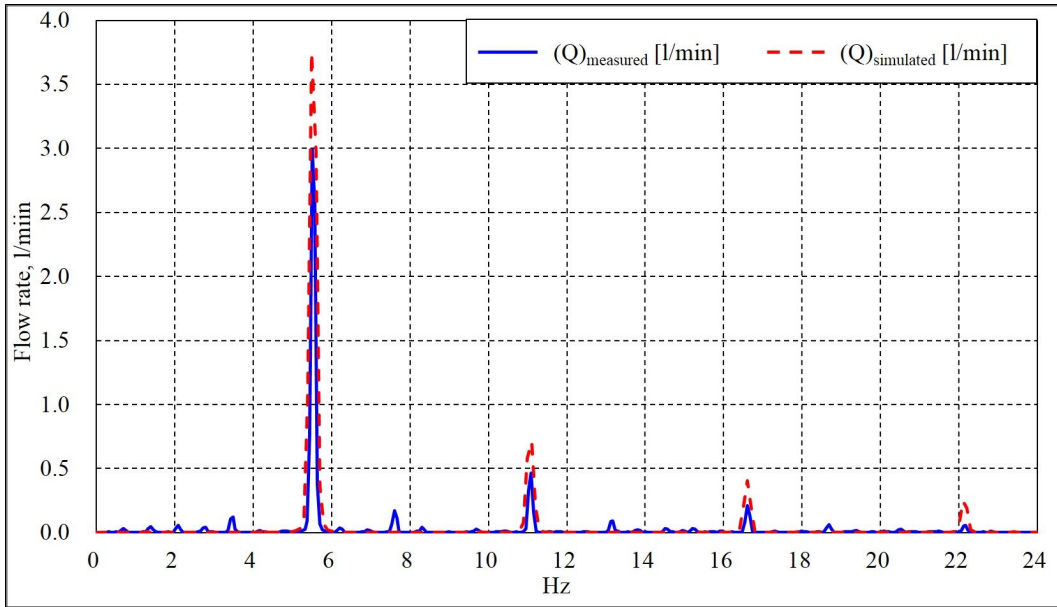


Fig.6.9. Comparison between the simulated and measured flow rates in the frequency domain.

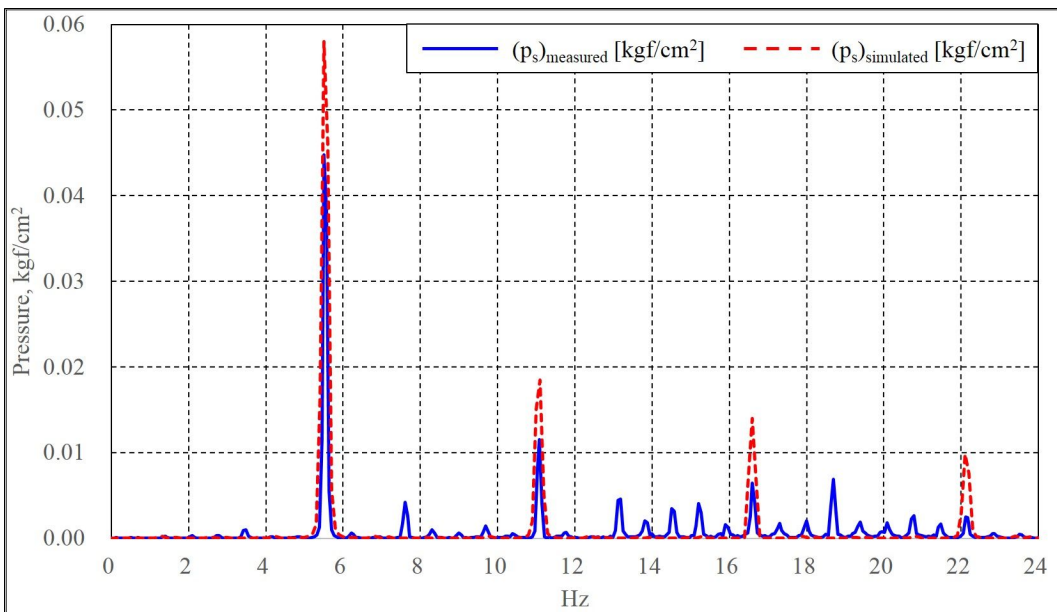


Fig.6.10. Comparison between the simulated and measured suction pressures in the frequency domain.

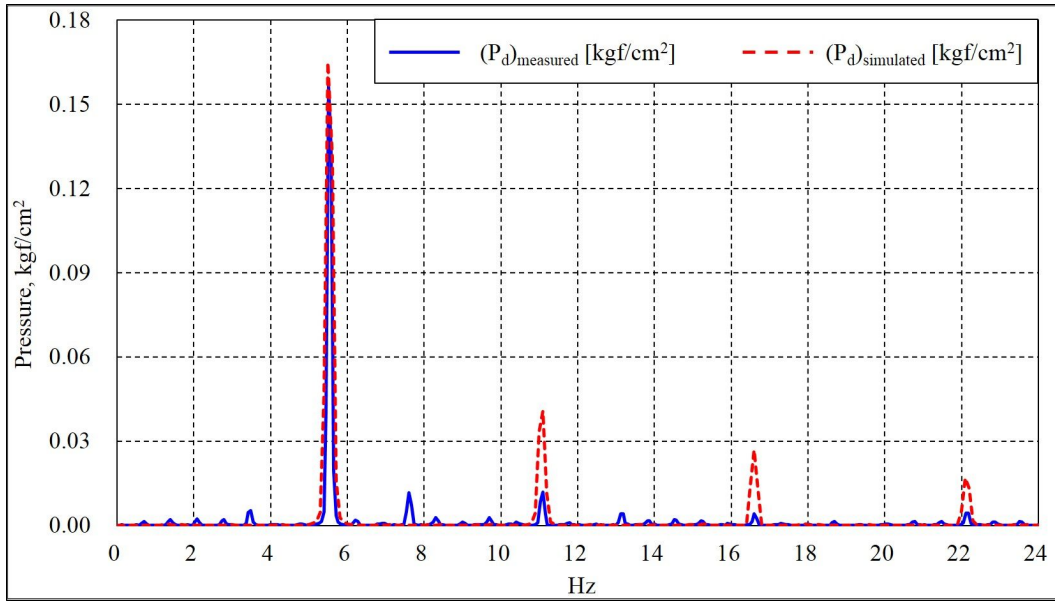


Fig.6.11. Comparison between the simulated and measured discharge pressures in the frequency domain.

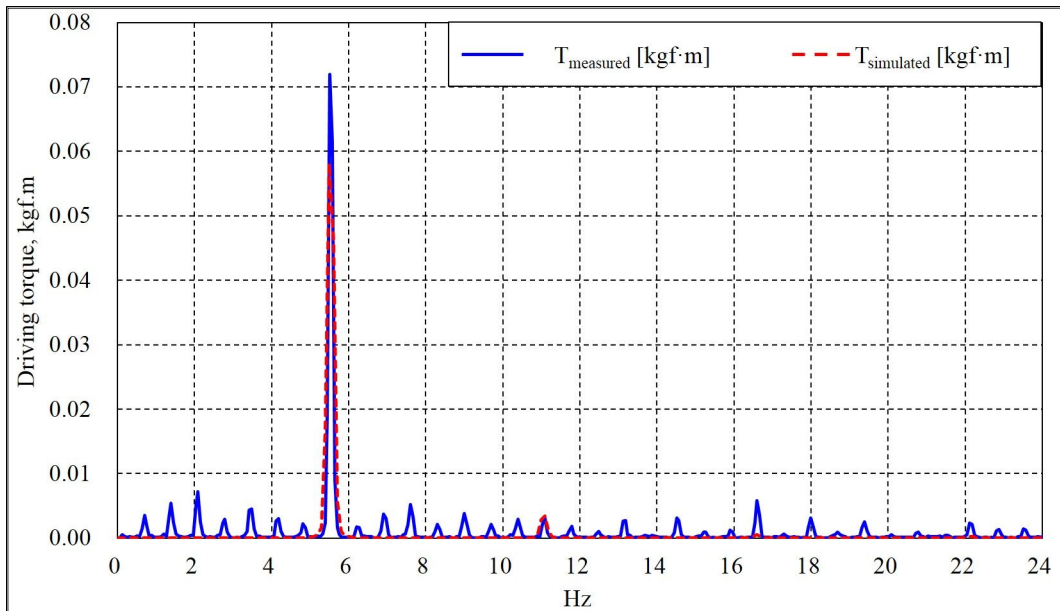


Fig.6.12. Comparison between the simulated and measured driving torque in the frequency domain.

Table 6.3 Percentage errors of the simulated suction pressure, discharge pressure, and driving torque at the primary frequency of 5.5 Hz.

	Flow rate Q, l/min	suction pressure p_s , kgf/cm ²	discharge pressure p_d , kgf/cm ²	Driving torque T, kgf · m
Measured	2.993	0.045	0.157	0.072
Simulated	3.745	0.058	0.165	0.058
Error, %	20.09	22.88	4.87	-23.89

Fig. 6.13 compares the measured and simulated efficiency characteristics of this pump as a function of the crank speed when the throttle valve was fully open. In general, the pressure of the discharge line is nearly zero when the throttle valve is fully open. However, in this pump, the pressure of the discharge line increased with the crank speed because of the pressure pulsation noted previously.

As discussed earlier, although the simulated volumetric efficiency agreed well with the measured data, it was very low compared with that of conventional pumps. This may be because the clearances between the pump chambers and rotor jaws were very large. Fig. 6.14 shows the clearances between the pump chambers and rotor jaws as measured with a feeler gauge. The clearances were between 0.25 and 0.28 mm. This result agreed well with the simulated values.

On the other hand, the simulated torque efficiency did not agree with the measured data, and the difference increased with the crank speed. The causes were estimated to be abnormal mechanical friction force caused by component misalignment. Fig. 6.15 shows the crank misalignment as measured with a dial gauge. The misalignment was measured as 0-0.2 mm under the dry condition after

all components were assembled. The misalignment of the components could be aggravated as the differential pressure and crank speed were increased.

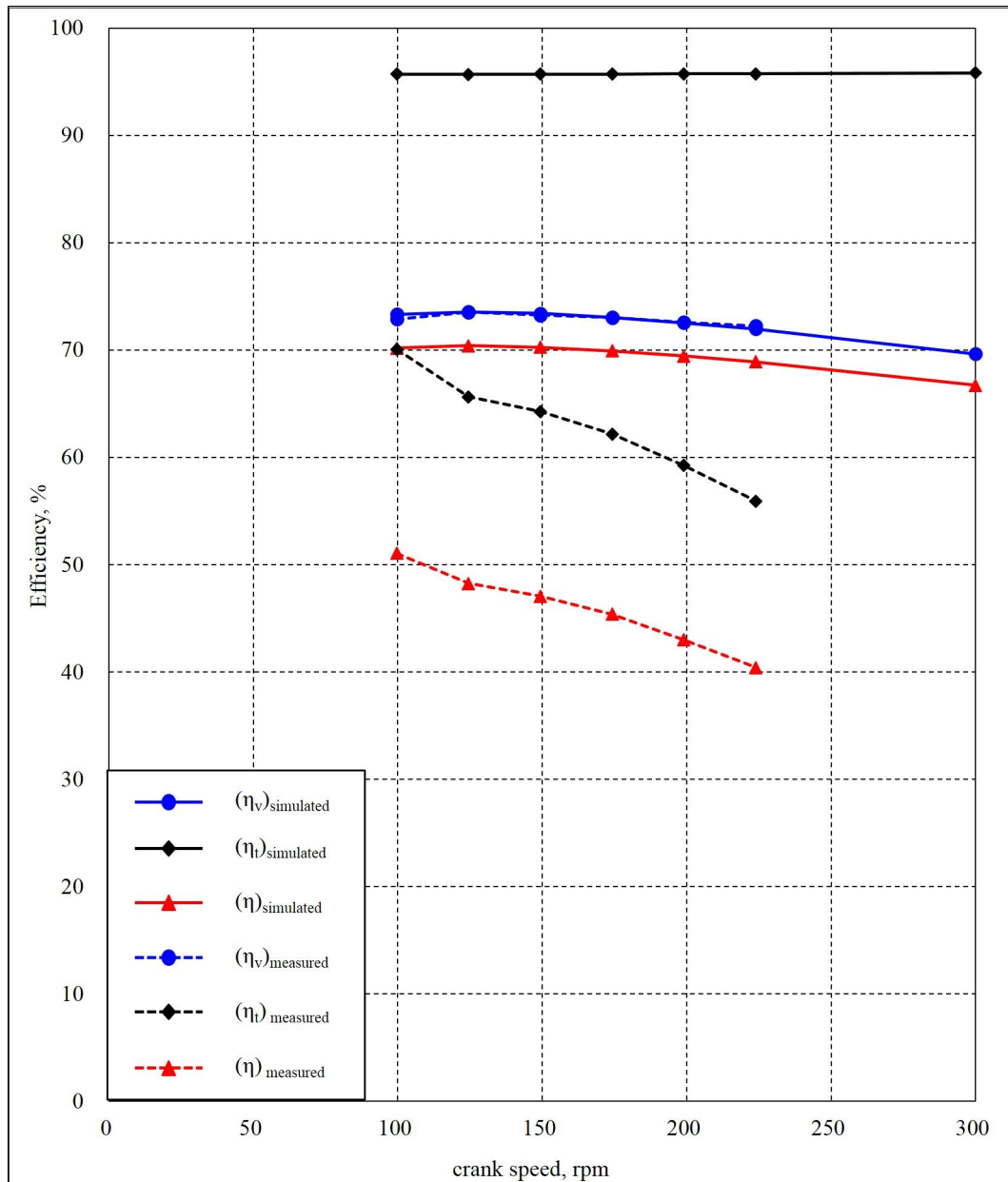


Fig.6.13. Comparison between the measured and simulated pump efficiency as a function of the crank speed.

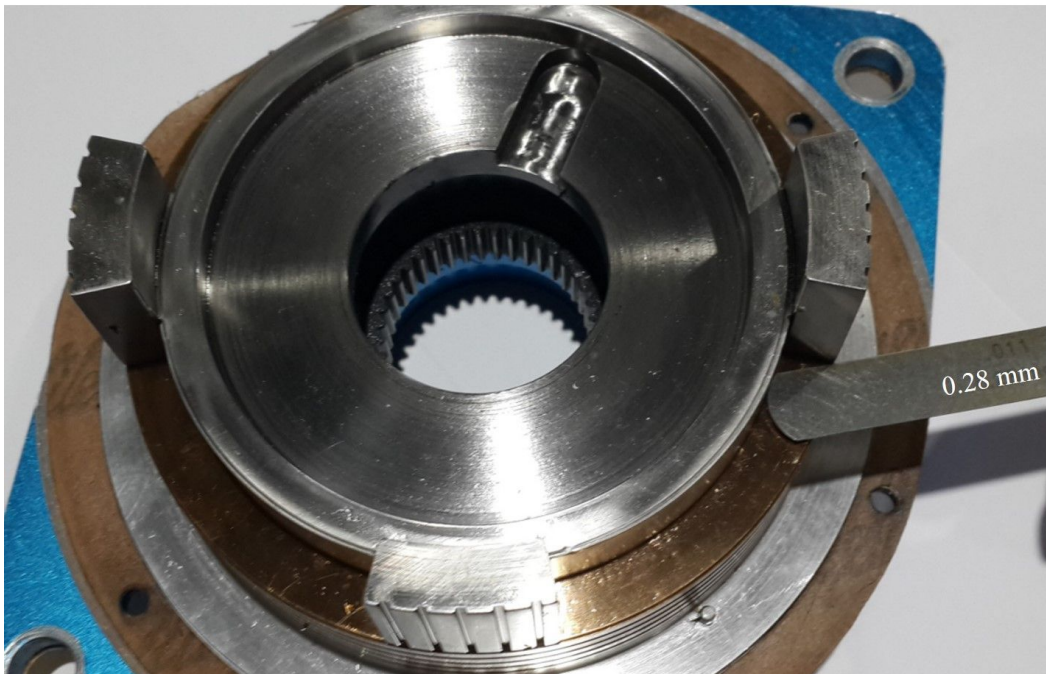
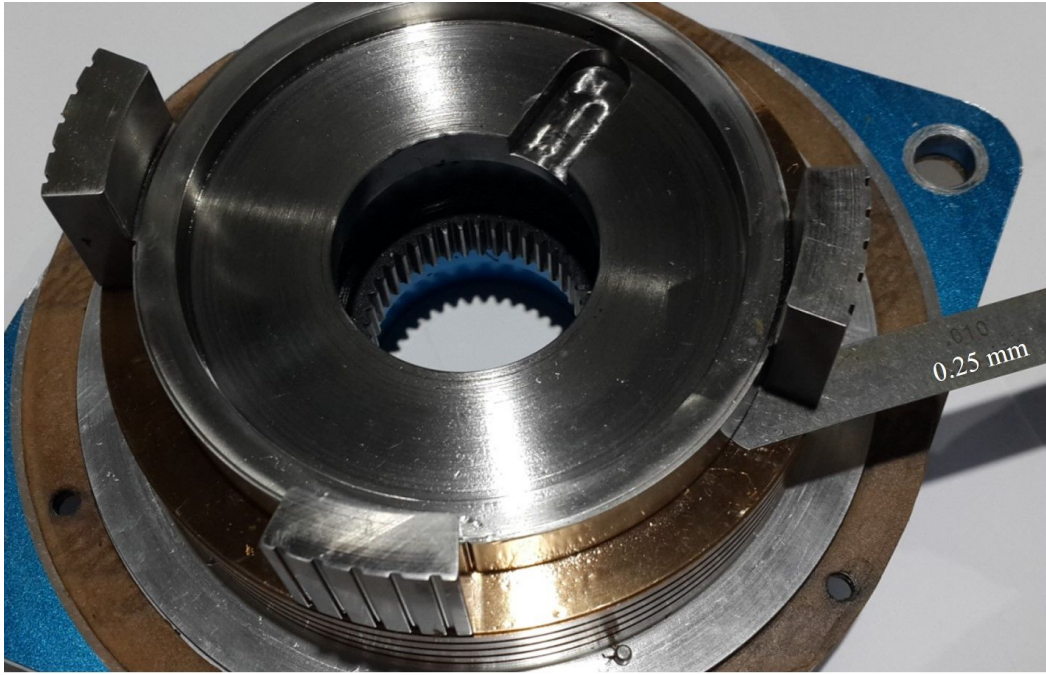


Fig.6.14. Measurement of the clearances with a feeler gauge.

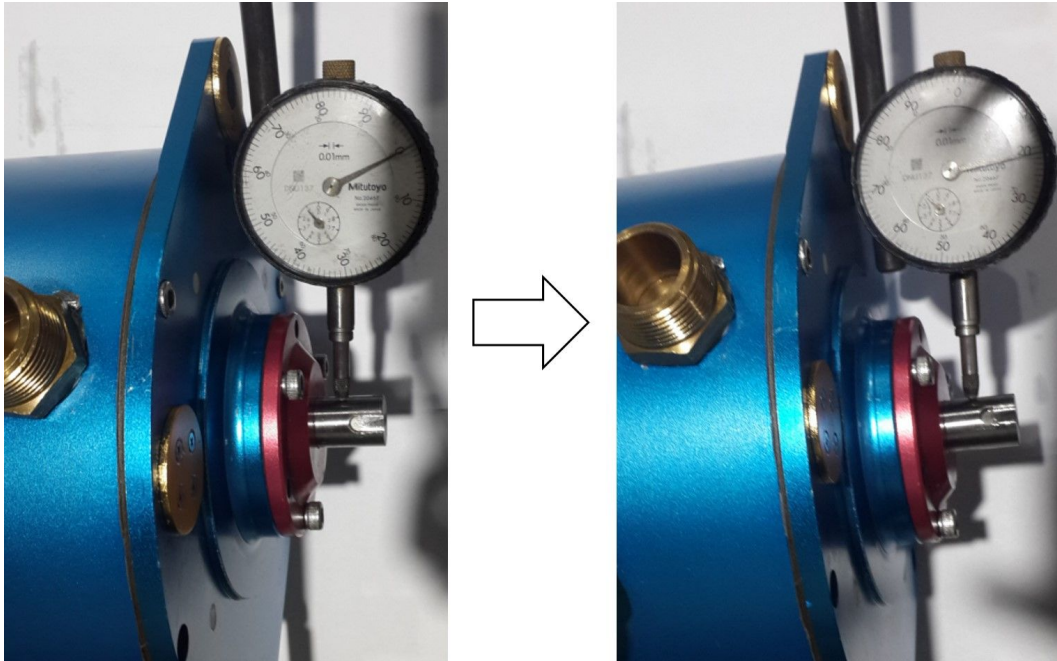


Fig.6.15. Measurement of the crank misalignment with a dial gauge.

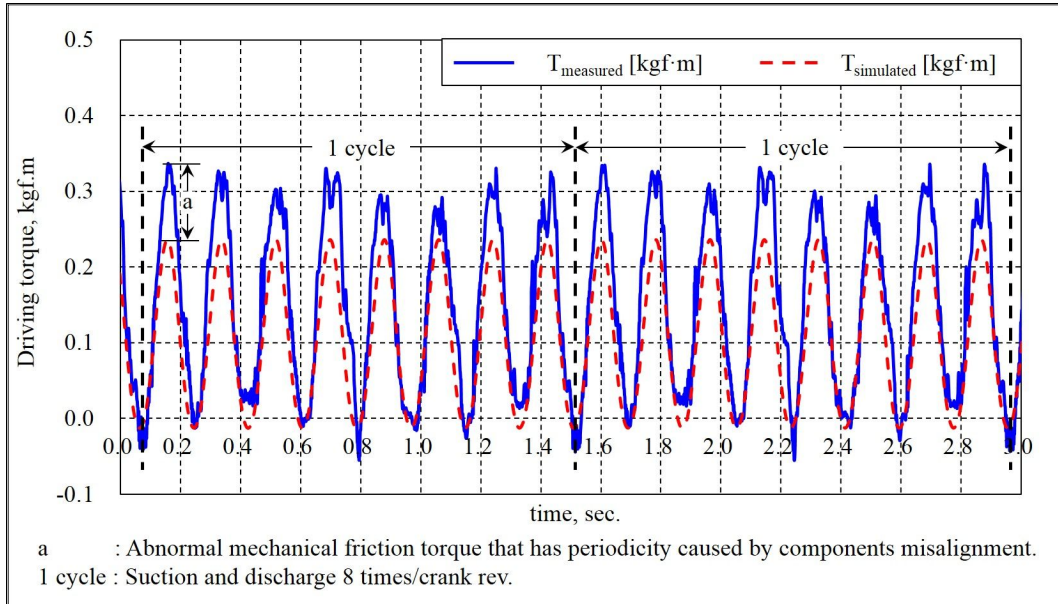


Fig.6.16. Fluctuation of friction torque caused by the crank misalignment.

6.3.2. Pressure pulsation and cavitation

Pressure pulsation and cavitation are very important factors especially in positive-displacement pumps, because they can have very severe effects on the system. Cavitation can also reduce delivery because the vapor occupies a much larger volume than the liquid from which it is derived. In this case, the accompanying loss in delivery must not be confused with slip (Wilson. 1950). In positive-displacement pumps, cavitation can generally be decreased with pressure pulsation damping. The representative method for decreasing the pressure pulsation in conventional pumps is to use multi-pumps or a pulsation dampener.

In the case of rotational clap pumps, pressure pulsation and cavitation are likely to occur because the kinematic characteristics cause very frequent and large the pressure changes. The effects of applying the above method to a rotational clap pump are presented below.

6.3.2.1. Using multi-pumps

In reciprocating pumps, the pulsation could be reduced by adding multi-cylinders, and timing the pumping strokes for small overlaps. In the same manner, the rotational clap pump could reduce the pressure pulsation. Table 6.4 shows a comparison of the effects of using different numbers of pistons on flow variations between the two types of pumps. It demonstrates that the pulsation of rotational clap pumps is smaller than that of reciprocating pumps when using the same number of pistons (rotor pairs).

Table 6.4 Effect of the number of pistons or rotor pairs on the flow variation.

Reciprocating pumps (Thompson. 2006; Karassik et al. 2008)			
No. of pistons	Above mean, %	Below mean, %	Total, %
1	-	-	-
2	60	100	160
3	6.1	16.9	23
4	24	22	46
5	2	5	7
rotational clap pumps			
No. of rotor pairs	Above mean, %	Below mean, %	Total, %
1	62.3	99	161.3
2	9.6	18.4	28
3	4.4	8.3	12.7
4	2.9	4.8	7.7
5	1.6	2.9	4.5

$$above\ mean = \frac{Q_{max} - Q_{mean}}{Q_{mean}} \times 100$$

$$below\ mean = \frac{Q_{mean} - Q_{min}}{Q_{mean}} \times 100$$

$$Total = above\ mean + below\ mean$$

6.3.2.2. Using a pulsation dampener

Pulsation dampeners have frequently been used to reduce piping pressure pulsations. However, there is no standard method for evaluating or ranking the dampener effectiveness (Lee. 2012; Singh, and Chaplis. 1990). Therefore, the initial volume of the pulsation dampener is generally determined based on the experience of the manufacturer. The gas charging pressures are commonly determined as follows (Lee. 2012):

$$0.5p_m \leq p_0 \leq 0.8p_m \quad (6.4)$$

where, p_0 = the gas charging pressure.

p_m = the mean pressure of pump system.

To confirm the effect of the pulsation dampener on this pump, pulsation dampeners for the discharge and suction line were added to the test equipment, as shown in fig.6.17. An air compressor was also installed to supply pressure in the pulsation dampeners.

Figs. 6.18 and 6.19 show the effects of the pulsation dampener on the variation in the flow and discharge pressure. The pulsation dampener was not used during the first half of the test period but was used during the second half. During the first half, the maximum, minimum, and mean flow rates were 35.18, 7.66, and 22 l/min respectively. The total variation was 125%. In contrast, during the second half, the maximum, minimum, and mean flow rates were 21.26, 17.49 l/min, and 19.80 l/min respectively. Thus, the total variation was 19%. In the same manner,

the total variation in the discharge pressure was 220 and 61% respectively. After a pulsation dampener was added, the flow fluctuation and discharge pressure pulsation were decreased to 15% and 28%, respectively, of the previous values. However, the mean flow rate and discharge pressure decreased 10% more than before pulsation dampeners were used. This means that the cavitation in the suction line was increased after the pulsation dampeners were used. This may be because the pulsation dampener was not optimized for the rotational clap pump conditions.

Figs.6.20-6.24 compare the measured and simulated pressure-flow rate curves as the crank speed was increased. The dotted curves represent the simulated data considering the cavitation. The pressures were calculated based on the measured flow rate. The simulated pressure was very similar to the measured value when the throttle valve was fully open. However, there were some differences between the data when the throttle valve was nearly closed. this means that the cavitation increased with the pressure when the crank speed was the same.

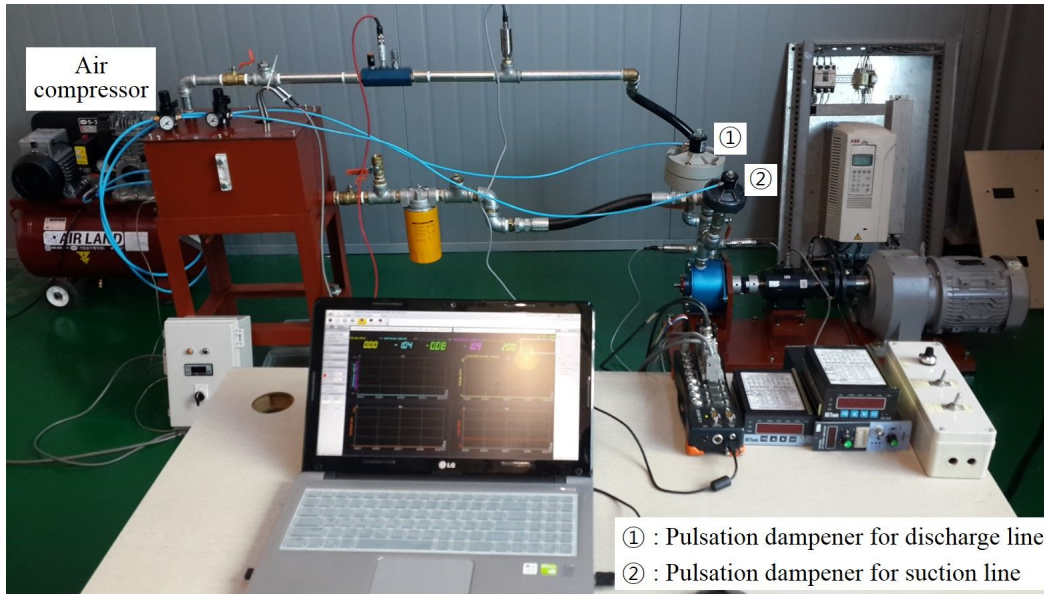


Fig.6.17. Pulsation dampeners installed in the pump testing system.

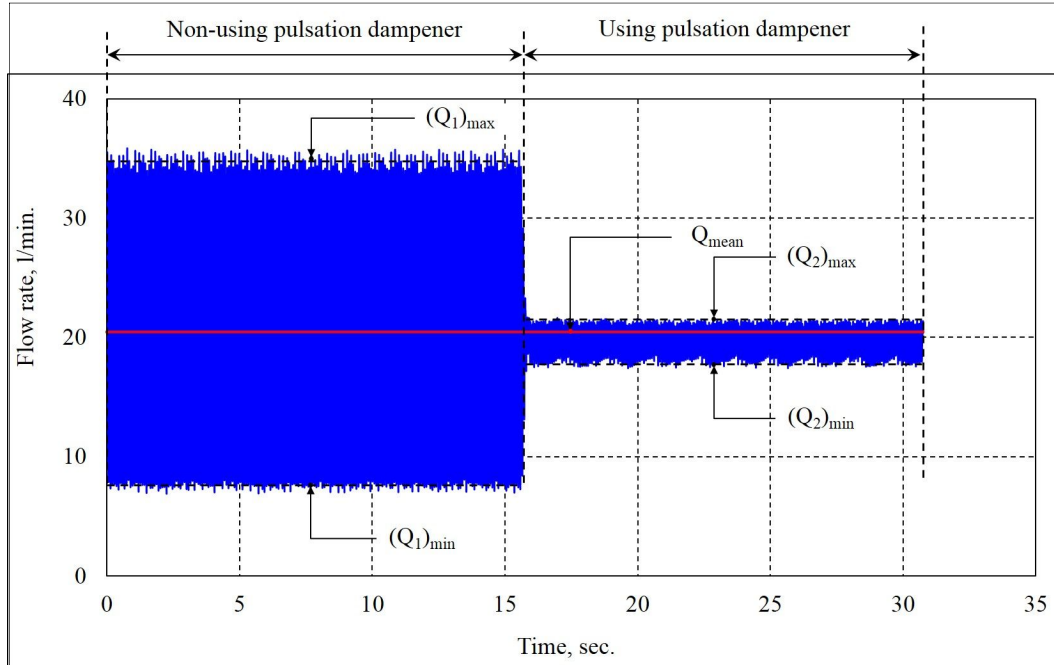


Fig.6.18. Effect of the pulsation dampener on flow variations.

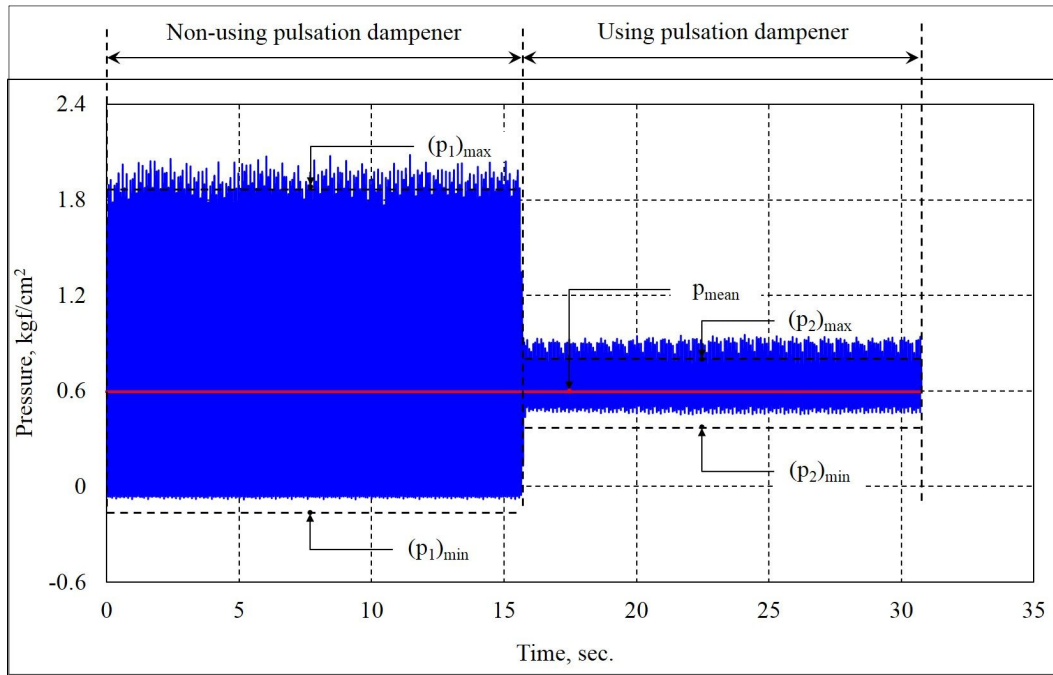


Fig.6.19. Effect of the pulsation dampener on discharge pressure variations.

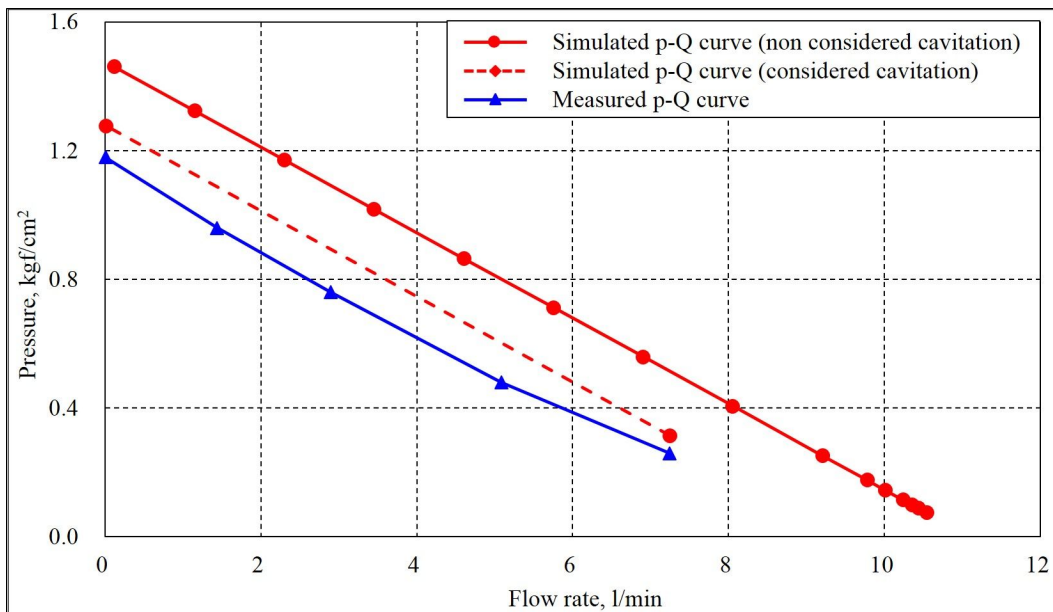


Fig.6.20. Comparison between measured and simulated p-Q curves when the crank speed was 100 rpm.

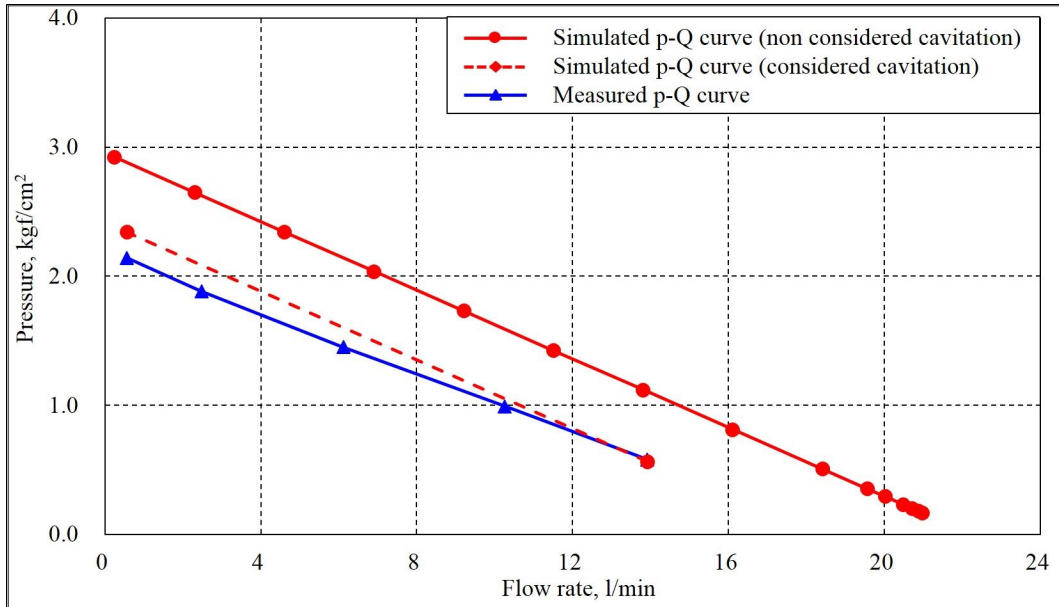


Fig.6.21. Comparison between measured and simulated p-Q curves when the crank speed was 200 rpm.

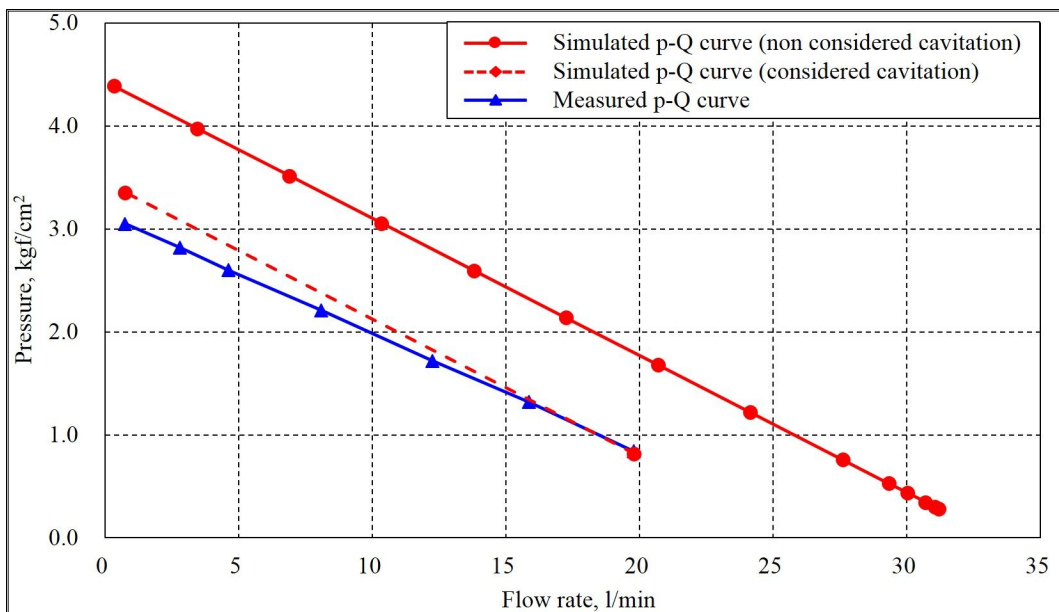


Fig.6.22. Comparison between measured and simulated p-Q curves when the crank speed was 300 rpm.

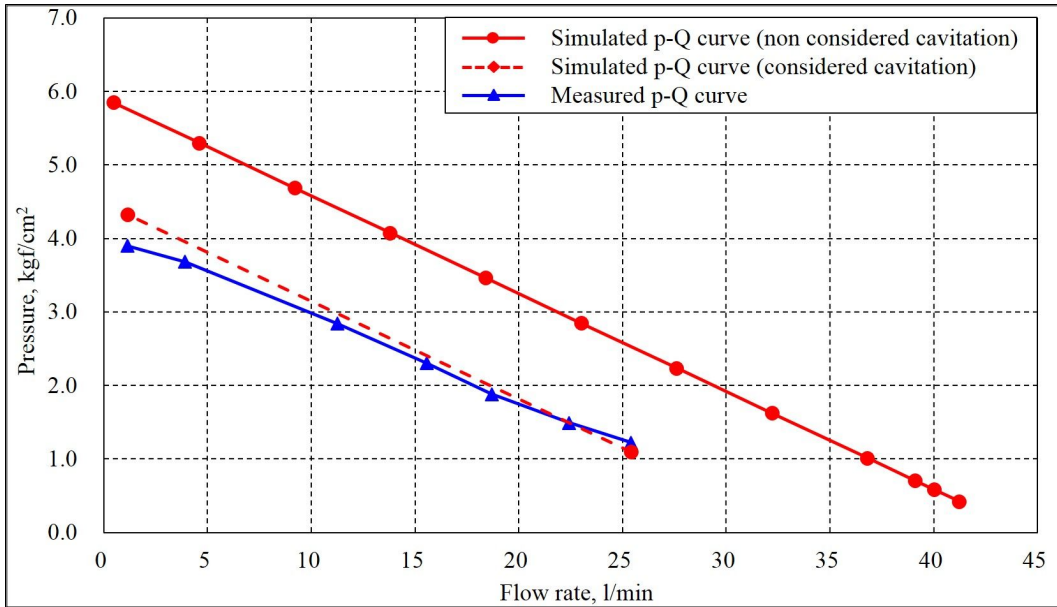


Fig.6.23. Comparison between measured and simulated p-Q curves when the crank speed was 400 rpm.

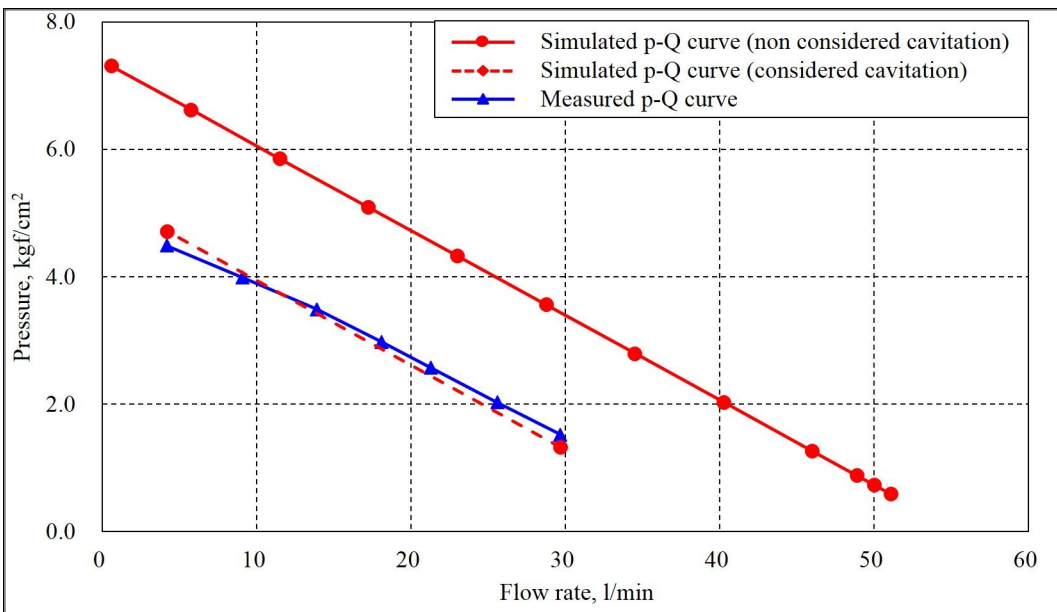


Fig.6.24. Comparison between measured and simulated p-Q curves when the crank speed was 500 rpm.

6.4. Conclusions

To verify the fundamental performances of this pump, a prototype was manufactured, and test equipment was installed. The performance of the pump was measured by using this prototype and test equipment.

The clearances between the rotor jaws and pump chamber were calculated based on the test results to be 0.2572 mm. The simulated data of the flow rate, differential pressure, driving torque, and efficiencies were verified by comparison with the experimental data. The flow rate, pressures, and driving torque agreed well in the time and frequency domains. The simulated volumetric efficiency also coincided well with the measured data. However, it was very low compared with that of conventional pumps. This may have been because the clearances between the pump chambers and rotor jaws were very large. In contrast, the simulated torque efficiency did not agree with the measured data, and the difference increased with the crank speed. The cause was estimated to be abnormal mechanical friction force caused by component misalignment.

To confirm the effect of the pulsation dampener on this pump, pulsation dampeners for the discharge and suction line were added to the test equipment. In the results, the total variation in the discharge pressure and flow rate decreased with a pulsation dampener. However, the mean flow rate, and discharge pressure decreased 10 and 17.7% compared to without a pulsation dampener. This means that the cavitation in the suction line was increased with the pulsation dampener.

Even though there were some differences between the simulation model and verification test, the causes were validated. Therefore, this simulation model can be used to predict the clap pump performance and compare it with conventional positive-displacement pumps.

7. Performance prediction

7.1. Introduction

Previous chapters presented the kinematic and performance characteristics and a verification of the pump. The results showed significant differences between the measured and simulated torque efficiencies. However, the causes of these problems were analyzed, and solutions were presented. Therefore, these results can be used to predict the performance of the rotational clap pump under any conditions.

This chapter presents the optimization of the main parameters that affect the pump performance and a prediction of the performance under these conditions.

7.2. Parametric study

The number of jaws N , jaw width W_j , and jaw height h are the main parameters that affect the pump performance, as shown in equations (3.41), (4.61), and (4.62). However, the parameters in table 5.6 that were used to design the prototype pump were not optimized. Therefore, this chapter presents an analysis of the effect of these parameters on the pump performance.

As discussed earlier, the clearances δ_1 and δ_2 between the jaws and chambers were calculated to be 0.2572 mm in the prototype pump. These the clearances are very large compared to those of conventional pumps. Based on equations (4.61) and (4.62), the flow slip $(Q_{slip})_{tot}$ increases with the clearances, while the forces caused by the fluid viscosity $(F'_{slip})_{tot}$ decrease with an increasing clearance. The efficiencies as the clearances increase were compared under the same conditions

given in table 5.6. As shown in fig. 7.1, the results showed that the volumetric efficiency decreased with the clearances, whereas the torque efficiency increased. Therefore, the overall efficiency reached its maximum value when the clearances δ_1 and δ_2 are 0.06 mm . The efficiencies according to the jaw height h and number of jaw N were also analyzed under the same conditions. The maximum volumetric, torque, and overall efficiencies were 98.98%, 96.07% and 95.07% for jaw heights of 16, 14, and 14 mm, respectively. The torque and overall efficiencies increased with the number of jaws but the volumetric efficiency decreased.

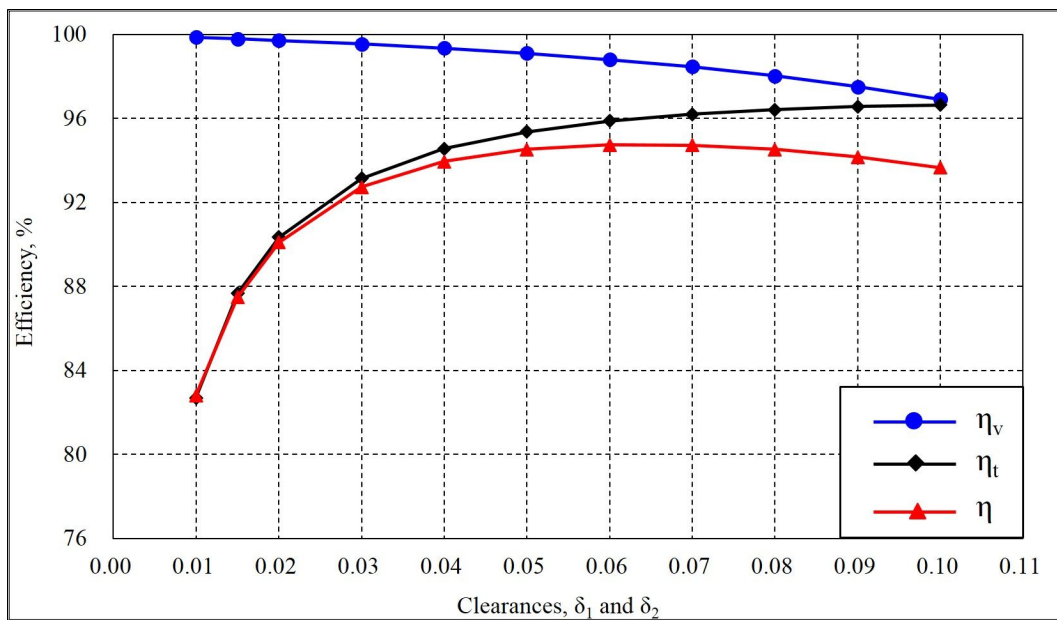


Fig.7.1. Efficiency vs. clearance when $n = 100\text{ rpm}$, $h = 10\text{ mm}$, and $N = 4$.

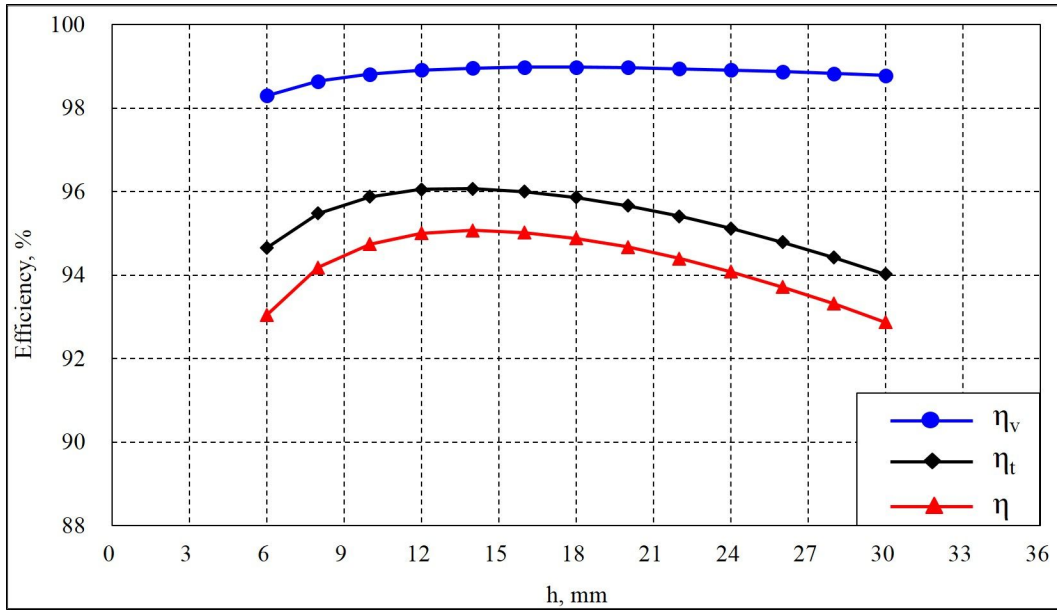


Fig.7.2. Efficiency vs. jaw height when $n = 100$ rpm, $\delta_1 = \delta_2 = 0.06$ mm, and $N = 4$.

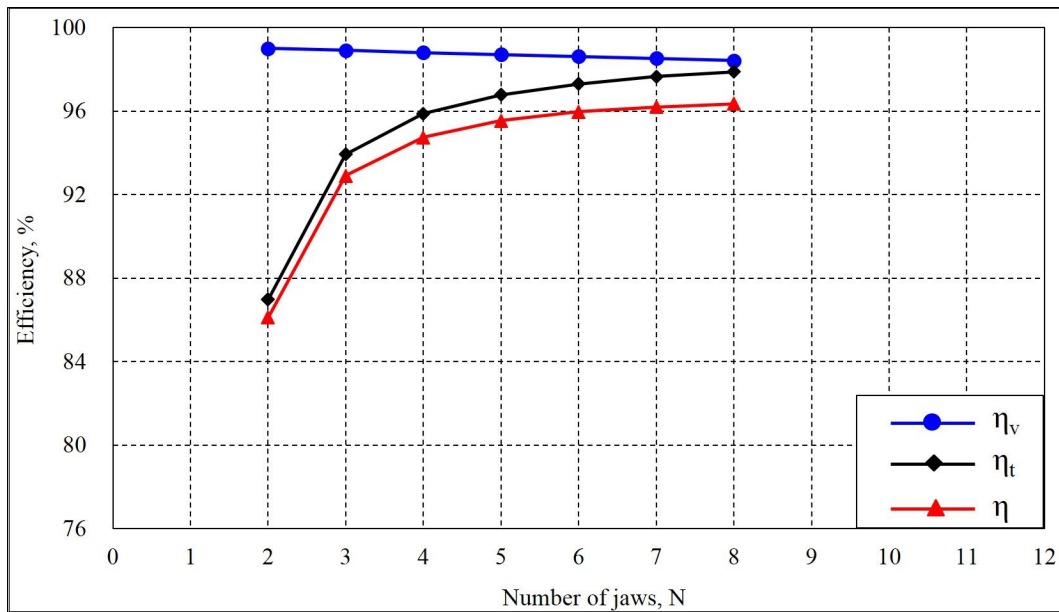


Fig.7.3. Efficiency vs. number of jaws when $n = 100$ rpm, $\delta_1 = \delta_2 = 0.06$ mm, and $h = 10$ mm.

7.3. Performance prediction

Previous chapters presented an analysis of the kinematic and performance characteristics of the rotary pumps, the design of the main components, and a comparison of the efficiencies according to the main parameters. This chapter presents the prediction of the performance for several cases based on the analysis results.

The first prediction was conducted under the following conditions.

- 1) The misalignment caused by manufacturing tolerances was neglected, and mechanical friction was not considered.
- 2) The clearances between the jaws and chambers δ_1 and δ_2 were 0.2572 mm.
- 3) The other conditions are given in table 5.6.

This means that the initial state of the prototype pump does not involve the problems discussed in chapter 6.3.1.

Figs.7.4 and 7.5 show the predicted performance curves and efficiency characteristics as a function of $\frac{\mu n}{\Delta p}$ under the initial conditions and the crank speed $n=100$ rpm. The overall efficiency was predicted to decrease from 83.11% to 57.54% as the differential pressure Δp was increased from 0.08 kgf/cm² to 0.56 kgf/cm². These predicted results show that the volumetric efficiency and overall efficiency were very low because the clearances δ_1 and δ_2 were large compared to those of conventional pumps. Therefore, the second performance curves were predicted when the clearances δ_1 and δ_2 had a maximum value of 0.06 mm. This caused the maximum overall efficiency to greatly increase from 83.14% to 95.86%. Figs.7.6 and 7.7 show the performance curves and efficiency characteristics as a

function of $\frac{\mu n}{\Delta p}$.

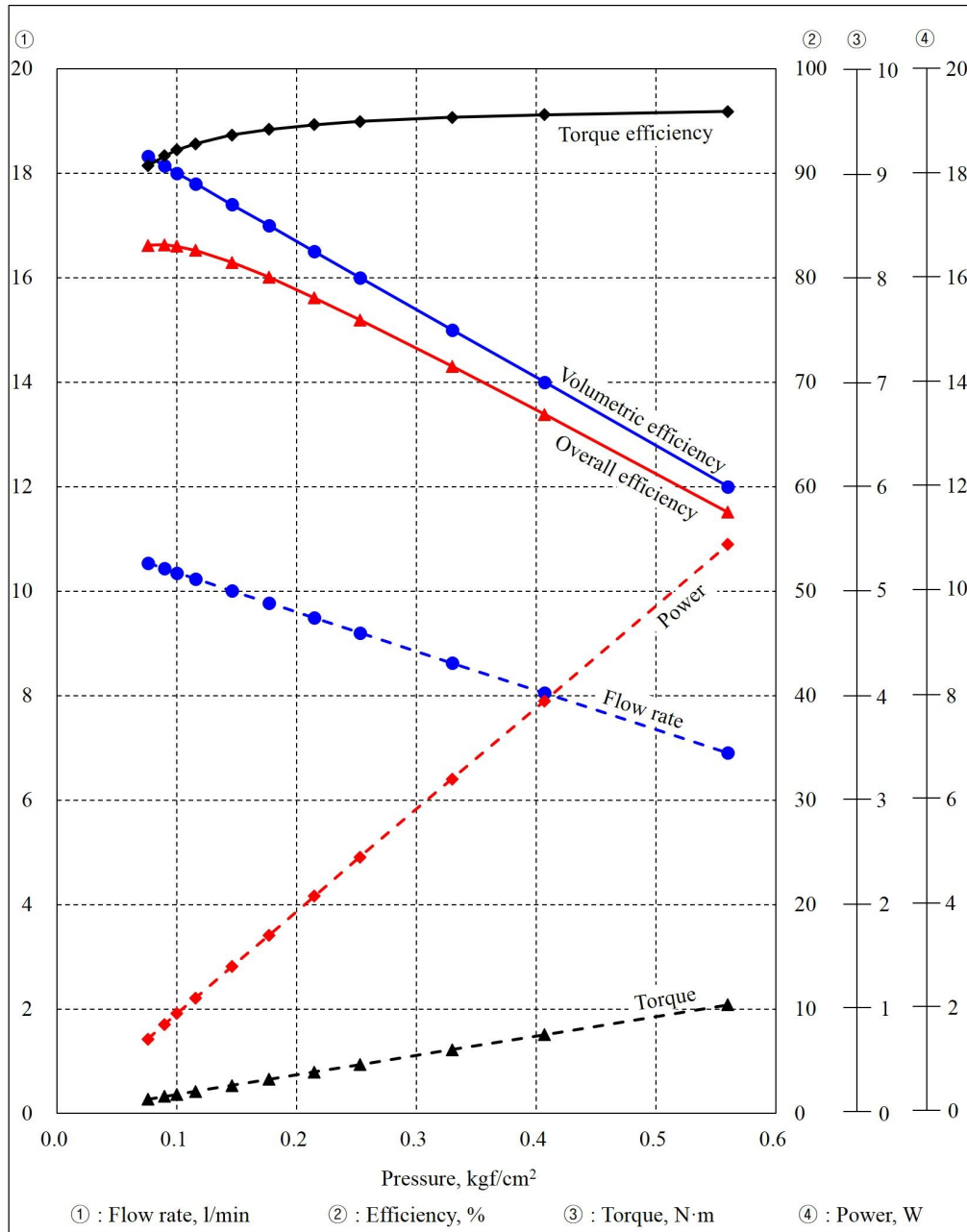


Fig.7.4. Performance curves under the initial conditions (crank speed $n = 100$ rpm).

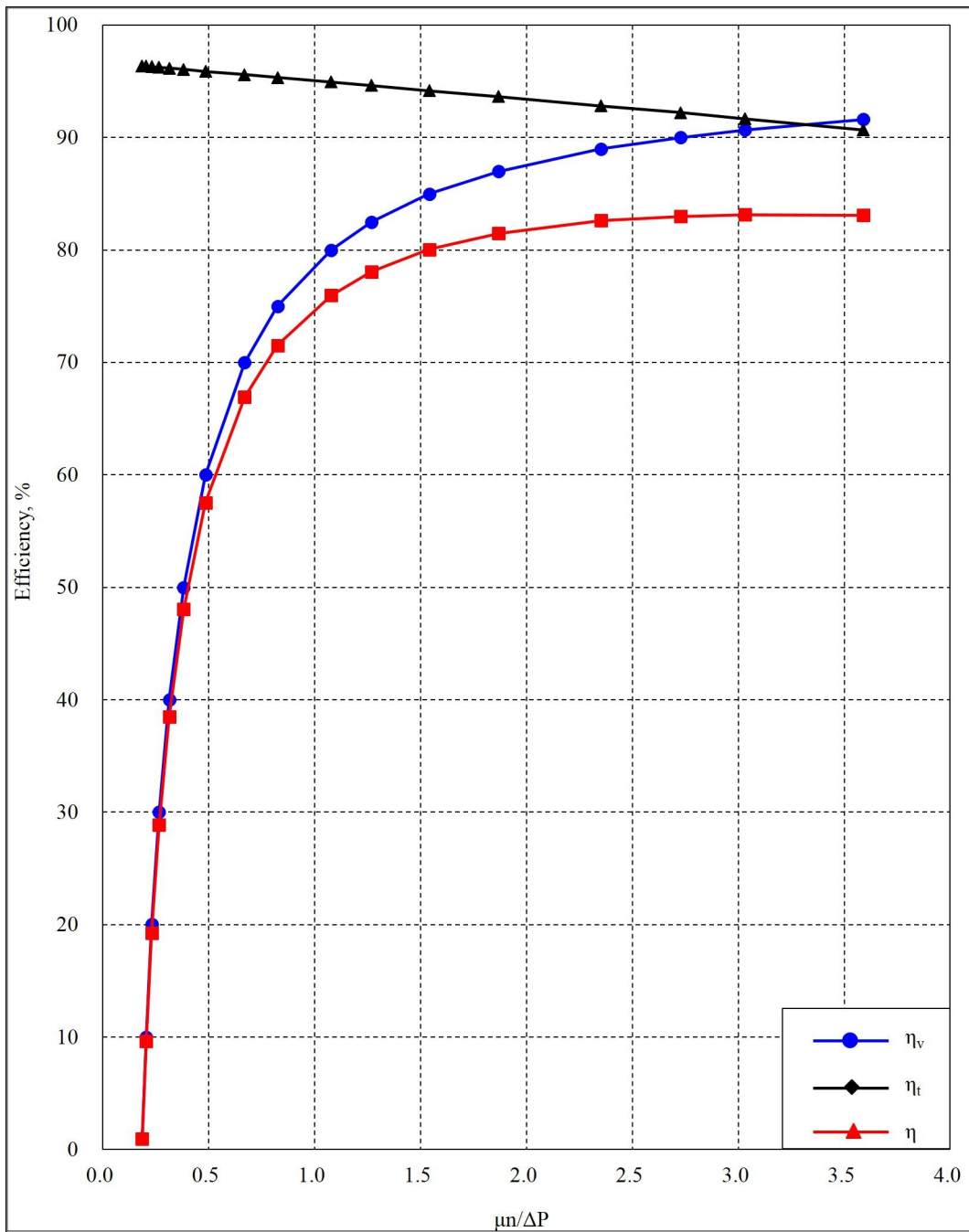


Fig.7.5. Pump efficiency as a function of $\frac{\mu n}{\Delta p}$ under the initial conditions (crank speed $n = 100$ rpm).

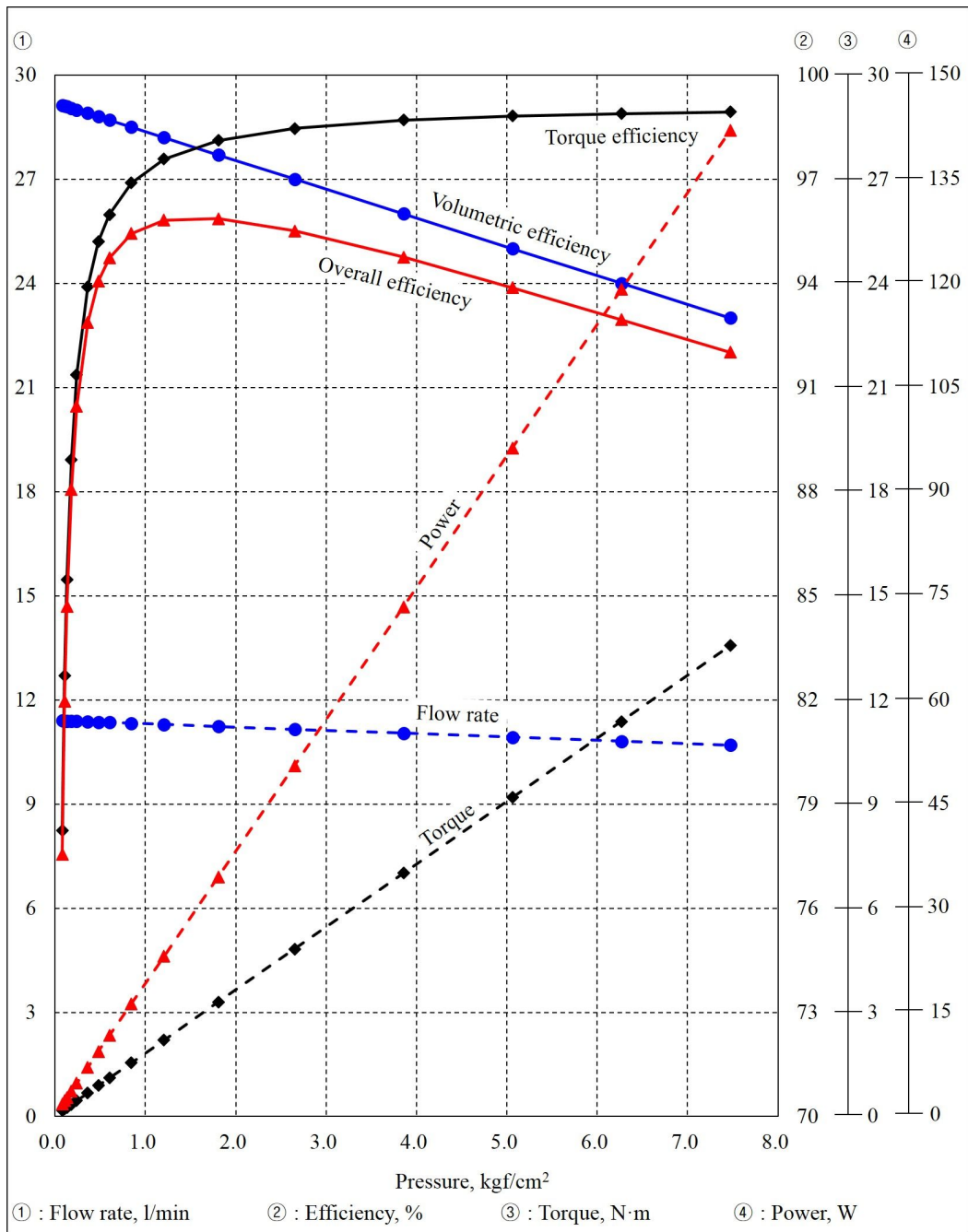


Fig.7.6. Performance curves under the second conditions (crank speed $n = 100$ rpm).

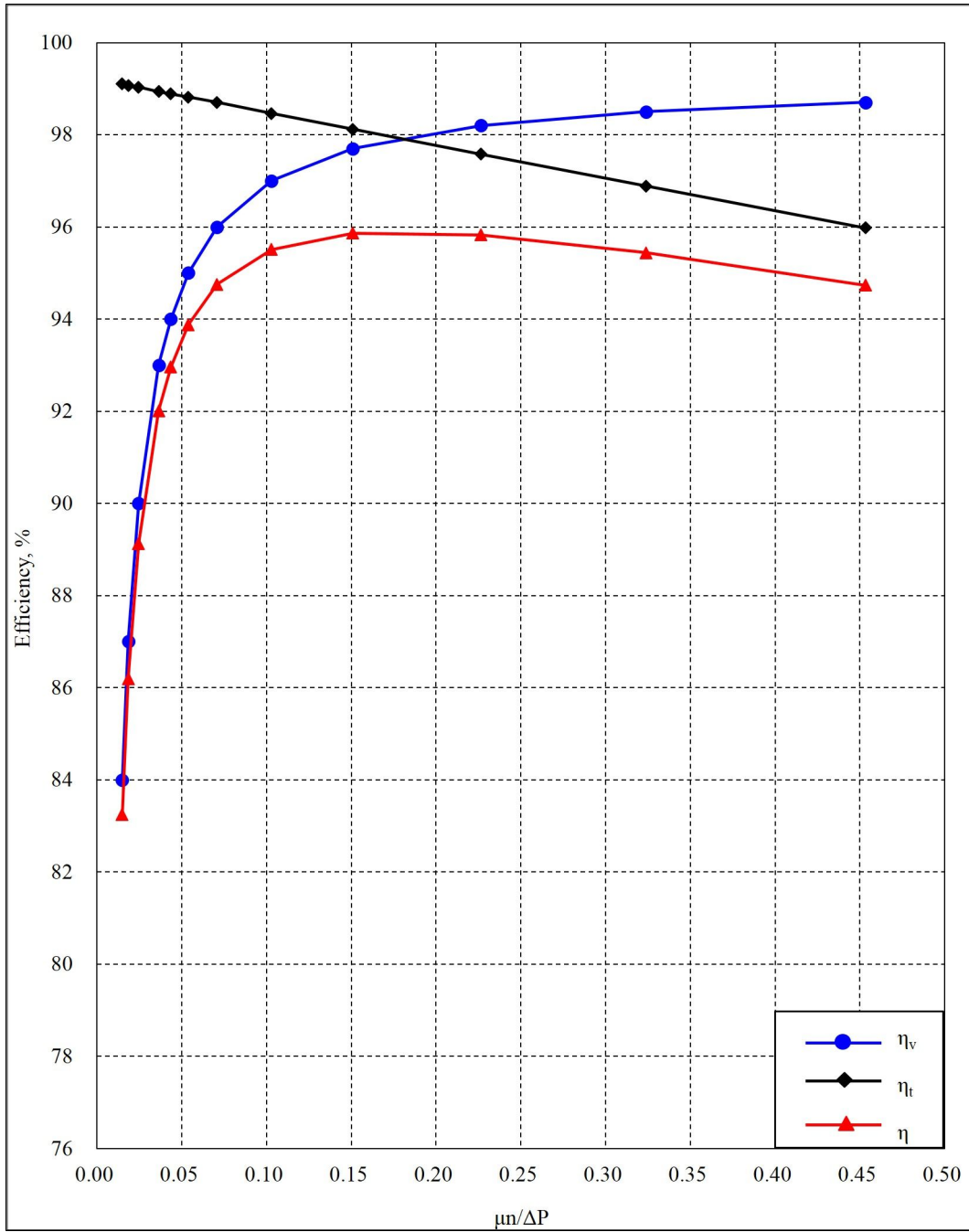


Fig.7.7. Pump efficiency as a function of $\frac{\mu n}{\Delta p}$ under the second conditions (crank speed $n = 100$ rpm).

The performances before and after the jaw height h was optimized were compared and analyzed. As discussed in chapter 7.2, the overall efficiency reached its maximum value when the jaw height $h=14$ mm. Therefore, the efficiency was predicted again after the jaw height h was increased from 10 mm to 14 mm. Figs.7.8-7.10 compare the efficiencies before and after jaw height optimization. All efficiencies after optimization were higher than before. Figs. 7.11 and 7.12 show the predicted performance curves and efficiency characteristics as a function of $\frac{\mu n}{\Delta p}$ under the final conditions and the crank speed $n=100$ rpm. The maximum overall efficiency was predicted to be 96.3%.

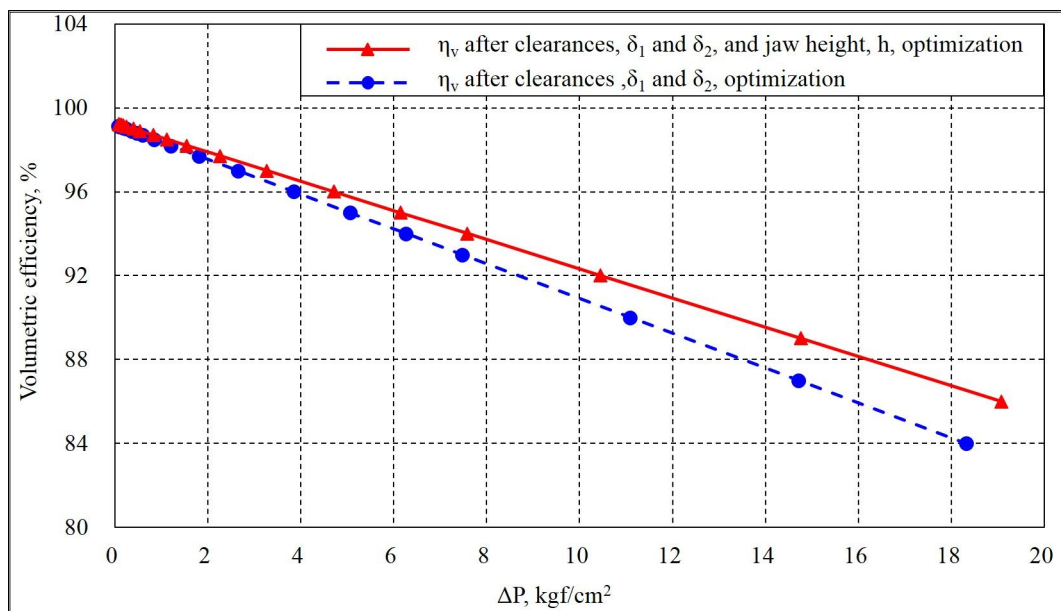


Fig.7.8. Volumetric efficiency before and after the parameter optimization (crank speed $n = 100$ rpm).

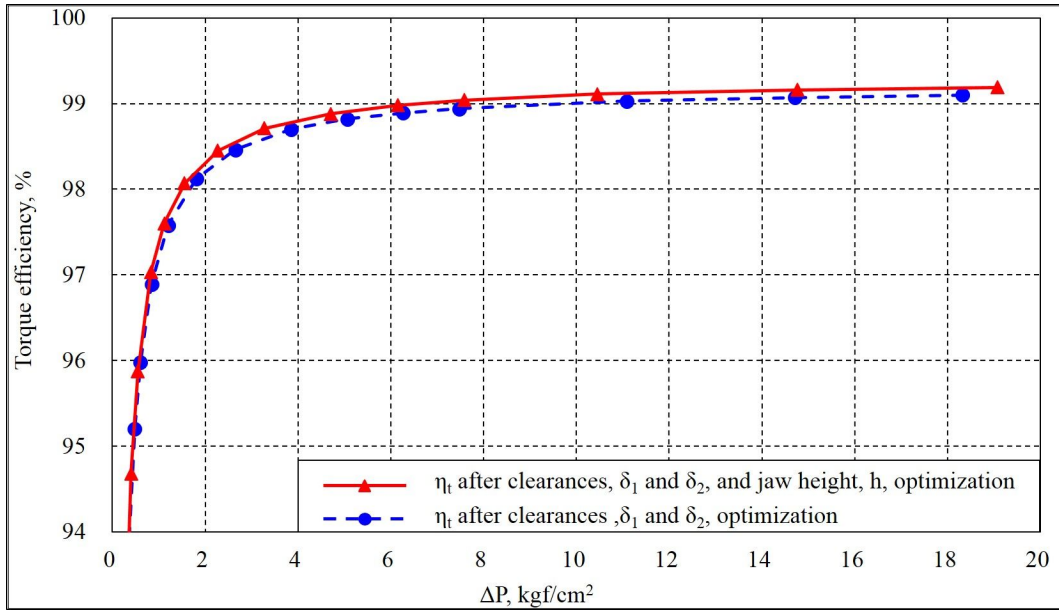


Fig.7.9. Torque efficiency before and after parameter optimization (crank speed $n = 100$ rpm).

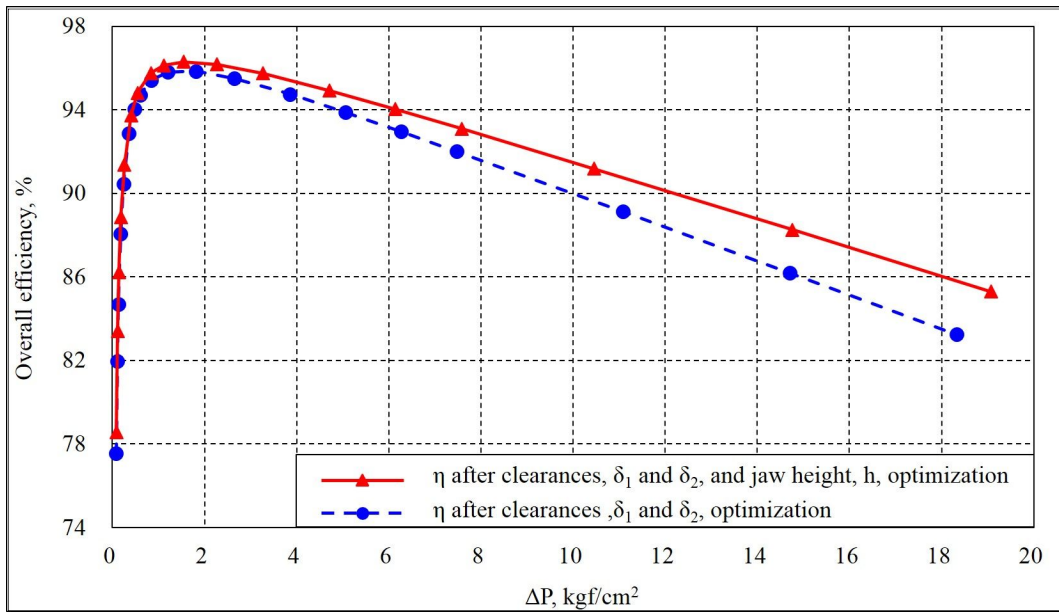


Fig.7.10. Pump efficiency before and after parameter optimization (crank speed $n = 100$ rpm).

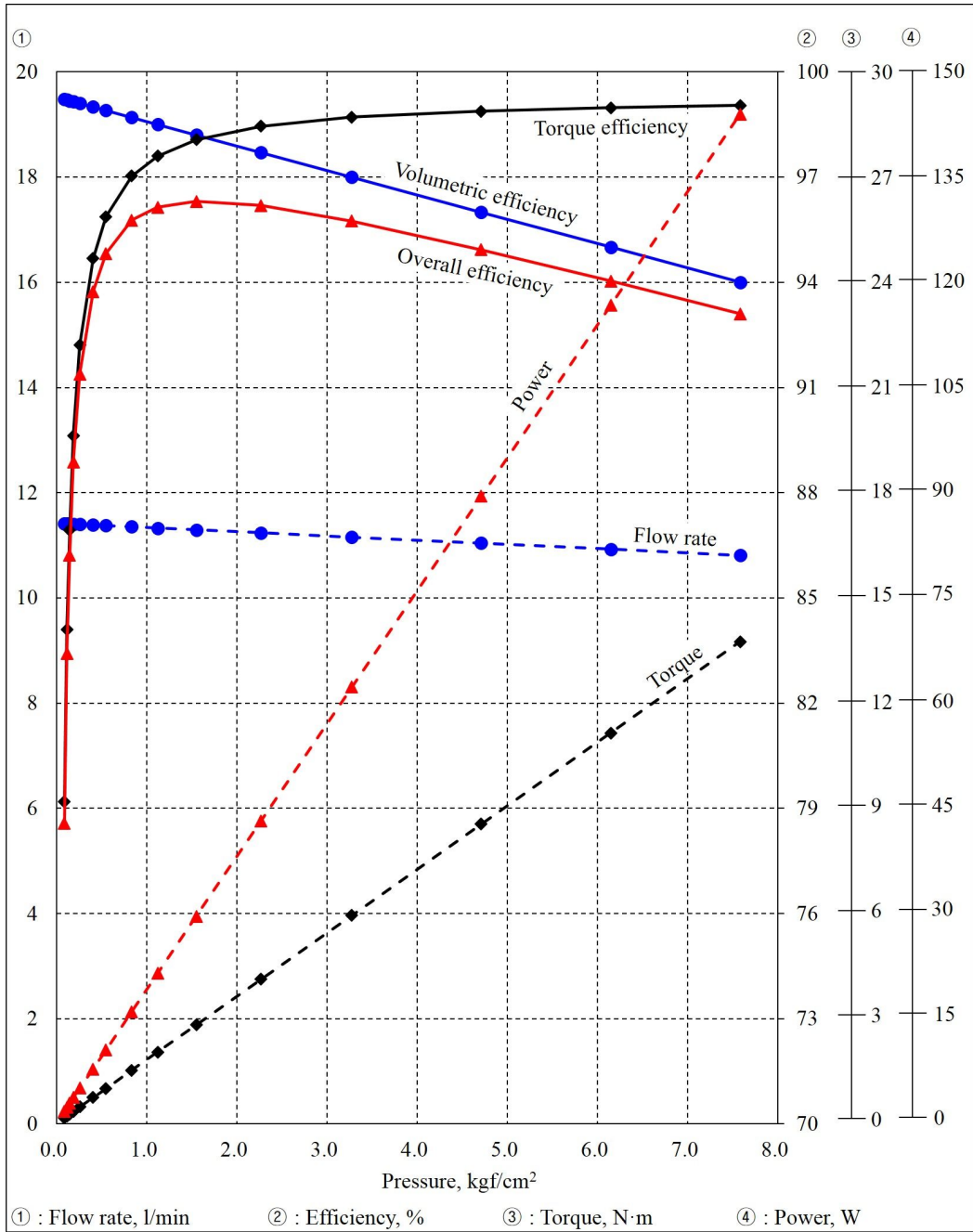


Fig.7.11. Performance curves under the final conditions (crank speed $n = 100$ rpm).

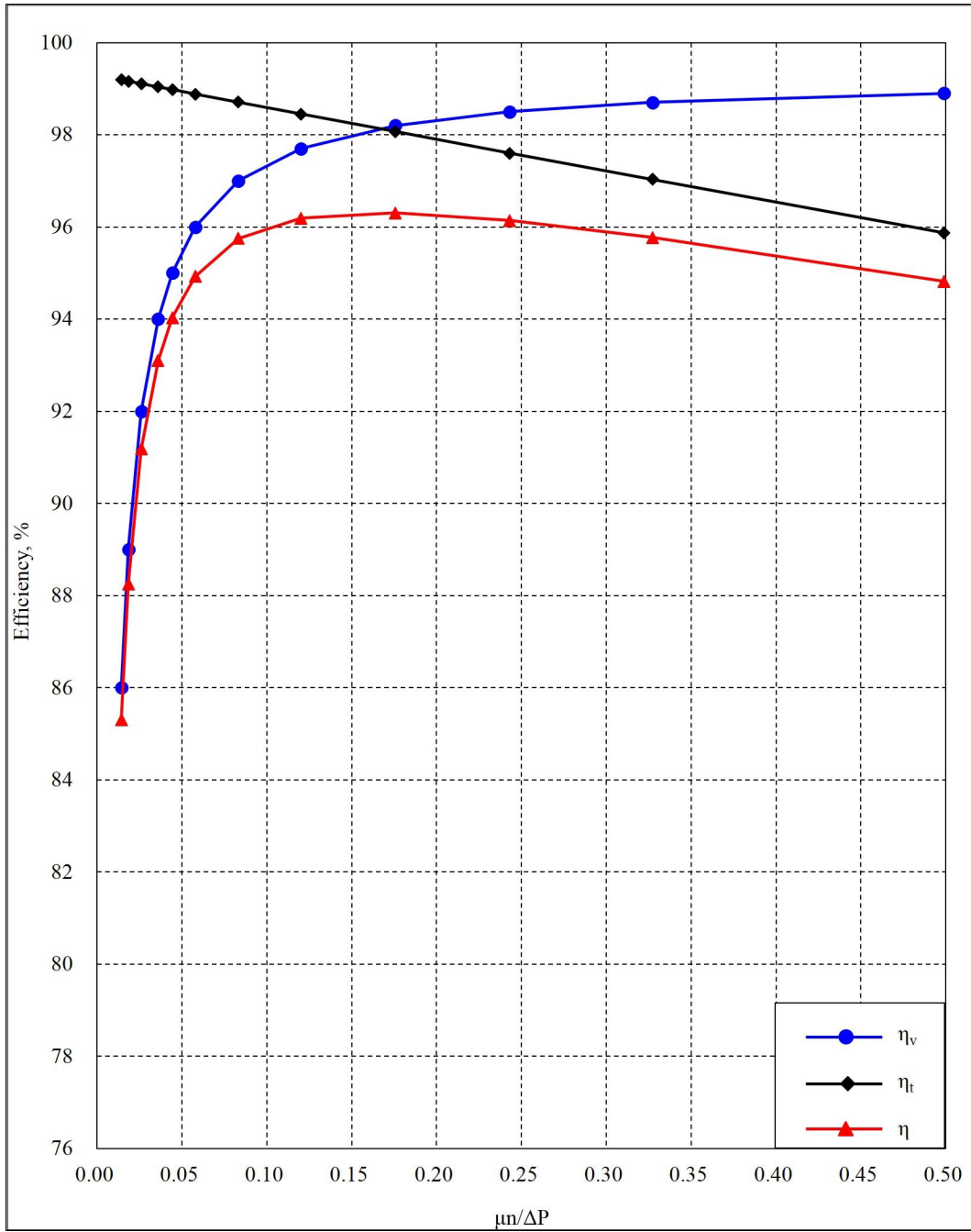


Fig.7.12. Pump efficiency as a function of $\frac{\mu n}{\Delta p}$ under the final conditions (crank speed $n = 100$ rpm).

7.4. Comparison among the conventional positive-displacement pumps and the clap pump

The main reasons for using the positive displacement pumps are for moving highly viscous fluid, maintaining constant flow, obtaining high vapor pressure conditions, and self-priming. However, it is very difficult to select positive-displacement pumps, because there are many types of pumping principles. Some types of pumps can be very suitable, but other pumps may have limitations that prevent their use under a given condition. The most representative factors for selecting positive-displacement pumps are flow, pressure, viscosity, and temperature. (Petersen, 2001).

To compare among the conventional positive-displacement pumps and rotational clap pumps, there is a need to present the most representative feature of the pump. Fig.7.13 shows the comparison of cross-section (chamber volume) in the conveying chamber between the rotors and the housing. External and internal gears and vane pumps have a relatively small cross-section. Conversely, lobe and reciprocating pumps have a relatively large cross-section. This means that a pump can be a compact size and reduce its rotational speed easily.

In equation 4.39, shear stress is proportional to shear rate with a viscosity. The shear rate is dv/dy . This term is a very important factor in pumps, when moving high viscous or shear sensitive fluid. It is not good for a pump to increase shear rate. When the fluid passes through the chamber of a pump, high viscous fluid can generate large viscous torque. Furthermore, shear sensitive fluid's properties can be altered. In these cases, shear rate should be kept as low as possible. The two main ways to minimize shear rate are to decrease pump speed and increase cross-section in the conveying chamber between the rotors and the housing. In this respect, the

rotational clap pump is structurally best. This pump can be used in a state of high viscosity fluid, high flow rate, and low and middle pressure, as shown in modified table 7.1 which was previously presented in a literature (Wilson, 1950).

There is a lot of literature which presents the positive-displacement pump selection guide or its features. However, this content can make readers confused, because its content can vary. This can be another reason it is difficult to select a positive-displacement pump. Table 7.2 shows comparisons among the conventional positive-displacement and rotational clap pumps. The features of conventional positive-displacement pump are common and representative ones were quoted from different literature (Forsthoffer, 2006; Garr et al., 2008; Karassik et al., 2008; Michael, 2005; Petersen, 2001; Wilson, 1950).

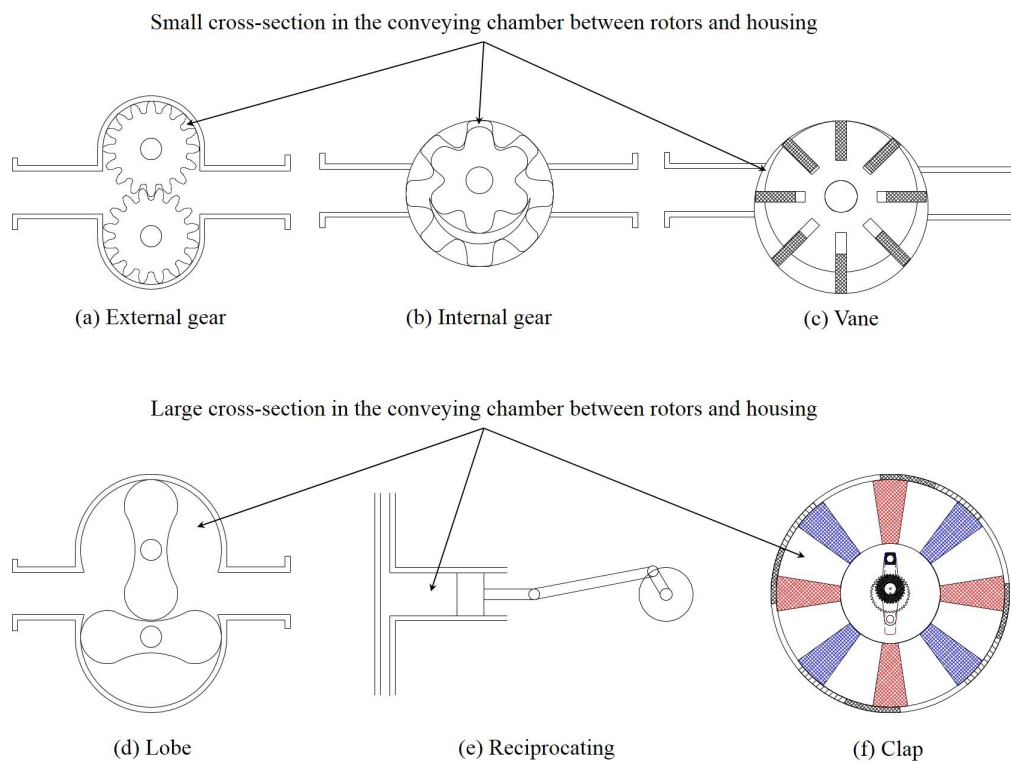


Fig.7.13. Space between different types of rotors and the housing.

Table 7.1 Serviceability of positive-displacement pumps.

Pressure	Delivery		
	Low	Middle	High
Low	Gear Vane Multi-piston	Vane Lobe Gear	Lobe rotational clap
Middle	Gear Vane Multi-piston	Vane Multi-piston Gear	Low speed single piston rotational clap
High	Multi-piston	Multi-piston	Low speed single piston

Table 7.2 Characteristics of conventional positive-displacement pumps and clap pump.

	Max. capacity	Max. pressure	Max. viscosity	Pulsation	Other features
Vane	N	N	B	G	<ul style="list-style-type: none"> ■ Good for thick liquids ■ Can run dry for short periods
External gear	N	N	N	G	<ul style="list-style-type: none"> ■ Simple ■ Bi-Directional ■ High speed
Internal gear	N	N	N	G	<ul style="list-style-type: none"> ■ Adjustable end clearance ■ Bi-Directional
Lobe	G	B	G	N	<ul style="list-style-type: none"> ■ Low shear ■ No metal-to-metal contact ■ Pass medium solids ■ Bi-Directional
Reciprocating	N	VG	B	VB	<ul style="list-style-type: none"> ■ High pressure capability ■ Excellent metering capability
Rotary clap	G	N	G	B	<ul style="list-style-type: none"> ■ Large cross-section ■ Low shear ■ Internal clearances can be adjusted freely ■ Bi-Directional

VG: Very good, G: Good, N: Normal, B: Bad, VB: Very bad

7.5. Conclusions

The performance of the clap pump was predicted after parameter studies that affect the pump performance, such as the clearances between the rotor jaws and chambers, the number of jaws, the jaw width, and the jaw height.

The overall efficiency reached its maximum value when the clearance was 0.06 mm, jaw height was 14 mm, and number of jaws was increased. After parameter optimization, the maximum volumetric, torque, and overall efficiencies were 99.22%, 99.19%, and 96.30% respectively.

Shear rate should be kept as low as possible, because it is not good for a pump. The two main ways to minimize shear rate are to decrease pump speed and increase cross-section in the conveying chamber between the rotors and the housing. In this respect, the rotational clap pump is structurally best. Therefore, this pump can be good in a state of high viscosity fluid, high flow rate, and low and middle pressure.

8. Overall conclusions and further studies

In this study, the rotational clap mechanism that was first presented by Kim (Kim, 2011; Kim, 2012) was improved, detailed mechanisms to realize the mechanism was developed, and the characteristics analysis and performance prediction of the rotational clap pump were conducted based on a prototype pump and its verification test.

A working principle of the mechanism and its design parameters were introduced with kinematic analysis of the pins and rotors. The vector equations developed in the analysis can be used to easily depict the motion characteristics of the mechanism for different design parameters. The inter-relationships between the design parameters were also examined to determine the proper crank radius and pin distance within the allowable number of gear teeth and rotor size. The thickness angle of the jaw and inner radius of the rotor were found to be most significant constraints that affect the crank radius and pin distance of the mechanism.

The pressure, driving torque, and efficiency characteristics of the pump were evaluated to analyze the fundamental performance of the pump. The design constraints of the fixed internal gear and gear of shaft link using involute curves were examined, and the strength of the main components was designed.

The involute-type internal gear has design limits caused by three kinds of interferences. The kinematic constraints can aggravate this limits. As a result, designing a pump for high-pressure and low flow rate conditions with an involute-type internal gear can be difficult.

To verify the fundamental performances of this pump, a prototype pump was manufactured, and pump test equipment was installed. The simulated data of the

flow rate, differential pressure, driving torque, and efficiencies were verified by comparison with experimental data.

The main parameters that affected the pump performance were the clearance between the rotor jaws and chambers, the number of jaws, the jaw width, and the jaw height. Therefore, the parameter studies that affect the pump performance were conducted, and the performance was then predicted under these conditions.

In these analysis results, the rotational clap mechanism can be realized as a pumping device on equal performance with conventional rotary pumps. In addition, it can have compact size, be good in a state of high viscosity and shear sensitive fluid, high flow rate, and works well with less vibration and power loss.

On the other hand, the performance of the rotational clap mechanism was very constrained by some parameters. In addition, some factors that need to be verified, such as mechanical frictional torque, were not conducted. Therefore, further studies are needed:

1. The performance constraints caused by the use of involute-type gears can be solved by replacing it with a modified trochoid gear. Therefore, studies on analysis of modified trochoid gear and its application are needed.
2. The mechanical frictional torque analysis needs to be conducted under many conditions.
3. A study on optimized design of the pulsation dampener to eliminate the cavitation is needed.
4. Even though this study predicted the advantage of this pump and presented comparisons of it with other pumps, they are not verified yet. Therefore, more comparison studies are needed to verify its advantage.

9. References

1. Da Vinci Co., Ltd. 2015. Rotary heat engine. Retrieved Oct. 14, 2015 from <http://davinci-mode.co.jp/e/technology.html#rhe>.
2. Fedorovich D. E. 2006. Rotary piston machine of volumetric expansion. Russian patent, 2439333.
3. Forsthoffer William E. 2006. Forsthoffer's Rotating Equipment Handbooks: Pump, UK. Elsevier Science.
4. Garr M. Jones, Robert L. Sanks, George Tchobanoglous, Bayard E. Bosserman. 2008. Pumping Station Design third Edition. Oxford, UK. Elsevier.
5. Hao Deng, Cunyun Pan, Xiaojun Xu, and Xiang Zhang. 2013. A twin-rotor piston engine with annular connecting chambers. Proceedings of Institution of Mechanical Engineers, Part C: Journal of Mechanical Engineering Science 227, no.5: 1080-1089.
6. Hege J. B. 2006. Wankel rotary engine: A history. North Carolina, US. McFarland Company, Inc.
7. Hong. 2013. Machine design - theory and practice 6th Edition. Seoul, Korea. Kyobobook (In Korean).
8. Hydraulic Institute. 1990. Engineering data book 2nd edition. NJ, US. Hydraulic Institute.
9. Hydrotechnik. 2015. Technical documents Hysense QT 100. Retrieved Jan. 24, 2015 from [http://www. Hydrotech-nik.com/en-us/downloads/technical-documents/](http://www.Hydrotech-nik.com/en-us/downloads/technical-documents/)
10. Joseph Marin. 1962. Mechanical behavior of engineering materials. Englewood Cliffs, N.J. Prentice-Hall.
11. Karassik I. J., Messina J. P., Cooper P., and Heald C. C. 2008. Pump

- handbook 4th edition. New York, US. McGraw Hill.
12. Kim J. M. 2011. Dual unequal rotational volumetric suction and discharging device. Korean patent, 101073159.
 13. Kim J. M. 2012. Rotational clap suction/pressure device. PCT, KR2012001710.
 14. Kohara Gear Industry Co., Ltd. 2015. Gear technical reference. Retrieved July 17, 2015 from http://www.khkgears.co.jp/en/gear_technology/pdf/gear_guide1.pdf.
 15. Lee I. Y. 2012. Hydraulic engineering. Seoul, Korea. Munundang (In Korean).
 16. Librovich B. V. 2003. Dynamics of rotary vane engine. *Journal of Mechanical Design* 125, no.3: 498-508.
 17. Librovich B. V. 2004. A. F. Nowakowski, Analysis, design, and modeling of a rotary vane engine (RVE). *Journal of Mechanical Design* 126, no.4: 711-720.
 18. Masmi Sakita, 2006. A cat-and-mouse type rotary engine: engine design and performance evaluation, *Proceedings of Institution of Mechanical Engineers, Part C: Journal of Mechanical Engineering Science* 220, no.8: 1139-1151.
 19. MatWeb. 2015. Material property data. Retrieved July 24, 2015 from <http://matweb.com/search/QuickText.aspx?SearchText=s45c>
 20. Mazda Motor Corporation. 1999. Rotary engine. Japan.
 21. Menon E. S., and Menon P. S. 2010. Working guide to pumps and pumping stations. Oxford, UK. Elsevier.
 22. Michael Volk. 2005. *Pump Characteristics and Applications Second Edition*. Boca Raton, FL, US. Taylor & Francis.
 23. Morgado R. G. 2004. Internal combustion engine and method. US patent, 6 739 307 B2.
 24. Murphy B. A. 2012. "Design and development of a novel troidal pneumatic motor." MD diss., Dalhousie University, Canada.

25. Petersen John E. 2001. Best practices in selecting and applying positive displacement pumps. Proceedings of 18th international Pump User Symposium: 109-118.
26. Reuleaux F. 1876. The kinematics of machinery - outlines of a theory of machines. London, UK. Macmillan and CO.
27. Schlücker E., Fritsch H., Stritzelberger M., and Schwarz J. 1997. A new evaluation method for estimating NPSH-values of reciprocating positive displacement pumps. ASME Fluid division summer meeting, British Columbia.
28. Shigley J. E., and Mischke C. R. 2001. Mechanical engineering design 6th Edition. New York, US. McGraw Hill.
29. Shih A. J. 1993a. Kinematics of the cycloidal internal combustion engine mechanism. Journal of Mechanical Design 115, no.4: 953-959.
30. Shih A. J. 1993b. Analysis and comparison of epicycloidal and hypocycloidal internal combustion engine mechanisms. Joournal of Mechanical Design 115, no.4: 960-966.
31. Singh P. J., and Chaplis W. K. 1990. Experimental evaluation of bladder type pulsation dampeners for reciprocating pumps. Proceedings of the 7th international pump users symposium. Houston, Texas: 39-48.
32. Thompson D. J. 2006. Using a pulsation dampener with a reciprocating pump. Pumps & Systems. July: 26-29.
33. Warren S., and Yang D. C. H. 2013. Design of rotary engines from the apex seal profile. Mechanism and machine theory 64: 200-209.
34. Wilson W. E. 1950. Positive-displacement pumps and fluid motors. NY, US. Pitman Publishing Corporation.
35. Xu X. 2014. A cam-quadrilateral mechanism for power trans-mission of a

twin-rotor piston engine. Journal of Mechanical Science and Technology 28 no.3:
953~961.

36. Yamamoto K. 1981. Rotary engine. Tokyo, Japan. Sankaido Co., Ltd.

Appendix A : Specifications of piping system for the pump

Fluid parameters			
Parameters	Value		
Fluid density	855 kgf/m ³		
Friction factor f	64/Re (Re: Reynold number ¹⁾)		
Suction line parameters		Discharge line parameters	
Parameters	Value	Parameters	Value
$l_{1-2,s}$	variation ⁴⁾	$l_{1-2,d}$	variation ⁴⁾
$l_{2-3,s}$	0.005 m	$l_{2-3,d}$	0.005 m
$l_{3-4,s}$	0.0065 m	$l_{3-4,d}$	0.0065 m
$l_{4-5,s}$	0.0100 m	$l_{4-5,d}$	0.0100 m
$l_{5-6,s}$	0.0700 m	$l_{5-6,d}$	0.0600 m
$l_{6-7,s}$	1.2400 m	$l_{6-7,d}$	1.8700 m
$A_{1-2,s}$	0.00120 m ²	$A_{1-2,d}$	0.00120 m ²
$A_{2-3,s}$	0.00038 m ²	$A_{2-3,d}$	0.00025 m ²
$A_{3-4,s}$	0.01678 m ²	$A_{3-4,d}$	0.01510 m ²
$A_{4-5,s}$	0.00051 m ²	$A_{4-5,d}$	0.00029 m ²
$A_{5-6,s}$	0.00051 m ²	$A_{5-6,d}$	0.00029 m ²
$A_{6-7,s}$	0.00051 m ²	$A_{6-7,d}$	0.00029 m ²
$h_{5-6,s}$	-0.07 m	$h_{5-6,d}$	0.0700 m
$h_{6-7,s}$	-0.35 m	$h_{6-7,d}$	0.6000 m
$W_{1-2,s}$	0.0300 m	$W_{1-2,d}$	0.0300 m
$W_{2-3,s}$	0.0120 m	$W_{2-3,d}$	0.0080 m
$W_{3-4,s}$	0.0400 m	$W_{3-4,d}$	0.0360 m
$D_{h1-2,s}$ ²⁾	0.0598 m	$D_{h1-2,d}$ ²⁾	0.0598 m
$D_{h2-3,s}$ ²⁾	0.0174 m	$D_{h2-3,d}$ ²⁾	0.0128 m
$D_{h3-4,s}$ ²⁾	0.0730 m	$D_{h3-4,d}$ ²⁾	0.0663 m
$D_{4-5,s}$	0.0254 m	$D_{4-5,d}$	0.0191 m
$D_{5-6,s}$	0.0254 m	$D_{5-6,d}$	0.0191 m
$D_{6-7,s}$	0.0254 m	$D_{6-7,d}$	0.0191 m
$\Sigma K_{1-2,s}$	0.00	$\Sigma K_{1-2,d}$	0.0000
$K_{2,s}$	variation ³⁾	$K_{2,d}$	variation ³⁾
$\Sigma K_{2-3,s}$	0.00	$\Sigma K_{2-3,d}$	0.0000
$\Sigma K_{3-4,s}$	0.00	$\Sigma K_{3-4,d}$	0.0000
$\Sigma K_{4-5,s}$	0.00	$\Sigma K_{4-5,d}$	0.0000
$\Sigma K_{5-6,s}$	0.8500	$\Sigma K_{5-6,d}$	0.9000
$\Sigma K_{6-7,s}$	5.5400	$\Sigma K_{6-7,d}$	5.8300

- 1) Reynolds number of fluid in the pump is lower than 2,300 at the given conditions.
- 2) The shape of pipe is not circular type. Therefore, hydraulic diameter, D_h , is used.

$$D_h = \frac{4A}{P} \quad (\text{A.1})$$

where, A is the cross sectional area

P is the wetted perimeter of the cross-section

- 3) Entrance areas at point 2,s and 2,d are changed periodically as shown in fig. 4.2 and 4.4. Therefore, it is assumed that sudden contraction and expansion occur at left and right sides of this points at the same time as shown in fig. A.1. The well-known loss coefficients of these are as follow:

$$K_2 = \left(1 - \frac{A_2}{A_{1-2}}\right)^2 \times \left(1 - \frac{A_{2-3}}{A_2}\right)^2 \quad (\text{A.2})$$

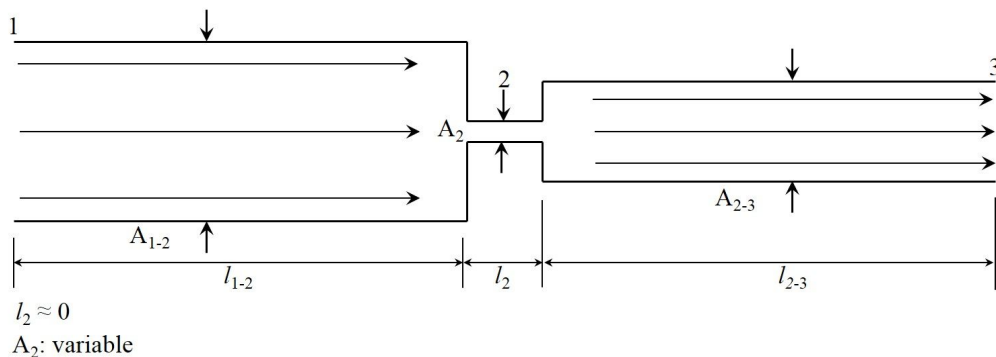


Fig.A.1. The flow in sudden contraction and expansion pipe.

A. Area of $A_{2,s}$

$$A_{2,s} = l_{2,s} \times W_j \quad (\text{A.3})$$

$$l_{2,s} = \left(r_o + \frac{h}{2} \right) \theta_{2,s} \quad (\text{A.4})$$

a. $2(\theta_{rel})_{\max} > \theta_t$

$$\textcircled{1} \quad 0 \leq \theta_{p1} < \frac{1}{2} \theta_t$$

$$\frac{1}{2} \theta_t - |\theta_{p1}| \quad (\text{A.5-a})$$

$$\textcircled{2} \quad \frac{1}{2} \theta_t \leq \theta_{p1} < \frac{3}{2} \theta_t$$

$$\theta_{front} \quad (\text{A.5-b})$$

$$\textcircled{3} \quad \frac{3}{2} \theta_t \leq \theta_{p1} < \phi - \frac{1}{2} \theta_t$$

$$\theta_{front} - \left(|\theta_{p1}| - \frac{3}{2} \theta_t \right) \quad (\text{A.5-c})$$

$$\textcircled{4} \quad (\theta_{rel})_{\max} + \frac{3}{2} \theta_t \leq \theta_{p2} < (\theta_{rel})_{\max} + \frac{5}{2} \theta_t$$

$$\theta_{back} \quad (\text{A.5-d})$$

$$\textcircled{5} \quad (\theta_{rel})_{\max} + \frac{5}{2} \theta_t \leq \theta_{p2} < \phi$$

$$\theta_{back} - \left(|\theta_{p2}| - (\theta_{rel})_{\max} - \frac{5}{2} \theta_t \right) \quad (\text{A.5-e})$$

b. $2(\theta_{rel})_{\max} \leq \theta_t$

$$\textcircled{6} \quad \frac{1}{2}\theta_t \leq \theta_{p1} < \frac{3}{2}\theta_t$$

$$\theta_{front} \tag{A.5-f}$$

$$\textcircled{7} \quad \frac{3}{2}\theta_t \leq \theta_{p1} < \frac{3}{2}\theta_t + 2(\theta_{rel})_{\max}$$

$$\theta_{front} - \left(|\theta_{p1}| - \frac{3}{2}\theta_t \right) \tag{A.5-g}$$

$$\textcircled{8} \quad \frac{3}{2}\theta_t + 2(\theta_{rel})_{\max} \leq \theta_{p1} < 2\theta_t + 2(\theta_{rel})_{\max}$$

$$\theta_{back} \tag{A.5-h}$$

$$\textcircled{9} \quad 0 \leq \theta_{p2} < \frac{1}{2}(\theta_t - 2(\theta_{rel})_{\max})$$

$$\theta_{back} \tag{A.5-i}$$

$$\textcircled{10} \quad \frac{1}{2}(\theta_t - 2(\theta_{rel})_{\max}) \leq \theta_{p2} < 2(\theta_{rel})_{\max}$$

$$\theta_{back} - \left(|\theta_{p2}| - \frac{1}{2}(\theta_t - 2(\theta_{rel})_{\max}) \right) \tag{A.5-j}$$

B. Area of $A_{2,d}$

$$A_{2,d} = l_{2,d} \times W_j \tag{A.6}$$

$$l_{2,d} = \left(r_o + \frac{h}{2} \right) \theta_{2,d} \tag{A.7}$$

$$\textcircled{1} \quad 0 \leq \theta_{p2} < (\theta_{rel})_{\max} - \frac{1}{2}\theta_t$$

$$\frac{1}{2}\theta_t + |\theta_{p1}| \tag{A.8-a}$$

$$\textcircled{2} \quad (\theta_{rel})_{\max} - \frac{1}{2}\theta_t \leq \theta_{p2} < \frac{1}{2}\theta_t$$

$$\theta_{front} \tag{A.8-b}$$

$$\textcircled{3} \quad \frac{1}{2}\theta_t \leq \theta_{p1} < \frac{1}{2}\theta_t + 2(\theta_{rel})_{\max}$$

$$|\theta_{p2}| - \frac{1}{2}\theta_t - (\theta_{rel})_{\max} \tag{A.8-c}$$

$$\textcircled{4} \quad \frac{1}{2}\theta_t + 2(\theta_{rel})_{\max} \leq \theta_{p1} < \frac{3}{2}\theta_t + 2(\theta_{rel})_{\max}$$

$$\theta_{back} \tag{A.8-d}$$

$$\textcircled{5} \quad \frac{3}{2}\theta_t + (\theta_{rel})_{\max} \leq \theta_{p2} < \phi$$

$$|\theta_{p1}| - 2(\theta_{rel})_{\max} - \frac{3}{2}\theta_t \tag{A.8-e}$$

4) Length of $l_{1-2,s}$ and $l_{1-2,d}$

$$l_{1-2,s} = \left(r_o + \frac{h}{2}\right) \times (\theta_{p2} - \theta_{p1}) \tag{A.9}$$

$$l_{1-2,d} = \left(r_o + \frac{h}{2}\right) \times (\theta_{p1} - \theta_{p2}) \tag{A.10}$$

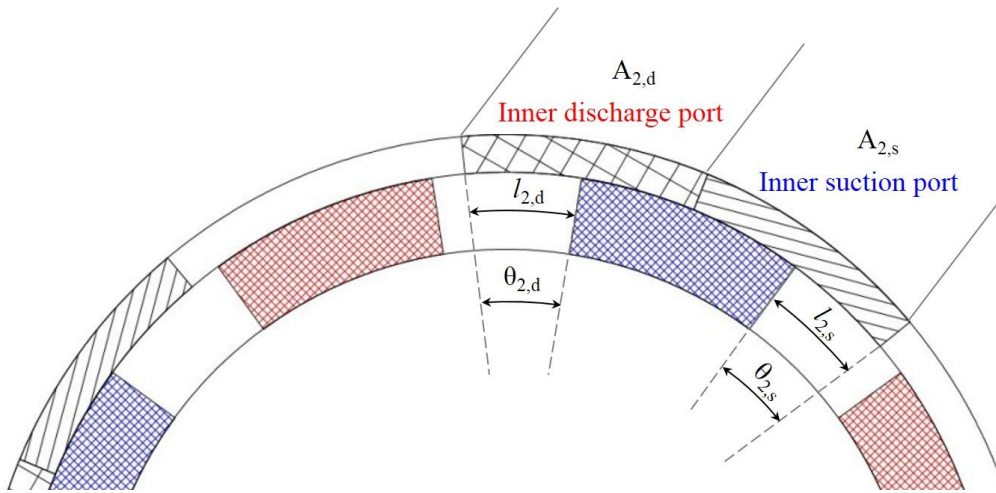


Fig.A.2. Dimensions of $A_{2,s}$, $A_{2,d}$, $l_{2,s}$, $l_{2,d}$, $\theta_{2,s}$, and $\theta_{2,d}$.

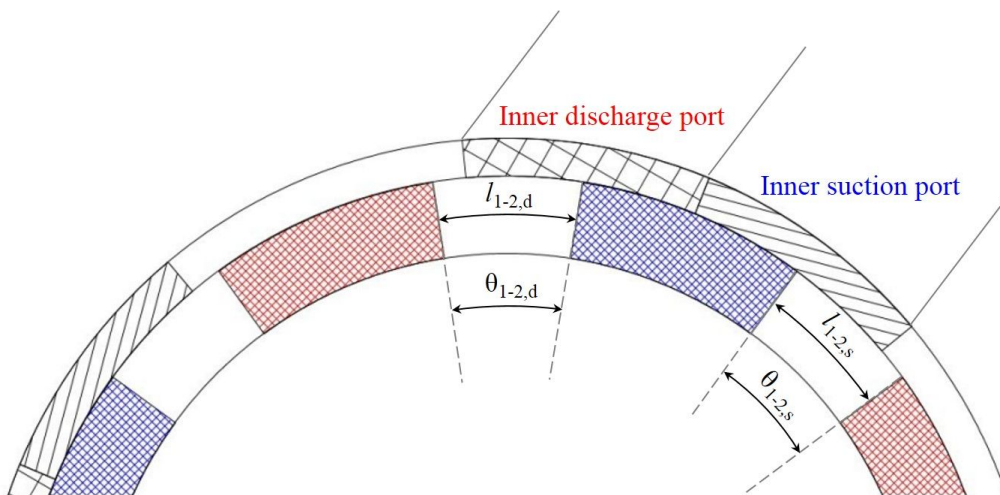


Fig.A.3. Dimensions of $l_{1-2,s}$, $l_{1-2,d}$, $\theta_{1-2,s}$ and $\theta_{1-2,d}$.

Appendix B : Pump performance curves

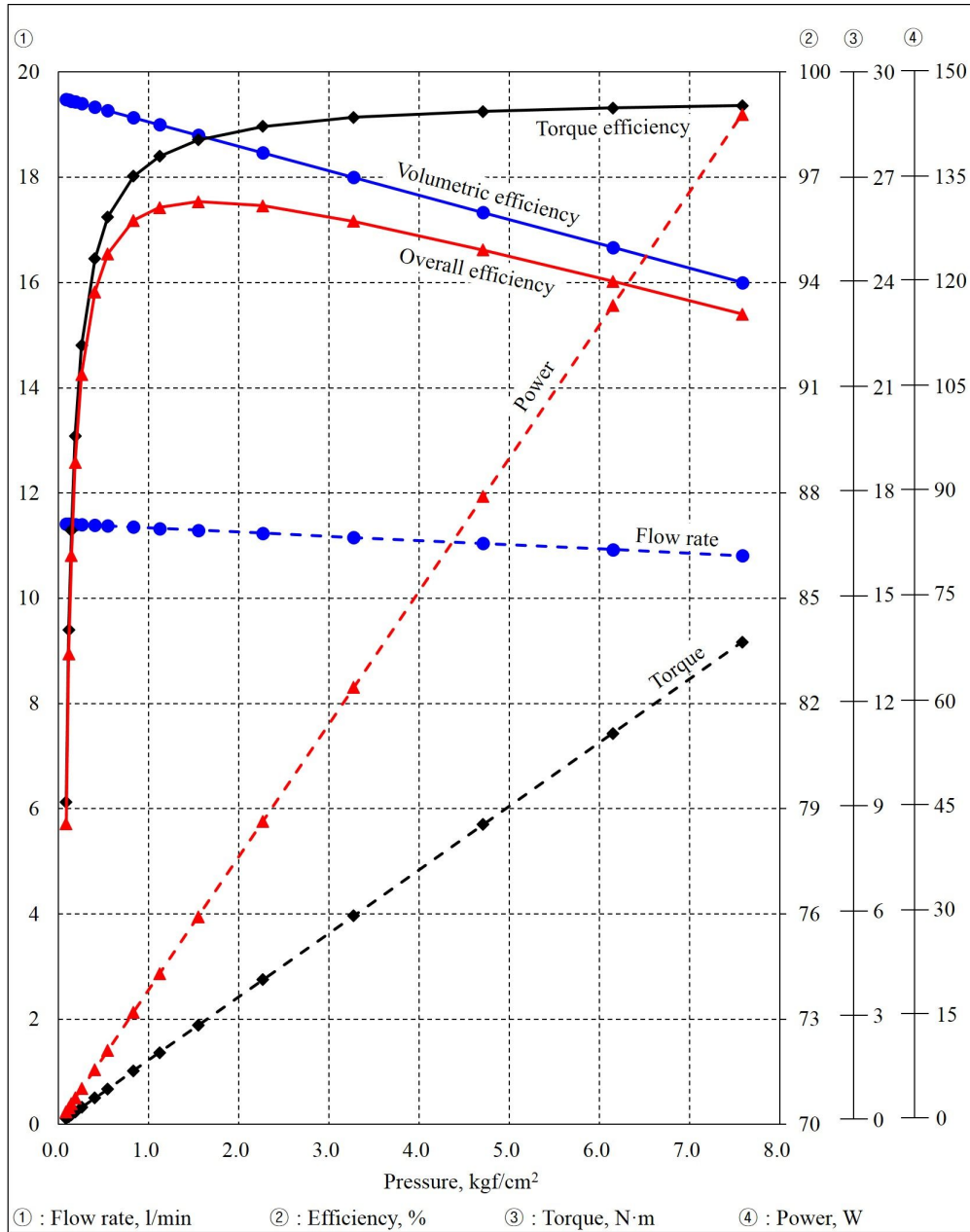


Fig.A.4. Performance curve when $N=4$, $\omega_c=100$ rpm, $d_1=d_2=0.06$ m, $h=14$ mm, $W=20.72$ mm

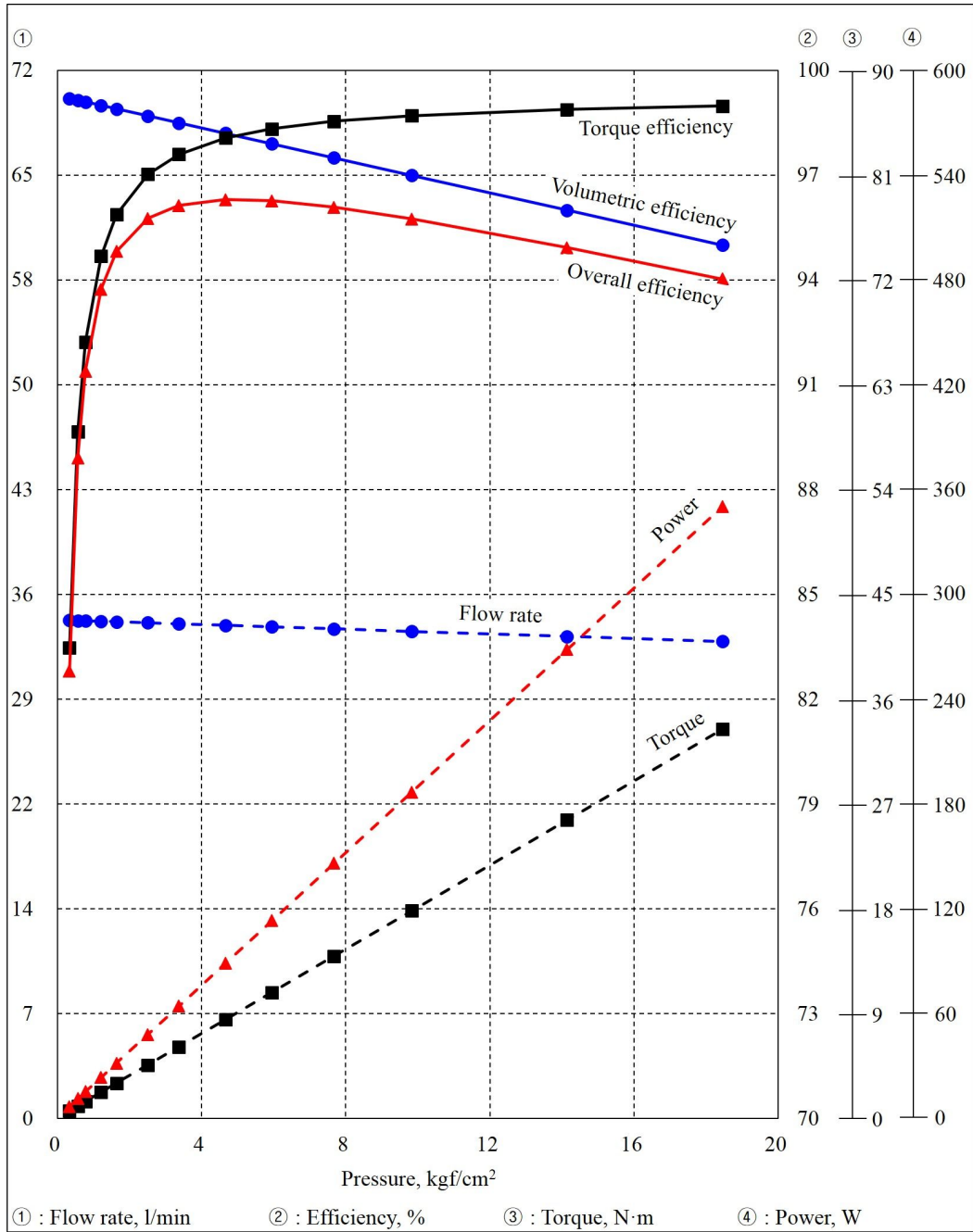


Fig.A.5. Performance curve when $N=4$, $\omega_c=300$ rpm, $d_1=d_2=0.06$ m, $h=14$ mm, $W=20.72$ mm

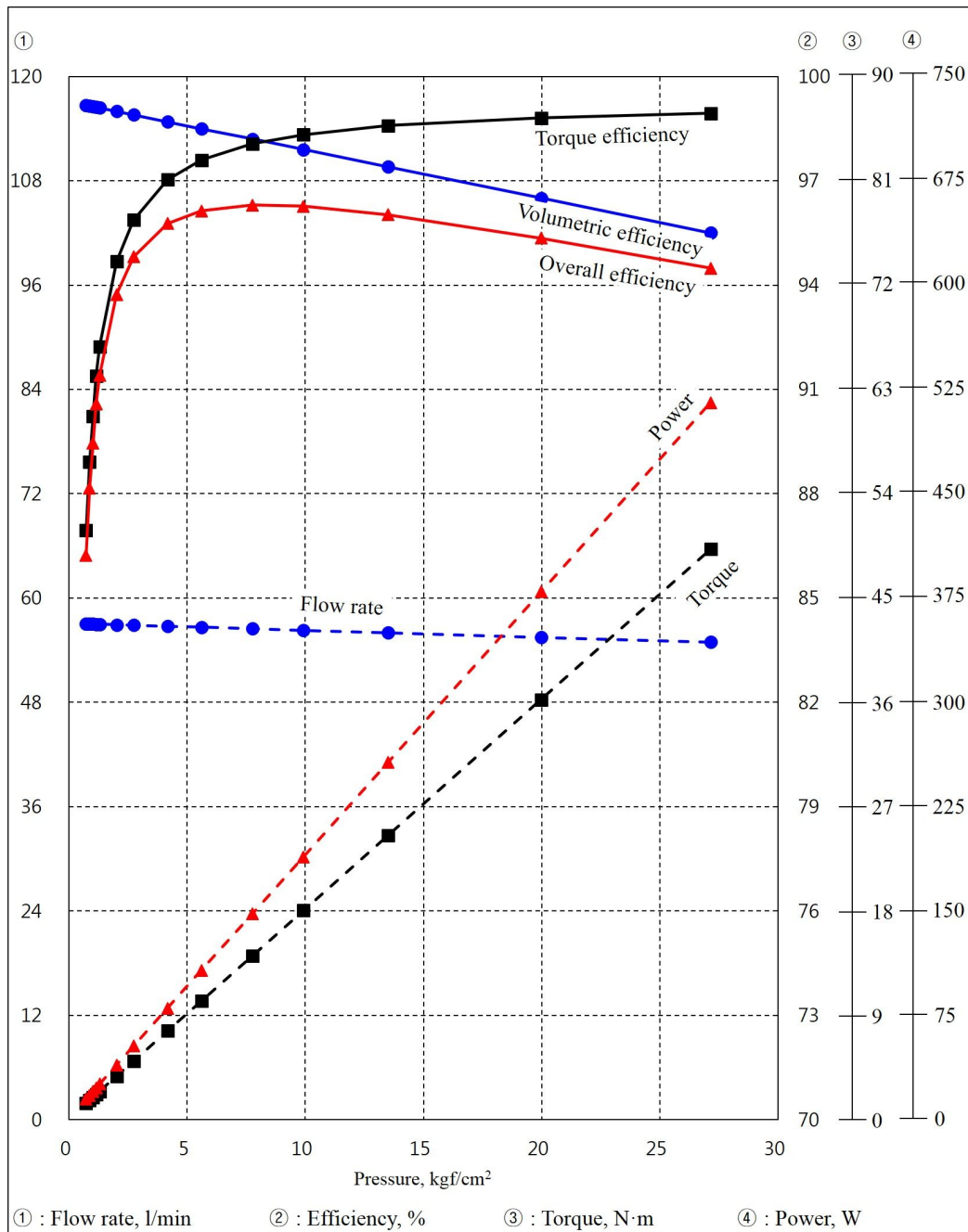


Fig.A.6. Performance curve when $N=4$, $\omega_c=500$ rpm, $d_1=d_2=0.06$ m, $h=14$ mm, $W=20.72$ mm

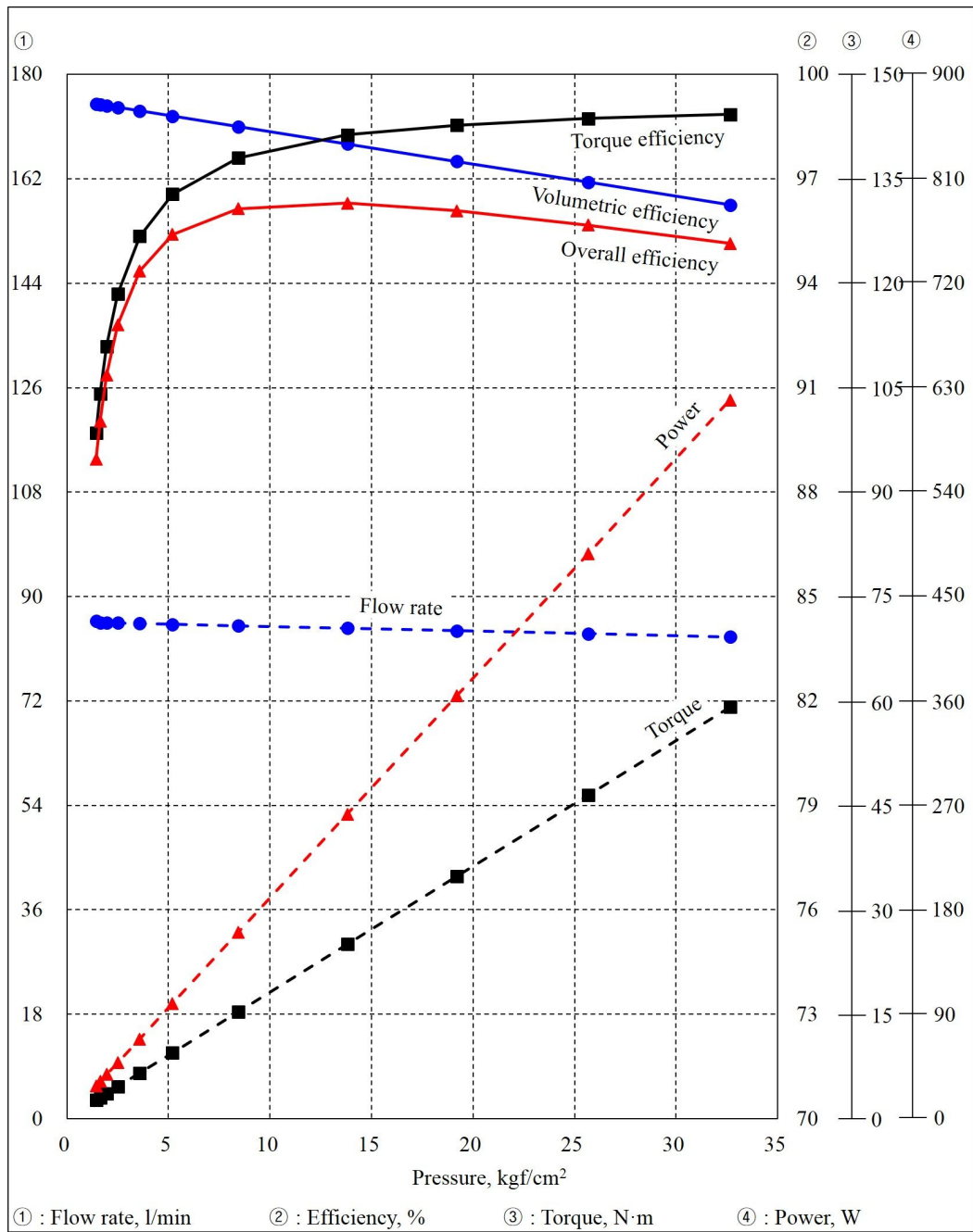


Fig.A.7. Performance curve when $N=4$, $\omega_c=750$ rpm, $d_1=d_2=0.06$ m, $h=14$ mm, $W=20.72$ mm

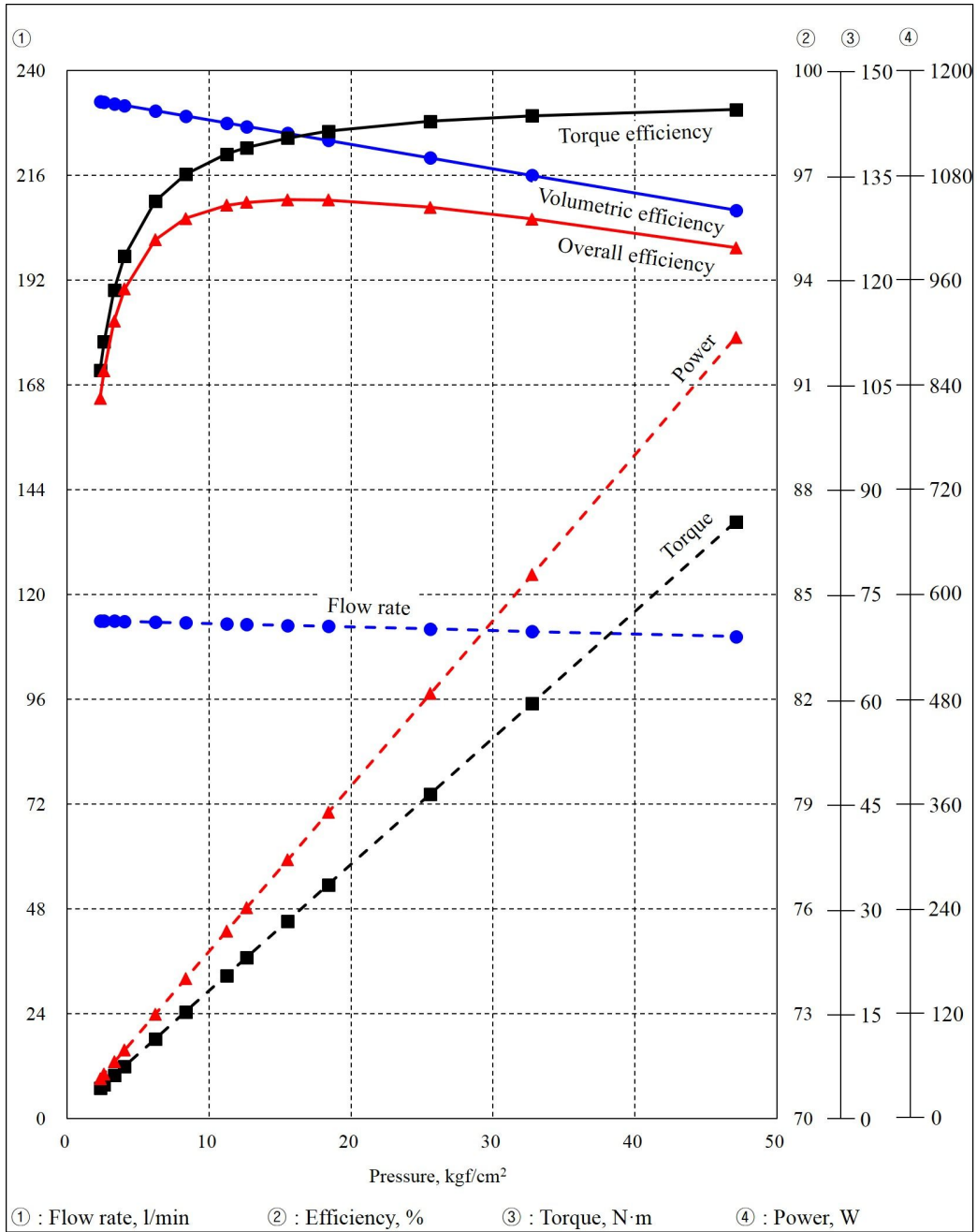


Fig.A.8. Performance curve when $N=4$, $\omega_c=1000$ rpm, $d_1=d_2=0.06$ m, $h=14$ mm, $W=20.72$ mm

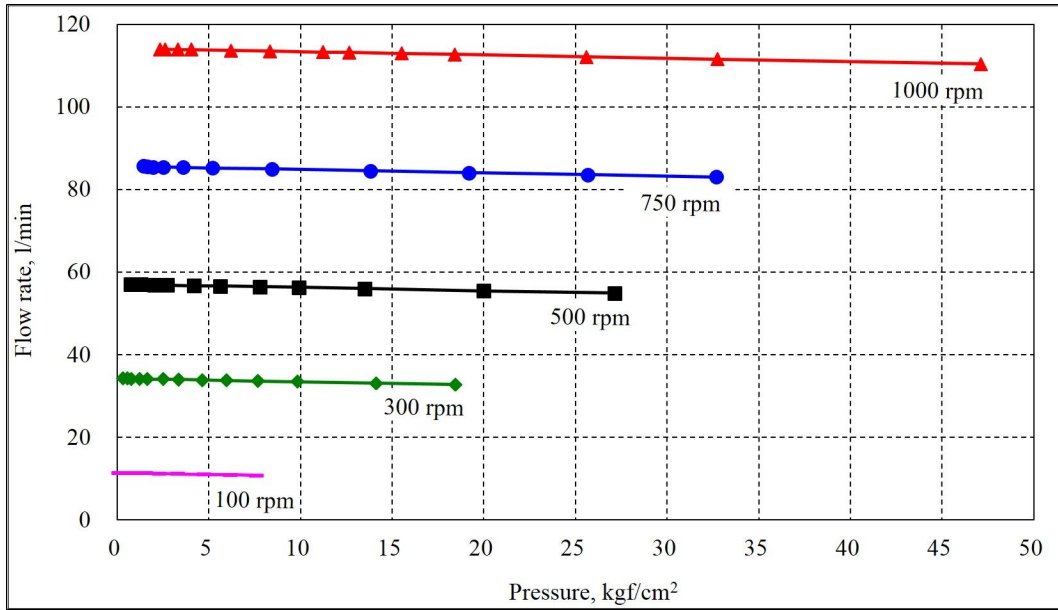


Fig.A.9. Comparison between flow rate vs pressure curves according to crank speed.

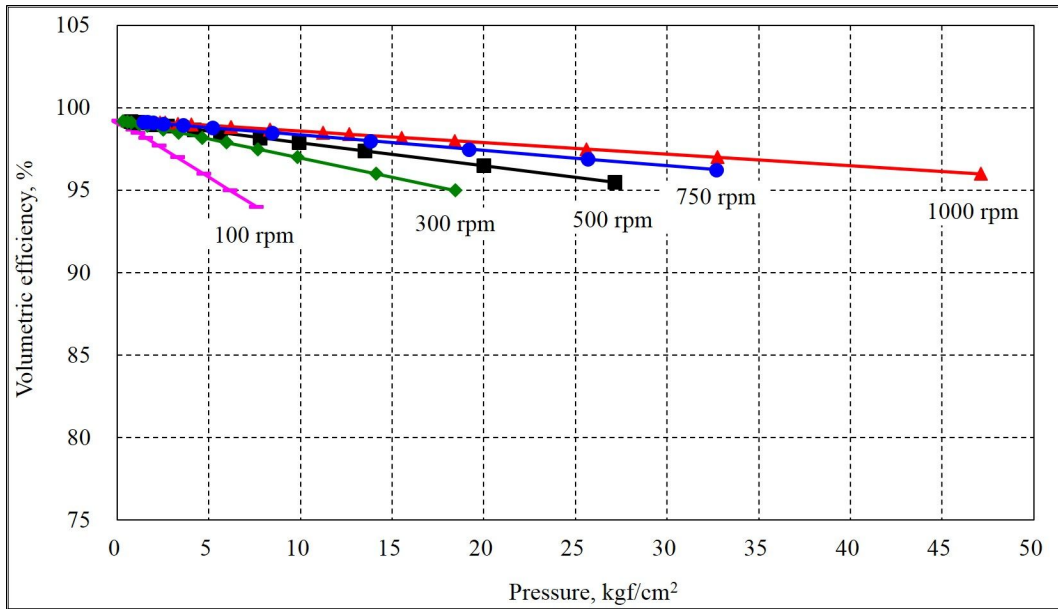


Fig.A.10. Comparison between volumetric efficiency vs pressure curves according to crank speed.

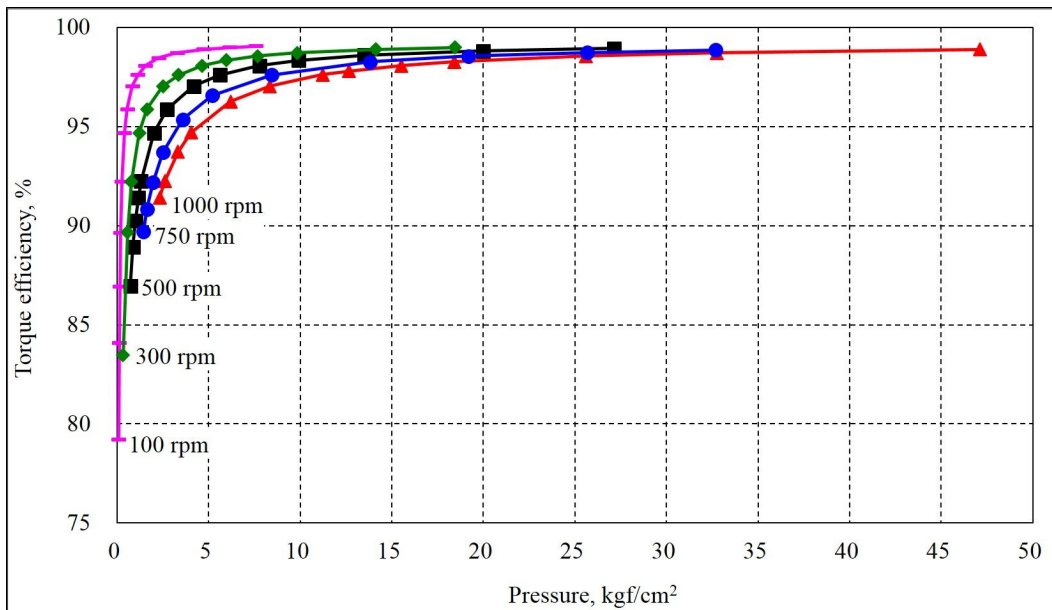


Fig.A.11. Comparison between torque efficiency vs pressure curves according to crank speed.

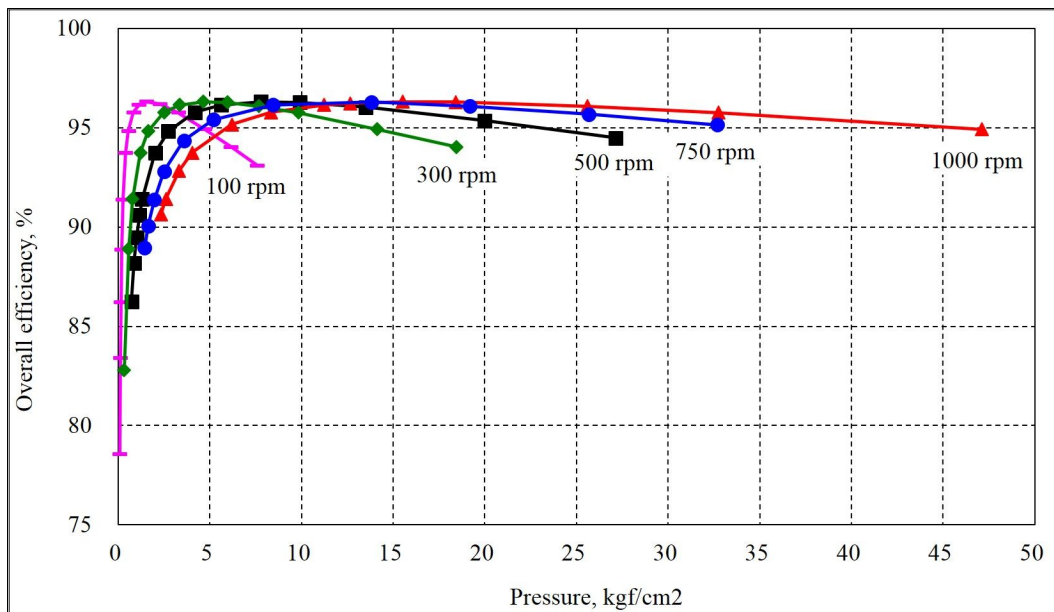
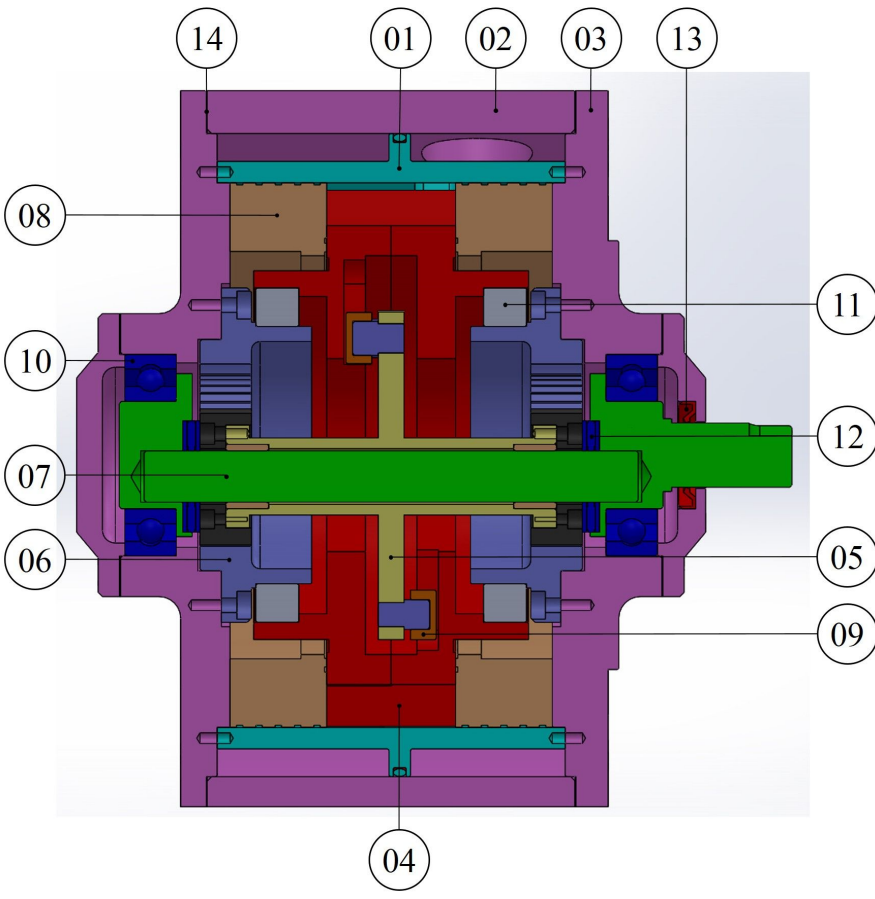


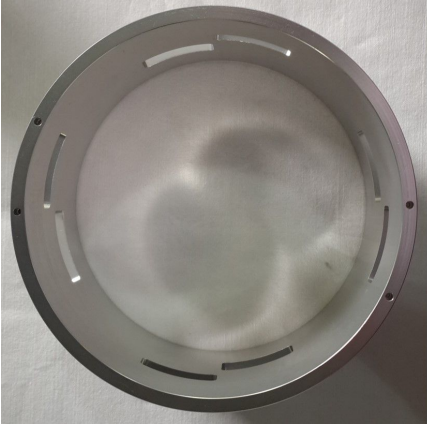
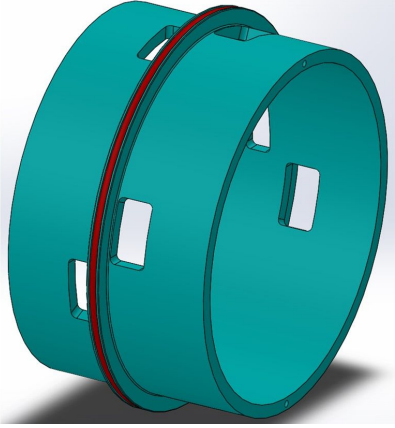
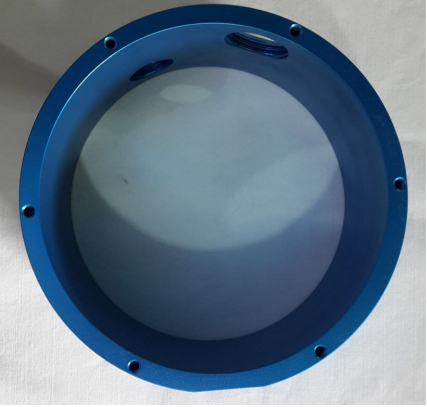
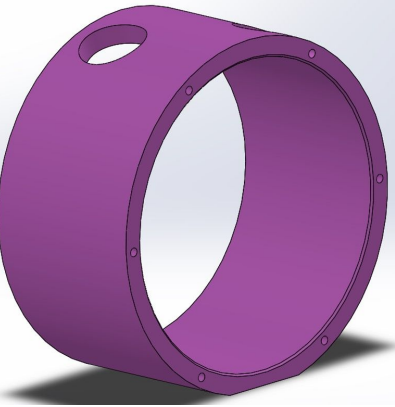
Fig.A.12. Comparison between overall efficiency vs pressure curves according to crank speed.

Appendix C : Manufacturing specifications

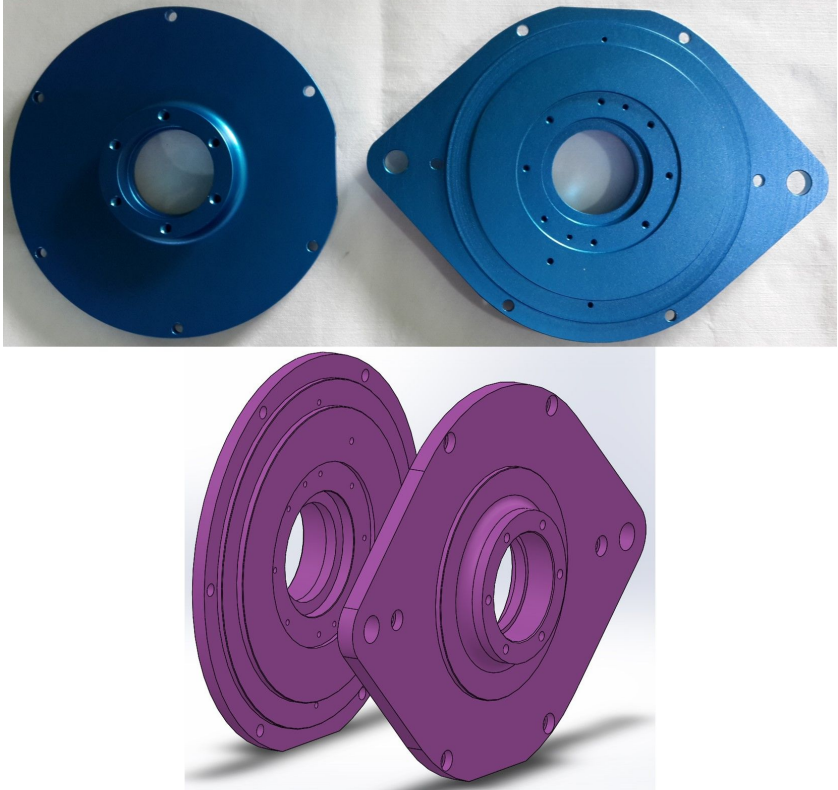
1. Clap pump assembly cross section

Picture		
parts list	<ul style="list-style-type: none"> 01 : Inner housing 02 : Outer housing 03 : Side covers 04 : Rotors 05 : Shaft link-pins-gears 06 : Fixed internal gears 07 : Crank 	<ul style="list-style-type: none"> 08 : Sliding plates 09 : Pin slide rings 10 : Ball bearings 11 : Roller bearings 12 : Needle roller bearings 13 : Oil seals 14 : Gaskets

2. Inner and outer housing

<p>Picture</p>	<div style="display: flex; justify-content: space-around; align-items: center;"> <div style="text-align: center;">  <p>Inner housing</p> </div> <div style="text-align: center;">  </div> </div> <div style="display: flex; justify-content: space-around; align-items: center; margin-top: 20px;"> <div style="text-align: center;">  <p>Outer housing</p> </div> <div style="text-align: center;">  </div> </div>
<p>Material</p>	<p>A6061-T6(KS D 6701)</p>
<p>Machining process</p>	<p>Lathe, milling, and grinding</p>
<p>Heat treatment</p>	<p>Anodizing</p>

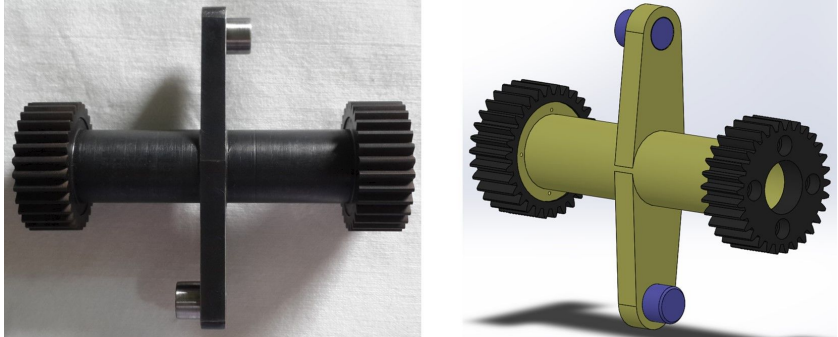
3. Side covers

Picture	 The image displays two physical blue side covers and their corresponding 3D CAD models. The physical parts are circular with a central hole and four mounting holes around the perimeter. The CAD models are shown in a purple color, illustrating the same design from a different perspective.
Material	A6061-T6(KS D 6701)
Machining process	Lathe, milling, and grinding
Heat treatment	Anodizing

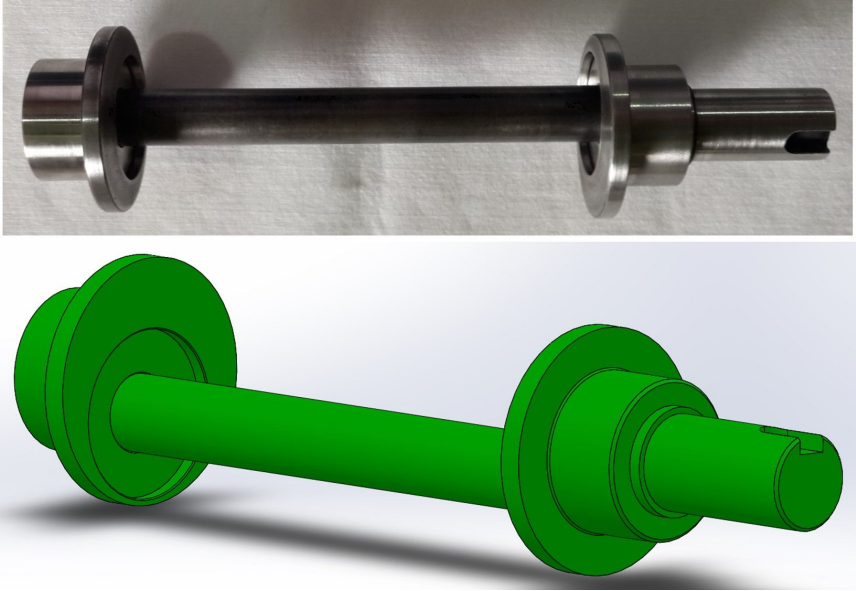
4. Rotors

<p>Picture</p>	
<p>Material</p>	<p>SCM 440(KS D 3711)</p>
<p>Machining process</p>	<p>Wire cutting, Lathe, milling, and grinding after assembling two rotor pairs</p>
<p>Heat treatment</p>	<p>Carbonizing</p>

5. Shaft link-pins-gears and fixed internal gears

<p>Picture</p>	
	<p style="text-align: center;">Shaft link-pins-gears</p>  <p style="text-align: center;">Fixed internal gears</p>
<p>Material</p>	<p>SCM 440(KS D 3711)</p>
<p>Machining process</p>	<p>Wire cutting, Lathe, milling, and grinding</p>
<p>Heat treatment</p>	<p>Shaft link-pins : Tempering after carbonizing Gear and fixed internal gear : induction surface hardened</p>

6. Crank

<p>Picture</p>	
<p>Material</p>	<p>SM 45C(KS D 3752)</p>
<p>Machining process</p>	<p>Lathe, milling, and grinding</p>
<p>Heat treatment</p>	<p>Carbonizing</p>

7. Sliding plates

<p>Picture</p>	
<p>Material</p>	<p>CAC203(KS D 6024)</p>
<p>Machining process</p>	<p>Lathe, milling, and grinding</p>
<p>Heat treatment</p>	<p>-</p>

8. Pin slide rings

Picture	
Material	SCM 440(KS D 3711)
Machining process	Lathe, milling, and grinding
Heat treatment	Tempering after carbonizing

회전 클랩 기구를 이용한 로터리 펌프 개발에 관한 연구

심 정보

국문 초록

왕복 슬라이더-크랭크 기구를 대체하기 위하여 많은 회전형 기구가 제안되었음에도 불구하고 반켈 엔진을 제외한 대부분의 아이디어가 상업화에 성공하지 못하였을 뿐만 아니라 기구 및 작동 원리 분석이외의 학문적 성과도 많이 보고되지 않았다. 하지만 가공 기술 등의 발달로 인하여 관련 연구들이 다시 주목받고 있다.

이러한 연구의 일환으로 수행된 본 연구에서는 다른 회전형 기구에 비하여 상대적으로 구조가 간단한 회전 클랩 기구를 펌프로 구현이 가능하도록 개선·발전시켰으며, 프로토타입 펌프의 성능 시험을 통하여 검증한 해석 모형을 이용하여 성능을 예측하였다.

이 연구를 통하여 먼저, 회전 클랩 기구의 기본 작동 원리와 주요 설계 변수에 대하여 제시하였으며, 핀과 로터의 기구학 분석을 통하여 변위, 속도 및 가속도의 벡터 식을 개발하였다. 뿐만 아니라 허용 가능한 기어 잇수와 로터 크기 내에서 적정 크랭크 반경과 핀 사이의 거리를 결정하기 위한 주요 설계 변수 사이의 관계 또한 구명하였다.

인볼류트 타입 기어를 사용한 내접 기어와 샤프트 링크 기어의 설계 조건에 대하여 분석한 결과, 인볼류트 타입 기어를 사용하여 펌프를 설계하는 것은 기어의 3가지 간섭 조건과 강도 문제 등으로 인하여 고압 및 저유량 조건일 경우

매우 제한적이었으나 이는 변형 트로코이드 기어를 사용하면 해결할 수 있다.

압력, 구동 토크 및 펌프의 효율 특성 분석을 통하여 성능 해석 모형을 개발하였으며, 프로토타입 펌프의 성능 시험을 통하여 이를 검증하였다. 이 모형을 활용하여 펌프 성능에 영향을 미치는 주요 설계 변수를 최적화 한 후 회전 클랩 펌프의 성능을 예측하였다.

분석 결과로 보았을 때 회전 클랩 펌프는 주어진 사용 조건에서 기존의 로터리 펌프와 유사한 성능을 보였으며 왕복식 펌프에 비하여 소음 · 진동이 작고 기존의 로터리 펌프에 비하여 상대적으로 유체를 이송하는 공간인 로터와하우징 사이의 부피가 크기 때문에 소형화가 가능하며, 고점도 및 유체 전단에 민감한 유체를 이송하는데 유리할 것으로 판단된다.

주요어 : 로터리 펌프, 로터리 클랩 메커니즘, 펌프 성능, 펌프 효율, 펌프 슬립

학번 : 2007-30311

